University of Nevada, Reno

**Computational Study of Nonadiabatic Spin-Forbidden Processes
in Metal-Sulfur Proteins**

A dissertation submitted in partial fulfillment of the
requirements for the degree of Doctor of Philosophy in
Chemistry

by

Danil S. Kaliakin

Dr. Sergey Varganov/Dissertation Advisor

May, 2017

THE GRADUATE SCHOOL

We recommend that the dissertation
prepared under our supervision by

DANIL S. KALIAKIN

Entitled

**Computational Study of Nonadiabatic Spin-Forbidden Processes
in Metal-Sulfur Proteins**

be accepted in partial fulfillment of the
requirements for the degree of

DOCTOR OF PHILOSOPHY

Sergey A. Varganov, Ph. D., Advisor

David M. Leitner, Ph. D., Committee Member

Alla Safronova, Ph. D., Committee Member

Jason M. Shearer, Ph. D., Committee Member

Victor R. Vasquez, Ph. D., Graduate School Representative

David W. Zeh, Ph. D., Dean, Graduate School

May, 2017

Abstract

We investigate the role of nonadiabatic spin-forbidden transitions in the catalytic and electron transfer processes in the active sites of metal-sulfur proteins. We focus on two biologically important metal-sulfur proteins, namely the [NiFe]-hydrogenase enzyme capable of catalytic H_2 oxidation and proton reduction, and the electron transfer protein rubredoxin. The synthetic analogs of [NiFe]-hydrogenase are the promising inexpensive alternative to platinum-based catalysts. Our studies indicate that nonadiabatic transitions between the electronic states with different spin multiplicities could be important for the catalytic activity of [NiFe]-hydrogenase. These transitions are mediated by spin-orbit coupling between the quasidegenerate singlet and triplet states of the Ni(II) center. As for rubredoxin, its ability to transfer electrons makes this small protein a promising starting model for the development of future self-sufficient biosensors and the novel catalysts. The presence of multiple low-lying electronic states with different spin multiplicities in the active site of rubredoxin indicates a possibility of nonadiabatic transitions during the electron transfer processes.

The probabilities and the rates of nonadiabatic spin-forbidden transitions in the metal-sulfur proteins predicted using the nonadiabatic transition state theory (NA-TST). The NA-TST calculations require the knowledge of molecular properties at a minimum energy crossing point (MECP), an analog of transition state in the traditional transition state theory. Therefore, part of the work was dedicated to implementation of the MECP search algorithm for the fragment molecular orbital (FMO) method that can be applied to systems with thousands of atoms, including large models of metal-sulfur proteins. The last part of the dissertation is dedicated to the design and manufacture of the 3D-printed

models of potential energy surfaces for different chemical reactions. These models proved to be valuable for the chemical dynamics and kinetics demonstrations in graduate and undergraduate chemistry classes.

Table of Contents

List of Tables

Chapter III Tables

Chapter IV Tables

List of Figures

Chapter I Figures

Chapter II Figures

Chapter III Figures

orbitals of Fe(II); (b) back-donation from $3d_{xz}$ and $3d_{yz}$ orbitals of Fe(II) to σ*-orbital of H_2. (75)

Figure 4. Energies of the singlet and triplet states of the active site as a function of torsion angle φ calculated with bs1 basis set and four different functionals: (a) PBE, (b) BP86, (c) TPSS and (d) B3LYP. The methyl groups and Fe ligands are not shown for clarity. The values of torsion angle are not equally spaced because of small uncontrollable rotations of the thiolate ligands during constrained geometry optimization. (78)

Figure 5. Landau-Zener transition probabilities between the singlet and triplet states of the bare active site and the active site with bound H_2 as functions of temperature. The mass-weighted gradients and spin-orbit coupling were calculated with PBE and MCQDPT2, respectively, using def2-TZVP basis set. (80)

Chapter IV Figures

Figure 1. Rubredoxin active site model. Torsion angle α describes rotation of planes p_1 (S1-Fe-S2) and p_2 (S3-Fe-S4) with respect to each other. Angle β is defined as the angle between planes S1-Fe-S3 and S2-Fe-S4; angle γ is defined as the angle between planes S2-Fe-S3 and S1-Fe-S4. (92)

Figure 2. Twist angles α, β, and γ of the $Fe(SCH_3)_4^0$ complex as functions of geometry. Geometry changes from the quintet state minimum (geometry 1) to the triplet state minimum (geometry 11). (100)

Figure 3. Energies of the spin states as functions of geometry interpolated between the minima of two crossing states. (a) Triplet and quintet states of the $Fe(SCH_3)_4^{2-}$ complex. (b) Quartet and sextet states of the $Fe(SCH_3)_4^-$ complex. (c) Triplet and quintet states of the $Fe(SCH_3)_4^0$ complex. Geometries of the minima and MECP (similar to the crossing geometries) are shown. Calculations were done at the PBE/def2-TZVP level of theory. (101)

Figure 4. Rate constants for transitions between electronic spin states of rubredoxin active site models calculated using LZ probabilities (solid lines) and assuming completely spin-allowed kinetics with unit probability (dashed lines) as functions of internal energy. Rate constant k_1 (red lines) represents the transition from high-spin state to low-spin states, whereas k_{-1} (blues lines) is the rate constant for opposite process. (a) Quintet-triplet transitions in the $Fe(SCH_3)_4^{2-}$ complex. (b) Sextet-quartet transitions in the $Fe(SCH_3)_4^{1-}$ complex. (c) Quintet-triplet transitions in the $Fe(SCH_3)_4^0$ complex. The geometries, energies, energy gradients and Hessians were obtained at the PBE/def2-TZVP level of theory. The SOC constants were calculated at the CASCI/def2-TZVP level of theory using the high-spin ROHF molecular orbitals. (104)

Figure 5. Molecular orbitals of the rubredoxin active site models at the MECP geometries: (a) $[Fe(SCH_3)_4]^{2-}$ complex; (b) $Fe(SCH_3)_4]^-$ complex; (c) $[Fe(SCH_3)_4]^0$ complex. Solid blue arrows represent the electrons that have the same spin in both electronic states, whereas red dashed arrows show the electrons that change spin as a result of spin-forbidden transition. Numbers labeling the orbitals that are expected to have the largest contribution to the SOC matrix elements are in red. Also reported are the orbital energies in hartree. These high-spin ROHF/def2-TZVP orbitals were used to calculate SOC at the CASCI/def2-TZVP level of theory. (107)

Chapter V Figures

Figure 1. (a) Three models of rubredoxin protein used in the study. (b) FMO fragmentation schemes for the three models. Model 1 contains 815 fragments of solvent with five water molecules in each, and one water fragment with four water molecules. Water molecules are omitted from the picture for clarity. (120)

Figure 2. Two representations of the crossing PES of electronic states with different spin multiplicities. (a) The three-dimensional representation showing the perpendicular and parallel gradients, as defined in GAMESS. (b) The two-dimensional representation of along the minimum energy reaction pathway. (123)

Figure 3. (a) Detailed representation of model 1 showing the structure of active site fragment, water fragments, and the solvation shell. (b) The scaling curve showing the time for one energy calculation as a function of the number of computer cores. Calculations are performed with the FMO1-LC-BPBE/def2-SV(P) level of theory. (125)

Figure 4. The scheme of the FMO-MECP search algorithm. (126)

Figure 5. Time for gradient calculations as a function of number of computer cores. Calculations were performed with the FMO2-UHF/3-21G level of theory. (128)

Figure 6. Comparison between the conventional MECP and FMO-MECP geometries. (a) An overlap between the MECP and FMO-MECP geometries. (b) The energies of quartet/sextet minima and MECP obtained with FMO-DFT and conventional DFT methods. The calculations were performed at the FMO2-LC-BPBE/6-31G and LC-BPBE/6-31G levels of theory. (129)

Figure 7. Torsion angles of Fe(III) rubredoxin active site at the MECP between the quartet and sextet electronic states. The values of torsion angles are obtained with the conventional MECP and FMO-MECP algorithms. The calculations were performed at the FMO2-LC-BPBE/6-31G and LC-BPBE/6-31G levels of theory. (130)

Chapter VI Figures

Figure 1. (a) Traditional 2D representation of a reaction path. (b) 3D printed potential energy surface for triatomic molecule ABC. The minimum corresponding to equilibrium geometry (Min ABC) and two possible reaction paths are shown. Path 1 corresponds to reaction ABC ⇆ A + BC. Path 2 corresponds to reaction ABC ⇆ AB + C. Transition states of these reaction paths are labeled as TS1 and TS2, respectively. The size of the 3D printed model is 12.5×12.5×4.5 cm.   (140)

Figure 2. Steps for computing and printing the 3D surface models.   (143)

Figure 3. Collinear potential energy surface for H_2+H reaction. (a) Reaction coordinates defined as the interatomic distances r_1 and r_2. (b) STL model with the minimal energy reaction path (dashed curve) and transition state (TS). (c) 3D printed PES model with two dissociation channels (H1-H2 + H3 and H1 + H2-H3).   (144)

Figure 4. PES cross section associated with rotations of two methyl groups in 1-fluoro-2-methylpropene. (a) Rotations of methyl groups are defined by the dihedral angles φ_1 and ϕ_2. (b) Structures of the minimum (Min), two transition states (TS1 and TS2), and second-order saddle point (SP). (c) 3D printed model with minimum energy reaction paths shown by dashed curves.   (146)

Figure 5. Funnel surface of protein folding. (a) STL model generated from analytical function using Mathematica and post processed in Blender. (b) 3D printed free energy surface. Global and two local minima corresponding to different protein conformations are shown.   (148)

Figure 6. PES of hypothetical linear triatomic molecule ABC. (a) Geometry of ABC molecule with labeled atoms and bond lengths. (b) STL model generated from analytical function using Mathematica and post processed in Blender. (c) 3D printed model of PES. Minimum (Min) and two transition states (TS1, TS2) are labeled. Dashed curves show three minimum energy reaction paths.   (150)

Figure 7. Model PES for adsorption on a surface. (a) STL model generated with Mathematica and post processed in Blender. (b) 3D printed model. Minima (Min), transition states (TS), and second-order saddle points (SP) are labeled.
Dashed lines show the minimum energy reaction paths for surface diffusion of adsorbed molecules or atoms.   (151)

Figure 8. Double minimum surface. (a) STL model generated in Mathematica and post processed in Blender. (b) 3D printed model with labeled transition state (TS) and global (Min 1) and local (Min 2) minima. Dashed curve shows the minimum energy reaction path.   (153)

Chapter I. Introduction

I. Context

In this work, we explore the importance of *nonadiabatic spin-forbidden transitions*, nonradiative transitions between the electronic states with different spin multiplicities, for the catalytic and electron transfer processes in the active sites of metal-sulfur proteins. Theoretical and computational studies are focused on two systems of high biological importance: the metalloenzyme [NiFe]-hydrogenase capable of catalytic hydrogen oxidation/reduction, and the electron transfer protein rubredoxin. This work aims to provide insight into the fundamental aspects of the metal-sulfur clusters functionality in biological systems and could help in the development of novel bioinspired catalysts and medications. The synthetic analogs of [NiFe]-hydrogenase are the promising inexpensive alternative to platinum-based catalysts.[1] Moreover, the [NiFe]-hydrogenase is the crucial element of life cycle of the human pathogen Salmonella enterica.[2–4] Thus, a better understanding of the [NiFe]-hydrogenase functions could facilitate the development of efficient drugs targeting Salmonnela enterica.[3] As for rubredoxin, the ability of this protein to transfer electrons is relevant to the design and manufacture of bionanowires,[5] thus the synthetic models of rubredoxin could be used in the novel self-sufficient biosensors.[5–7] The knowledge about the functionality and structure of rubredoxin could be also used in the design of new catalysts.[8] The structure, properties and biological roles of rubredoxin and [NiFe]-hydrogenase are discussed in Chapter I.

The presence of multiple low-lying electronic states with different spin multiplicities in the active site of rubredoxin indicates the possibility of nonadiabatic

transitions during electron transfer in this protein.[9,10] As for the active site of [NiFe]-hydrogenase, our previous studies indicate the possibility of nonadiabatic transitions between the electronic states with different spin multiplicities upon the change in coordination of the terminal thiolate ligands on the Ni(II) center from planar to tetrahedral.[11,12] We believe that the presence of nonadiabatic transitions in the active sites of rubredoxin and [NiFe]-hydrogenase is an important factor that must be accounted for in any study of the reaction mechanisms in these metal-sulfur proteins.

The quantitative description of the nonadiabatic transition probabilities and rates in metal-sulfur proteins performed using the nonadiabatic transition state theory (NA-TST).[13–15] The main aspects of NA-TST, as well as the electronic structure methods used to obtain the molecular properties required for the NA-TST rate calculations, are described in Chapter II. The studies of nonadiabatic transitions in the active sites of [NiFe]-hydrogenase and rubredoxin are presented in Chapters III and IV, respectively.

The accurate description of nonadiabatic transitions in the active sites of metal-sulfur proteins requires the inclusion of protein chains in the computational models. Standard methodology of nonadiabatic transition state theory (NA-TST) has a limitation for the size of models that could be used during the search of the minimum energy crossing point (MECP), which plays the same role in NA-TST as the transition state in the traditional TST. Therefore, part of the work was dedicated to the development of the MECP search algorithm for the fragment molecular orbital (FMO) method that is applicable to large protein models. The development and validation of this new FMO-MECP search algorithm is discussed in Chapter V.

Chapter VI is focused on the design and production of 3D-printed models of potential energy surfaces (PESs) for demonstrations in chemistry classes. The produced PES models provide a hands-on approach to teaching complex concepts of physical chemistry, and could serve as educational tools for visually impaired students.[16] Finally, the conclusions and future outlook are discussed in Chapter VII.

II. Hydrogenase Proteins

Hydrogenases are the proteins that are capable of oxidation of molecular hydrogen and reduction of protons.[17,18] This ability results in hydrogenases playing crucial roles in the life cycles of many chemotrophs using hydrogen as their energy source.[19] Hydrogenase-utilizing chemotrophs include archaea, bacteria and some of the eukaryotes.[20] The main types of hydrogenases are [NiFe]-, [FeFe]- and [Fe]-hydrogenases.[19,21–24] All three types of hydrogenases have different structural features but contain the active sites with the Fe or NiFe metal centers.[19]

Chemotrophs were forced to develop their way of energy production due to unusual conditions of their natural environment associated with lack of oxygen and light. For example, many bacteria and archaea that utilizes hydrogenases are found deep in the ocean. Thus, most of the hydrogenases have no need for oxygen resistance since this factor is not essential for the survival of their host.[25] However, some of the [NiFe]-hydrogenases are capable of functioning under both anaerobic and aerobic conditions.

The O_2-tolerance of [NiFe]-hydrogenases allows for a very broad application of these proteins and their synthetic analogs, unlike other two types of hydrogenases with catalytic activity limited to anaerobic conditions.[26] In terms of functionality of [NiFe]-

hydrogenase, there is a catalytic bias towards oxidation of molecular hydrogen.[18,27] However, electrochemical studies show that reversible catalytic activity is possible for [NiFe]-hydrogenase, and the reaction direction can be controlled by change of pH and the redox potential.[18,28–30] Reversible catalytic activity and oxygen tolerance of [NiFe]-hydrogenase makes this enzyme a highly active research topic of microbial bioenergetics.[1]

A. Classification of Hydrogenases

Currently, [FeFe]-hydrogenase arguably is the most studied type of hydrogenase. The active site of [FeFe]-hydrogenase consist of the diiron subcluster [2Fe] that is connected to the cubane cluster [4Fe-4S] through a cysteine residue. The diiron subcluster [2Fe] contains two metal centers that are ligated with CN^-, CO and two sulfur bridge-heads. Most of [FeFe]-hydrogenases contain a single catalytic active site (H-cluster). However, some [FeFe]-hydrogenases contain multiple subunits and could be as complex as heterotetramers.[21] Second type of hydrogenases is the monometallic [Fe]-hydrogenases. This type is less common than other hydrogenases and could be found only in methanogenic archaea. The active sites of [FeFe]- and [Fe]-hydrogenases are shown in Figure 1.
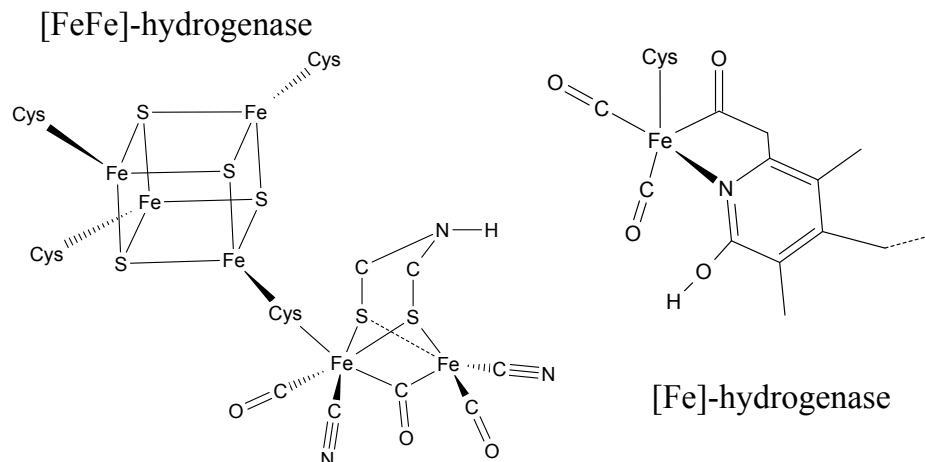
Figure 1. The active sites of [FeFe]- and [Fe]-hydrogenases.

The [Fe]-hydrogenase catalyzes the reversible reduction of methenyl-H4MPT$^+$ with H_2 to methylene-H4MPT, which is one of the crucial steps in methanogenesis. Unlike other types of hydrogenases, [Fe]-hydrogenase does not include any metal-sulfur clusters, but rather contains a unique Fe-guanylylpyrodinol cofactor. Moreover, the H_2 activation in this particular type of hydrogenases occurs only in the presence of the substrate.[21]

Finally, [NiFe]-hydrogenase is the protein that consists of two subunits that often referred as the α (large) and β (small) subunits. The large subunit (≈60 kDa) includes the active site itself, which is directly responsible for conversion of hydrogen, while the small subunit (≈35 kDa) contains three iron-sulfur clusters that carry electrons to and from the active site. The active site of [NiFe]-hydrogenase is bimetallic and contains the Fe and Ni metal centers. The Fe center is coordinated by two CN$^-$ and one CO ligand, while the Ni center is surrounded by four cysteine ligands, two of which are the bridging

ligands between the Fe and Ni centers.[31] The subunits of [NiFe]-hydrogenase, the active site, and the iron-sulfur clusters of β subunit are depicted on Figure 2.
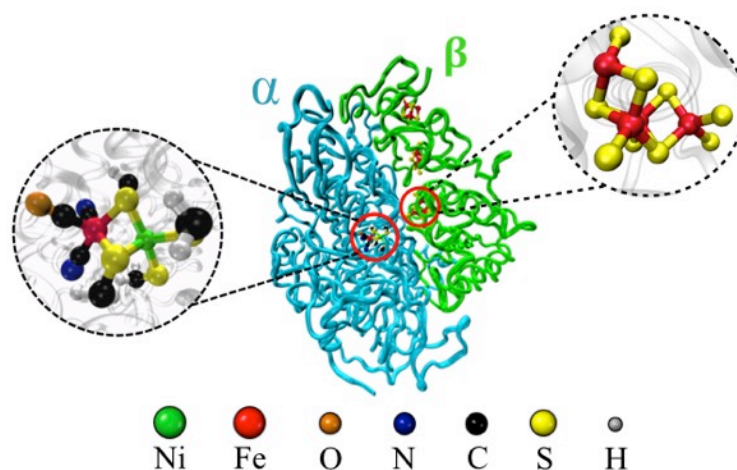
Figure 2. The structure of [NiFe]-hydrogenase and the metal-sulfur clusters within the enzyme.

Based on the O_2 tolerance, [NiFe]-hydrogenases can be classified as "standard" (oxygen-sensitive) or "nonstandard" (oxygen-tolerant).[31,32] Among the nonstandard NiFe-hydrogenases one could define four classes, namely hydrogen sensing hydrogenases, bidirectional heteromultimeric cytoplasmic hydrogenases, energy-conserving hydrogenases, and membrane bound hydrogenases.[32] Interesting feature of the latter one is the attachment of small subunit to dihaem cytochrome subunit.[33,34] Finally, recent study demonstrated the existence of new actinobacterial [NiFe]-hydrogenase (AH) of *R. eutropha*. An exciting feature of this hydrogenase is its extreme tolerance to molecular oxygen to the degree that has never been observed before.[35] The relations between the different types and classes of hydrogenases are summarized in Figure 3.
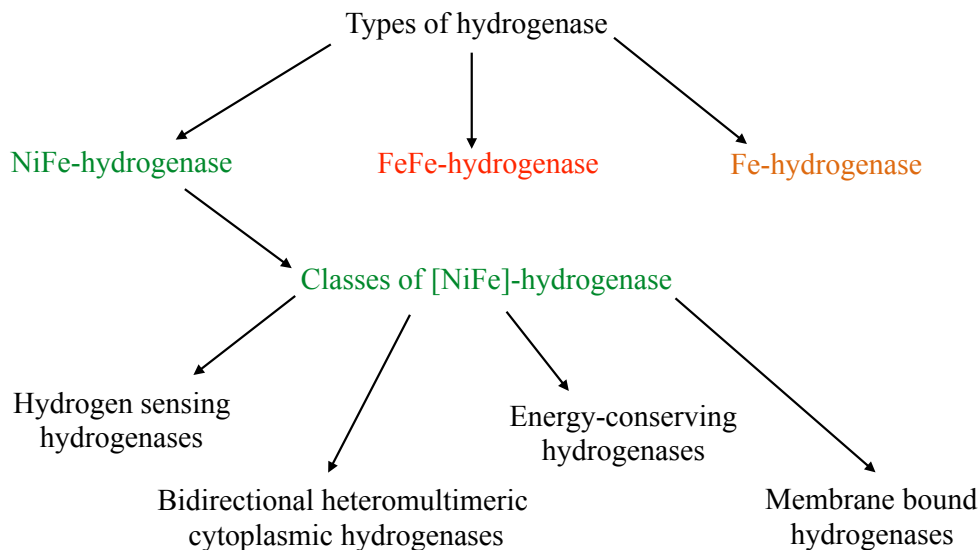
Figure 3. Types of hydrogenases and classes of [NiFe]-hydrogenase.

The oxygen tolerance of the nonstandard [NiFe]-hydrogenases comes from many factors. Most comprehensive knowledge about the mechanisms and the source of O_2-tolerance was obtained from the studies of membrane-bound hydrogenase. Thus, the oxygen tolerance of [NiFe]-hydrogenases will be discussed within the context of this particular group of hydrogenases.[33]

B. Oxygen Tolerance of [NiFe]-Hydrogenase

The oxygen-tolerant species of [NiFe]-hydrogenases were the subject of different studies that demonstrated the potential involvement of variety of factors in O_2-tolerance. Main directions of these studies could be defined as elucidation of the gas channels within hydrogenases[36–38], exploration of unusual structures of the iron-sulfur clusters in the smaller protein subunit[20,38–40] and study of the residues that are surrounding the active site.[41] Moreover, several studies demonstrate that the presence of rubredoxin in the

proximity of [NiFe]-hydrogenase could be one of the factors controlling the oxygen tolerance of the membrane bound [NiFe]-hydrogenases.[42,43]

The oxygen that present in the environment around [NiFe]-hydrogenase becomes harmful for catalytic activity of this protein upon entrance into vicinity of the active site, thus it is important to gain a detailed knowledge about the gas channels and entrance points within the protein. The oxygen-tolerant hydrogenases have roughly twice fewer openings and hydrophobic gas channels than the oxygen-sensitive hydrogenases. The narrow points of the gas channels in the oxygen-tolerant hydrogenases do not exceed 1.6 Å. Moreover, some oxygen-sensitive hydrogenases have narrow points as small as 1.0 Å. Such narrow channels limit the access to the active site for both the O_2 and H_2 molecules making the passing of these molecules through the gas channels a limiting factor in catalysis. Differences in amino acids within the gas channels between the oxygen-sensitive and the oxygen-tolerant hydrogenases are less pronounced towards the surface of the proteins, while the residues close to the active site vary more dramatically.[38]

Mutagenic study of the active site of Hyd-1, an oxygen-tolerant membrane-bound [NiFe]-hydrogenase from *Escherichia coli*, identified specific residues around the active site that are most important for the catalytic activity of this protein.[41] Four highly conserved residues of Hyd-1 form a "canopy" that is crucial for the catalytic activity. Two of these residues, namely arginine 509 and aspartate 118 form a salt bridge above the coordination site of the catalytic center, thus impacting the reactivity the most. Replacement of one of these two residues by a different amino acids leads to the dramatic decrease of catalytic activity. The other two residues within the "canopy" are aspartate 574 and proline 508. Despite the fact that aspartate 574 forms salt bridge with arginine

509, and proline 508 is directly attached to aspartate 574, replacement of either of these residues have no significant effect on the catalytic activity.[41]

The oxygen tolerance of [NiFe]-hydrogenase is not only caused by the physical restrictions of the space within the gas channels and interactions between the active site and nearby residues, but also is highly dependent on the structure of the FeS clusters in the smaller subunit of the protein (Figure 4a). These FeS clusters are responsible for transferring the electrons that are required for the O_2 transformation to water molecules.[38] A unique feature of the oxygen-tolerant [NiFe]-hydrogenases is the presence of a nonstandard proximal FeS cluster in their structures. In contrast, the distal [4Fe-4S] and medial [3Fe-4S] clusters are preserved among all [NiFe]-hydrogenases (Figure 4b). The oxygen-tolerant [NiFe]-hydrogenase contains the proximal [4Fe-3S] cluster, which is ligated differently from the proximal [4Fe-4S] cluster of the oxygen-sensitive [NiFe]-hydrogenase.

a
b
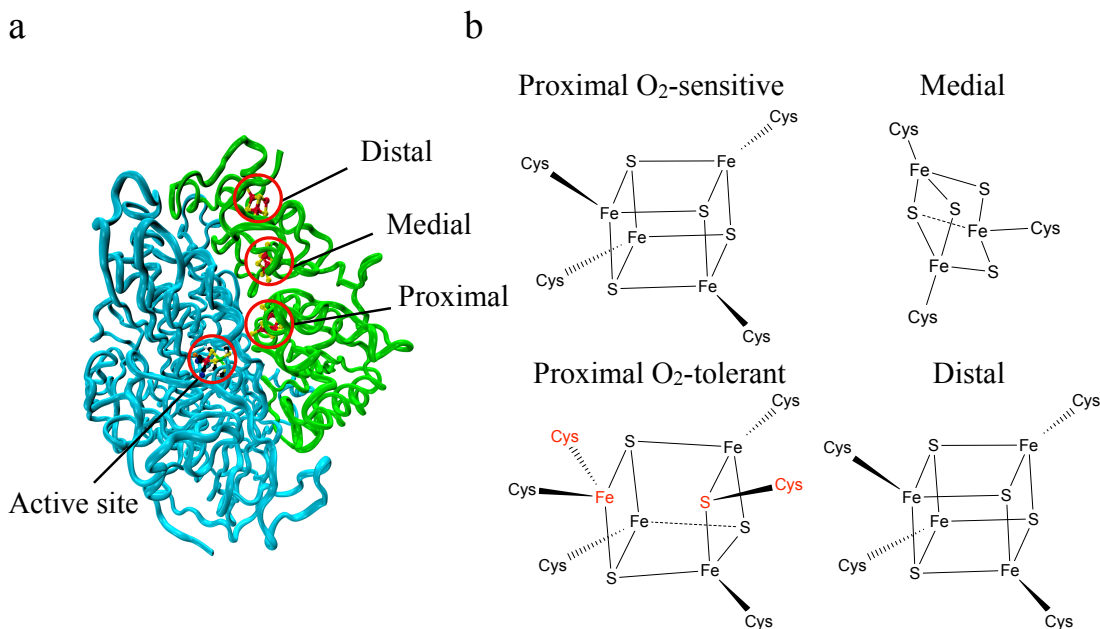
Figure 4. Three FeS clusters of [NiFe]-hydrogenase. a) Locations of FeS clusters with respect to the active site. b) Structural differences (highlighted in red) between the proximal FeS clusters from the O$_2$-sensitive and O$_2$-tolerant [NiFe]-hydrogenases. Also shown the medial and distal FeS clusters.

The conventional [4Fe-4S] cluster is ligated by four cysteines, while the nonstandard [4Fe-3S] cluster is ligated by six cysteines.[20] This structural difference leads to a different redox behavior because the standard [4Fe-4S] cluster is only capable of a single one-electron transfer, while the [4Fe-3S] cluster is capable of two sequential one-electron transfers required for an efficient O$_2$ conversion into H$_2$O.[39,40]

C. Catalytic Activity and Intermediates of [NiFe]-Hydrogenase

Pursuing of any practical applications of [NiFe]-hydrogenase or its mimics requires a deep understanding of the their structural and functional features.[18,20,40,44–46] Experimentally, this can be achieved by studying the structure of the protein using different spectroscopic techniques, such as the X-ray,[47–51] IR[52–57] and EPR spectroscopies,[58–60] and by synthesizing the active site analogs.[45,46,61–66] There are two types of the active site analogs, namely biomimetic (structural) models[61,62,64] and bioinspired (functional) models.[65,66] Combination of these approaches with computational studies allows to gain a comprehensive knowledge about the structure and functionality of [NiFe]-hydrogenase. However, the mechanism of proton reduction and hydrogen oxidation on the [NiFe]-hydrogenase synthetic models and its relevance to the catalytic activity of the [NiFe]-hydrogenase metalloenzyme are not completely understood. Therefore, further computational and experimental efforts are required.[17,48]

The binding position of molecular hydrogen and protons on the active site is one of the cornerstones in the description of the catalytic activity of [NiFe]-hydrogenase. Most of the studies performed up to this point suggest the heterolytic mechanism of hydrogen cleavage, which implies the importance of both metal centers during the catalytic cycle.[20,29,46] In addition, the sulfur atoms of the cysteine ligand are believed to participate in the catalytic cycle as well.[67,68] It is also important to consider the influence of the arginine group proximal to the active site because this group could play an important role in the hydrogen oxidation/reduction on [NiFe]-hydrogenase.[17]

Recent studies of a structural model of [NiFe]-hydrogenase demonstrate that the initial binding of the proton could serve as a trigger for conformational changes in the

active site.[45] At the same time, our study indicate that similar conformational changes could trigger a change of the electronic spin state of the active site, which could be a key feature in the catalytic cycle.[12] As for the binding of molecular hydrogen, experimental studies of the gas channel within the [NiFe]-hydrogenase demonstrate that the gas channel is directed towards the Ni center, which suggests H_2 binding on Ni.[19,37,38] On the other hand, this conclusion could be argued against because the two metal centers (Ni and Fe) are only about 3.00 Å apart.[47,50] Another experimental highlight of the potential favorability of the H_2 binding on Ni is a recently synthesized bioinspired functional models of [NiFe]-hydrogenase with a single Ni metal center.[65,66] However, these models lack the Fe center within the active site and have a different ligand environment. Thus, the catalytic mechanisms in these models could be different from the mechanism in [NiFe]-hydrogenase.

The argument for the favorability of H_2 binding on the Fe center comes from the unusual nature of the Fe ligands. Two CN^- and one CO ligands lead to a high crystal field splitting, which "locks" Fe in the low-spin state. Additionally, the Fe center has square-pyramidal coordination due to the presence of the bridging cysteine ligands between Fe and Ni. This coordination and the spin state of the Fe(II) center lead to unoccupied d-orbitals that can accept electrons from the σ-orbital of H_2, which allows for the formation of energetically favorable non-classical three-center, two-electron bonding between H_2 and the Fe center.[46,69,70]

The computational studies of hydrogen binding show a potential possibility of binding on the Ni, Fe, and the Ni-Fe bridging position. The preference for the binding site often depends on the active site model and the spin states of the metal centers.[71–80] In our

computational study, we investigated how the H_2 binding energy is affected by the changing Ni coordination, which could be accompanied by the nonadiabatic transitions between the singlet and triplet electronic states. The results of this study are presented in Chapter III.

III. Rubredoxin Proteins

Rubredoxins are the group of the small (5 to 6 kDA)[81,82] electron transferring proteins[83] that are crucial for a variety of biological processes, including nitrate reduction,[84] alkane oxidation,[85] methanogenesis,[86] carbon fixation,[87] detoxification of reactive oxygen species,[88,89] and transformation of polyglucose in *D. gigas*.[90] Recently, it was shown that the presence of rubredoxin is the critical condition for activity of photosystem II in many organisms.[91] Moreover, rubredoxin-like centers are involved in the repair of catalytic centers of certain proteins through donation of the iron atom.[92] The active site of rubredoxin consists of an iron center with four cysteine ligands.[82] The ability of rubredoxin protein to transfer electrons originates from the transition between Fe(II) and Fe(III) oxidation states in the active site of this protein.[93–97] Structures of rubredoxin and its active site are depicted in Figure 5.
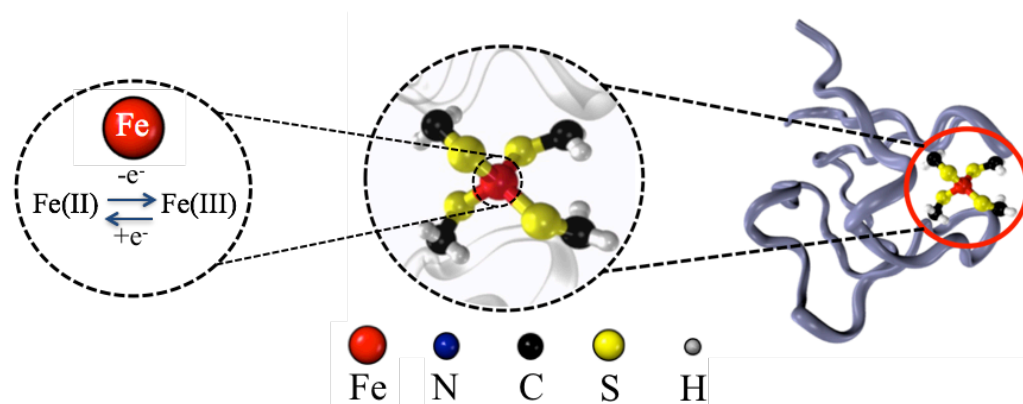
Figure 5. Rubredoxin protein, its active site, and the Fe center.

The study of rubredoxin not only provides fundamental understanding of electron transfer in biological systems, but also could be used for the design and manufacture of bionanowires.[5] Thus, the rubredoxin and its synthetic models could be potentially used in a variety of biomedical devices such as the self-sufficient biosensors.[5–7] Moreover, the knowledge about the functionality of this particular protein could be used in the design of the novel transition-metal-based catalysts.[8] The industrial applications of rubredoxin proteins and its synthetic analogs are expected to be very broad due to the thermal stability of some of the rubredoxins.[98–101] The rubredoxin from *Pyrococcus furiosus* (PfRd) is one of the most thermostable proteins among the proteins known to date.[99,100]

The redox properties of rubredoxin, and thus its ability to transfer electrons, depend not only on the presence of the certain residues within the protein chain, but are also strongly influenced by the type and composition of the solvent, as well as the fluctuations of the protein that affect the accessibility of the active site to the solvent.[102,103] Among other interactions and factors defining the redox properties of rubredoxin are the dispersion interactions within the hydrophobic core of the protein,

hydrogen bonds of between the active site and the protein backbone, composition of charged groups, formation of salt bridges, polarization, the influence of the second shell backbone, as well as pH.[95,96,104–106]

The study of electronic spin states of the active site of rubredoxin is challenging due to the fact that the active site is buried deeply in the protein chain.[82] For that matter, the study of synthetic analogs of the rubredoxin active site is very important.[107] Most of the synthetic analogs of the rubredoxin active site are stable in the gas phase and could be studied with spray photoelectron spectroscopy (SPES). This fact allows for the direct comparison of theoretical results from the electronic structure calculations on isolated active site and experimental data.[9,10,97,107–110]

The theoretical and experimental studies of the isolated active site of rubredoxin and its synthetic analogs give knowledge about the electronic states that are involved in electron transfer within the rubredoxin.[9,10,97,107–110] However, the comprehensive description of electron transfer within rubredoxin requires the use of large models that include significant portion of the protein chain and the solvent molecules.[95] This increases the importance of the fragment-based computational methods, that allow for full quantum mechanical description of very large models with thousands of atoms, in the rubredoxin studies.[111–116] Combination of the state-of-the-art quantum mechanical methods and the large-scale models allow the accurate treatment of the quantum mechanical interactions between the active sites and the protein chains.[112,117]

A. Factors Affecting Thermal Stability and Electron Transfer in Rubredoxin

The thermally stable species of rubredoxin have much slower kinetic rates of unfolding and lower redox potentials[118] compared to mesophilic types, which shows that the thermal stability of rubredoxins is likely based on the kinetic factor rather than thermodynamic equilibrium.[99] Thermostable proteins are characterized by presence of a large number of charged residues, while mesophilic proteins are rich in solvent-accessible polar residues.[99] Presence of the charged groups is important for thermal resistance since clamping of the protein by the ion pairs slows downs the protein unfolding, and thus increases its thermal stability.[118] However, recent studies show that composition of the charged groups and the number of salt bridges seem to have a significant effect on the thermal stability, but has rather small impact on the redox potential of the protein, which demonstrates that the hydrogen bonds are prevail in the control of redox properties, while the presence of the charged groups is more crucial for thermal stability.[106]

Another important factor in thermal resistance and redox properties of rubredoxin is the presence, composition, and concentration of the solvent. A recent study of interaction between diglycerol-phosphate (DGP) and rubredoxin from *Desulfovibrio gigas* (DgRd) showed that increase in the thermal stability of the protein is not due to the straightforward compression of the protein by the solvent, but rather related to the interaction between DGP and specific regions of the rubredoxin protein chains. This interaction is related to the negative charge on DGP and presence of the electropositive groups in the protein chain, and also the ability of DGP to interact with the hydrogen bonds of the protein chain.[103]

Most of the studies of the redox properties and thermal resistance of rubredoxins highlight the importance of the hydrogen bonds between the active site and the protein chain.[99,105] Hydrogen bonds between the active site and the protein chains include two types of interaction, firstly Fe-S⋯H-N bond between the active site and the peptide backbone, and secondly Fe-S⋯H-O interaction with the amino acids of the side chains.[105] Not only this hydrogen bonds are responsible for controlling the thermal resistance of the protein by regulating the unfolding of the protein, but they also responsible for direct interaction between the active site and the protein chain. Moreover, these hydrogen bonds seem to be the key factor in the regulation of motions and fluctuations of the protein that allow for access of the solvent molecules to the active site of rubredoxin.[102,105]

Finally, it is important to conclude that despite the dominant influence of hydrogen bonds between the active site and the protein chain on the overall properties of the rubredoxin, this system is full of different interactions between not only active site and the protein chain, but also between the residues within the protein chain itself. Therefore, the computational studies of the rubredoxin properties often require the use of large models that allows for accurate treatment of all these factors.[105]

B. Electronic States of the Rubredoxin Active Site and its Synthetic Analogs

The stability of the synthetic analogs of rubredoxin active site in the gas phase makes it possible to study the electronic properties of the active site with spray photoelectron spectroscopy (SPES). By measuring the vertical dissociation energy (VDE) and the adiabatic detachment energy (ADE), which are differ by the Frank-Condon factor

between the vibrational levels of electronic states, before and after electron detachment (Figure 6), SPES allows to probe the electronic states of the system without environmental influence. This becomes possible because a one-electron oxidation reaction could be approximated by electron detachment in the gas phase. Thus, the contributions of the active site and the protein chain to the electron transferring ability of rubredoxin can be separated.[97,119]
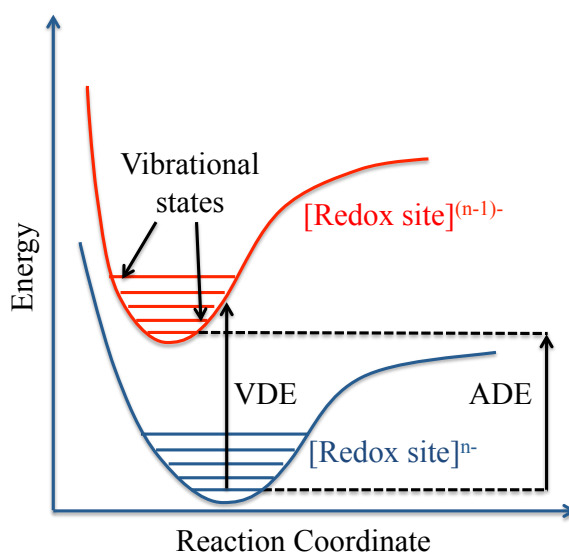
Figure 6. Diagram of vibrational states during the electron excitation showing the difference between VDE and ADE.

Synthetic analogs of the rubredoxin active site of $[Fe(SR)_4]$-type are only stable for the oxidation state Fe(III), i.e. the $[Fe(SR)_4]^{2-}$ complex is unstable in the gas phase, thus only $[Fe(SCH_3)_4]^-$ could be studied experimentally. The instability of the $[Fe(SR)_4]^{2-}$ complex in the gas phase requires to use other types of rubredoxin active site analogs, such as $Na^+[Fe(SR)_4]^{2-}$ that has enhanced stability due to the presence of sodium ion.[93,97] Another approach to the synthesis of the rubredoxin active site analogs that contain Fe(II) metal center and are stable in the gas phase is the utilization of three-ligand analogues,

such as $[Fe(SCH_3)_3]^{-}$.[93] Thus the obtained ADE and VDE values should be corrected with the thermodynamic cycle calculations. In case of $Na^{+}[Fe(S_2\text{-o-xyl})_2]^{-/2-}$, the presence of Na^{+} is accounted for by calculating the energy of Na^{+} and the binding energy of Na^{+} to $[Fe(SCH_3)_4]^{2-}$. This approach gives ADE of $[Fe(S_2\text{-o-xyl})_2]^{2-}$ that is experimentally inaccessible in the gas phase. The use of the three-ligand analogs of the active site, such as $[Fe(SCH_3)_3]^{-}$, to calculate ADE of $[Fe(SCH_3)_4]^{2-}$ requires additional calculations of the SCH_3^{-} energy and the binding energies of SCH_3^{-}.[93] The structures of the rubredoxin active site analogs are shown in Figure 7.
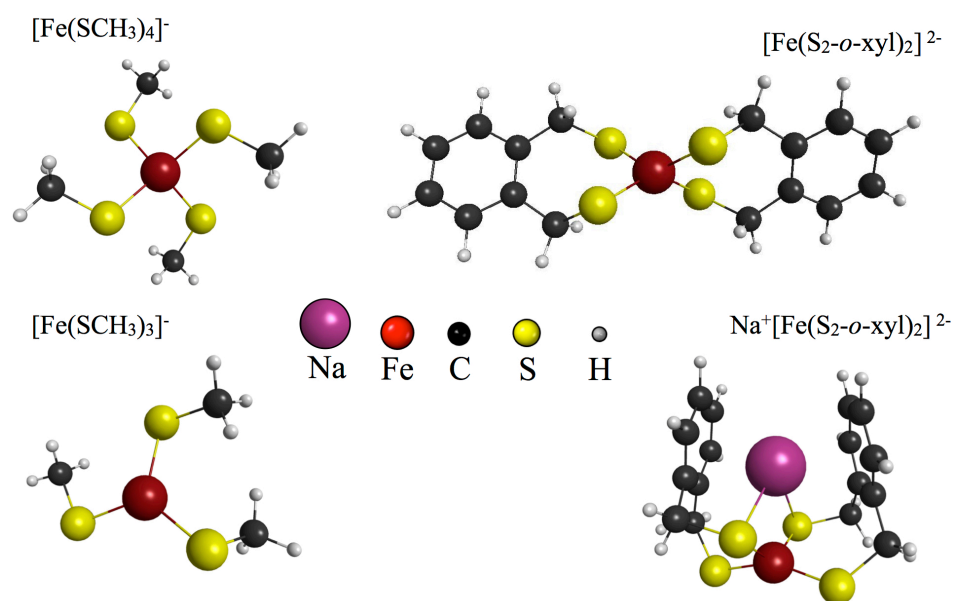
Figure 7. Structures of the $[Fe(SCH_3)_4]^{-}$, $Na^{+}[Fe(S_2\text{-o-xyl})_2]^{2-}$ and $[Fe(SCH_3)_3]^{-}$ synthetic analogs of the rubredoxin active. Also shown the experimentally inaccessible $[Fe(S_2\text{-o-}xyl)_2]^{2-}$.

Electronic structure calculations show that the valence molecular orbitals of the rubredoxin active site consist of the Fe d-orbitals with significant contribution from the atomic orbitals of sulfur. The amount of the ligand orbitals contribution into the valence molecular orbitals of the active site is strongly correlated with the oxidation state of the

iron metal center. The tetrahedral arrangement of the ligands leads to relatively low energy gaps between the valence orbitals. As a result, the electronic states with higher spin multiplicities are more energetically favorable for the synthetic analogs of the rubredoxin active site.[9,10,93,97,109] The presence of multiple low-lying electronic states with different spin multiplicities, together with small energy gap between these states, leads to the possibility of spin-forbidden nonadiabatic transitions in the active site of rubredoxin. These transitions could play a role in the electron transfer in the rubredoxin protein. The nature and kinetics of these spin-forbidden transitions are investigated in Chapter IV.

IV. Potential Energy Surfaces for Teaching Chemistry

A. 3D-printed Models of Potential Energy Surfaces

The studies of reaction mechanisms are largely based on the modeling of potential energy surfaces (PES) and finding the critical points on these surfaces. Bellow we discuss how the PES calculated using electronic structure methods and simple analytical functions can be converted into 3D-printed models to teach basic concepts of physical chemistry.

The concept of reaction mechanism plays one of the central roles in chemistry, thus understanding of this concept is crucial in learning chemistry. This concept is introduced to students in early general chemistry courses. The concept of reaction mechanism is a "silver lining" that goes through all the flavors of chemistry and plays central role in building comprehensive understanding of organic, inorganic, and physical chemistry.

The most common way of depicting a chemical reaction mechanism is a 2D curve that shows the dependence of potential energy on a single reaction coordinate. Despite the simplicity of such approach, such depiction takes away an important property of PES that is its multidimensionality. The multidimensional nature of PES can be demonstrated by utilizing 3D-printed models.[120–122] We discuss our work aimed to design and manufacture the 3D models of PES for teaching chemistry in Chapter VI.

B. Previous 3D-Printed PES Models

In this subsection we discuss several studies that were focused on the design of PES for various chemical reactions and processes. Lolur and Dawes created a 3D-printed models of the PES for the ozone molecule and for the following reaction $CO + O(^3P) \rightarrow CO_2$. This reaction is spin-forbidden, therefore three PES for the three lowest energy electronic states were printed and combined in the single model.[123] Blauch and Carroll designed and 3D printed the PES that describes the conformational changes of butane. In addition, they manufactured the surface describing a generic S_N2 reaction.[124] Teplukhin and Babikov demonstrated that the 3D printed models can be used to represent the PES with more than three dimensions. In order to achieve that, the authors had to implement an isoenergy approach. This approach is based on using the volume of the model rather than only its surface, which provides the extra dimension.[125]

An interesting aspect of the 3D-printed models is the capability to include multiple colors in a single model. This capability was fully exploit in the work of Chen, Lee, Flood and Miljanic.[126] The authors proposed a simple procedure that allows for direct conversion of the crystallographic database entrances into the color models using

only freely available software. This methodology was fully embraced during the

production of more than 30 models of different metallorganic frameworks.[126]

References

(1)   Microbial Bioenergy : Hydrogen Production. In *Microbial bioenergy: hydrogen production In: Advances in Photosynthesis and Respiration*; Zannoni, D.; De Philippis, R., Eds.; Springer Netherlands: Dordrecht, 2014; Vol. 38.

(2)   Benoit, L.; Maier, R. J.; Zbell, A. L. Differential Expression of NiFe Uptake-Type Hydrogenase Genes in Salmonella Enterica Serovar Typhimurium. *Microbiology* **2007**, *153*, 3508–3516.

(3)   Bowman, L.; Balbach, J.; Walton, J.; Sargent, F.; Parkin, A. Biosynthesis of Salmonella Enterica [NiFe]– Hydrogenase – 5: Probing the Roles of System – Specific Accessory Proteins. *J. Biol. Inorg. Chem.* **2016**, *21*, 865–873.

(4)   Parkin, A.; Bowman, L.; Roessler, M. M.; Davies, R. A.; Palmer, T.; Armstrong, F. A.; Sargent, F. How Salmonella Oxidises H_2 under Aerobic Conditions. *FEBS Lett.* **2012**, *586*, 536–544.

(5)   Altamura, L.; Horvath, C.; Rengaraj, S.; Rongier, A.; Elouarzaki, K.; Gondran, C.; Maçon, A. L. B.; Vendrely, C.; Bouchiat, V.; Fontecave, M.; et al. A Synthetic Redox Biofilm Made from Metalloprotein–prion Domain Chimera Nanowires. *Nat. Chem.* **2017**, *9*, 157–163.

(6)   Goff, A. Le; Holzinger, M.; Cosnier, S. Enzymatic Biosensors Based on SWCNT-Conducting Polymer Electrodes. *Analyst* **2011**, *136*, 1279–1287.

(7)   Holzinger, M.; Goff, A. Le; Cosnier, S. Carbon Nanotube / Enzyme Biofuel Cells. *Electrochim. Acta* **2012**, *82*, 179–190.

(8)   Lin, Y. Rational Design of Metalloenzymes : From Single to Multiple Active Sites. *Coord. Chem. Rev.* **2017**, *336*, 1–27.

(9)   Niu, S.; Wang, X. Bin; Nichols, J. A.; Wang, L. S.; Ichiye, T. Combined Quantum Chemistry and Photoelectron Spectroscopy Study of the Electronic Structure and Reduction Potentials of Rubredoxin Redox Site Analogues. *J. Phys. Chem. A* **2003**, *107*, 2898–2907.

(10)   Tran, V. T.; Hendrickx, M. F. A. Molecular Structures for $FeS_4^{-/0}$ As Determined from an Ab Initio Study of the Anion Photoelectron Spectra.

J. Phys. Chem. A **2013**, *117*, 3227–3234.

(11) Pandelia, M.-E.; Ogata, H.; Lubitz, W. Intermediates in the Catalytic Cycle of [NiFe] Hydrogenase: Functional Spectroscopy of the Active Site. *ChemPhysChem* **2010**, *11*, 1127–1140.

(12) Yson, R. L.; Gilgor, J. L.; Guberman, B. A.; Varganov, S. A. Protein Induced Singlet–triplet Quasidegeneracy in the Active Site of [NiFe]-Hydrogenase. *Chem. Phys. Lett.* **2013**, *577*, 138–141.

(13) Lykhin, A. O.; Kaliakin, D. S.; DePolo, G. E.; Kuzubov, A. A.; Varganov, S. A. Nonadiabatic Transition State Theory: Application to Intersystem Crossings in the Active Sites of Metal-Sulfur Proteins. *Int. J. Quantum Chem.* **2016**, *116*, 750–761.

(14) Harvey, J. N. Spin-Forbidden Reactions: Computational Insight into Mechanisms and Kinetics. *WIREs Comput. Mol. Sci.* **2014**, *4*, 1–14.

(15) Cui, Q.; Morokuma, K.; Bowman, J. M. The Spin-Forbidden Reaction $CH(^2\Pi)$ + $N_2 \rightarrow HCN + N(^4S)$ Revisited. II. Nonadiabatic Transition State Theory and Application. *J. Chem. Phys* **1999**, *110*, 9469–9482.

(16) Papaza, N.; Fanucci, L.; Leporini, B.; Pelagatti, S.; Roncella, R. Haptic Models of Arrays Through 3D Printing for Computer Science Education. In *International Conference on Computers Helping People with Special Needs*; 2016; pp. 491–498.

(17) Evans, R. M.; Brooke, E. J.; Wehlin, S. A. M.; Nomerotskaia, E.; Sargent, F.; Carr, S. B.; Phillips, S. E. V; Armstrong, F. A. Mechanism of Hydrogen Activation by [NiFe] Hydrogenases. *Nat. Chem. Biol.* **2015**, *12*, 46–50.

(18) Kaur-Ghumaan, S.; Stein, M. [NiFe] Hydrogenases: How Close Do Structural and Functional Mimics Approach the Active Site? *Dalton Trans.* **2014**, *43*, 9392–9405.

(19) Fontecilla-Camps, J. C.; Amara, P.; Cavazza, C.; Nicolet, Y.; Volbeda, A. Structure-Function Relationships of Anaerobic Gas-Processing Metalloenzymes. *Nature* **2009**, *460*, 814–822.

(20) Higuchi, Y. Structure and Function of [NiFe] Hydrogenases. *J. Biochem.* **2016**, *160*, 251–258.

(21) Lubitz, W.; Ogata, H.; Rüdiger, O.; Reijerse, E. Hydrogenases. *Chem. Rev.* **2014**, *114*, 4081–4148.

(22) Thauer, R. K.; Klein, A. R.; Hartmann, G. C. Reactions with Molecular Hydrogen in Microorganisms: Evidence for a Purely Organic Hydrogenation Catalyst. *Chem. Rev.* **1996**, *96*, 3031–3042.

(23) Albracht, S. P. J. Nickel Hydrogenases: In Search of the Active Site. *Biochim. Biophys. Acta - Bioenerg.* **1994**, *1188*, 167–204.

(24) Adams, M. W. W. The Structure and Mechanism of Iron-Hydrogenases. *Biochim. Biophys. Acta - Bioenerg.* **1990**, *1020*, 115–145.

(25) Vignais, P. M.; Billoud, B. Occurrence, Classification, and Biological Function of Hydrogenases: An Overview. *Chem. Rev.* **2007**, *107*, 4206–4272.

(26) Shafaat, H. S.; Rüdiger, O.; Ogata, H.; Lubitz, W. [NiFe] Hydrogenases: A Common Active Site for Hydrogen Metabolism under Diverse Conditions. *Biochim. Biophys. Acta* **2013**, *1827*, 986–1002.

(27) Vincent, K. A.; Parkin, A.; Armstrong, F. A. Investigating and Exploiting the Electrocatalytic Properties of Hydrogenases. *Chem. Rev.* **2007**, *2*, 4366–4413.

(28) Armstrong, F. A.; Hirst, J. Reversibility and Efficiency in Electrocatalytic Energy Conversion and Lessons from Enzymes. *Proc. Natl. Acad. Sci.* **2011**, *108*, 14049–14054.

(29) Armstrong, F. A.; Evans, R. M.; Hexter, S. V; Murphy, B. J.; Roessler, M. M.; Wul, P. Guiding Principles of Hydrogenase Catalysis Instigated and Clarified by Protein Film Electrochemistry. *Acc. Chem. Res.* **2016**, *49*, 884–892.

(30) Flanagan, L. A.; Parkin, A. Electrochemical Insights into the Mechanism of NiFe Membrane-Bound Hydrogenases. *Biochem. Soc. Trans* **2016**, *44*, 315–328.

(31) Parkin, A.; Sargent, F. The Hows and Whys of Aerobic H_2 Metabolism. *Curr. Opin. Chem. Biol.* **2012**, *16*, 26–34.

(32) Stiebritz, M. T.; Reiher, M. Hydrogenases and Oxygen. *Chem. Sci.* **2012**, *3*, 1739–1751.

(33) Pandelia, M.; Fourmond, V.; Tron-infossi, P.; Lojou, E.; Bertrand, P.; Le, C. Membrane-Bound Hydrogenase I from the Hyperthermophilic Bacterium Aquifex Aeolicus : Enzyme Activation , Redox Intermediates and Oxygen Tolerance. *J. Am. Chem. Soc.* **2010**, *132*, 6991–7004.

(34) Wulff, P.; Thomas, C.; Sargent, F.; Armstrong, F. A. How the Oxygen Tolerance of a [NiFe]‒ Hydrogenase Depends on Quaternary Structure. *J Biol Inorg Chem* **2016**, *21*, 121–134.

(35) Schafer, C.; Bommer, M.; Hennig, S. E.; Jeoung, J.; Dobbek, H.; Lenz, O. Structure of an Actinobacterial-Type [NiFe]-Hydrogenase Reveals Insight into O_2-Tolerant H_2 Oxidation. *Structure* **2016**, *24*, 285–292.

(36)   Dementin, S.; Leroux, F.; Cournac, L.; Lacey, A. L. De; Volbeda, A.; Le, C.; Martin, L.; Sanganas, O.; Haumann, M.; Rousset, M. Introduction of Methionines in the Gas Channel Makes [NiFe] Hydrogenase Aero-Tolerant. *J. Am. Chem. Soc.* **2009**, *131*, 10156–10164.

(37)   Buhrke, T.; Lenz, O.; Krauss, N.; Friedrich, B. Oxygen Tolerance of the H_2-Sensing [NiFe] Hydrogenase from Ralstonia Eutropha H16 Is Based on Limited Access of Oxygen to the Active Site. *J. Biol. Chem.* **2005**, *280*, 23791–23796.

(38)   Hydrogenase, N.; Kalms, J.; Schmidt, A.; Frielingsdorf, S.; Linden, P. Van Der; Stetten, D. Von; Lenz, O.; Carpentier, P.; Scheerer, P. Krypton Derivatization of an O 2 -Tolerant Membrane-Bound [NiFe] Hydrogenase Reveals a Hydrophobic Tunnel Network for Gas Transport. *Angew. Chem. Int. Ed.* **2016**, *55*, 5586–5590.

(39)   Wulff, P.; Day, C. C.; Sargent, F.; Armstrong, F. A. How Oxygen Reacts with Oxygen-Tolerant Respiratory [NiFe] -Hydrogenases. *Proc. Natl. Acad. Sci.* **2014**, *111*, 6606–6611.

(40)   Stiebritz, M. T.; Reiher, M. Hydrogenases and Oxygen. *Chem. Sci.* **2012**, *3*, 1739.

(41)   Brooke, E. J.; Evans, R. M.; Islam, S. T. A.; Roberts, G. M.; Wehlin, S. A. M.; Carr, S. B.; Phillips, S. E. V; Armstrong, F. A. Importance of the Active Site " Canopy " Residues in an O_2 ‑ Tolerant [NiFe]-Hydrogenase. *Biochemistry* **2017**, *56*, 132–142.

(42)   Fritsch, J.; Lenz, O.; Friedrich, B. The Maturation Factors HoxR and HoxT Contribute to Oxygen Tolerance of Membrane-Bound [NiFe] Hydrogenase in Ralstonia Eutropha H16. *J. Bacteriol.* **2011**, *193*, 2487–2497.

(43)   Kurtz, D. M. Microbial Detoxification of Superoxide : The Non-Heme Iron Reductive Paradigm for Combating Oxidative Stress. *Acc. Chem. Res* **2004**, *37*, 902–908.

(44)   Simmons, T. R.; Berggren, G.; Bacchi, M.; Fontecave, M.; Artero, V. Mimicking Hydrogenases: From Biomimetics to Artificial Enzymes. *Coord. Chem. Rev.* **2014**, *270–271*, 127–150.

(45)   Ulloa, O. A.; Huynh, M. T.; Richers, C. P.; Bertke, J. A.; Nilges, M. J.; Hammes-Schiffer, S.; Rauchfuss, T. B. Mechanism of H 2 Production by Models for the [NiFe]-Hydrogenases: Role of Reduced Hydrides. *J. Am. Chem. Soc.* **2016**, *138*, 9234−9245.

(46)   Schilter, D.; Camara, J. M.; Huynh, M. T.; Hammes-Schiffer, S.; Rauchfuss, T. B. Hydrogenase Enzymes and Their Synthetic Models: The Role of Metal Hydrides.

Chem. Rev. **2016**, *116*, 8693–8749.

(47) Volbeda, A.; Martin, L.; Barbier, E.; Gutiérrez-Sanz, O.; De Lacey, A. L.; Liebgott, P.-P.; Dementin, S.; Rousset, M.; Fontecilla-Camps, J. C. Crystallographic Studies of [NiFe]-Hydrogenase Mutants: Towards Consensus Structures for the Elusive Unready Oxidized States. *J. Biol. Inorg. Chem.* **2015**, *20*, 11–22.

(48) Schilter, D. Nickel-Iron Hydrogenases: High-Resolution Crystallography Resolves the Hydride, but Not the Debate. *ChemBioChem* **2015**, *16*, 1712–1714.

(49) Higuchi, Y.; Yagi, T.; Yasuoka, N. Unusual Ligand Structure in Ni – Fe Active Center and an Additional Mg Site in Hydrogenase Revealed by High Resolution X-Ray Structure Analysis. *Structure* **1997**, *5*, 1671–1680.

(50) Gu, Z.; Dong, J.; Allan, C. B.; Choudhury, S. B.; Franco, R.; Moura, J. G.; Moura, I.; Legall, J.; Przybyla, A. E.; Roseboom, W.; et al. Structure of the Ni Sites in Hydrogenases by X-Ray Absorption Spectroscopy . Species Variation and the Effects of Redox Poise. *J. Am. Chem. Soc.* **1996**, *118*, 11155–11165.

(51) Bagyinka, C. An X-Ray Absorption Spectroscopic Study of Nickel Redox Chemistry in Hydrogenase. *J. Am. Chem. Soc.* **1993**, *115*, 3576–3585.

(52) Hidalgo, R.; Ash, P. A.; Healy, A. J.; Vincent, K. A. Infrared Spectroscopy During Electrocatalytic Turnover Reveals the Ni-L Active Site State During H_2 Oxidation by a NiFe Hydrogenase. *Angew. Chemie Int. Ed.* **2015**, *54*, 7110–7113.

(53) Tai, H.; Nishikawa, K.; Inoue, S.; Higuchi, Y.; Hirota, S. FT-IR Characterization of the Light-Induced Ni-L2 and Ni-L3 States of [NiFe] Hydrogenase from Desulfovibrio Vulgaris Miyazaki F. *J. Phys. Chem.* **2015**, *119*, 13668−13674.

(54) Kellers, P.; Pandelia, M.; Currell, L. J.; Go, H.; Lubitz, W. FTIR Study on the Light Sensitivity of the [NiFe] Hydrogenase from Desulfovibrio Vulgaris Miyazaki F : Ni – C to Ni – L Photoconversion, Kinetics of Proton Rebinding and H / D Isotope Effect. *Phys. Chem. Chem. Phys.* **2009**, *11*, 8680–8683.

(55) Bagley, K. A.; Duin, E. C.; Roseboom, W.; Albracht, S. P. J.; Woodruffs, W. H. Infrared-Detectable Groups Sense Changes in Charge Density on the Nickel Center in Hydrogenase from Chromatium Vinosum. *Biochemistry* **1995**, *34*, 5527–5535.

(56) Pandelia, M.-E.; Infossi, P.; Stein, M.; Giudici-Orticoni, M.-T.; Wolfgang, L. Spectroscopic Characterization of the Key Catalytic Intermediate Ni–C in the O_2-Tolerant [NiFe] Hydrogenase I from Aquifex Aeolicus: Evidence of a Weakly Bound Hydride. *Chem. Commun.* **2012**, *48*, 823–825.

(57) Tai, H.; Nishikawa, K.; Suzuki, M.; Higuchi, Y.; Hirota, S. Control of the Transition between Ni-C and Ni-SI a States by the Redox State of the Proximal Fe À S Cluster in the Catalytic Cycle of [NiFe]. *Angew. Chem. Int. Ed.* **2014**, *53*, 13817–13820.

(58) Roessler, M. M.; Evans, R. M.; Davies, R. A.; Armstrong, F. A. EPR Spectroscopic Studies of the Fe − S Clusters in the O_2 − Tolerant [NiFe]-Hydrogenase Hyd − 1 from Escherichia Coli and Characterization of the Unique [4Fe−3S] Cluster by HYSCORE. *J. Am. Chem. Soc.* **2012**, *134*, 15581−15594.

(59) Bleijlevens, B.; Faber, W.; Albracht, S. P. J. The [NiFe] Hydrogenase from Allochromatium Vinosum Studied in EPR-Detectable States : H/D Exchange Experiments That Yield New Information about the Structure of the Active Site. *J Biol Inorg Chem* **2001**, *6*, 763–769.

(60) Agrawal, A. G.; Gastel, M. Van; Ga, W.; Lubitz, W. Hydrogen Bonding Affects the [NiFe] Active Site of Desulfovibrio Vulgaris Miyazaki F Hydrogenase : A Hyperfine Sublevel Correlation Spectroscopy and Density Functional Theory Study. *J. Phys. Chem. B* **2006**, *110*, 8142–8150.

(61) Brazzolotto, D.; Gennari, M.; Queyriaux, N.; Simmons, T. R.; Pécaut, J.; Demeshko, S.; Meyer, F.; Orio, M.; Artero, V.; Duboc, C. Nickel-Centred Proton Reduction Catalysis in a Model of [NiFe] Hydrogenase. *Nat. Chem.* **2016**, *8*, 1054–1060.

(62) Schilter, D.; Gray, D. L.; Fuller, A. L.Synthetic Models for Nickel − Iron Hydrogenase Featuring Redox-Active Ligands. *Aust. J. Chem* **2017**, doi: 0.1071/CH16614_AC.

(63) Barton, B. E.; Olsen, M. T.; Rauchfuss, T. B. Artificial Hydrogenases. *Curr. Opin. Biotechnol.* **2010**, *21*, 292–297.

(64) Ohki, Y.; Tatsumi, K. Thiolate-Bridged Iron-Nickel Models for the Active Site of [NiFe] Hydrogenase. *Eur. J. Inorg. Chem.* **2011**, *2011*, 973–985.

(65) Helm, M. L.; Stewart, M. P.; Bullock, R. M.; DuBois, M. R.; DuBois, D. L. A Synthetic Nickel Electrocatalyst with a Turnover Frequency above 100,000 S^{-1} for H_2 Production. *Science* **2011**, *333*, 863–866.

(66) Priyadarshani, N.; Dutta, A.; Ginovska, B.; Buchko, G. W.; Hagan, M. O.; Raugei, S.; Shaw, W. J. Achieving Reversible H_2 /H^+ Interconversion at Room Temperature with Enzyme-Inspired Molecular Complexes: A Mechanistic Study. *ACS Catal.* **2016**, *6*, 6037–6049.

(67) Ogata, H.; Nishikawa, K.; Lubitz, W. Hydrogens Detected by Subatomic Resolution Protein Crystallography in a [NiFe] Hydrogenase. *Nature* **2015**, *520*, 571–574.

(68) Breglia, R.; Antonio, M.; Rodriguez, R.; Vitriolo, A.; Francisco, R.; Laredo, G.; Gioia, L. De; Greco, C. Theoretical Insights into [NiFe]− Hydrogenases Oxidation Resulting in a Slowly Reactivating Inactive State. *J Biol. Inorg. Chem.* **2017**, *22*, 137–151.

(69) Gordon, J. C.; Kubas, G. J. Perspectives on How Nature Employs the Principles of Organometallic Chemistry in Dihydrogen Activation in Hydrogenases. *Organometallics* **2010**, *29*, 4682–4701.

(70) Kaliakin, D. S.; Zaari, R. R.; Varganov, S. A. Effect of H_2 Binding on the Nonadiabatic Transition Probability between Singlet and Triplet States of the [NiFe]-Hydrogenase Active Site. *J. Phys. Chem. A* **2015**, *119*, 1066–1073.

(71) Keith, J. M.; Hall, M. B. Potential Hydrogen Bottleneck in Nickel-Iron Hydrogenase. *Inorg. Chem.* **2010**, *49*, 6378–6380.

(72) Pardo, A.; De Lacey, A. L.; Fernández, V. M.; Fan, H.-J.; Fan, Y.; Hall, M. B. Density Functional Study of the Catalytic Cycle of Nickel-Iron [NiFe] Hydrogenases and the Involvement of High-Spin Nickel(II). *J. Biol. Inorg. Chem.* **2006**, *11*, 286–306.

(73) Siegbahn, P. E. M. Proton and Electron Transfers in [NiFe] Hydrogenase. *Adv. Inorg. Chem.* **2004**, *56*, 101–125.

(74) Vedha, S. A.; Solomon, R. V.; Venuvanalingam, P. Atomic Partitioning of M-H_2 Bonds in [NiFe] Hydrogenase-a Test Case of Concurrent Binding. *Phys. Chem. Chem. Phys.* **2014**, *16*, 10698–10707.

(75) Krämer, T.; Kampa, M.; Lubitz, W.; van Gastel, M.; Neese, F. Theoretical Spectroscopy of the Ni(II) Intermediate States in the Catalytic Cycle and the Activation of [NiFe] Hydrogenases. *ChemBioChem* **2013**, *14*, 1898–1905.

(76) Söderhjelm, P.; Ryde, U. Combined Computational and Crystallographic Study of the Oxidised States of [NiFe] Hydrogenase. *J. Mol. Struct. THEOCHEM* **2006**, *770*, 199–219.

(77) Wu, H.; Hall, M. B. Density Functional Theory on the Larger Active Site Models for [NiFe] Hydrogenases: Two-State Reactivity? *Comptes Rendus Chim.* **2008**, *11*, 790–804.

(78) Jayapal, P.; Sundararajan, M.; Hillier, I. H.; Burton, N. A. QM/MM Studies of Ni-

Fe Hydrogenases: The Effect of Enzyme Environment on the Structure and Energies of the Inactive and Active States. *Phys. Chem. Chem. Phys.* **2008**, *10*, 4249–4257.

(79) Amara, P.; Volbeda, A.; Fontecilla-camps, J. C.; Field, M. J. A Hybrid Density Functional Theory/Molecular Mechanics Study of Nickel-Iron Hydrogenase: Investigation of the Active Site Redox States. *J. Am. Chem. Soc.* **1999**, *121*, 4468–4477.

(80) Bruschi, M.; Tiberti, M.; Guerra, A.; De Gioia, L. Disclosure of Key Stereoelectronic Factors for Efficient H_2 Binding and Cleavage in the Active Site of [NiFe]-Hydrogenases. *J. Am. Chem. Soc.* **2014**, *136*, 1803–1814.

(81) Dauter, Z.; Wilson, K. S.; Siekert, L. C.; Moulist, J.; Meyer, J. Zinc- and Iron-Rubredoxins from Clostridium Pasteurianum at Atomic Resolution : A High-Precision Model of a ZnS4 Coordination Unit in a Protein. *Proc. Natl. Acad. Sci. USA* **1996**, *93*, 8836–8840.

(82) Chen, C.-J.; Lin, Y.-H.; Huang, Y.-C.; Liu, M.-Y. Crystal Structure of Rubredoxin from Desulfovibrio Gigas to Ultra-High 0.68Å Resolution. *Biochem. Biophys. Res. Commun.* **2006**, *349*, 79–90.

(83) Lovenberg, W.; Sobel, B. E. Rubredoxin: A New Electron Transfer Protein from Clostridium Pasteurianum. *Proc. Natl. Acad. Sci. U. S. A.* **1965**, *54*, 193–199.

(84) Vicente, J. B.; Teixeira, M. Redox and Spectroscopic Properties of the Escherichia Coli Nitric Oxide-Detoxifying System Involving Flavorubredoxin and Its NADH-Oxidizing Redox Partner. *J. Biol. Chem.* **2005**, *280*, 34599–34608.

(85) Van Beilen, J. B.; Neuenschwander, M.; Smits, T. H. M.; Roth, C.; Balada, S. B.; Witholt, B. Rubredoxins Involved in Alkane Oxidation. *J. Bacteriol.* **2002**, *184*, 1722–1732.

(86) Nolling, J.; Ishii, M.; Koch, J.; Pihl, T. D.; Reeve, J. N.; Thauer, R. K.; Hedderich, R. Characterization of a 45-kDa Flavoprotein and Evidence for a Rubredoxin, Two Proteins That Could Participate in Electron Transport from H_2 to CO_2 in Methanogenesis in Methanobacterium Thermoautotrophicum. *Eur. J. Biochem.* **1995**, *231*, 628–638.

(87) Yoon, K. S.; Hille, R.; Hemann, C.; Tabita, F. R. Rubredoxin from the Green Sulfur Bacterium Chlorobium Tepidum Functions as an Electron Acceptor for Pyruvate Ferredoxin Oxidoreductase. *J. Biol. Chem.* **1999**, *274*, 29772–29778.

(88) Chen, L.; Liu, M. Y.; LeGall, J.; Fareleira, P.; Santos, H.; Xavier, A V. Rubredoxin Oxidase, a New Flavo-Hemo-Protein, Is the Site of Oxygen Reduction

to Water by The "strict anaerobe" Desulfovibrio Gigas. *Biochem. Biophys. Res. Commun.*, 1993, *193*, 100–105.

(89)   Ma, K.; Adams, M. W. W. A Hyperactive NAD(P)H : Rubredoxin Oxidoreductase from the Hyperthermophilic Archaeon Pyrococcus Furiosus. *J. Bacteriol.* **1999**, *181*, 5530–5533.

(90)   Santos, H.; Fareleira, P.; Xavier, A. V.; Chen, L.; Liu, M. Y.; Legall, J. Aerobic Metabolism of Carbon Reserves by the "Obligate Anaerobe" Desulfovibrio Gigas. *Biochem. Biophys. Res. Commun.* **1993**, *195*, 551–557.

(91)   Calderon, R. H.; García-Cerdán, J. G.; Malnoë, A.; Cook, R.; Russell, J. J.; Gaw, C.; Dent, R. M.; De Vitry, C.; Niyogi, K. K. A Conserved Rubredoxin Is Necessary for Photosystem II Accumulation in Diverse Oxygenic Photoautotrophs. *J. Biol. Chem.* **2013**, *288*, 26688–26696.

(92)   Liu, F.; Geng, J.; Gumpper, R. H.; Barman, A.; Davis, I.; Ozarowski, A.; Hamelberg, D.; Liu, A. An Iron Reservoir to the Catalytic Metal: The Rubredoxin Iron in an Extradiol Dioxygenase. *J. Biol. Chem.* **2015**, *290*, 15621–15634.

(93)   Luo, Y.; Niu, S.; Ichiye, T. Understanding Rubredoxin Redox Sites by Density Functional Theory Studies of Analogues. *J. Phys. Chem. A* **2012**, *116*, 8918–8924.

(94)   Xiao, Z.; Lavery, M. J.; Ayhan, M.; Scrofani, S. D. B.; Wilce, M. C. J.; Guss, J. M.; Tregloan, P. A.; George, G. N.; Wedd, A. G.; Uni, V.; et al. The Rubredoxin from Clostridium Pasteurianum : Mutation of the Iron Cysteinyl Ligands to Serine. Crystal and Molecular Structures of Oxidized and Dithionite-Treated Forms of the Cys42Ser Mutant. *J. Am. Chem. Soc.* **1998**, *120*, 4135–4150.

(95)   Sulpizi, M.; Raugei, S.; VandeVondele, J.; Carloni, P.; Sprik, M. Calculation of Redox Properties: Understanding Short- and Long-Range Effects in Rubredoxin. *J. Phys. Chem. B* **2007**, *111*, 3969–3976.

(96)   Stephens, P. J.; Jollie, D. R.; Warshel, A. Protein Control of Redox Potentials of Iron − Sulfur Proteins. *Chem. Rev.* **1996**, *96*, 2491–2513.

(97)   Yang, X.; Wang, X. Bin; Fu, Y. J.; Wang, L. S. On the Electronic Structure of [1Fe] Fe-S Complexes from Anionic Photoelectron Spectroscopy. *J. Phys. Chem. A* **2003**, *107*, 1703–1709.

(98)   Sterpone, F.; Melchionnab, S. Thermophilic Proteins : Insight and Perspective from in Silico Experiments. *Chem. Soc. Rev.* **2012**, *41*, 1665–1676.

(99)   Karshikoff, A.; Nilsson, L.; Ladenstein, R. Rigidity versus Flexibility : The Dilemma of Understanding Protein Thermal Stability.

FEBS J. **2015**, *282*, 3899–3917.

(100) Jenney, F. E.; Adams, M. W. W.; Lemaster, D. M. Millisecond Time Scale Conformational Flexibility in a Hyperthermophile Protein at Ambient Temperature. *Proc. Natl. Acad. Sci.* **1999**, *97*, 3166–3170.

(101) Pica, A.; Graziano, G.; Ii, F.; Universitario, C.; Angelo, S.; Cintia, V.; Graziano, G. Shedding Light on the Extra Thermal Stability of Thermophilic Proteins. *Biopolymers* **2016**, *105*, 856–863.

(102) Borreguero, J. M.; He, J.; Meilleur, F.; Weiss, K. L.; Brown, C. M.; Myles, D. A.; Herwig, K. W.; Agarwal, P. K. Redox-Promoting Protein Motions in Rubredoxin. *J. Phys. Chem. B* **2011**, *115*, 8925–8936.

(103) Micaelo, N. M.; Victor, B. L.; Soares, C. M. Protein Thermal Stabilization by Charged Compatible Solutes: Computational Studies in Rubredoxin from Desulfovibrio Gigas. *Proteins Struct. Funct. Genet.* **2008**, *72*, 580–588.

(104) Berka, K.; Hobza, P.; Vondrášek, J. Analysis of Energy Stabilization inside the Hydrophobic Core of Rubredoxin. *ChemPhysChem* **2009**, *10*, 543–548.

(105) Gámiz-Hernández, A. P.; Galstyan, A. S.; Knapp, E. W. Understanding Rubredoxin Redox Potentials: Role of H-Bonds on Model Complexes. *J. Chem. Theory Comput.* **2009**, *5*, 2886–2897.

(106) Gamiz-Hernandez, A. P.; Kieseritzky, G.; Ishikita, H.; Knapp, E. W. Rubredoxin Function: Redox Behavior from Electrostatics. *J. Chem. Theory Comput.* **2011**, *7*, 742–752.

(107) Luo, Y.; Niu, S.; Ichiye, T. Understanding Rubredoxin Redox Sites by Density Functional Theory Studies of Analogues. *J. Phys. Chem. A* **2012**, *116*, 8918–8924.

(108) Maelia, L. E.; Millar, M.; Koch, S. A. General Synthesis of Iron(III) Tetrathiolate Complexes. Structural and Spectroscopic Models for the [Fe(Cys-S)$_4$] Center in Oxidized Rubredoxin. *Inorg. Chem.* **1992**, *31*, 4594–4600.

(109) Niu, S.; Nichols, J. a.; Ichiye, T. Optimization of Spin-Unrestricted Density Functional Theory for Redox Properties of Rubredoxin Redox Site Analogues. *J. Chem. Theory Comput.* **2009**, *5*, 1361–1368.

(110) DePolo, G. E.; Kaliakin, D. S.; Varganov, S. A. Spin-Forbidden Transitions between Electronic States in the Active Site of Rubredoxin. *J. Phys. Chem. A* **2016**, *120*, 8691–8698.

(111) Fedorov, D. G.; Asada, N.; Nakanishi, I.; Kitaura, K. The Use of Many-Body

Expansions and Geometry Optimizations in Fragment-Based Methods. *Acc. Chem. Res.* **2014**, *47*, 2846−2856.

(112) Fedorov, D. G.; Alexeev, Y.; Kitaura, K. Geometry Optimization of the Active Site of a Large System with the Fragment Molecular Orbital Method. *J. Phys. Chem. Lett.* **2011**, *2*, 282–288.

(113) Fedorov, D. G.; Nagata, T.; Kitaura, K. Exploring Chemistry with the Fragment Molecular Orbital Method. *Phys. Chem. Chem. Phys.* **2012**, *14*, 7562.

(114) Gordon, M. S.; Fedorov, D. G.; Pruitt, S. R.; Slipchenko, L. V. Fragmentation Methods: A Route to Accurate Calculations on Large Systems. *Chem. Rev.* **2012**, *112*, 632–672.

(115) Tanaka, S.; Mochizuki, Y.; Komeiji, Y.; Okiyama, Y.; Fukuzawa, K. Electron-Correlated Fragment-Molecular-Orbital Calculations for Biomolecular and Nano Systems. *Phys. Chem. Chem. Phys.* **2014**, *16*, 10310–10344.

(116) Alexeev, Y.; Mahajan, A.; Leyffer, S.; Fletcher, G.; Fedorov, D. G. Heuristic Static Load-Balancing Algorithm Applied to the Fragment Molecular Orbital Method. In *International Conference for High Performance Computing, Networking, Storage and Analysis, SC*; Salt Lake City, Utah, USA, 2012.

(117) Fedorov, D. G.; Kitaura, K. Subsystem Analysis for the Fragment Molecular Orbital Method and Its Application to Protein-Ligand Binding in Solution. *J. Phys. Chem. A* **2016**, *120*, 2218–2231.

(118) Rubredoxins, M.; Cavagnero, S.; Debe, D. A.; Zhou, Z. H.; Adams, M. W. W.; Chan, S. I. Kinetic Role of Electrostatic Interactions in the Unfolding of Hyperthermophilic and Mesophilic Rubredoxins. *Biochemistry* **1998**, *37*, 3369–3376.

(119) Wang, X.; Wang, L. Probing the Electronic Structure of Redox Species and Direct Determination of Intrinsic Reorganization Energies of Electron Transfer Reactions. *J. Chem. Phys.* **2000**, *112*, 6959–6962.

(120) Cakmakci, G. Identifying Alternative Conceptions of Chemical Kinetics among Secondary School and Undergraduate Students in Turkey. *J. Chem. Educ.* **2010**, *87*, 449–455.

(121) Kaliakin, D. S.; Zaari, R. R.; Varganov, S. A. 3D Printed Potential and Free Energy Surfaces for Teaching Fundamental Concepts in Physical Chemistry. *J. Chem. Educ.* **2015**, *92*, 2106−2112.

(122) Bauer, S. H.; Wilcox, C. F. What's in a Name-Transition State or Critical

Transition Structure? *J. Chem. Educ.* **1995**, *72*, 13–16.

(123) Lolur, P.; Dawes, R. 3D Printing of Molecular Potential Energy Surface Models. *J. Chem. Educ.* **2014**, *91*, 1181–1184.

(124) Blauch, D. N.; Carroll, F. A. 3D Printers Can Provide an Added Dimension for Teaching Structure–Energy Relationships. *J. Chem. Educ.* **2014**, *91*, 1254–1256.

(125) Teplukhin, A.; Babikov, D. Visualization of Potential Energy Function Using an Isoenergy Approach and 3D Prototyping. *J. Chem. Educ.* **2015**, *92*, 305–309.

(126) Chen, T.-H.; Lee, S.; Flood, A. H.; Miljanić, O. Š. How to Print a Crystal Structure Model in 3D. *CrystEngComm* **2014**, *16*, 5488–5493.

Chapter II. Computational Methods and Theory

I. Density Functional Theory

A. Electronic Density and the Basics of Density Functional Theory

All of the wave-function methods are based on solving the Schrödinger equation.

$$H\phi = E\phi$$

(1)

In eq 1, E is the energy, and the electronic Hamiltonian, H, can be written as,

$$H = -\sum_i \frac{1}{2}\nabla_i^2 - \sum_{iA} \frac{Z_A}{|r_i - r_A|} + \sum_{i>j} \frac{1}{r_{ij}}$$

(2)

Here r_i is the spatial coordinate of electron i, r_{ij} is the distance between electrons i and j, r_A and Z_A are the spatial coordinate and the charge of nuclei A, respectively.

Eq 1 shows that the total energy of the system, E, could be obtained by acting with H on the antisymmetric wave functions, $\phi(x_1, x_2, x_3 ... x_N)$ that describes the behavior of the electrons (x_i represents r_i and spin σ_i). Minimization of the energy by varying ϕ yields the ground state energy of the system.

A conceptual difference between the wave-function methods and density functional theory (DFT) is the use of *electron density* instead of wave function by the later. Electron density, ρ, can be expressed as,

$$\rho(r) = \sum_i |\phi_i(r)|^2$$

(3)

Here ϕ_i is the one-electron wave function (molecular orbital) of electron i. The fundamental idea of the density functional theory is the Hohenberg-Kohn theorem, which states that the properties of the N-electron system are uniquely determined by an electron density. Based on this theorem, the ground state energy is represented as an electron

density functional, $E[\rho]$. This density functional can be written as a sum of the kinetic energy functional of electrons ($T[\rho]$), the nuclear-electron interaction ($V_{ne}[\rho]$), and the electron-electron interaction ($V_{ee}[\rho]$).

$$E[\rho] = T[\rho] + V_{ne}[\rho] + V_{ee}[\rho]$$
(4)

The exact forms of the $V_{ee}[\rho]$ and $T[\rho]$ are not known, thus the total energy of the system within DFT is described as,

$$E[\rho] = T_s[\rho] + V_{ne}[\rho] + J[\rho] + E_{XC}[\rho]$$
(5)

Where $T_s[\rho]$ is the kinetic energy functional of the system with non-interacting electrons, $J[\rho]$ is the classical Coulomb electron-electron repulsion, and $E_{XC}[\rho]$ is the exchange-correlation functional that also accounts for the kinetic energy correction due to electron interaction.

$$E_{XC}[\rho] = (T[\rho] - T_s[\rho]) + (V_{ee}[\rho] - J[\rho])$$
(6)

Finally, individual terms of eq 5 are expressed as,

$$T_s[\rho] = \sum_i \left\langle \phi_i \left| -\frac{1}{2}\nabla^2 \right| \phi_i \right\rangle$$
(7)

$$V_{ne}[\rho] = \int \rho(r)v_{ext}(r)$$
(8)

$$J[\rho] = \frac{1}{2} \int \int \frac{\rho(r_1)\rho(r_2)}{|r_1 - r_2|} dr_1 dr_2$$
(9)

Where r_1 and r_2 are the spatial coordinates of the interacting electrons, and $v_{ext}(r)$ is the external potential of the nuclei that is written as,

$$v_{ext}(r) = \sum_{iA} \left(\frac{Z_A}{|r_i - R_A|} \right)$$

(10)

One can obtain the set of one-electron Kohn-Sham orbital equations by variational minimization of the energy functional in eq 5 with respect to molecular orbitals,

$$-\frac{1}{2}\nabla^2 \phi_i + v_{KS}\phi_i = \varepsilon_i \phi_i$$

(11)

$$v_{KS} = v_{ext} + v_{el} + \frac{\delta E_{XC}}{\delta \rho}$$

(12)

Here ε_i is the one-electron energy, and v_{el} is the mean-field potential due to the surrounding electrons.[1,2]

As seen from eqs 1-12, the only part of the energy density functional that is not known exactly is the $E_{XC}[\rho]$. The expression for $E_{XC}[\rho]$ is not trivial and varies between different DFT functionals. The specific approaches to derivation of $E_{XC}[\rho]$ are discussed in the next subsection.

B. Exchange-Correlation Functionals and Corrections

Main types of exchange correlation functional can be separated into four groups: local density approximation (LDA), general gradient approximation (GGA), meta-GGA, and hybrid functionals. In LDA, the E_{XC} is a functional of electron density only. The exchange part, E_X, of the E_{XC} is obtained from the uniform electron gas model,[1,2]

$$E_X^{LDA}[\rho] = -\frac{3}{4}\left(\frac{3}{\pi}\right)^{1/3}\int \rho^{4/3}dr = \frac{-3e^2 k_F}{4\pi}$$

(13)

In eq 13, k_F is the Fermi wavenumber, and e is the electron charge. The correlation part, E_C, of the E_{XC} cannot be expressed in a simple analytical form leading to the use of different complex expressions. The example of such expression is the widely used functional of Vosko, Wilk and Nusair (VWN).

$$\epsilon(r_s) = A \left(ln\frac{x^2}{X(x)} + \frac{2b}{Q}tan^{-1}\frac{Q}{2x+b} - \right.$$

$$\left. - \frac{bx_0}{X(x_0)} \left[ln\frac{(x-x_0)^2}{X(x)} + \frac{2(b+2x_0)}{Q}tan^{-1}\frac{Q}{2x+b} \right] \right) \tag{14}$$

Here ϵ is the energy per particle, $x=r_s^{1/2}$ and r_s is the local Seitz radius,

$$r_s = \sqrt[3]{\frac{4\pi\rho}{3}} \tag{15}$$

Other parameters within the eq 14 are defined as, $X(x)=x^2+bx+c$ and $Q=(4c-b^2)^{1/2}$, where x_0, b and c are the empirical constants.[3] The LDA usually overestimates the binding between atoms in molecules, which could lead to very large errors, especially when applied to chemical reactions.[4]

The natural development of the E_{XC} is making it a functional of not only electron density, but also the gradient of density. This approach is called general gradient approximation (GGA).

$$E_{XC}^{GGA}[\rho_\uparrow, \rho_\downarrow] = \int d^3rf(\rho_\uparrow, \rho_\downarrow, \nabla\rho_\uparrow, \nabla\rho_\downarrow) \tag{16}$$

In eq 16 the $\rho_\uparrow$ and $\rho_\downarrow$ terms represent the density of electrons with spin +1/2 and -1/2, respectively.

One of the most popular functionals of the GGA-type was developed by Perdew, Burke and Ernzerhof (PBE). In the PBE functional, which is used in this work (Chapters III and IV), the correlation energy is written as,

$$E_C^{GGA}[\rho_\uparrow, \rho_\downarrow] = \int d^3r\rho[\epsilon_C^{LDA}(r_s, \zeta) + H(r_s, \zeta, t)]$$

(17)

Here ζ is the relative spin polarization and t is the dimensionless gradient. These variables are defined as $\zeta=[\rho\uparrow-\rho\downarrow]/\rho$ and $t=|\nabla\rho|/2\vartheta k_s\rho$, where ϑ is the spin-scaling factor, and k_s is the Thomas-Fermi screening wave number, which are expressed as $\vartheta(\zeta)=[(1+\zeta)^{2/3}+(1-\zeta)^{2/3}]/2$ and

$$k_s = \sqrt{4k_F/\pi a_0}$$

$$a_0 = \hbar^2/me^2$$

(21)

Here $\hbar$ is the Planck constant, and m is the mass of electron.

Finally, the expression for H is written as,

$$H = (e^2/a_0)\gamma\vartheta^3 \times ln\left(1 + \frac{\beta}{\gamma}t^2\left[\frac{1 + At^2}{1 + At^2 + A^2t^4}\right]\right)$$

(22)

$$A = \frac{\beta}{\gamma}[exp\left(-\epsilon_C^{LDA}(r_s, \zeta)/\left(\gamma\vartheta^3 e^2/a_0\right)\right) - 1]^{-1}$$

(23)

In eqs 22-23, β and γ are empirical constants. As for E_X, it is expressed as,

$$E_X^{GGA}[\rho] = \int d^3r\rho\epsilon_X^{LDA}(\rho)F_X(s)$$

(24)

The dimensionless gradient s is,

$$s = \frac{|\nabla\rho|}{2k_F\rho} = \frac{(r_s/a_0)^{1/2}\vartheta t}{c}$$

(25)

Here c is an empirical constant, and $F_x(s)$ is,

$$F_X(s) = 1 + \kappa - \frac{\kappa}{(1 + \mu s^2/\kappa)}$$

(26)

In the above equation, κ and μ are empirical constants.[5] Despite the higher accuracy of GGA compared to LDA, the former has certain limitations, such as overestimating the atomization energies.[4]

A further improvement of the exchange correlation functional can be achieve by inclusion of the higher derivative of electron density and/or the orbital kinetic energy density (τ), as in meta-GGA functionals (MGGA)

$$E_{XC}^{MGGA}[\rho_\uparrow, \rho_\downarrow] = \int d^3 r \rho \epsilon_{XC}(\rho_\uparrow, \rho_\downarrow, \nabla\rho_\uparrow, \nabla\rho_\downarrow, \tau_\uparrow, \tau_\downarrow)$$

$$\tau(r) = \sum_i^{occup} \frac{1}{2}|\nabla\phi_i(r)|^2$$

(27)

Here ϕ_i are the occupied Kohn-Sham orbitals, as in the eq 11. The TPSS functional developed by Tao, Perdew, Staroverov and Scuseria is one of the most widely used MGGA-type functionals. In this functional, used in Chapter III, the exchange part is defined as,[6]

$$E_X^{MGGA}[\rho] = \int d^3 r \rho \epsilon_X^{LDA}(\rho) F_X(p, z)$$

(28)

In eq 28, F_x is defined as,

$$F_X(x) = 1 + \kappa - \frac{\kappa}{(1 + x/\kappa)}$$

(30)

The density of kinetic energy, z, is expressed as,

$$z = \tau^W/\tau \qquad \tau = \sum_i \tau_i \qquad \tau^W = \frac{1}{8}|\triangle\rho|^2/\rho$$

(31)

The argument *x* in eq 30 is defined as,

$$x = \left(\left[\frac{10}{81} + c\frac{z^2}{(1+z^2)^2}\right]p + \frac{146}{2025}\tilde{q}_b^2 - \right.$$

$$-\frac{73}{405}\tilde{q}_b\sqrt{\frac{1}{2}\left(\frac{3}{5}z\right)^2 + \frac{1}{2}p^2} + \frac{1}{\kappa}\left(\frac{10}{81}\right)^2 p^2 +$$

$$\left. + 2\sqrt{e}\frac{10}{81}\left(\frac{3}{5}z\right)^2 + e\mu p^3\right)/(1+\sqrt{e}p)^2$$

(32)

Here $\tilde{q}_b$ is written as,

$$\tilde{q}_b = \frac{(9/20)(\alpha - 1)}{[1 + b\alpha(\alpha - 1)]^{1/2}} + 2p/3$$

(33)

In eq 33, α has the following form,

$$\alpha = (\tau - \tau^W)/\tau^{unif} = (5p/3)(z^{-1} - 1)$$

(34)

Here τ^{unif} is the kinetic energy density of uniform electron gas,

$$\tau^{unif} = \frac{3}{10}(3\pi^2)^{2/3}\rho^{5/3}$$

(35)

As for the correlation energy in TPSS, it is based on the refined functional of Perdew, Kurth, Zupan and Blaha (PKZB)[7] and is defined as,

$$E_C^{MGGA}[\rho\uparrow, \rho\downarrow] = \int d^3r\rho\epsilon_C^{revPKZB} \times [1 + d\epsilon_C^{revPKZB}(\tau^W/\tau)^3]$$

(36)

where $\epsilon_C^{revPKZB}$ is expressed as,

$$\epsilon_C^{revPKZB} = \epsilon_C^{PBE}(\rho\uparrow, \rho\downarrow, \nabla\rho\uparrow, \nabla\rho\downarrow)[1 + C(\zeta, \xi)(\tau^w/\tau)^2] -$$

$$-[1 + C(\zeta, \xi)](\tau^w/\tau)^2 \sum_i \frac{\rho_i}{\rho} \tilde{\epsilon}_c$$

(37)

The last term of eq 37 is,

$$\tilde{\epsilon}_c = max[\epsilon_C^{PBE}(\rho_i, 0, \nabla\rho_i, 0), \epsilon_C^{PBE}(\rho\uparrow, \rho\downarrow, \nabla\rho\uparrow, \nabla\rho\downarrow))$$

(38)

As for $C(\zeta, \xi)$, it is expressed as,

$$C(\zeta, \xi) = \frac{C(\zeta, 0)}{(1 + \xi^2[(1+\zeta)^{-4/3} + (1-\zeta)^{-4/3}]/2)^4}$$

(39)

where $C(\zeta, 0)$ and ξ are,

$$C(\zeta, 0) = 0.53 + 0.87\zeta^2 + 0.50\zeta^4 + 2.26\zeta^6$$

(40)

$$\xi = \frac{|\nabla\zeta|}{2(3\pi^2\rho)^{1/3}}$$

(41)

In general, the accuracy of the GGA and meta-GGA functionals can be improved by addition of the Hartree-Fock (HF) exchange energy.[4] The functionals that contain the HF exchange are called hybrid functionals. The E_X within the HF formalism can be expressed as,[1]

$$E_X^{HF} = -\frac{1}{2} \sum_{ij} \int \int \frac{\phi_i^*(r_1)\phi_j(r_1)\phi_j^*(r_2)\phi_i^*(r_2)}{|r_1 - r_2|} dr_1 dr_2$$

(42)

One of the most popular hybrid functional developed by Becke, Lee, Yang, Parr (B3LYP) is a linear combination of multiple density functionals and the Hartree-Fock exchange,[8–11]

$$E_X^{B3LYP} = 0.20E_X^{HF} + 0.80E_X^{LDA} + 0.72E_X^{B88} + 0.81E_C^{LYP} + 0.19E_C^{VWN}$$

(43)

Here the exchange contribution (E_X) is coming from *HF, LDA* and *B88,*[11] while E_C is defined by *LYP*[10] and *VWN* functionals.

The accuracy of the hybrid functionals sometimes can be further improved by introducing the long-range correction. The idea of the long-range correction is based on the assumption that the mixture of E_X^{HF} and E_X^{GGA} in the hybrid GGA DFT exchange should be depend on the distance between the interacting electrons.[12] The two-electron operator describing electron-electron interaction can be separated into the long-range (LR) and short-range (SR) potentials using the error function, *erf(x)*.[13]

$$\frac{1}{r_{12}} = \frac{1 - erf(yr_{12})}{r_{12}} + \frac{erf(yr_{12})}{r_{12}}$$

(44)

Here *y* is the parameter that defines the transition between the SR and LR potentials. The first term in eq 44 is for the SR potential and it goes to zero when r_{12} goes to infinity, while the second term governs the long-range potential. In long range corrected density functional theory (LC-DFT), the hybrid GGA exchange is applied in SR, while the full Hartree-Fock exchange is utilized in LR,

$$E_{XC}^{LC} = E_C + (1 - C_{HF})E_{X,SR}^{GGA} + C_{HF}E_{X,SR}^{HF} + E_{X,LR}^{HF}$$

(45)

In eq 45 the E_{XC}^{LC} is the total long-range corrected exchange-correlation energy, C_{HF} is the portion of HF exchange in hybrid functional, while the $E_{X,SR}^{GGA}$, $E_{X,SR}^{HF}$ and $E_{X,LR}^{HF}$ are the GGA exchange energy in SR, HF exchange energy in SR, and HF energy in LR, respectively.

Another correction that is often crucial for the DFT calculations is a dispersion correction. This correction can be important because DFT, in its original form, does not provide accurate description of the dispersion interactions. This is due to the fact that these interactions not only have long-range nature, but also are the result of electron

correlation. Thus the description of dispersion interactions purely by density-based formalism is nontrivial. Combination of DFT and the empirical dispersion correction (DFT-D) has been proven to be a computationally efficient way to treat systems with significant dispersion interactions, such as multiple layers of the graphene sheets.[14,15] Within the DFT-D formalism, the total energy of the system, E_{DFT-D}, is defined as,

$$E_{DFT\text{-}D} = E_{DFT} - E_{disp} \tag{46}$$

Here the E_{DFT} is the energy of the uncorrected DFT, and E_{disp} is the dispersion correction. The negative sign in eq 46 is a result of a convention. The empirical dispersion correction is defined as,

$$E_{disp} = \sum_{AB} \sum_{n=6,8,10,\ldots} s_n \frac{C_n^{AB}}{r_{AB}^n} f_{d,n}(r_{AB}) \tag{47}$$

In eq 47 C_n^{AB}, r_{AB}^n, s_n are the dispersion coefficients of the n-th order for atom pair AB, the internuclear distance of this pair, and the scaling factor, respectively. As for $f_{d,n}(r_{AB})$, it is the damping function that helps to avoid near singularities for small internuclear distances and double-counting effects of correlation from E_{XC}.

$$f_{d,n}(r_{AB}) = \frac{1}{1 + 6(r_{AB}/(s_{r,n} R_0^{AB}))^{-\alpha_n}} \tag{48}$$

Here α_n are the empirical parameter, $s_{r,n}$ is the scaling factor, and R_0^{AB} is the cutoff radii.

Despite all advances in modern functionals, the DFT applicability and accuracy are not universal across the different molecular systems. In general, the results obtained with a given flavor of DFT can be trusted only if the methodology was validated on reference systems for witch the experimental data or the high-level computational results

are available.[16,17] The reference systems should have the similar electronic structure, but can have the smaller size, thus this approach is feasible for majority of the computational problems.[18,19]

II. High-Level Electronic Structure Methods

A. Multi-Reference Configuration Interaction

In configuration interaction (CI) method the wave function, ϕ, is represented as,[20,21]

$$|\phi\rangle = \sum_{j=1}^{N_{dim}} c_j \, |j\rangle$$

(49)

Where $|j\rangle$ and c_j are the expansion functions (ground and excited Slater determinants) and expansion coefficients, respectively. The expansion coefficients are defined variationally by energy minimization, which is mathematically can be expressed as $\partial E^{trial}/\partial c = 0$. Here the energy, E^{trial}, is defined as an expectation value for the CI trial wave function,

$$E^{trial} = \frac{\langle \phi \,|H|\, \phi \rangle}{\langle \phi | \phi \rangle}$$

(50)

where H is the electronic Hamiltonian. Based on the eqs 50 and 51, the minimization energy problem can be defined as eigenvalue equation,

$$H c^k = E_k c^k$$

(51)

Here k represents the order of excitation. The electronic Hamiltonian can be defined in terms of the creation (a^+) and annihilation (a) operators for the molecular spin orbitals p, q, r, and s.

$$H = \sum_{p,q} h_{pq} a_p^+ a_q + \frac{1}{2} \sum_{p,q,r,s} (pq|rs) a_p^+ a_r^+ a_s a_q$$

$$(52)$$

In eq 54, h_{pq} is a one-electron integrals and $(pq|rs)$ are the two-electron repulsion integrals. Alternatively, the Hamiltonian could be represented in terms of spin-adapted generators (E_{pq}) and generator products (e_{pqrs}).

$$H = \sum_{p,q} h_{pq} E_{pq} + \frac{1}{2} \sum_{p,q,r,s} (pq|rs) e_{pqrs}$$

$$(53)$$

In the simpler single-reference version of configuration interaction, the CI expansion space is generated as the excitation from the reference Hartree-Fock determinant ϕ_0,

$$(|l\rangle\,; l = 1 \ldots N_{dim}) = (|\phi_0\rangle\,|\phi_i^a\rangle\,|\phi_{ij}^{ab}\rangle\,|\phi_{ijk}^{abc}\rangle\,, \ldots)$$

$$|\phi_i^a\rangle = a_a^+ a_i\,|\phi_0\rangle\,;\,|\phi_{ij}^{ab}\rangle = a_a^+ a_b^+ a_j a_a\,|\phi_0\rangle\,;$$

$$|\phi_{ijk}^{abc}\rangle = a_a^+ a_b^+ a_c^+ a_k a_j a_i\,|\phi_0\rangle\,; \ldots$$

$$(54)$$

Here indices $i, j, k, \ldots$ denote occupied orbitals, while $a, b, c, \ldots$ label unoccupied (virtual) orbitals. Using the expansion function (excited determinants), ϕ_i^a describing single excitations, ϕ_{ij}^{ab} double excitations, ϕ_{ijk}^{acb} describing triple excitations, etc., one can construct the CI wave function as,

$$|\phi\rangle = c_0\,|\phi_0\rangle + \sum_{i,a} c_i^a\,|\phi_i^a\rangle + \sum_{i>j,a>b} c_{ij}^{ab}\,|\phi_{ij}^{ab}\rangle + \sum_{i>j>k,a>b>c} c_{ijk}^{abc}\,|\phi_{ijk}^{abc}\rangle + \ldots$$

$$(55)$$

In the multi-reference version of CI (MRCI), the reference determinant is replaced by a set of reference determinants,

$$\left|\phi(m)_i^a\right\rangle = a_a^+ a_i \left|m; ref\right\rangle ;$$

$$\left|\phi(m)_{ij}^{ab}\right\rangle = a_a^+ a_b^+ a_j a_i \left|m; ref\right\rangle ;$$

$$\left|\phi(m)_{ijk}^{abc}\right\rangle = a_a^+ a_b^+ a_c^+ a_k a_j a_i \left|m; ref\right\rangle ; \dots$$

$$for \ m = 1 \dots N_{ref} \tag{56}$$

Here N_{ref} is the number of reference determinants in the expansion function. Based on the multi-reference expansions of eq 56, the MRCI wave function can be written as,

$$\left|\phi_{MRCI}\right\rangle = \sum_m c_m \left|m\right\rangle + \sum_m \sum_{i,a} c(m)_i^a \left|\phi(m)_i^a\right\rangle +$$

$$+ \sum_m \sum_{i>j,a>b} c(m)_{ij}^{ab} \left|\phi(m)_{ij}^{ab}\right\rangle +$$

$$+ \sum_m \sum_{i>j>k,a>b>c} c(m)_{ijk}^{abc} \left|\phi(m)_{ijk}^{abc}\right\rangle + \dots \tag{57}$$

The multi-reference wave function for MRCI is obtained using the multi-reference self-consistent field (MCSCF) method. In MCSCF both configuration expansion coefficients and molecular orbital coefficients are variationally optimized.[20,21] To reduce the number of reference determinants the concept of orbital active space is introduced. Only excitations between the active space orbitals are included into MCSCF wave function. The electrons and orbitals within the active space are called the active electrons and active orbitals, respectively. The most common form of the MCSCF is the one in which the active electrons are distributed in all possible ways within the active space. This particular form of MCSCF, called complete active space self-consistent field (CASSCF), is widely used in MRCI and mutli-reference perturbation theory methods.[22]

B. Multi-Reference Perturbation Theory

Multi-reference perturbation theory is a less computationally expensive way to recover a large portion of electron correlation without relying on often very long CI expansion. In perturbation theory the total Hamiltonian, H, is split into the unperturbed Hamiltonian, $H^{(0)}$, and the perturbation operator, V, such that $H=H^{(0)}+V$.[23] The multi-reference version of perturbation theory comes in several forms. In quasi-degenerate perturbation theory (QDPT), the effective Hamiltonian is based on the pure CI functions basis, and the energies of the states of interest are obtained upon diagonalization of this basis. The effective Hamiltonian to the second-order within QDPT, H_{eff}, is defined by the expression,[24]

$$H_{eff}^{(0-2)} = \left\langle A \left| H^{(0)} \right| B \right\rangle + \frac{1}{2} \sum_{I} \left(\frac{\langle A|V|I\rangle \langle I|V|B\rangle}{E_B^{(0)} - E_I^{(0)}} + \frac{\langle B|V|I\rangle \langle I|V|A\rangle}{E_A^{(0)} - E_I^{(0)}} \right) \tag{58}$$

Where A and B are the CI functions within the active space, I are the basis functions outside the active space, and $E^{(0)}$ are the zero-order (unperturbed) energies. The functions A and B are single configurations (determinants) and are mixed after the diagonalization of H_{eff}, thus the QDPT is a single-configuration basis multi-state perturbation theory.

Another common form of multi-reference perturbation theory is the Rayleigh-Schrödinger perturbation theory (RSPT) in which the reference function has a multi-configurational character. If the CI and molecular orbital coefficients of the zero-order wave function are determined with CASSCF, and then the perturbation theory is applied on these wave functions, such approach is called multi-reference Moller-Plesset perturbation theory (MRMP). The effective Hamiltonian to the second-order within this approach is defined as,

$$H_{eff}^{(0-2)} = \left\langle \alpha \left| H^{(0)} \right| \alpha \right\rangle + \frac{1}{2} \sum_I \frac{\langle \alpha |V| I \rangle \langle I |V| \alpha \rangle}{E_\alpha^{(0)} - E_I^{(0)}}$$

(59)

Here α is the CASSCF wave functions, thus MRMP is a multi-configuration basis single-state perturbation theory.

Yet another multi-reference perturbation theory approach comes from combination of QDPT and MRMP. This approach is called quasidegenerate perturbation theory with MCSCF reference functions (MCQDPT) and $H_{eff}^{(0-2)}$ in this approach could be defined by the formula,

$$H_{eff}^{(2)} = \left\langle \alpha \left| H^{(0)} \right| \beta \right\rangle + \frac{1}{2} \sum_I \left(\frac{\langle \alpha |V| I \rangle \langle I |V| \beta \rangle}{E_\beta^{(0)} - E_I^{(0)}} + \frac{\langle \beta |V| I \rangle \langle I |V| \alpha \rangle}{E_\alpha^{(0)} - E_I^{(0)}} \right)$$

(60)

In eq 60, the reference functions α and β are multi-configurational. These reference functions are based on the state-averaged CASSCF, which makes MCQDPT a multi-configuration basis multi-state perturbation theory.

C. Coupled Cluster Methods

The coupled cluster methods are based on the description of ground-state wave function, ϕ, as the truncated many-body expansion, T, of Hartree-Fock determinant, ϕ_0,[25]

$$\phi = e^T \phi_0$$

(61)

If the truncated many-body expansions are restricted to singly and doubly excited determinants, such approach is called coupled clusters with singles and doubles (CCSD). The addition of triply excited determinants expands CCSD to a coupled clusters with singles, doubles and triples (CCSDT), which could be further expanded with quadruples,

pentuples and so on. The differences between CCSD, CCSDT and higher expansions could be represented as,

$$T=T_1+T_2 \Rightarrow CCSD$$

$$T=T_1+T_2+T_3 \Rightarrow CCSDT$$

$$T_N = T_1+T_2+T_3 +...+T_N \Rightarrow CCSDT...N \tag{62}$$

In eq 62, N represents the order of excitation. The T_N are obtained through the connected-clusters form of the electronic Schrödinger equation,

$$(H_N e^T)_C \left| \phi \right\rangle = \Delta E \left| \phi \right\rangle \qquad H_N = H - \left\langle \phi \left| H \right| \phi \right\rangle$$

$$\triangle E = E - \left\langle \phi \left| H \right| \phi \right\rangle \tag{63}$$

In eq 63 the ΔE is the correlation energy unaccounted by Hartree-Fock, H_N is the part of Hamiltonian that describes correlation energy, H is the total electronic Hamiltonian, and subscript C denotes the connected clusters part of the Schrödinger equation. In case of CCSD, the T_N are obtained by solving the following equations,

$$\left\langle \phi_i^a \left| (H_N e^{T_1+T_2})_C \right| \phi \right\rangle = 0$$
$$\left\langle \phi_{ij}^{ab} \left| (H_N e^{T_1+T_2})_C \right| \phi \right\rangle = 0 \tag{64}$$

Here ϕ_i^a and ϕ_{ij}^{ab} are singly- and doubly-occupied excited configurations. After solving eq 64 for T_N , one can calculate ΔE as,

$$\triangle E = \left\langle \phi \left| (H_N e^{T_1+T_2})_C \right| \phi \right\rangle \tag{65}$$

It is possible to reduce the computational cost of CCSDT by calculating the contribution from triple excitations using the perturbation theory, as in CCSD(T). [25,26]

III. Fragment Molecular Orbital Method

A. Basics of Fragment Molecular Orbital Method

Fragment molecular orbital (FMO) method is based on the replacement of the molecular orbitals (MO) of entire system with the MO of the system's fragments. Such replacement significantly reduces the computational cost and makes the fully quantum mechanical calculations feasible for a very large systems. The fragment MOs are calculated under the constraints that insure the MO localization within the individual fragment. To compensate for that localization the calculations of fragments' energies are performed in the Coulomb field produced by the electron density of all other fragments. After the fragment energies are calculated, the calculations for all fragment pairs are performed. These calculations recover the quantum mechanical interactions between the fragments and partially account for possible charge transfer between the fragments. However, the pair fragment calculations recover the charge transfer only to a limited extent, which makes the FMO method suitable for systems with electron transfer localized to the neighboring fragments and inapplicable to the systems with a high degree of electron delocalization.

The FMO calculation on propanol could be used as an example of the fragmentation scheme and the distribution of electrons between the fragments. The FMO calculation on propanol are not very meaningful from the practical point of view since the system is already relatively small, but it gives a clear example of the FMO fragmentation algorithm. The propanol molecule is divided into 4 fragments: one CH_3, two CH_2, and one OH fragments. The partition is done in such a way that both electrons from the covalent bond between two fragments are localized within one of the fragments. In case

of propanol, 8 electrons are assigned to the CH_3 fragment (6 electrons from three C-H bonds, and 2 electrons from the carbon's 1s orbital), 8 electrons are assigned to each of the CH_2 fragment (4 electrons from two C-H bonds, 2 electrons from C-C bond, and 2 electrons from the carbon's 1s orbital), and 10 electrons are assigned to the OH fragment (2 electrons from C-O bond, 2 electrons from O-H bond and 6 electrons from oxygen that are not involved in bonding).[27]

To obtain the energies of each fragment, the following fragment Hamiltonian, H_I, is used,

$$H_I = \sum_i^{n_I} \left\{ -\frac{1}{2}\nabla_i^2 - \sum_s^{all\_atoms} \frac{Z_s}{|r_i - R_s|} + \sum_{J \neq I}^{N} \int dr_2 \frac{p_J(r_2)}{|r_i - r_2|} \right\} + \sum_{i>j}^{n_I} \frac{1}{|r_i - r_j|} \tag{66}$$

Where n_I is the number of electrons in the fragment I, N is the number of fragments in the molecule, Z_s is the nuclear charge of atom s, and $p_J(r_2)$ is the electron density of the fragment J. The fragment Hamiltonian includes the electrostatic potential from the electrons in the surrounding $(N-1)$ fragments, as well as the electron-nuclear attractions from all nuclei in the molecule.

To make the FMO calculations more accurate, it is important to include a two-body fragment-fragment interaction. This is done using the fragment pair Hamiltonian,[27]

$$H_{IJ} = \sum_i^{n_I+n_J} \left\{ -\frac{1}{2}\nabla_i^2 - \sum_s^{all\_atoms} \frac{Z_s}{|r_i - R_s|} + \sum_{K \neq I,J}^{N} \int dr_2 \frac{p_K(r_2)}{|r_i - r_2|} \right\} + \sum_{i>j}^{n_I+n_J} \frac{1}{|r_i - r_j|} \tag{67}$$

Here K is the label for each pair of fragments. Similarly to H_I, the Hamiltonian H_{IJ} includes the electrostatic potential from electrons and nuclei in the surrounding $(N-2)$ fragments. It is important to note that the electron distribution, $p_K(r)$, is obtained from the single fragment calculations and is not varied in the pair calculations. Solving the

Schrödinger equation using the Hamiltonians from eqs 66 and 67, with the selected level of theory, one can obtain the fragment energies E_I, and the fragment pair energies E_{IJ}. Based on these energies, the total energy of the whole system can be evaluated. If only the energies of individual fragments are used, than this type of the FMO calculations is denoted as FMO1, while the FMO calculations with fragment pairs is called FMO2. The total FMO2 energy can be expressed by the following equation.[28]

$$E^{FMO2} = E^{FMO1} + \sum_{I>J}^{N}(E_{IJ} - E_I - E_J) \qquad (68)$$

In eq 68, the E^{FMO1} and E^{FMO2} are the FMO1 and FMO2 energies, respectively. The FMO accuracy can be improved by including the calculation on fragment triples (FMO3), but this method is computationally expensive, and the previous studies demonstrate that the accuracy of FMO2 is sufficient for most of the systems.

B. Scope and Applicability of FMO Method

The FMO method has been applied to many different complex systems. For example, using the FMO method, the structure of helical heparin oligosaccharides was predicted with RMSD of 0.586 Å compared to the experimental NMR structure. The FMO1-CIS(D) method was used to study the lowest n-p* state of hydrated formaldehyde. The solvatochromic shifts of uracyl and cytosine were characterized with FMO1-MCSCF and FMO1-CI. The FMO method was also successfully applied to study solid state systems and nanosystems. Examples include the study of the adsorption of small molecules on faujasite zeolites and solid phases of quinacridone.[29]

In biochemistry, the FMO method was applied to a variety of problems, from DNA and RNA binding to protein-ligand interaction and enzymatic reactions.[29,30] One of the reasons why the FMO method is proved to be useful in biochemical application is its ability to provide a pair density interaction analysis based on the fragment pairs calculations. The pair fragment analysis predicts not only the magnitude of the interaction between fragments, but also the contribution of the electrostatic and dispersion interactions to the total fragment interaction.[31] Since the proteins consist of the amino acids, which are the "building blocks" of the protein chains, the pair fragment interaction analysis can be used as a tool to identify the residues that play a key role in different biochemical processes.

When it comes to quantum mechanical (QM) description of the large molecular systems, the alternative to fully QM fragment based methods is the quantum mechanics / molecular mechanics (QM/MM) method. In QM/MM, only part of the system is described with QM, while the rest of the system is treated with a classical MM force field.[32] Despite the fact that QM/MM is less computationally demanding, the QM part of the system in these calculations is usually significantly smaller than the MM part, and treatment of the interactions between the QM and MM parts is a complicated task. In contrast, the FMO method simulates the entire system with a fully quantum mechanical approach and removes the problem of interaction between QM and MM regions, thus making the FMO method more universal than QM/MM.[31] Moreover, the fragment-based nature of the FMO allows utilization of thousands of computational cores. Thanks to effective parallelization, the fully QM FMO calculations were carried out on the systems containing tens of thousands atoms.[33] The universality and the computational efficiency

of FMO makes it an ideal method to study complex biological systems, such as the metal-sulfur proteins.[31]

IV. Nonadiabatic Spin-Forbidden Transitions Between Electronic States

A. Nature and Role of Nonadiabatic Reactions

The conventional understanding of chemical reaction mechanisms implies the change of the nuclear arrangement as the reaction proceeds from reactants to products through transition state with nuclei moving on a single electronic potential energy surface (PES). However, many chemical reactions are accompanied by transitions between PESs of different electronic states. Reactions undergoing through such transitions are called nonadiabatic, as oppose to the conventional (adiabatic) reactions in which the nuclei are assumed to be moving on a single PES. Nonadibatic transitions could happen with or without change of the electronic spin and are called intersystem crossings (ISC) or internal conversions (IC), respectively.[34] Therefore, the treatment of nonadiabatic reactions requires not only exploration of multiple PESs, but also prediction of the transition rates between these PESs. In statistical approach, the ISC transitions between PESs are assumed to happen at a minimum energy crossing point (MECP), which plays a similar role to a transition state in the adiabatic reactions (Figure 1).
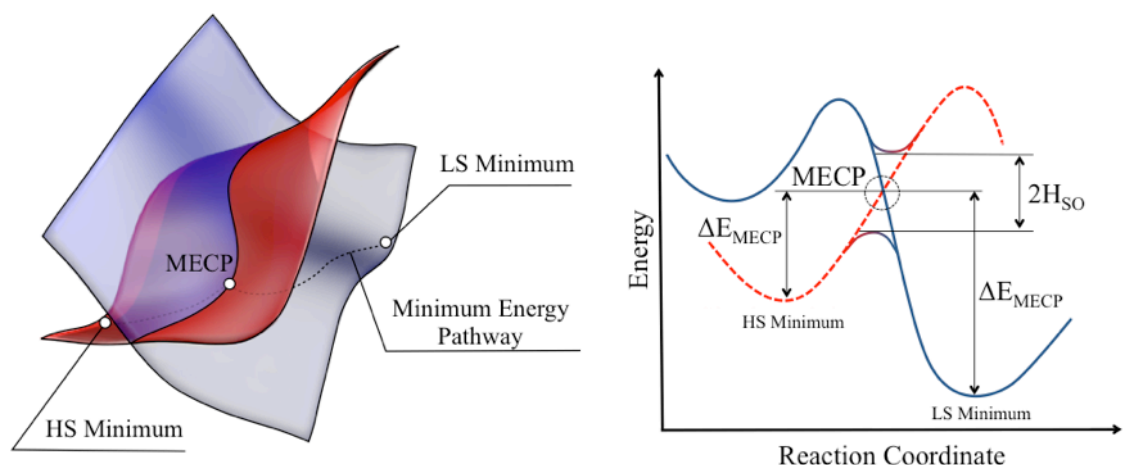
Figure 1. Representation of an intersystem crossing between the potential energy surfaces of low spin (LS) and high spin (HS) electronic states. The gap between two adiabatic surfaces is approximately twice the spin-orbit coupling H_{SO}, and ΔE_{MECP} is the barrier between the minima and MECP.

Examples of ISC include combustion,[35,36] reactions in the atmosphere and in interstellar space,[37,38] transition metal-based catalysis,[39] and binding of small molecules to the active sites of metalloproteins.[40–43] As for the IC, it plays a critical role in the visual perception,[44,45] and in protection of living organism from UV light.[34,46–50]

B. Nonadiabatic Transition State Theory

In order to investigate the influence of spin-forbidden reactions for a given system one needs to calculate the probability of transition between two spin states. One way of calculating the transition probability is the Landau-Zener (LZ) theory, where it is assumed that the transition between two spin states is possible only at MECP (Figure 1). The double passage Landau-Zener (LZ) transition probability is defined as,[51–53]

$$P_{trans} = (1 - P_{LZ})(1 + P_{LZ})$$

$$\text{(69)}$$

$$P_{LZ} = \frac{2\pi H_{SO}^2}{h\triangle F} \sqrt{\frac{\mu}{2(E - E_{MECP})}}$$

$$\text{(70)}$$

To calculate the transition probability (P_{LZ}), it is necessary to know spin-orbit coupling, H_{SO}, reduced mass along the reaction coordinate, μ, and the difference between the energy gradients of two spin states, ΔF, at MECP.

By knowing the energy of the MECP structure, relative to reactants, and the probability of transition between spin states, it is possible to calculate the rate constant $k(E)$ of spin-forbidden reaction,[54–60]

$$k(E) = \frac{N_{MECP}^*(E)}{h\rho_R(E)}$$

$$\text{(71)}$$

Here h is the Planck constant, $\rho_R(E)$ is the density of rovibrational states of the reactant, i.e. the density of rovibrational states at the minimum of initial electronic state, and $N_{MECP}^*(E)$ is the effective number of rovibrational states at the MECP that could be written as,

$$N_{MECP}^*(E) = \int_0^E \rho_{MECP}(E - \varepsilon_\perp)P_{trans}(\varepsilon_\perp)d\varepsilon_\perp$$

$$\text{(72)}$$

Here $\rho_{MECP}(E)$ is the density of rovibrational states at the MECP, E is the total internal energy of the system, and $\varepsilon_\perp$ is the component of internal energy along the reaction coordinate that is orthogonal to the crossing seam

The main disadvantage of the LZ formula is its inability to account for quantum tunneling through the barrier, which could be important for systems containing light

atoms. The LZ theory fails to predict non-zero probability of transition for internal energies of the system below the energy of MECP. To account for quantum tunneling through the MECP barrier the transition probability can be calculated using the weak coupling (WC) formula,[53,61]

$$p_{WC} = 4\pi^2 H_{SO}^2 \left(\frac{2\mu}{\hbar^2 F \triangle F} \right)^{2/3} Ai^2 \left[(E - E_{MECP}) \left(\frac{2\mu \triangle F^2}{\hbar^2 F^4} \right)^{1/3} \right] \quad (74)$$

Here *Ai* is the Airy function, and *F* is the geometric mean of the energy gradients. The quantum effects recovered by the WC formula are shown to be especially crucial for the reactions containing light atoms.[62]

References

(1)   Cohen, A. J.; Mori-Sanchez, P.; Yang, W. Challenges for Density Functional Theory. *Chem. Rev.* **2012**, *112*, 289–320.

(2)   Becke, A. D. Perspective : Fifty Years of Density-Functional Theory in Chemical Physics. *J. Chem. Phys.* **2014**, *140*, 18A301.

(3)   Wilk, L.; Nusair, M. Accurate Spin-Dependent Electron Liquid Correlation Energies for Local Spin Density Calculations: A Critical Analysis. *Can. J. Phys.* **1980**, *58*, 1200–1211.

(4)   Perdew, J. P. Climbing the Ladder of Density Functional Approximations. *MRS Bull.* **2013**, *38*, 743–750.

(5)   Perdew, J. P.; Burke, K.; Ernzerhof, M. Generalized Gradient Approximation Made Simple. *Phys. Rev. Lett.* **1996**, *77*, 3865–3868.

(6)   Tao, J.; Perdew, J.; Staroverov, V.; Scuseria, G. Climbing the Density Functional Ladder: Nonempirical Meta–Generalized Gradient Approximation Designed for Molecules and Solids. *Phys. Rev. Lett.* **2003**, *91*, 146401.

(7)   Perdew, J. P.; Kurth, S.; Blaha, P. Accurate Density Functional with Correct Formal Properties : A Step Beyond the Generalized Gradient Approximation. *Phys. Rev. Lett.* **1999**, *82*, 2544–2547.

(8)   Hertwig, R. H.; Koch, W. On the Parameterization of the Local Correlation

Functional. What Is Becke-3-LYP? *Chem. Phys. Lett.* **1997**, *268*, 345–351.

(9)　Becke, A. D. Density-Functional Thermochemistry. III. The Role of Exact Exchange. *J. Chem. Phys.* **1993**, *98*, 5648–5652.

(10)　Lee, C.; Hill, C.; Carolina, N. Development of the Colle-Salvetti Correlation-Energy Formula into a Functional of the Electron Density. *Phys. Rev. A* **1988**, *37*, 785–789.

(11)　Becke, A. D. Density-Functional Exchange-Energy Approximation with Correct Asymptotic Behavior. *Phys. Rev. A* **1988**, *38*, 3098–3100.

(12)　Iikura, H.; Tsuneda, T.; Yanai, T.; Hirao, K. A Long-Range Correction Scheme for Generalized-Gradient-Approximation Exchange Functionals. *J. Chem. Phys.* **2001**, *115*, 3540–3544.

(13)　You, Z.; Hung, Y.; Hsu, C. Calculating Electron-Transfer Coupling with Density Functional Theory : The Long-Range-Corrected Density Functionals. *J. Phys. Chem. B* **2015**, *119*, 7480−7490.

(14)　Grimme, S.; Antony, J.; Ehrlich, S.; Krieg, H. A Consistent and Accurate Ab Initio Parametrization of Density Functional Dispersion Correction (DFT-D) for the 94 Elements H-Pu. *J. Chem. Phys.* **2010**, *132*, 154104.

(15)　Peverati, R.; Baldridge, K. K. Implementation and Performance of DFT-D with Respect to Basis Set and Functional for Study of Dispersion Interactions in Nanoscale Aromatic Hydrocarbons. *J. Chem. Theory Comput.* **2008**, *4*, 2030–2048.

(16)　Hammes-Schiffer, S. A Conundrum for Density Functional Theory. *Science.* **2017**, *355*, 28–29.

(17)　Medvedev, M. G.; Bushmarinov, I. S.; Sun, J. Density Functional Theory Is Straying from the Path toward the Exact Functional. *Science.* **2017**, *355*, aah5975.

(18)　Delcey, M. G.; Pierloot, K.; Phung, Q. M.; Vancoillie, S.; Lindh, R.; Ryde, U. Accurate Calculations of Geometries and Singlet-Triplet Energy Differences for Active-Site Models of [NiFe] Hydrogenase. *Phys. Chem. Chem. Phys.* **2014**, *16*, 7927–7938.

(19)　Radoń, M. Spin-State Energetics of Heme-Related Models from DFT and Coupled Cluster Calculations. *J. Chem. Theory Comput.* **2014**, *10*, 2306–2321.

(20)　Szalay, G. P.; Muller, T.; Gidofalvi, G.; Lischka, H.; Shepard, R. Multiconfiguration Self-Consistent Field and Multireference Configuration

Interaction Methods and Applications. *Chem. Sci.* **2012**, *112*, 108–181.

(21) Cheung, L. M. The Multiconfiguration Self-Consistent Field Method for Many-Electron Systems and Its Application to the Dissociation of Ethylene. *Retrosp. Theses Diss.* **1975**, Paper 5464.

(22) Schmidt, M. W.; Gordon, M. S. The Construction and Interpretation of MCSCF Wavefunctions. *Annu. Rev. Phys. Chem.* **1998**, *49*, 233–266.

(23) Møller, C.; Plesset, M. S. Note on an Approximation Treatment for Many-Electron Systems. *Phys. Rev.* **1934**, *46*, 618–622.

(24) Nakano, H.; Otsuka, N.; Hirao, K. Analytic Energy Gradients for Second-Order Multireference Perturbation Theory. In *Recent Advances in Computational Chemistry*; 1999; Vol. 4, pp. 1–26.

(25) Piecuch, P.; Kucharski, S. A.; Kowalski, K.; Musiał, M. Efficient Computer Implementation of the Renormalized Coupled-Cluster Methods : The R-CCSD [T], R-CCSD (T), CR-CCSD [T], and CR-CCSD (T) Approaches. *Comput. Phys. Commun.* **2002**, *149*, 71–96.

(26) Knowles, P. J.; Hampel, C.; Werner, H.-J. Coupled Cluster Theory for High Spin, Open Shell Reference Wave Functions. *J. Chem. Phys.* **1993**, *99*, 5219.

(27) Kitaura, K.; Ikeo, E.; Asada, T.; Nakano, T.; Uebayasi, M. Fragment Molecular Orbital Method: An Approximate Computational Method for Large Molecules. *Chem. Phys. Lett.* **1999**, *313*, 701–706.

(28) Gordon, M. S.; Fedorov, D. G.; Pruitt, S. R.; Slipchenko, L. V. Fragmentation Methods: A Route to Accurate Calculations on Large Systems. *Chem. Rev.* **2012**, *112*, 632–672.

(29) Fedorov, D. G.; Nagata, T.; Kitaura, K. Exploring Chemistry with the Fragment Molecular Orbital Method. *Phys. Chem. Chem. Phys.* **2012**, *14*, 7562.

(30) Tanaka, S.; Mochizuki, Y.; Komeiji, Y.; Okiyama, Y.; Fukuzawa, K. Electron-Correlated Fragment-Molecular-Orbital Calculations for Biomolecular and Nano Systems. *Phys. Chem. Chem. Phys.* **2014**, *16*, 10310–10344.

(31) Fedorov, D. G.; Kitaura, K. Subsystem Analysis for the Fragment Molecular Orbital Method and Its Application to Protein-Ligand Binding in Solution. *J. Phys. Chem. A* **2016**, *120*, 2218–2231.

(32) Duarte, F.; Amrein, B. A.; Blaha-Nelson, D.; Kamerlin, S. C. L. Recent Advances in QM/MM Free Energy Calculations Using Reference Potentials. *Biochim.*

Biophys. Acta **2015**, *1850*, 954–965.

(33) Alexeev, Y.; Mahajan, A.; Leyffer, S.; Fletcher, G.; Fedorov, D. G. Heuristic Static Load-Balancing Algorithm Applied to the Fragment Molecular Orbital Method. In *International Conference for High Performance Computing, Networking, Storage and Analysis, SC*; Salt Lake City, Utah, USA, 2012.

(34) Mai, S.; Marquetand, P.; González, L. A General Method to Describe Intersystem Crossing Dynamics in Trajectory Surface Hopping. *Int. J. Quantum Chem.* **2015**, *115*, 1215–1231.

(35) Jasper, A. W.; Dawes, R. Non-Born-Oppenheimer Molecular Dynamics of the Spin-Forbidden Reaction $O(^3P) + CO(X^1\sum^+) \rightarrow CO_2(X^1\sum g^+)$. *J. Chem. Phys.* **2013**, *139*.

(36) Balucani, N.; Leonori, F.; Casavecchia, P.; Fu, B.; Bowman, J. M. Crossed Molecular Beams and Quasiclassical Trajectory Surface Hopping Studies of the Multichannel Nonadiabatic $O(^3P)$ + Ethylene Reaction at High Collision Energy. *J. Phys. Chem. A* **2015**, *119*, 12498−12511.

(37) Maeda, S.; Taketsugu, T.; Ohno, K.; Morokuma, K. From Roaming Atoms to Hopping Surfaces: Mapping Out Global Reaction Routes in Photochemistry. *J. Am. Chem. Soc.* **2015**, *137*, 3433–3445.

(38) Ahmadvand, S.; Zaari, R. R.; Varganov, S. A. Spin-Forbidden and Spin-Allowed Cyclopropenone (c-H_2C_3O) Formation in Interstellar Medium. *Astrophys. J.* **2014**, *795*, 1–5.

(39) Goodrow, A.; Bell, A. T.; Head-Gordon, M. Are Spin-Forbidden Crossings a Bottleneck in Methanol Oxidation? *J. Phys. Chem. C* **2009**, *113*, 19361–19364.

(40) Strickland, N.; Harvey, J. N. Spin-Forbidden Ligand Binding to the Ferrous-Heme Group: Ab Initio and DFT Studies. *J. Phys. Chem. B* **2007**, *111*, 841–852.

(41) Alcantara, R. E.; Xu, C.; Spiro, T. G.; Guallar, V. A Quantum-Chemical Picture of Hemoglobin Affinity. *Proc. Natl. Acad. Sci.* **2007**, *104*, 18451–18455.

(42) Yson, R. L.; Gilgor, J. L.; Guberman, B. A.; Varganov, S. A. Protein Induced Singlet–triplet Quasidegeneracy in the Active Site of [NiFe]-Hydrogenase. *Chem. Phys. Lett.* **2013**, *577*, 138–141.

(43) Kaliakin, D. S.; Zaari, R. R.; Varganov, S. A. Effect of H_2 Binding on the Nonadiabatic Transition Probability between Singlet and Triplet States of the [NiFe]-Hydrogenase Active Site. *J. Phys. Chem. A* **2015**, *119*, 1066–1073.

(44) Santoro, F.; Ferre, N.; Olivucci, M.; Frutos, L. M.; Andrunio, T. Tracking the Excited-State Time Evolution of the Visual Pigment with Multiconfigurational Quantum Chemistry. *Proc. Natl. Acad. Sci.* **2007**, *104*, 7764–7769.

(45) Schoenlein, R. W.; Peteanu, L. A.; Mathies, R. .; Shank, C. V. The First Step in Vision: Femtosecond Isomerization of Rhodopsin. *Science.* **1991**, *254*, 5030.

(46) Crespo-Hernandez, C. E.; Cohen, B.; Hare, P. M.; Kohler, B. Ultrafast Excited-State Dynamics in Nucleic Acids. *Chem. Rev.* **2004**, *104*, 1977–2019.

(47) Weinkauf, R.; Schermann, J.; Vries, M. S. De; Kleinermanns, K. Molecular Physics of Building Blocks of Life under Isolated or Defined Conditions. *Eur. Phys. J. D* **2002**, *20*, 309–316.

(48) Stephansen, A. B.; Brogaard, R. Y.; Kuhlman, T. S.; Klein, L. B.; Christensen, J. B.; Sølling, T. I. Surprising Intrinsic Photostability of the Disulfide Bridge Common in Proteins. *J. Am. Chem. Soc.* **2012**, *134*, 20279–20281.

(49) Vries, M. S. De; Hobza, P. Gas-Phase Spectroscopy of Biomolecular Building Blocks. *Annu. Rev. Phys. Chem.* **2007**, *58*, 585–612.

(50) Pe, M.; Lucas, B.; Barat, M.; Fayeton, J. A. Mechanisms of UV Photodissociation of Small Protonated Peptides. *J. Phys. Chem. A* **2010**, *114*, 3147–3156.

(51) Zener, C. Non-Adiabatic Crossing. *Proceeding R. Soc. London. Ser. A* **1932**, *137*, 696–702.

(52) Wittig, C. The Landau - Zener Formula. *J. Phys. Chem. B* **2005**, *109*, 8428–8430.

(53) Harvey, J. N. Understanding the Kinetics of Spin-Forbidden Chemical Reactions. *Phys. Chem. Chem. Phys.* **2007**, *9*, 331–343.

(54) Harvey, J. N. Spin-Forbidden Reactions: Computational Insight into Mechanisms and Kinetics. *Wiley Interdiscip. Rev. Comput. Mol. Sci.* **2014**, *4*, 1–14.

(55) Harvey, J. N.; Aschi, M. Spin-Forbidden Dehydrogenation of Methoxy Cation: A Statistical View. *Phys. Chem. Chem. Phys.* **1999**, *1*, 5555–5563.

(56) Heller, E. J.; Brown, R. C. Radiationless Transitions in a New Light. *J. Chem. Phys.* **1983**, *79*, 3336.

(57) Lorquet, J. C.; Leyh-Nihant, B. Nonadiabatic Unimolecular Reactions. 1. A Statistical Formulation for the Rate Constants. *J. Phys. Chem.* **1988**, *92*, 4778–4783.

(58) Tully, J. C. Collision Complex Model for Spin Forbidden Reactions: Quenching of O(^{1}D) by N$_2$. *J. Chem. Phys.* **1974**, *61*, 61.

(59) Zahr, G. E.; Preston, R. K.; W.H., M. Theoretical Treatment of Quenching in O(^{1}D) + N$_2$ Collisions. *J. Chem. Phys.* **1975**, *62*, 1127–1135.

(60) Cui, Q.; Morokuma, K.; Bowman, J. M.; Klippenstein, S. J. The Spin-Forbidden Reaction CH($^2\Pi$)+N$_2$→HCN+N(^{4}S) Revisited. II. Nonadiabatic Transition State Theory and Application. *J. Chem. Phys.* **1999**, *110*, 9469.

(61) Delos, J. B. On the Reactions of N$_2$ with O. *J. Chem. Phys.* **1973**, *59*, 2365.

(62) Jasper, A. W. Multidimensional Effects in Nonadiabatic Statistical Theories of Spin-Forbidden Kinetics: A Case Study of ^{3}O + CO → CO$_2$. *J. Phys. Chem. A* **2015**, *119*, 7339−7351.

Chapter III. Effect of H$_2$ Binding on the Nonadiabatic Transition Probability Between Singlet and Triplet States of the [NiFe]-Hydrogenase Active Site

Danil S. Kaliakin, Ryan R. Zaari, Sergey A. Varganov

Abstract

We investigate the effect of H$_2$ binding on the spin-forbidden nonadiabatic transition probability between the lowest energy singlet and triplet electronic states of [NiFe]-hydrogenase active site model, using a velocity averaged Landau-Zener theory. Density functional and multireference perturbation theories were used to provide parameters for the Landau-Zener calculations. It was found that variation of the torsion angle between the terminal thiolate ligands around the Ni center induces an intersystem crossing between the lowest energy singlet and triplet electronic states in the bare active site and in the active site with bound H$_2$. Potential energy curves between the singlet and triplet minima along the torsion angle and H$_2$ binding energies to the two spin states were calculated. Upon H$_2$ binding to the active site, there is a decrease in the torsion angle at the minimum energy crossing point between the singlet and triplet states. The probability of nonadiabatic transitions at temperatures between 270 and 370 K ranges from 35% to 32% for the active site with bound H$_2$ and from 42% to 38% for the bare active site, thus indicating the importance of spin-forbidden nonadiabatic pathways for H$_2$ binding on the [NiFe]-hydrogenase active site.

I. Introduction

Hydrogenases are enzymes that catalyze both the proton reduction and oxidation of molecular hydrogen: $2H^+ + 2e^- \rightleftharpoons H_2$, reactions relevant to clean energy storage and utilization.[1–5] In nature the different classes of hydrogenases [NiFe]-hydrogenase,[6] [FeFe]-hydrogenase[7] and [Fe]-hydrogenase[8] are found in a variety of bacterial and archaeal organisms. [NiFe]-hydrogenase is arguably the most promising for future applications in catalyzing hydrogen production and oxidation in the presence of oxygen.[9,10] Many *structural* models that resemble the [NiFe]-hydrogenase active sites and *functional bioinspired* models that mimic the [NiFe]-hydrogenase reactivity have been synthesized in the past decade.[11–16] However, the reaction mechanism of proton reduction and hydrogen oxidation on functional models and its relevance to the true catalytic activity of [NiFe]-hydrogenase metalloenzyme are not completely understood.[17,18] Further insight into the H_2 binding on the active site is needed to understand the catalytic properties of [NiFe]-hydrogenase and aid into the creation of a functioning synthetic counterpart.

Different catalytic states of [NiFe]-hydrogenase were investigated using pure quantum mechanics and hybrid quantum mechanics/molecular mechanics (QM/MM) methods.[19–22] Several studies were dedicated to H_2 binding on various models of the [NiFe]-hydrogenase active site, including isolated cluster models using density functional theory (DFT),[23–26] and large partial protein chain models using a full DFT approach[27,28] and QM/MM technique.[29] These studies demonstrate that the binding position and energy of H_2 is highly dependent on the active site model and spin states of the metal centers. Thus, it is important to consider both the position of H_2 binding and the possibility of H_2

binding to different spin states of the active site.

Our recent computational study of the EPR-silent Ni-SI model[30] of hydrogenase suggests that the spin multiplicity of the ground electronic state strongly depends on the active site geometry.[31] Rotation of the terminal thiolate ligands changes the Ni(II) coordination from planar to tetrahedral and results in an intersection of the lowest energy singlet and triplet electronic states. The triplet state of the active site has two unpaired electrons localized on the Ni(II) center, with the Fe(II) center in its low-spin singlet state. The unoccupied d-orbitals of the singlet state Fe(II) can accept electrons from the σ-orbital of H_2 thus making Fe(II) a possible binding site for H_2.[32] The strong-field CN^- and CO ligands are bound to the Fe(II) center keeping it in the low-spin singlet state regardless of the Ni center coordination.

This study extends our previous work on the quasidegeneracy of electronic states with different spin multiplicities in the bare active site of [NiFe]-hydrogenase.[31] Here we investigate the different H_2 binding positions on the singlet and triplet states of the EPR-silent Ni-SI model of the active site. We also study the probability of spin-forbidden transitions between the singlet and triplet states of the bare active site and the active site with bound H_2 using Landau-Zener theory.[33–36] The computational details and Landau-Zener theory are described in Section II. Subsection A describes the singlet-triplet conformers and H_2 binding energies; subsection B presents the minimum energy crossing point (MECP) results; and subsection C discusses the nonadiabatic transition probability between singlet and triplet states. All results are summarized in section IV.

II. Computational Details

The electronic structure calculations were done with unrestricted DFT using PBE,[37] BP86,[38,39] TPSS[40] and B3LYP[41–43] functionals combined with bs1[44] and def2-TZVP[45] basis sets. The bs1 basis set consists of a Stuttgart basis set in combination with ECP10MDF effective core potential for Ni and Fe,[46] and the 6-31G** basis set for all other atoms,[47,48] whereas the larger def2-TZVP basis set provides a full electron description of Fe and Ni. It was previously shown that the PBE/bs1 level of theory is in semiquantitative agreement with CCSD(T)[49] calculations on small complexes with a single Ni center.[44] A recent study also demonstrated that singlet-triplet energy differences in the bare [NiFe]-hydrogenase active site calculated with PBE, BP86 and TPSS functionals are in close agreement with the CCSD(T) results.[50]

A model of the [NiFe]-hydrogenase active site was constructed by replacing the cysteine (Cys) ligands with SCH_3 groups (Figure 1a). The total electronic charge of the model was set to -2 to simulate the formal oxidation states of Ni(II) and Fe(II), corresponding to the EPR-silent Ni-SI form of the active site. A total of five initial H_2 binding positions were sampled by placing molecular hydrogen in the proximity of the Fe or Ni atoms, or in the three bridging positions between two metal atoms (Figure S1, Supporting Information). Initial geometries were optimized using the PBE, BP86, TPSS and B3LYP functionals with the bs1 basis set. Single point energy calculations were carried out using the def2-TZVP basis set on the optimized structures of the active site with bound H_2. The binding energies were corrected with zero-point vibrational energy (ZPE) obtained from bs1 Hessian calculations. All calculations of binding energies were performed using the following formula:

$$E_{bind} = E_{act+H_2} - E_{act} - E_{H_2}, \tag{1}$$

where E_{act+H_2} is the energy of active site with bound H_2, E_{act} is the energy of the bare active site, and E_{H_2} is the energy of H_2. The effect of dispersion interactions on the H_2 binding energy was investigated through calculations utilizing the DFT-D3 Grimme scheme[51,52] with def2-TZVP basis set. The effect of entropy on the binding energy was estimated using ideal gas, rigid rotor, and harmonic normal mode approximations at standard ambient temperature and pressure (T=298 K, P=1.01×10^5 Pa).
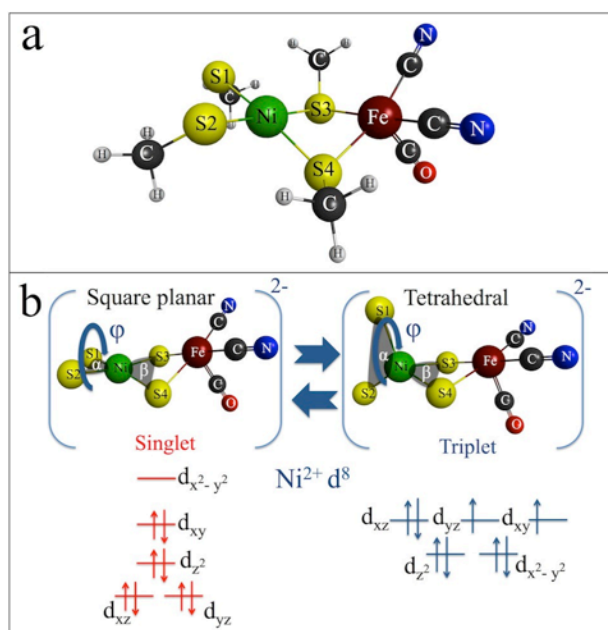
Figure 1. (a) Small model of [NiFe]-hydrogenase active site. (b) Crystal field diagrams for square planar and tetrahedral geometries of Ni(II). Also shown is the torsion angle φ between planes α and β. Square planar and tetrahedral geometries correspond to φ equal to 0° and 90°, respectively. Methyl groups of the model are not shown for clarity.

The torsion angle φ in Figure 1b is defined as an angle between planes α (S1-Ni-S2) and β (S3-Ni-S4). Because of the difficulty in constraining the torsion angle directly during geometry optimizations, the S2-Ni-S3 and S1-Ni-S4 bond angles were

frozen instead. A similar approach for freezing the torsion angle was previously used in the study of $Ni[(SPR_2)_2N]_2$ complexes (R = Ph, Pr).[53] The torsion angle was used as the reaction coordinate to study the triplet and singlet state energies as a function of the active site geometry. The crystal field diagram in Figure 1b, shows that a change of Ni coordination from square planar to tetrahedral leads to a change in the splitting of d-orbitals. Because of this splitting, the singlet electronic configuration is more favorable for square planar geometry, while the tetrahedral geometry favors the triplet state.

Eight intermediate active site geometries were generated by linear interpolation of the internal coordinates between the lowest energy singlet and triplet minima. To generate a potential energy curve along the torsion angle, constrained optimization of the intermediate geometries was carried out. The MECP was located using the four density functionals in combination with the bs1 basis set, and also using the PBE/def2-TZVP level of theory. The GAMESS suite of programs was used for all electronic structure calculations.[54,55]

The velocity averaged Landau-Zener (LZ) transition probability, $\langle P_{LZ} \rangle$, between the singlet and triplet spin states at the MECP was calculated in mass-weighted coordinates and atomic units as,[34,36]

$$\langle P_{LZ} \rangle = \int_0^\infty P_{LZ}(\upsilon)p(\upsilon)d\upsilon \bigg/ \int_0^\infty p(\upsilon)d\upsilon. \tag{2}$$

The LZ probability for the mass-weighted component of the nuclear velocity perpendicular to the intersection seam is defined as

$$P_{LZ}(\upsilon) = 1 - \exp\left(\frac{-2\pi H_{SO}^2}{\upsilon|\Delta g|}\right), \tag{3}$$

with the Maxwell-Boltzmann weighted velocity distribution

$$p(\upsilon) = \exp\left(\frac{-\upsilon^2}{2k_B T}\right).$$

(4)

Substitution of eqs 3 and 4 into 2 yields the final expression for the velocity averaged LZ transition probability,

$$\langle P_{LZ}\rangle = 1 - \left(\frac{2}{\pi k_B T}\right)^{1/2} \int_0^\infty \exp\left(\frac{-2\pi H_{SO}^2}{\upsilon|\Delta g|} - \frac{\upsilon^2}{2k_B T}\right) d\upsilon,$$

(5)

where H_{SO} is the spin-orbit coupling between two spin states, $|\Delta g|$ is the difference in the mass-weighted energy gradients of the potential energy surfaces at the MECP between the two spin states, k_B is the Boltzmann constant, T is the temperature and υ is the mass weighted velocity. The details of obtaining $|\Delta g|$ from MECP calculations are described in the Supporting Information. Spin-orbit coupling (SOC) at the MECP was calculated using the Breit-Pauli approximation[56] by multiconfigurational quasidegenerate second-order perturbation theory (MCQDPT2).[57,58] The zero-order wave function for MCQDPT2 calculations was of the CASSCF(2,2)[59,60] type with two electrons on the HOMO and LUMO orbitals in the singlet state, and with two electrons on the SOMO orbitals in the triplet state (Figure S2, Supporting Information).

III. Results and Discussion

A. H_2 Binding to the [NiFe]-Hydrogenase Active Site

Of the five total conformations sampled, after geometry optimization, only two lowest energy singlet (S1, S2) and two lowest energy triplet (T1, T2) conformers were obtained with bound H_2 (Figure 2a). The lowest energy singlet (S) and triplet (T)

geometries of the bare active site are shown in Figure 2b. All density functionals used in this study produce similar optimized geometries. In all cases of H_2 adsorption on the unconstrained active site, only binding to the Fe center is observed, and the structures with H_2 bound to Ni were not found. The main differences between the conformers of a given spin state can be attributed to the relative positions of the methyl groups. The Ni coordination is found to be pseudo square planar for singlet conformers (S, S1, S2) and pseudo tetrahedral for triplet conformers (T, T1, T2).
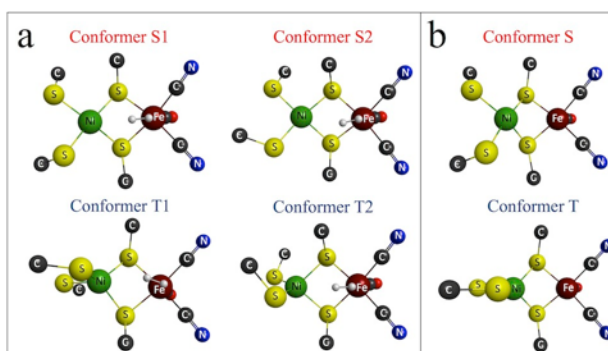
Figure 2. (a) Lowest energy singlet (S1, S2) and triplet (T1, T2) state conformers of the active site with bound H_2. (b) Lowest energy singlet (S) and triplet (T) state conformers of bare active site. The hydrogen atoms of methyl groups are not shown for clarity.

Table 1 summarizes the relative energies of the singlet and triplet conformers obtained with different levels of theory. For bare active site conformers, the energy of the singlet state (S) is lower than the energy of the triplet state (T) according to PBE, BP86, and TPSS calculations, whereas B3LYP predicts the triplet state to be lower in energy. The ordering of the states predicted by B3LYP for the bare active site is inconsistent with recently reported CCSD(T) results.[50] The bare active site relative energy between singlet and triplet states obtained using PBE and BP86 functionals with def2-TZVP basis set are 12.5 and 12.9 kcal/mol, respectively. These values are in reasonable agreement with the

CCSD(T) relative energy of 13.6 kcal/mol that is obtained using a smaller active site model with SCH_3 ligands replaced by SH groups. It was estimated that the SCH_3 ligands stabilize the singlet state by an additional 4.8 kcal/mol.[50]

Table 1. Relative Energies (kcal/mol) of the Singlet (S) and Triplet (T) Conformers of Bare Active Site and Active Site Conformers with Bound H_2 (S1, S2, T1, T2) Obtained with Different Levels of Theory.

	PBE		BP86		TPSS		B3LYP	
	bs1	def2-TZVP	bs1	def2-TZVP	bs1	def2-TZVP	bs1	def2-TZVP
Bare active site								
S	0.0	0.0	0.0	0.0	0.0	0.0	0.0	0.0
T	7.5	12.5	7.2	12.9	4.5	10.6	-5.6	-0.4
Active site with bound H_2								
S2	0.0	0.0	0.0	0.0	0.0	0.0	0.0	0.0
S1	1.4	2.2	1.3	2.1	1.5	2.3	1.3	1.4
T2	2.6	8.9	2.6	8.9	-0.3	6.6	-9.5	-2.6
T1	5.0	11.7	4.9	11.2	2.1	9.1	-7.0	-0.3

[a]For the bare active site, the energies are relative to the singlet conformer (S). For the active site with bound H_2, the energies are relative to the singlet conformer (S2). The geometries were optimized with bs1 basis set.

Regarding the active site with bound H_2, the PBE, BP86, and TPSS functionals with def2-TZVP basis set predict the same energy ordering of the conformers ($E_{S2} < E_{S1} < E_{T2} < E_{T1}$), with the singlet states being lower in energy than the triplet states. As in the case of the bare active site, B3LYP predicts the triplet conformers to have lower energies than the singlet conformers ($E_{T2} < E_{T1} < E_{S2} < E_{S1}$). H_2 binding leads to a decrease in the relative energy between the lowest energy singlet (S2) and triplet (T2) states by $2.2 - 4.0$ kcal/mol according to the calculations with def2-TZVP basis set. Table 1 shows that the use of a larger def2-TZVP basis set is necessary to obtain accurate relative energies for the singlet and triplet states. In contrast, the basis set effect on optimized geometries is negligible as evident from the relative energy of the T2 state calculated with PBE/def2-TZVP for the bs1 optimized geometry (8.9 kcal/mol) and for geometry optimized with the larger def2-TZVP basis set (8.8 kcal/mol).

The H_2 binding energies, with and without ZPE correction, calculated with def2-TZVP basis set using bs1 optimized geometries are shown in Table 2. Calculations using the bs1 basis set predict similar values for the binding energies (Table S1, Supporting Information). Negative binding energies, defined by eq 1, correspond to energetically favorable stable bound states, while positive binding energies indicate metastable states. The H_2 binding energies for the singlet (S1, S2) and triplet (T1, T2) conformers were calculated with respect to the energies of the singlet (S) and triplet (T) conformers of the bare active site, respectively. As can be seen from Table 2, the ZPE correction reduces the binding strength of H_2 by as much as 5.5 kcal/mol (TPSS T2 conformer) due to a gain in the vibrational degrees of freedom. The ZPE corrected H_2 binding energy for the T2 conformer varies between -2.4 kcal/mol (PBE and TPSS) and -1.1 kcal/mol (BP86). These values are in reasonable agreement with other studies using the active site model with B3LYP (-2.7 kcal/mol),[24] and the active site model constrained to the X-ray structure with B3LYP and TPSS (-2.7 and -3.6 kcal/mol).[25] To estimate the basis set effect we calculated the H_2 binding energy for S2 and T2 conformers using the PBE functional with large def2-QZVPP basis set. These calculations yield ZPE-corrected binding energies of 0.3 and -2.1 kcal/mol for S2 and T2 conformers, respectively. These energies are different by only 0.4 and 0.3 kcal/mol from the values calculated with def2-TZVP basis set. Thus the basis set errors in the def2-TZVP calculations are expected to be smaller than 1 kcal/mol.

Table 2. Binding Energies of H_2 (kcal/mol), with and without ZPE Correction, for the Singlet (S1, S2) and Triplet (T1, T2) Active Site Conformers Calculated with def2-TZVP Basis Set Using Equation 1.

	PBE	BP86	TPSS	B3LYP
S2	-3.9	-1.9	-3.9	-4.0
S1	-1.7	0.2	-1.6	-2.6
T2	-7.5	-5.9	-7.9	-6.3
T1	-4.6	-3.6	-5.4	-3.9
ZPE Corrected Calculations				
S2	0.7	2.4	0.7	0.9
S1	2.3	5.0	2.6	1.7
T2	-2.4	-1.1	-2.4	-2.2
T1	-0.4	1.6	-0.8	-0.1

We also investigated the effects of dispersion interactions and the loss of translational and rotational entropy on the H_2 binding energies (Table S2, Supporting Information). The addition of the Grimme's dispersion correction lowers the binding energies (predicts binding to be more energetically favorable) by as much as 6.7 kcal/mol. In contrast, the loss of entropy increases the binding energies by as much as 11.1 kcal/mol. Binding energies for the T2 conformer calculated with ZPE, dispersion and entropy corrections are positive (from 2.1 to 4.7 kcal/mol depending on the functional) indicating a metastable binding of H_2 to the active site. It is important to point out that including dispersion and entropy corrections does not change the prediction that T2 and S2 conformers are the most stable among the triplet and singlet conformers, respectively.

The bonding between H_2 and Fe was analyzed for the T2 conformer using Foster-Boys localized molecular orbitals. The nonclassical three-center, two-electron bonding between H_2 and the Fe center involves two types of partial electron transfers.[32] Electron donation occurs from the σ-orbital of H_2 to the $3d_{z^2}$ and 4s orbitals of Fe (Figure 3a).

Electron back-donation from the $3d_{xz}$ and $3d_{yz}$ orbitals of Fe to the σ*-orbital of H_2 is also observed (Figure 3b).
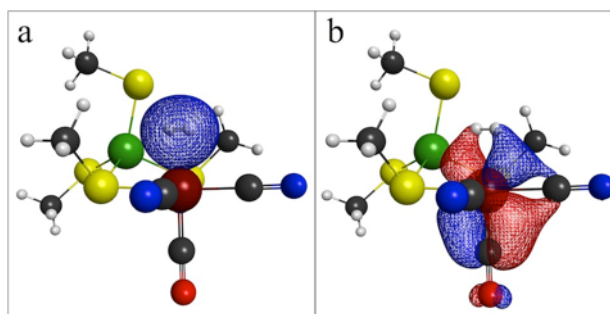
Figure 3. Foster-Boys localized molecular orbitals involved in the H_2 binding to the Fe(II) center of the active site; (a) electron donation from σ-orbital of H_2 to $3d_{z^2}$ and 4s orbitals of Fe(II); (b) back-donation from $3d_{xz}$ and $3d_{yz}$ orbitals of Fe(II) to σ*-orbital of H_2.

B. Singlet-Triplet States Crossing

To investigate the intersystem crossing between the singlet and triplet states of the lowest energy conformers S2 and T2, we calculated the potential energy curves between S2 and T2 minima and located the singlet-triplet MECP. The relative energies and torsion angles for the singlet minimum, triplet minimum, and MECP are shown in Table 3, for the bare active site and for the active site with bound H_2. All four functionals produce similar values of the torsion angle for the singlet and triplet minima. The torsion angle for the bare active site ranges from 14.5° to 20.2° for the singlet minimum and from 90.8° to 93.9° for the triplet minimum. For the active site with bound H_2, the torsion angle ranges from 16.4° to 19.2° and from 76.4° to 78.1° for the singlet (S2) and triplet (T2) states, respectively. The geometry of the triplet (T2) state becomes less tetrahedral upon H_2 binding, resulting in a 15° reduction of the torsion angle. With respect to the MECP(S/T) for the bare active site, the calculated PBE, BP86, and TPSS torsion angles (58.7° −

64.1°) are in good agreement with our earlier estimated range (59.2° − 65.6°) based on CCSD(T) calculations.[31] The binding of H_2 to the active site decreases the MECP(S2/T2) torsion angle to between 48.7° and 54.0°, as calculated with the three functionals above. The B3LYP functional underestimates the MECP torsion angle, predicting more square planar geometries. Using the larger def2-TZVP basis set with the PBE functional results in an MECP(S2/T2) torsion angle of 56.9°, only 2.9° larger than calculated with PBE/bs1.

Table 3. Relative Energies (kcal/mol) and Torsion Angles (Degrees) for the Singlet Minima, Triplet Minima and MECP for the Bare Active Site (S, T, MECP (S/T)) and for the Active Site with Bound H_2 (S2, T2, MECP (S2/T2)) Obtained with the bs1 Basis Set.[a]

	PBE	*BP86*	*TPSS*	*B3LYP*
Conformer S				
E_S	0.0	0.0	0.0	0.0
E_T	21.6	22.6	20.8	6.8
φ	16.5	14.5	18.5	20.2
Conformer T				
E_S	14.0	14.2	13.9	7.7
E_T	7.5	7.2	4.5	-5.8
φ	91.2	90.8	90.8	93.9
MECP (S/T)				
$E_{S=T}$	9.9[b]	9.8	8.2[b]	0.8[b]
φ	63.6[b]	64.1	58.7[b]	33.8[b]
Conformer S2				
E_S	0.0	0.0	0.0	0.0
E_T	16.2	16.1	11.8	1.8
φ	19.2	19.2	16.4	17.5
Conformer T2				
E_S	9.9	9.8	9.0	19.3
E_T	2.6	2.6	-0.3	-9.5
φ	76.4	76.9	76.7	78.1
MECP (S2/T2)				
$E_{S=T}$	5.4	5.3	4.1	1.6
φ	54.0	53.9	48.7	28.9

[a]For the bare active site, the energies are relative to the singlet conformer (S). For the active site with bound H_2, the energies are relative to the singlet conformer (S2). The energies of singlet and triplet states are labeled as E_S and E_T, respectively. [b]Values from the previous study (ref. 31).

The potential energies of the singlet and triplet states with varying torsion angle, calculated for the active site with bound H_2, are shown in Figure 4a (PBE), b (BP86), c (TPSS) and d (B3LYP). The strong dependence of the relative energies of the singlet and

triplet states on the torsion angle between the thiolate ligands is clearly shown. There is an intersection between the potential energy curves of the two spin states, as predicted by all four functionals. The intersection geometries and energies in Figure 4 are similar to those found using the MECP search algorithm and reported in Table 3. The value of the torsion angle at the intersection (and at the MECP(S2/T2)) predicted by B3LYP differ significantly from the other functionals. In the next section we focus on the probability of nonadiabatic spin-forbidden transitions between the singlet and triplet states of the active site at the MECP geometry.

Figure 4. Energies of the singlet and triplet states of the active site as a function of torsion angle φ calculated with bs1 basis set and four different functionals: (a) PBE, (b) BP86, (c) TPSS and (d) B3LYP. The methyl groups and Fe ligands are not shown for clarity. The values of torsion angle are not equally spaced because of small uncontrollable rotations of the thiolate ligands during constrained geometry optimization.

C. Probability of Transition Between Spin States

In order to calculate the Landau-Zener probability of transition between the singlet and triplet states (eq 5), the SOC was obtained with the MCQDPT2 method using 6-31G** and def2-TZVP basis sets. The all-electron 6-31G** basis set was used to calculate the SOC for active site geometries optimized with the bs1 basis set to account for core electron contributions. The MECP geometries found with the PBE/bs1 and PBE/def2-TZVP levels of theory were used in the SOC calculations.

For the active site with bound H_2, the SOC values calculated with 6-31G** and def2-TZVP basis sets are 79 and 83 cm^{-1}, respectively. As for the bare active site, the def2-TZVP calculation produced a SOC of 102 cm^{-1}. These values are comparable to the SOC in another iron-containing complex, $Fe(CO)_4$ with a SOC of 66 cm^{-1}.[61] The difference between the singlet and triplet mass-weighted gradients, $|\Delta g|$, for the active site with bound H_2, obtained at the PBE/bs1 level of theory is 1.04×10^{-4} E_h $m_e^{-1/2}$ a_0^{-1}. Calculations with the larger def2-TZVP basis set predict a similar value of 1.57×10^{-4} E_h $m_e^{-1/2}$ a_0^{-1}. As for the bare active site, $|\Delta g|$ was found to be 1.71×10^{-4} E_h $m_e^{-1/2}$ a_0^{-1} based on the PBE/def2-TZVP calculation.

The Landau-Zener probability of transition between the singlet and triplet states of the bare active site and the active site with bound H_2, in the 0-500 K temperature range is shown in Figure 5. In the earlier study[31] we demonstrated that the MECP geometry closely resembles the X-ray structure of the active site in [NiFe]-hydrogenase.[27,62-64] We assume that the energy required to reach the MECP from the singlet or triplet minimum is provided by the protein backbone, and the temperature corresponds to the energy of the active site with respect to the MECP geometry. Therefore, the calculated probabilities

represent the statistical likelihood of transition between the spin states of the active site at the MECP. To investigate the influence of different factors on the singlet-triplet transition probability we focused on the temperature range of 270-370 K. In this temperature range the transition probability for the bare active site, calculated with the SOC and $|\Delta g|$ values obtained using PBE/def2-TZVP MECP geometry, decreases from 42% to 38%. The binding of H_2 to the active site reduces the transition probability, resulting in values spanning the range of 35%−32%. Thus for the bare active site and the active site with bound H_2, the transition probability changes only by 4% and 3%, respectively, in 270-370 K temperature range. The choice of density functional has small effect (less than 3%) on the transition probability (Figure S3, Supporting Information), with $|\Delta g|$ obtained using the three functionals (PBE, BP86 and TPSS) with the bs1 basis set. Increasing the basis set size from bs1 to def2-TZVP shifts the transition probability down by 7%.
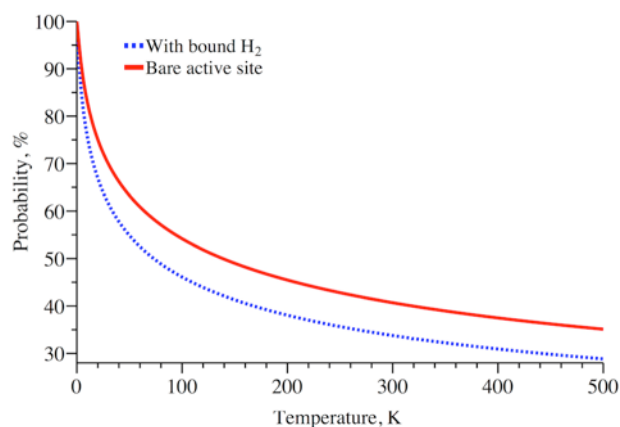
Figure 5. Landau-Zener transition probabilities between the singlet and triplet states of the bare active site and the active site with bound H_2 as functions of temperature. The mass-weighted gradients and spin-orbit coupling were calculated with PBE and MCQDPT2, respectively, using def2-TZVP basis set.

IV. Conclusions

We investigated the nonadiabatic spin-forbidden transitions between the lowest energy singlet and triplet states of the bare active site of [NiFe]-hydrogenase and the active site with H_2 bound on the Fe center. Density functional and multireference perturbation theories were used to provide parameters for the Landau-Zener calculation of transition probabilities. Binding of H_2 to the active site preserves the singlet-triplet intersystem crossing, induced by rotation of the terminal thiolate ligands, as demonstrated in our earlier work on the bare active site.[31] In comparison to the bare active site, the MECP geometry of the active site with bound H_2 is characterized by a smaller torsion angle between the terminal thiolate ligands.

Landau-Zener theory predicts changes in the spin-forbidden transition probability of the bare active site model from 42% to 38%, in the temperature range of 270-370 K. For the active site with bound H_2 the transition probability is reduced, with values from 35% to 32% along the same temperature range. Our predicted transition probabilities are of a greater magnitude than the values calculated for other Fe containing reactions, such as the addition of carbon monoxide to iron tetracarbonyl (5%),[61] and CO ligand recombination in myoglobin (<1%).[65] The higher transition probabilities between the singlet and triplet states of the active site are primarily related to the nature of the reaction coordinate associated with intersystem crossing. This reaction coordinate is best described by the internal rotation of the terminal thiolate ligands in the active site rather than by the distance change between the molecules as in other Fe containing reactions. The internal rotation is characterized by the smaller value of the gradient difference between the PESs of two spin states and therefore by the higher transition probability.

The high transition probabilities indicate that the nonadiabatic spin-forbidden transitions between the lowest energy singlet and triplet states could play an important role in the catalytic activity of [NiFe]-hydrogenase. The active site model used in this study does not fully account for the effect of the protein backbone on the active site. In the future we plan to investigate how the protein backbone influences the probability and rate of nonadiabatic transitions between the spin states of the [NiFe]-hydrogenase active site.

Associated Content

Supporting Information

Sampled initial positions of H_2 on the active site of [NiFe]-hydrogenase; CASSCF active space molecular orbitals used in calculations of spin-orbit coupling; transition probabilities for the active site with bound H_2 calculated using the gradients obtained with different level of theory; transition probabilities calculated using velocity distribution from (Ref. 34); binding energies of H_2 calculated with bs1 basis set; ZPE, dispersion and entropy corrections for the H_2 binding energies; difference between the singlet and triplet mass-weighted gradients obtained with different levels of theory; derivation of velocity averaged Landau-Zener transition probability formula; calculations of difference between the singlet and triplet mass-weighted gradients; atomic Cartesian coordinates of conformers. This material is available free of charge via the Internet at http://pubs.acs.org.

Author Information

 Corresponding Author *E-mail: svarganov@unr.edu. Phone: +1 (775) 784-1406.

Notes

The authors declare no competing financial interest.

References

(1)   Fontecilla-Camps, J. C.; Amara, P.; Cavazza, C.; Nicolet, Y.; Volbeda, A.
        Structure-Function Relationships of Anaerobic Gas-Processing Metalloenzymes.
        Nature **2009**, *460*, 814–822.

(2)   Wait, A. F.; Parkin, A.; Morley, G. M.; dos Santos, L.; Armstrong, F. A.
        Characteristics of Enzyme-Based Hydrogen Fuel Cells Using an Oxygen-Tolerant
        Hydrogenase as the Anodic Catalyst. *J. Phys. Chem. C* **2010**, *114*, 12003–12009.

(3)   Lojou, E. Hydrogenases as Catalysts for Fuel Cells: Strategies for Efficient
        Immobilization at Electrode Interfaces. *Electrochim. Acta* **2011**, *56*, 10385–10397.

(4)   Matsumoto, T.; Eguchi, S.; Nakai, H.; Hibino, T.; Yoon, K.-S.; Ogo, S.
        [NiFe]Hydrogenase from Citrobacter Sp. S-77 Surpasses Platinum as an Electrode
        for H_2 Oxidation Reaction. *Angew. Chem., Int. Ed.* **2014**, *53*, 8895–8898.

(5)   Lubitz, W.; Ogata, H.; Rüdiger, O.; Reijerse, E. Hydrogenases. *Chem. Rev.* **2014**,
        114, 4081–4148.

(6)   Albracht, S. P. J. Nickel Hydrogenases: In Search of the Active Site. *Biochim.
        Biophys. Acta, Bioenerg.* **1994**, *1188*, 167–204.

(7)   Adams, M. W. W. The Structure and Mechanism of Iron-Hydrogenases. *Biochim. Biophys. Acta, Bioenerg.* **1990**, *1020*, 115–145.

(8)   Thauer, R. K.; Klein, A. R.; Hartmann, G. C. Reactions with Molecular Hydrogen in Microorganisms: Evidence for a Purely Organic Hydrogenation Catalyst. *Chem. Rev.* **1996**, *96*, 3031–3042.

(9)   Buhrke, T.; Lenz, O.; Krauss, N.; Friedrich, B. Oxygen Tolerance of the H_2-Sensing [NiFe] Hydrogenase from Ralstonia Eutropha H16 Is Based on Limited Access of Oxygen to the Active Site. *J. Biol. Chem.* **2005**, *280*, 23791–23796.

(10)   Frielingsdorf, S.; Fritsch, J.; Schmidt, A.; Hammer, M.; Löwenstein, J.; Siebert, E.; Pelmenschikov, V.; Jaenicke, T.; Kalms, J.; Rippers, Y. et al. Reversible [4Fe-3S] Cluster Morphing in an O_2-Tolerant [NiFe] Hydrogenase. *Nat. Chem. Biol.* **2014**, *10*, 378–385.

(11)   Barton, B. E.; Olsen, M. T.; Rauchfuss, T. B. Artificial Hydrogenases. *Curr. Opin. Biotechnol.* **2010**, *21*, 292–297.

(12)   Helm, M. L.; Stewart, M. P.; Bullock, R. M.; DuBois, M. R.; DuBois, D. L. A Synthetic Nickel Electrocatalyst with a Turnover Frequency above 100,000 S^{-1} for H_2 Production. *Science* **2011**, *333*, 863–866.

(13)   Weber, K.; Kra, T.; Shafaat, H. S.; Weyhermu, T.; Bill, E.; Gastel, M.; Van Neese, F.; Lubitz, W. A Functional [NiFe]-Hydrogenase Model Compound That Undergoes Biologically Relevant Reversible Thiolate Protonation. *J. Am. Chem. Soc.* **2012**, *134*, 20745−20755.

(14)   Ogo, S.; Ichikawa, K.; Kishima, T.; Matsumoto, T.; Nakai, H.; Kusaka, K.; Ohhara, T. A Functional [NiFe]hydrogenase Mimic That Catalyzes Electron and Hydride Transfer from H_2. *Science* **2013**, *339*, 682–684.

(15)   Huynh, M. T.; Schilter, D.; Hammes-Schiffer, S.; Rauchfuss, T. B. Protonation of Nickel-Iron Hydrogenase Models Proceeds after Isomerization at Nickel. *J. Am. Chem. Soc.* **2014**, *136*, 12385–12395.

(16)   Simmons, T. R.; Berggren, G.; Bacchi, M.; Fontecave, M.; Artero, V. Mimicking Hydrogenases: From Biomimetics to Artificial Enzymes. *Coord. Chem. Rev.* **2014**, *270-271*, 127–150.

(17)   Ohki, Y.; Tatsumi, K. Thiolate-Bridged Iron-Nickel Models for the Active Site of [NiFe] Hydrogenase. *Eur. J. Inorg. Chem.* **2011**, *2011*, 973–985.

(18)   Kaur-Ghumaan, S.; Stein, M. [NiFe] Hydrogenases: How Close Do Structural and Functional Mimics Approach the Active Site? *Dalton Trans.* **2014**, *43*, 9392–9405.

(19)   Amara, P.; Volbeda, A.; Fontecilla-camps, J. C.; Field, M. J. A Hybrid Density Functional Theory/Molecular Mechanics Study of Nickel-Iron Hydrogenase: Investigation of the Active Site Redox States. *J. Am. Chem. Soc.* **1999**, *121*, 4468–4477.

(20)   Söderhjelm, P.; Ryde, U. Combined Computational and Crystallographic Study of the Oxidised States of [NiFe] Hydrogenase. *J. Mol. Struct.* **2006**, *770*, 199–219.

(21)   Kampa, M.; Lubitz, W.; van Gastel, M.; Neese, F. Computational Study of the Electronic Structure and Magnetic Properties of the Ni-C State in [NiFe] Hydrogenases Including the Second Coordination Sphere. *J. Biol. Inorg. Chem.* **2012**, *17*, 1269–1281.

(22)   Krämer, T.; Kampa, M.; Lubitz, W.; van Gastel, M.; Neese, F. Theoretical Spectroscopy of the Ni(II) Intermediate States in the Catalytic Cycle and the Activation of [NiFe] Hydrogenases. *ChemBioChem* **2013**, *14*, 1898–1905.

(23)   Siegbahn, P. E. M. Proton and Electron Transfers in [NiFe] Hydrogenase. *Adv. Inorg. Chem.* **2004**, *56*, 101–125.

(24)   Pardo, A.; De Lacey, A. L.; Fernández, V. M.; Fan, H.-J.; Fan, Y.; Hall, M. B. Density Functional Study of the Catalytic Cycle of Nickel-Iron [NiFe] Hydrogenases and the Involvement of High-Spin Nickel(II). *J. Biol. Inorg. Chem.* **2006**, *11*, 286–306.

(25)   Keith, J. M.; Hall, M. B. Potential Hydrogen Bottleneck in Nickel-Iron Hydrogenase. *Inorg. Chem.* **2010**, *49*, 6378–6380.

(26)   Vedha, S. A.; Solomon, R. V.; Venuvanalingam, P. Atomic Partitioning of M-H_2 Bonds in [NiFe] Hydrogenase: a Test Case of Concurrent Binding. *Phys. Chem. Chem. Phys.* **2014**, *16*, 10698–10707.

(27)   Wu, H.; Hall, M. B. Density Functional Theory on the Larger Active Site Models for [NiFe] Hydrogenases: Two-State Reactivity? *C.R. Chim.* **2008**, *11*, 790–804.

(28)   Bruschi, M.; Tiberti, M.; Guerra, A.; De Gioia, L. Disclosure of Key Stereoelectronic Factors for Efficient H_2 Binding and Cleavage in the Active Site of [NiFe]-Hydrogenases. *J. Am. Chem. Soc.* **2014**, *136*, 1803–1814.

(29)   Jayapal, P.; Sundararajan, M.; Hillier, I. H.; Burton, N. A. QM/MM Studies of Ni-Fe Hydrogenases: The Effect of Enzyme Environment on the Structure and Energies of the Inactive and Active States. *Phys. Chem. Chem. Phys.* **2008**, *10*, 4249–4257.

(30)   Pandelia, M.-E.; Ogata, H.; Lubitz, W. Intermediates in the Catalytic Cycle of [NiFe] Hydrogenase: Functional Spectroscopy of the Active Site. *ChemPhysChem* **2010**, *11*, 1127–1140.

(31)   Yson, R. L.; Gilgor, J. L.; Guberman, B. A.; Varganov, S. A. Protein Induced Singlet–Triplet Quasidegeneracy in the Active Site of [NiFe]-Hydrogenase. *Chem. Phys. Lett.* **2013**, *577*, 138–141.

(32)   Gordon, J. C.; Kubas, G. J. Perspectives on How Nature Employs the Principles of Organometallic Chemistry in Dihydrogen Activation in Hydrogenases. *Organometallics* **2010**, *29*, 4682–4701.

(33)   Zener, C. Non-Adiabatic Crossing. *Proc. R. Soc. London Ser. A* **1932**, *137*, 696–702.

(34)   Kuki, A. Adiabaticity Factor for Electron Transfer in the Multimode Case: An Energy Velocity Perspective. *J. Phys. Chem.* **1993**, *97*, 13107–13116.

(35)   Wittig, C. The Landau - Zener Formula. *J. Phys. Chem. B* **2005**, *109*, 8428–8430.

(36)   Goodrow, A.; Bell, A. T.; Head-Gordon, M. Are Spin-Forbidden Crossings a Bottleneck in Methanol Oxidation? *J. Phys. Chem. C* **2009**, *113*, 19361–19364.

(37)   Perdew, J. P.; Burke, K.; Ernzerhof, M. Generalized Gradient Approximation Made Simple. *Phys. Rev. Lett.* **1996**, *77*, 3865–3868.

(38)   Becke, A. D. Density-Functional Exchange-Energy Approximation with Correct Asymptotic Behavior. *Phys. Rev. A* **1988**, *38*, 3098–3100.

(39)   Perdew, J. P. Density-Functional Approximation for the Correlation Energy of the Inhomogeneous Electron Gas. *Phys. Rev. B* **1986**, *33*, 8822–8824.

(40)   Tao, J.; Perdew, J.; Staroverov, V.; Scuseria, G. Climbing the Density Functional Ladder: Nonempirical Meta–Generalized Gradient Approximation Designed for Molecules and Solids. *Phys. Rev. Lett.* **2003**, *91*, 146401.

(41)   Becke, A. D. Density-Functional Thermochemistry. III. The Role of Exact Exchange. *J. Chem. Phys.* **1993**, *98*, 5648.

(42)   Stephens, P. J.; Devlin, F. J.; Chabalowski, C. F.; Frish, M. J. Ab Initio Calculations of Vibrational Absorption and Circular Dichroism Spectra Using Density Functional Force Field. *J. Phys. Chem.* **1994**, *98*, 11623–11627.

(43)   Hertwig, R. H.; Koch, W. On the Parameterization of the Local Correlation Functional. What Is Becke-3-LYP? *Chem. Phys. Lett.* **1997**, *268*, 345–351.

(44)   Chen, S.; Raugei, S.; Rousseau, R.; Dupuis, M.; Bullock, R. M. Homogeneous Ni Catalysts for H_2 Oxidation and Production: An Assessment of Theoretical Methods, from Density Functional Theory to Post Hartree-Fock Correlated Wave-Function Theory. *J. Phys. Chem. A* **2010**, *114*, 12716–12724.

(45)   Weigend, F.; Ahlrichs, R. Balanced Basis Sets of Split Valence, Triple Zeta Valence and Quadruple Zeta Valence Quality for H to Rn: Design and Assessment of Accuracy W. *Phys. Chem. Chem. Phys.* **2005**, *7*, 3297–3305.

(46)   Dolg, M.; Wedig, U.; Stoll, H.; Preuss, H. Energy-Adjusted Ab Initio Pseudopotentials for the First Row Transition Elements. *J. Chem. Phys.* **1987**, *86*, 866.

(47)   Hehre, W. J. Self-Consistent Molecular Orbital Methods. XII. Further Extensions of Gaussian-Type Basis Sets for Use in Molecular Orbital Studies of Organic Molecules. *J. Chem. Phys.* **1972**, *56*, 2257.

(48)   Francl, M. M. Self-Consistent Molecular Orbital Methods. XXIII. A Polarization-Type Basis Set for Second-Row Elements. *J. Chem. Phys.* **1982**, *77*, 3654.

(49)   Knowles, P. J.; Hampel, C.; Werner, H.-J. Coupled Cluster Theory for High Spin, Open Shell Reference Wave Functions. *J. Chem. Phys.* **1993**, *99*, 5219.

(50)   Delcey, M. G.; Pierloot, K.; Phung, Q. M.; Vancoillie, S.; Lindh, R.; Ryde, U. Accurate Calculations of Geometries and Singlet-Triplet Energy Differences for Active-Site Models of [NiFe] Hydrogenase. *Phys. Chem. Chem. Phys.* **2014**, *16*, 7927–7938.

(51)   Peverati, R.; Baldridge, K. K. Implementation and Performance of DFT-D with Respect to Basis Set and Functional for Study of Dispersion Interactions in Nanoscale Aromatic Hydrocarbons. *J. Chem. Theory Comput.* **2008**, *4*, 2030–2048.

(52)   Grimme, S.; Antony, J.; Ehrlich, S.; Krieg, H. A Consistent and Accurate Ab Initio Parametrization of Density Functional Dispersion Correction (DFT-D) for the 94 Elements H-Pu. *J. Chem. Phys.* **2010**, *132*, 154104.

(53)   Maganas, D.; Grigoropoulos, A.; Staniland, S. S.; Chatziefthimiou, S. D.; Harrison, A.; Robertson, N.; Kyritsis, P.; Neese, F. Tetrahedral and Square Planar Ni[(SPR$_2$)$_2$N]$_2$ Complexes, R = Ph & ^{i}Pr Revisited: Experimental and Theoretical Analysis of Interconversion Pathways, Structural Preferences, and Spin Delocalization. *Inorg. Chem.* **2010**, *49*, 5079–5093.

(54)   Schmidt, M. W.; Baldridge, K. K.; Boatz, J. A.; Elbert, S. T.; Gordon, M. S.; Jensen, J. H.; Koseki, S.; Matsunaga, N.; Nguyen, K. A.; Su, S. J. et al. General

Atomic and Molecular Electronic Structure System. *J. Comput. Chem.* **1993**, *14*, 1347–1363.

(55)   Gordon, M. S.; Schmidt, M. W. Advances in Electronic Structure Theory: GAMESS a Decade Later. In *Theory and Applications of Computational Chemistry*; Dykstra, C. E., Frenking, G., Kim, K.S., Scuseria, G.E., Eds.; Elsevier: Amsterdam, The Netherlands, 2005; pp 1167–1189.

(56)   Fedorov, D. G.; Koseki, S.; Schmidt, M. W.; Gordon, M. S. Spin-Orbit Coupling in Molecules: Chemistry beyond the Adiabatic Approximation. *Int. Rev. Phys. Chem.* **2003**, *22*, 551–592.

(57)   Nakano, H. Quasidegenerate Perturbation Theory with Multiconfigurational Self-Consistent-Field Reference Functions. *J. Chem. Phys.* **1993**, *99*, 7983.

(58)   Nakano, H. MCSCF Reference Quasidegenerate Perturbation Theory with Epstein-Nesbet Partitioning. *Chem. Phys. Lett.* **1993**, *207*, 372–378.

(59)   Roos, B. O.; Szulkin, M.; Jaszufiski, M. Dynamic Correlation for MCSCF Wave Functions : An Effective Potential Method. *Theor. Chim. Acta* **1987**, *71*, 375–384.

(60)   Ivanic, J.; Ruedenberg, K. Identification of Deadwood in Configuration Spaces through General Direct Configuration Interaction. *Theor. Chem. Acc.* **2001**, *106*, 339–351.

(61)   Harvey, J. N. Spin-Forbidden CO Ligand Recombination in Myoglobin. *Faraday Discuss.* **2004**, *127*, 165.

(62)   Volbeda, A.; Charon, M.-H.; Piras, C.; Hatchikian, E. C.; Frey, M.; Fontecilla-, J. C.; Camps. Crystal Structure of the Nickel–Iron Hydrogenase from Desulfovibrio Gigas. *Nature* **1995**, *373*, 580–587.

(63)   Higuchi, Y.; Ogata, H.; Miki, K.; Yasuoka, N.; Yagi, T. Removal of the Bridging Ligand Atom at the Ni–Fe Active Site of [NiFe] Hydrogenase upon Reduction with H_2, as Revealed by X-Ray Structure Analysis at 1.4 Å Resolution. *Structure* **1999**, *7*, 549–556.

(64)   Ogata, H.; Mizoguchi, Y.; Mizuno, N.; Miki, K.; Adachi, S.; Yasuoka, N.; Yagi, T.; Yamauchi, O. Structural Studies of the Carbon Monoxide Complex of [NiFe] Hydrogenase from Desulfovibrio Vulgaris Miyazaki F: Suggestion for the Initial Activation Site for Dihydrogen. *J. Am. Chem. Soc.* **2002**, *124*, 11628–11635.

(65)   Carreón-Macedo, J.-L.; Harvey, J. N. Computational Study of the Energetics of $^3Fe(CO)_4$, $^1Fe(CO)_4$ and $^1Fe(CO)_4(L)$, L = Xe, CH_4, H_2 and CO. *Phys. Chem. Chem. Phys.* **2006**, *8*, 93–100.

Chapter IV. Spin-Forbidden Transitions Between Electronic States in the Active Site of Rubredoxin

Gwen E. dePolo, Danil S. Kaliakin, Sergey A. Varganov

Abstract

Rubredoxin is a small iron-sulfur protein involved in biological electron transfer, which is accomplished by changing the oxidation state of the iron atom in the active site. We investigate the possibility of spin-forbidden transitions between the lowest energy electronic states with different spin multiplicities in the rubredoxin active site models $[Fe(SCH_3)_4]^n$ (n=2-, 1-, 0) using nonadiabatic transition state theory (NA-TST). The equilibrium structures, minimum energy crossing point structures and Hessians were obtained with density functional theory. The spin-orbit coupling (SOC) was calculated with the complete active space configuration interaction method using the two-electron spin-orbit Breit-Pauli Hamiltonian. We found several crossings between the lowest energy spin states associated with the changes in Fe coordination. However, only triplet/quintet crossings in $[Fe(SCH_3)_4]^{2-}$ and $[Fe(SCH_3)_4]^0$, as well as a quartet/sextet crossing in $[Fe(SCH_3)_4]^{1-}$ are characterized by nonzero first-order SOC responsible for transitions between these spin states. The rates of spin-forbidden transitions in the $[Fe(SCH_3)_4]^{2-}$ complex are 1 and 2 orders of magnitude higher than the rates in the

$[Fe(SCH_3)_4]^{1-}$ and $[Fe(SCH_3)_4]^0$ complexes, respectively. These rate differences are related to a large variation of the SOC between the complexes with different charges, which in turn comes from different molecular orbitals involved in the spin-flip transitions. Finally, we demonstrate that the differences between the NA-TST rates and the rates calculated under the assumption of completely spin-allowed transitions could be as large as 4 orders of magnitude. This means that even in qualitative discussions of the reaction mechanisms involving changes in spin states the partially spin-forbidden nature of the transitions between these states must be taken into account.

I. Introduction

Rubredoxin is a protein that is essential for electron transfer in many biological systems.[1] It is involved in variety of enzyme-catalyzed processes, such as nitrate reduction,[2] alkane oxidation,[3] methanogenesis,[4] carbon fixation[5] and detoxification of reactive oxygen species.[6,7] Rubredoxin plays a crucial role in photosystem II activity within a broad variety of oxygenic organisms.[8] Finally, the recent study suggests that the rubredoxin-like site could act as an auxiliary iron source to the damaged catalytic center.[9] Because the investigation of electronic properties of the rubredoxin active site within the protein is challenging, often the studies are focused on synthetic analogs of the active site.[10] The simplest synthetic analog that resembles the active site of rubredoxin is the $[Fe(SCH_3)_4]^{n-}$ complex in which the cysteines of rubredoxin are replaced by SCH_3 ligands. The electron adiabatic detachment energy (ADE) of the $[Fe(SCH_3)_4]^-$ complex has been obtained from both theoretical approaches[10,11] and spray photoelectron spectroscopy (SPES),[12,13] and thus can be used to estimate the accuracy of chosen

computational methods. Among the benefits of SPES is the capability of measuring the ADE in the gas phase, which makes the experimental conditions similar to the conditions of electronic structure calculations in vacuum.

The $[Fe(SCH_3)_4]^{2-}$ and $[Fe(SCH_3)_4]^{-}$ complexes have the iron atom in the most biologically relevant formal oxidation states Fe(II) and Fe(III), respectively. In the $[Fe(SCH_3)_4]^{0}$ complex, the loss of the extra electron is mostly associated with ionization of sulfur atoms of the ligands.[14] Nonetheless, in the present study, the analysis of the molecular orbitals of $[Fe(SCH_3)_4]^{0}$ shows that the valence orbitals of this complex have some contributions from the atomic orbitals of Fe. Therefore, here we consider complexes with three different charges, $[Fe(SCH_3)_4]^{n}$ (n=2-, 1-, 0).

The rubredoxin active site has several low-lying electronic states with different spin multiplicities[11,12] indicating a potential importance of nonadiabatic spin-forbidden transitions during electron transfer. Moreover, earlier it was shown that rubredoxin active site exhibits spin crossover during the homolytic cleavage of the Fe-S bond.[15] Thus, spin-forbidden transitions induced by a minor change in the geometry of the active site could affect the efficiency of electron attachment to or detachment from the active site. Earlier we showed that the spin-forbidden transitions between the lowest energy spin states in the metal-sulfur protein [NiFe]-hydrogenase could be responsible for the unique catalytic activity of this enzyme toward hydrogen oxidation/reduction.[16,17] In this work, we investigate the possibility of similar spin-forbidden transitions between the lowest energy electronic states in the rubredoxin active site models using the nonadiabatic transition state theory (NA-TST).[18–20] The electronic structure methods and NA-TST are described in sections II and III, respectively. The results are presented in section IV: in Subsection

A, we discuss crossings between the low lying electronic states with different spin multiplicities; in subsection B, we focus on the NA-TST rate constants for spin-forbidden transition between these states. The main findings are summarized in section V.

II. Computational Details

The rubredoxin active site model $[Fe(SCH_3)_4]^n$ was assumed to be in the "crystal" S_4-like conformation[10] (Figure 1). The total charge of the model was set to n=2-, 1- and 0 to simulate the different oxidation states of the active site. We focused on three lowest-energy electronic spin states (singlet, triplet and quintet for n=2-, 0; and doublet, quartet and sextet for n=1-). The geometry of the active site model was optimized with unrestricted density functional theory (DFT) using PBE,[21] B3LYP[22–24] and LC-BLYP[25,26] functionals with 6-31G**[27,28] and def2-TZVP[29] basis sets.
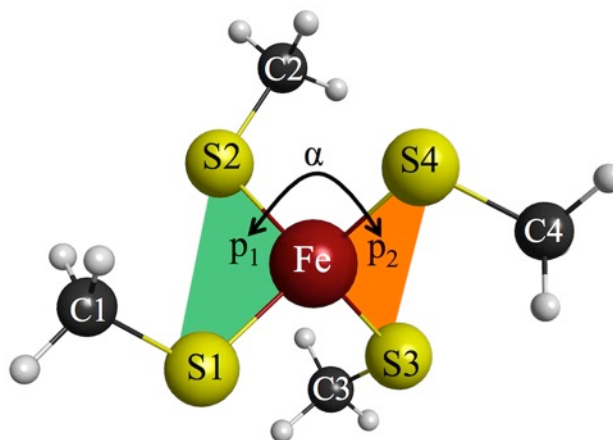
Figure 1. Rubredoxin active site model. Torsion angle α describes rotation of planes p_1 (S1-Fe-S2) and p_2 (S3-Fe-S4) with respect to each other. Angle β is defined as the angle between planes S1-Fe-S3 and S2-Fe-S4; angle γ is defined as the angle between planes S2-Fe-S3 and S1-Fe-S4.

For each pair of spin states, the cross sections of potential energy surfaces were built by linearly interpolating geometries between the equilibrium structures of the two states optimized with the PBE density functional. Single-point energy calculations were carried out at each interpolated geometry. For each pair of crossing spin states, the geometry closest to the intersection was used as an initial guess in the minimal energy point (MECP) search calculation. At the MECPs, energy gradients and Hessians were calculated for each crossing spin state. The spin-orbit coupling (SOC) at MECP was computed using the complete active space configuration interaction (CASCI) method[30] with (n, n) active space, where n is the number of singly occupied molecular orbitals in the high-spin state. The molecular orbitals for the CASCI-SOC calculations were obtained from the restricted open-shell Hartree-Fock (ROHF) calculations on the high-spin state. The GAMESS suite of programs[31,32] was used for the DFT, ROHF and CASCI-SOC calculations. To obtain high accuracy ADEs we also carried out the CCSD(T) calculations using the Molpro package.[33,34] The ADEs were calculated as the energy differences between the $[Fe(SCH_3)_3]^{2-}$/$[Fe(SCH_3)_3]^{-}$ and the $[Fe(SCH_3)_3]^{-}$ /$[Fe(SCH_3)_3]^0$ minima for triplet/quartet and quintet/sextet spin states, respectively. In these calculations the def2-TZVP basis set was used. In addition, to compare our optimized geometries and ADEs with previously reported B3LYP/6-31G** values[10] we calculated these properties at the same level of theory.

We calculated the canonical (temperature-dependent) and microcanonical (energy dependent) probabilities of spin-forbidden transitions between the pairs of spin states at the MECPs. The canonical probabilities were obtained by convoluting the velocity-dependent version of the Landau-Zener (LZ) formula with Maxwell-Boltzmann velocity

distribution for the temperature range between 200 and 300 K. The microcanonical probabilities were obtained with the energy-dependent LZ and weak coupling (WC) formulas. These probabilities were used to calculate the microcanonical rate constants of spin-forbidden transitions with NA-TST for the internal energy range from 0 to 30 kcal/mol.

III. Theoretical Methods

The rate constants for transitions between electronic spin states were calculated with nonadiabatic transition state theory (NA-TST).[18,19,35,36] In NA-TST, the microcanonical rate constant $k(E)$ for transition between electronic spin states can be calculated as[19,36–41]

$$k(E) = \frac{N^*_{MECP}(E)}{h\rho_R(E)}, \tag{1}$$

where h is the Planck's constant and ρ_R is the density of rovibrational states of reactants. The effective number of rovibrational states at the MECP, $N^*_{MECP}(E)$, is

$$N^*_{MECP}(E) = \int_0^E \rho_{MECP}(E - \varepsilon_\perp) P_{trans}(\varepsilon_\perp) d\varepsilon_\perp, \tag{2}$$

where ρ_{MECP} is the density of rovibrational states at the MECP, E is the total internal energy of the system, and $\varepsilon_\perp$ is the component of internal energy along the reaction coordinate (and orthogonal to the crossing seam). Harmonic frequencies at the MECP were calculated by diagonalizing the effective Hessian.[36,42] The rovibrational density of states were calculated by convoluting the vibrational density of states, obtained using direct counting method,[43] with densities of rotational states for classical asymmetric

top.[44,45] The transition probability between spin-diabatic states was calculated using the double passage LZ formula[46–49]

$$P_{trans} = P^{LZ} + (1 - P^{LZ})P^{LZ} , \tag{3}$$

$$P^{LZ}(\varepsilon_\perp) = 1 - \exp\left(-\frac{2\pi H_{SO}^2}{\hbar|\Delta G|}\sqrt{\frac{\mu_\perp}{2(\varepsilon_\perp - E_{MECP})}}\right), \tag{4}$$

where H_{SO} is the SOC constant, E_{MECP} is the MECP energy relative to reactants, $\mu_\perp$ is the reduced mass along the reaction coordinate, and ΔG is the difference of energy gradients of the two crossing spin states at MECP. The SOC constant, used to calculate the transition probability between the spin-diabatic states with spins S and S' and magnetic quantum numbers M_S and M_S',

$$H_{SO}^2 = \sum_{M_S = -S}^{S} \sum_{M_S' = -S'}^{S'} \left|\langle SM_S|\hat{H}_{SO}^{BP}|S'M_S'\rangle\right|^2 , \tag{5}$$

is obtained using the Breit-Pauli Hamiltonian $\hat{H}_{SO}^{BP}$.[50] To estimate the importance of quantum tunneling through the MECP barrier the transition probability was also calculated using the WC formula[49,51] (Supporting Information).

Because NA-TST is a generalization of traditional transition state theory (TST) to nonadiabatic processes, it is based on similar assumptions and has same limitations. As a local theory, NA-TST is expected to fail in cases where nonlocal dynamic effects are important, including multistep reactions with short-lived intermediates and reactions at high temperature. In general, the nonlocal nature of reaction trajectories that do not follow along the minimal energy reaction path through MECP can be described with nonadiabatic molecular dynamics.[45,52–55] However, the applicability of nonadiabatic

molecular dynamics is restricted to relatively small systems and fast reaction rates, whereas NA-TST can be used to study large complex systems with both fast and slow spin-forbidden transitions.[18,19,56] Here we focus on a simple one-step unimolecular reaction at biologically relevant temperatures; therefore, the use of NA-TST is well justified.

To obtain a simple estimate for the temperature-dependent transition probability, the velocity-averaged probability was calculated as[17,57,58]

$$\left\langle P^{LZ}(T)\right\rangle = 1 - \left(\frac{2}{\pi k_B T}\right)^{1/2} \int_0^\infty \exp\left(\frac{-2\pi H_{SO}^2}{\hbar \upsilon \left|\Delta G_\mu\right|} - \frac{\upsilon^2}{2 k_B T}\right) d\upsilon, \tag{6}$$

where ΔG_μ is the difference of mass-weighted energy gradients of two crossing spin states at MECP, k_B is the Boltzmann constant, T is the temperature, and υ is the mass weighted velocity along the reaction coordinate. It is important to notice that in eq 6, it is assumed that at T=0 the system is already at the MECP. This assumption can be justified if the active site structure is constrained to the MECP geometry by the protein backbone, as in NiFe-hydrogenase.[16,17] This is not necessary the case in rubredoxin; however, the velocity-averaged transition probability is still useful as a simple parameter characterizing the probability of transition in the active site model.

IV. Results and Discussion

A. State Crossings and MECPs

Because it was demonstrated that pure density functionals are more accurate than hybrid functionals at predicting the energy gap between the lowest energy spin states of the metal-sulfur complexes similar to $Fe(SCH_3)_4$[16,59] most of the calculations were

performed using the PBE functional. However, we also carried out the B3LYP calculations to compare our results with previously reported theoretical geometries and adiabatic detachment energies (ADEs) of $Fe(SCH_3)_4$ complexes. The ADEs were also calculated with MP2, CCSD, and CCSD(T) methods at the PBE/def2-TZVP optimized geometries. The obtained results, with possible exception of the ADE for $[Fe(SCH_3)_4]^-$ calculated with PBE density functional, are in reasonable agreement with the previously reported theoretical and experimental values (Tables S1 and S2).[10,12,13]

To determine if crossings between the lowest energy spin states can occur as the geometry of the $[Fe(SCH_3)_4]^n$ complexes changes between the equilibrium geometries (minima) corresponding to different spin states, we calculated energies of all spin states at each equilibrium geometry. We found four different crossings between the lowest energy singlet, triplet and quintet states in the $[Fe(SCH_3)_4]^{2-}$ and $[Fe(SCH_3)_4]^0$ complexes, as well as two crossings between the lowest energy doublet, quartet, and sextet states in the $[Fe(SCH_3)_4]^-$ complex. However, there are no singlet-triplet crossings in $[Fe(SCH_3)_4]^{2-}$ and $[Fe(SCH_3)_4]^0$, and no doublet-quartet crossings in $[Fe(SCH_3)_4]^-$. Among the six found state crossings, only triplet/quintet in $[Fe(SCH_3)_4]^{2-}$ and $[Fe(SCH_3)_4]^0$, as well as a quartet/sextet in $[Fe(SCH_3)_4]^{1-}$ are characterized by nonzero first-order SOC. Therefore, we focus on these three state crossings where spin-forbidden transitions are expected to occur with a relatively fast rate.

In the $[Fe(SCH_3)_4]^{2-}$ complex, quintet is the lowest energy state (Table 1). At the quintet state geometry, the triplet state lies 19.9 kcal/mol higher in energy than the quintet. However, at the triplet state geometry, the quintet state becomes higher in energy than the triplet, indicating a state crossing. The equilibrium geometries of these spin

states can be characterized by the twist angles α and β. The values of 0° correspond to square-planar geometry, whereas 90° indicates tetrahedral geometry. As can be seen from the values of α and β in Table 1, the triplet state has nearly square planar geometry, while the quintet state geometry is almost tetrahedral. In the case of the $[Fe(SCH_3)_4]^-$ complex, quartet is the lowest energy state with the geometry between square planar and tetrahedral. The first excited sextet state is 21.1 kcal/mol higher in energy at the quartet geometry. The order of the states changes at the sextet optimized geometry, which is almost tetrahedral, again indicating a state crossing. For the $[Fe(SCH_3)_4]^0$ complex, the triplet state is the lowest energy state with the quintet lying 16.3 kcal/mol higher at the triplet geometry. The change between triplet and quintet geometries is harder to describe in simple terms because all three twist angles change (Figure 2). The α and β angles increase from about 65° to between 75° and 80°, and the γ angle decreases from about 90° to 83°. These changes indicate that the $[Fe(SCH_3)_4]^0$ model becomes more tetrahedral (less planar) as it transitions from the quintet to the triplet state. Because at the quintet geometry the triplet state become higher in energy than quintet the two states must cross.

Table 1. Relative Energies of the High-Spin (HS) and Low-Spin (LS) States ΔE (kcal/mol), Twist Angles (Degrees), and $<S^2>$ Values.

Geometry	ΔE		Twist Angles			$<S^2>$ value	
	HS	LS	α	β	γ	HS	LS
$[Fe(SCH_3)_4]^{2-}$							
S=1 minimum	27.5	6.3	13.8	13.8	90.0	6.029	2.051
S=2 minimum	0.0	19.9	87.7	87.7	90.0	6.019	2.754
MECP S=1, 2	10.4	10.4	49.6	49.5	90.0	6.030	2.049
$[Fe(SCH_3)_4]^{1-}$							
S=3/2 minimum	21.1	0.0	55.1	55.1	90.0	8.764	3.821
S=5/2 minimum	4.3	12.5	91.5	88.5	90.0	8.764	3.909
MECP S=3/2, 5/2	6.1	6.1	79.4	79.5	90.0	8.764	3.849
$[Fe(SCH_3)_4]^{0}$							
S=1 minimum	16.3	0.0	80.0	72.2	81.9	6.048	2.067
S=2 minimum	7.2	12.4	63.7	64.4	90.4	6.056	2.125
MECP S=1, 2	7.6	7.6	63.4	63.4	89.8	6.056	2.077

[a]The active site geometries correspond to the minima of triplet (S=1), quartet (S=3/2), quintet (S=2), and sextet (S=5/2) states. High-spin state is the S=2 state in the $[Fe(SCH_3)_4]^{2-}$ and $[Fe(SCH_3)_4]^{0}$ complexes, and the S=5/2 state in the $[Fe(SCH_3)_4]^{1-}$ complex.
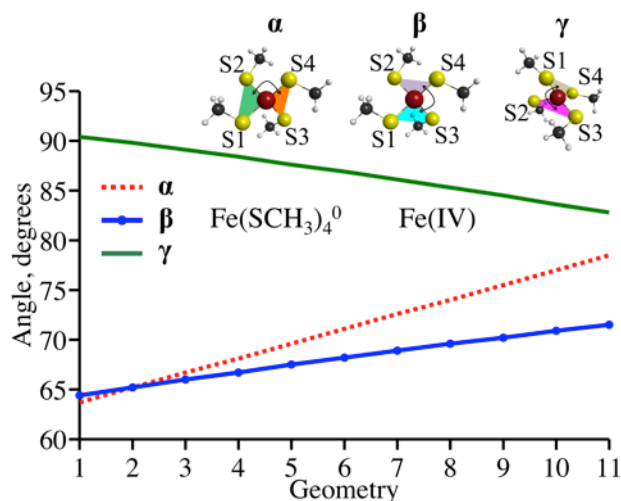
Figure 2. Twist angles α, β, and γ of the $Fe(SCH_3)_4^0$ complex as functions of geometry. Geometry changes from the quintet state minimum (geometry 1) to the triplet state minimum (geometry 11).

We calculated potential energy cross sections for the crossing spin states by interpolating geometries of the complexes between the equilibrium structures of the spin states (Figure 3). The interpolated geometries closest to the crossings were used as initial guesses for the MECP search. The MECP energies are always higher than the equilibrium structure energies of the crossing spin states indicating peaked intersections (Table 1). The spin contamination, characterized by the $<S^2>$ values, could have a significant negative effect on the accuracy of the calculated energies. Because $<S^2>=S(S+1)$, where S is the total electron spin, for noncontaminated states, $<S^2>$ should be equal to 2, 3.75, 6, and 8.75 for the triplet, quartet, quintet and sextet states, respectively. The $<S^2>$ values reported in Table 1 indicate that the spin contamination is relatively small for all spin states.
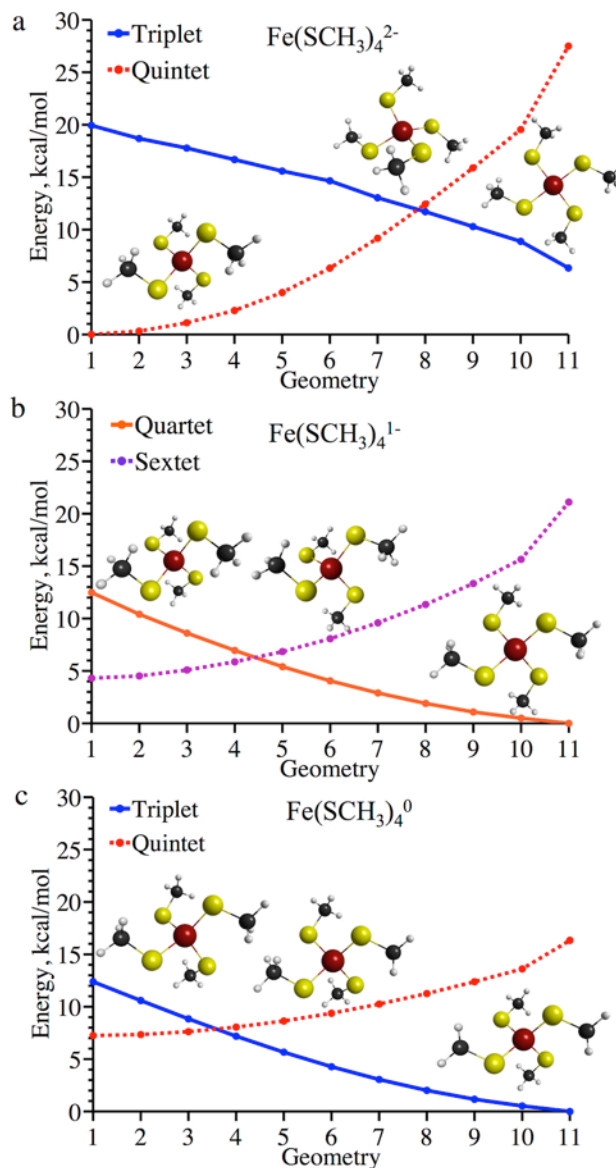
Figure 3. Energies of the spin states as functions of geometry interpolated between the minima of two crossing states. (a) Triplet and quintet states of the $Fe(SCH_3)_4^{2-}$ complex. (b) Quartet and sextet states of the $Fe(SCH_3)_4^-$ complex. (c) Triplet and quintet states of the $Fe(SCH_3)_4^0$ complex. Geometries of the minima and MECP (similar to the crossing geometries) are shown. Calculations were done at the PBE/def2-TZVP level of theory.

To estimate probability of the spin-forbidden transitions between the crossing spin states, we calculated the necessary properties at the MECP geometries (Table 2). As stated before, for the crossings between quintet/singlet and sextet/doublet states, SOC

(calculated using first-order perturbation theory) and transition probabilities are zero because more than one spin flip would be required to transition between these spin states. For the crossings with nonzero SOC, the gradient differences at the MECPs are similar. Therefore, differences in the probability of transitions mostly come from the SOC, which varies dramatically from 8 cm^{-1}, for triplet-quintet crossing in [Fe(SCH$_3$)$_4$]^0, to 157 cm^{-1}, for triplet-quintet crossing in Fe(SCH$_3$)$_4$]$^{2-}$. These SOC values give the probability of transition at 300 K of 0.7% and 67.3%, respectively. Again, it is important to point out that the MECP energy barriers (ΔE_{MECP}) do not contribute to the canonical probability of transition <P^{LZ}>$_{300K}$ calculated using eq 6. However, these barriers are taken into account in the rate constant calculations described in the next subsection.

Table 2. SOC Constant H$_{SO}$ (cm^{-1}), Absolute Value of Gradients Difference |ΔG| (hartree/bohr) and Probability of Transition <P^{LZ}>$_{300K}$ (%) at the MECPs[a]

	H$_{SO}$	|ΔG|$\times 10^{-4}$	<P^{LZ}>$_{300K}$	ΔE_{MECP}	ΔE_{HS}	ΔE_{LS}
[Fe(SCH$_3$)$_4$]$^{2-}$						
MECP S=1, 2	157	1.41	67.3	10.4	0.0	6.3
MECP S=0, 2	0	1.94	0.0	19.3	0.0	17.3
[Fe(SCH$_3$)$_4$]$^{1-}$						
MECP S= 3/2, 5/2	23	1.42	5.7	6.1	4.3	0.0
MECP S= 1/2, 5/2	0	2.12	0.0	12.4	4.3	11.0
[Fe(SCH$_3$)$_4$]^0						
MECP S=1, 2	8	1.92	0.7	7.6	7.2	0.0
MECP S=0, 2	0	1.94	0.0	8.3	7.2	4.0

[a]Relative energy ΔE (kcal/mol) for MECPs, low-spin (LS) and high-spin (HS) minima. Spin states are labeled as S=0 (singlet), S=1/2 (doublet), S=1 (triplet), S=3/2 (quartet), S=2 (quintet), and S=5/2 (sextet).

B. Rates of Spin-Forbidden Transition

The rate constants of spin-forbidden transitions between the states with nonzero SOC calculated using NA-TST are shown in Figure 4. The rate constants for transitions from high-spin to low-spin states are labeled as forward constants (k_1), whereas the rate constants for opposite transitions are labeled as k_{-1}. These rate constants were calculated using the LZ formula for transition probability. Calculations using the WC formula produced very similar results with exception of small tunneling rates at the energies below the MECP energy (Figure S1). We also plotted the same rate constants calculated by assuming completely spin-allowed transitions with unit transition probability. The rate constant curves intersect the horizontal axis at the MECP energies calculated with respect to the reactant minima. As internal energy increases the differences between the NA-TST rates and the spin-allowed rates become noticeable. These differences are directly related to the SOC strength. For $[Fe(SCH_3)_4]^{2-}$ with SOC of 157 cm^{-1}, at high internal energies, the NA-TST rates are about an order of magnitude lower than the spin-allowed rates. For $[Fe(SCH_3)_4]^-$, this difference increases to more than 2 orders of magnitude reflecting the weaker SOC of 27 cm^{-1}. Finally, for $[Fe(SCH_3)_4]^0$ with SOC of only 8 cm^{-1}, the NA-TST rates are about 4 orders of magnitude lower than the spin-allowed rates. These results demonstrate that, in general, even for the purpose of qualitative discussion of reaction mechanisms involving crossings of electronic states with different spin, transitions between spin states cannot be treated as either completely spin-forbidden or completely spin-allowed.

Figure 4. Rate constants for transitions between electronic spin states of rubredoxin active site models calculated using LZ probabilities (solid lines) and assuming completely spin-allowed kinetics with unit probability (dashed lines) as functions of internal energy. Rate constant k_1 (red lines) represents the transition from high-spin state to low-spin states, whereas k_{-1} (blues lines) is the rate constant for opposite process. (a) Quintet-triplet transitions in the $Fe(SCH_3)_4^{2-}$ complex. (b) Sextet-quartet transitions in the $Fe(SCH_3)_4^{1-}$ complex. (c) Quintet-triplet transitions in the $Fe(SCH_3)_4^{0}$ complex. The geometries, energies, energy gradients and Hessians were obtained at the PBE/def2-TZVP level of theory. The SOC constants were calculated at the CASCI/def2-TZVP level of theory using the high-spin ROHF molecular orbitals.

Because a rate constant depends approximately quadratically on the SOC constant and exponentially on the reaction (MECP) barrier, one may assume that a transition rate between two spin states is mostly determined by the MECP barrier. However, as can be seen by comparing the transition rates for complexes with different charges, for high internal energy this assumption is not necessary correct. In the $[Fe(SCH_3)_4]^{2-}$ complex, despite the highest MECP barrier (Figure 3), the rate constants at high energy are larger than in the $[Fe(SCH_3)_4]^{-/0}$ complexes (Figure 4) due to having the strongest SOC.

Given the profound effect of SOC on the transition rates between different spin states we attempted to understand why SOC is so different in the complexes with different charges. For simplicity, we limit our analysis to the dominant one-electron contribution to SOC, which grows rapidly with nuclear charge.[50] The highest occupied and lowest unoccupied molecular orbitals for the complexes with different charges are shown in Figure 4. The main contribution to the SOC matrix elements should come from the orbital pairs that have different occupations in two coupled spin states.[60] These are orbital pairs (2, 5), (1, 5), and (1, 4) for the clusters with charges 2-, 1- and 0, respectively. Three components (x, y, and z) of the spin-orbit operator act on a molecular orbital by rotating it by 90° around x-, y-, or z-axis. Therefore, one would expect a strong SOC if the two orbitals involved in the spin-flip transition are centered on the same heavy atoms, which should maximize the overlap after orbital rotation. In the $[Fe(SCH_3)_4]^{2-}$ complex, molecular orbital 2 consists of the Fe d_{z2} orbital and some contributions from the other Fe orbitals, whereas molecular orbital 5 has a significant contribution from the Fe d_{x2-y2} orbital. Rotation of one of these orbitals around x- or y-axis should produce a large overlap and a strong SOC (157 cm^{-1}). In the $Fe(SCH_3)_4]^{1-}$ complex, molecular

orbitals 1 and 5 have large contributions from the ligands' orbitals resulting in a weaker SOC (23 cm^{-1}). Finally, in the Fe(SCH$_3$)$_4$]^0 complex, molecular orbital 1 has large contribution from the ligands, whereas orbital 4 is mostly consist of the Fe d$_{yz}$ orbital, which leads to a very weak SOC (8 cm^{-1}). It is important to note that for [Fe(SCH$_3$)$_4$]$^{2-}$, the SOC value is sensitive to the geometry of the complex (see Tables S3 and S4 for the PBE and LC-BLYP optimized geometries and SOC values). This sensitivity is related to different contributions of the Fe atomic orbitals into the ROHF molecular orbital 2 (Figure 5a). At the PBE optimized geometry, mixing of the d$_{z2}$ orbital with other orbitals of Fe is significant. In contrast, at the LC-BLYP geometry, molecular orbital 2 is almost identical to the d$_{z2}$ orbital of Fe (Figure S2). This reduction in the mixing of different orbitals of Fe results in a smaller overlap between molecular orbitals 2 and 5 after spin-orbit rotation. The smaller orbital overlap leads to significantly weaker SOC.

Figure 5. Molecular orbitals of the rubredoxin active site models at the MECP geometries: (a) $[Fe(SCH_3)_4]^{2-}$ complex; (b) $Fe(SCH_3)_4^-$ complex; (c) $[Fe(SCH_3)_4]^0$ complex. Solid blue arrows represent the electrons that have the same spin in both electronic states, whereas red dashed arrows show the electrons that change spin as a result of spin-forbidden transition. Numbers labeling the orbitals that are expected to have the largest contribution to the SOC matrix elements are in red. Also reported are the orbital energies in hartree. These high-spin ROHF/def2-TZVP orbitals were used to calculate SOC at the CASCI/def2-TZVP level of theory.

V. Conclusions

We investigated the kinetics of spin-forbidden transitions between the lowest energy electronic states with different spin multiplicities in the rubredoxin active site models $[Fe(SCH_3)_4]^n$ (n=2-, 1-, 0) using the nonadiabatic transition state theory. The lowest energy spin states in the $[Fe(SCH_3)_4]^n$ complexes tend to cross as the geometries of the complexes change between tetrahedral and square planar. Potentially, such

geometric changes could be induced by the protein backbone, as in [NiFe]-hydrogenase.[16,17] The obtained rate constants for transitions between different spin states can be smaller by up to 4 orders of magnitude than the rate constants obtained under the assumption of completely spin-allowed transitions. This indicates that even in qualitative discussions of reaction mechanisms associated with changes of the Fe coordination the spin-forbidden nature of the transitions between different spin states must be taken into account.

The rate constants of spin-forbidden transitions change by several orders of magnitude depending on the charge of the $Fe(SCH_3)_4$ cluster. These changes are related to large variation in the SOC strength, which in turn can be explained by the different nature of the highest occupied molecular orbitals in the complexes with different charges. We speculate that electron transfer in rubredoxin, which occurred by changing the charge of the active site, could proceed through a nonadiabatic mechanism involving spin-forbidden transitions between electronic states with different spin multiplicities. Investigation of the possibility of such nonadiabatic spin-forbidden electron transfer is currently underway in our group.

Supporting Information.

The Supporting Information is available free of charge on the ACS Publications website at DOI: 10.1021/acs.jpca.6b07717. NA-TST

NA-TST rate constants for transitions between the spin states calculated using the weak coupling formula, geometries of the rubredoxin active site models and spin–orbit

coupling obtained with different levels of theory, adiabatic detachment energies, MECP geometries and twist angles, ROHF molecular orbital diagrams, atomic coordinates of the rubredoxin active site models.

Author Information

Corresponding Author

*S. A. Varganov. E-mail: svarganov@unr.edu. Phone: +1 (775) 784-1406.

Notes

The authors declare no competing financial interest.

References

(1)   Zanello, P. The Competition between Chemistry and Biology in Assembling Iron-Sulfur Derivatives. Molecular Structures and Electrochemistry. Part I. {Fe(S$^\gamma_{Cys}$)$_4$}. *Coord. Chem. Rev.* **2013**, *257*, 1777–1805.

(2)   Vicente, J. B.; Teixeira, M. Redox and Spectroscopic Properties of the Escherichia Coli Nitric Oxide-Detoxifying System Involving Flavorubredoxin and Its NADH-

Oxidizing Redox Partner. *J. Biol. Chem.* **2005**, *280*, 34599–34608.

(3)   Van Beilen, J. B.; Neuenschwander, M.; Smits, T. H. M.; Roth, C.; Balada, S. B.; Witholt, B. Rubredoxins Involved in Alkane Oxidation. *J. Bacteriol.* **2002**, *184*, 1722–1732.

(4)   Nolling, J.; Ishii, M.; Koch, J.; Pihl, T. D.; Reeve, J. N.; Thauer, R. K.; Hedderich, R. Characterization of a 45-kDa Flavoprotein and Evidence for a Rubredoxin, Two Proteins That Could Participate in Electron Transport from H_2 to CO_2 in Methanogenesis in Methanobacterium Thermoautotrophicum. *Eur. J. Biochem.* **1995**, *231*, 628–638.

(5)   Yoon, K. S.; Hille, R.; Hemann, C.; Tabita, F. R. Rubredoxin from the Green Sulfur Bacterium Chlorobium Tepidum Functions as an Electron Acceptor for Pyruvate Ferredoxin Oxidoreductase. *J. Biol. Chem.* **1999**, *274*, 29772–29778.

(6)   Chen, L.; Liu, M. Y.; LeGall, J.; Fareleira, P.; Santos, H.; Xavier, A. V. Rubredoxin Oxidase, a New Flavo-Hemo-Protein, Is the Site of Oxygen Reduction to Water by The "Strict Anaerobe" Desulfovibrio Gigas. *Biochem. Biophys. Res. Commun.*, **1993**, *193*, 100–105.

(7)   Ma, K.; Adams, M. W. W. A Hyperactive NAD(P)H: Rubredoxin Oxidoreductase from the Hyperthermophilic Archaeon Pyrococcus furiosus. *J. Bacteriol.* **1999**, *181*, 5530–5533.

(8)   Calderon, R. H.; García-Cerdán, J. G.; Malnoë, A.; Cook, R.; Russell, J. J.; Gaw, C.; Dent, R. M.; De Vitry, C.; Niyogi, K. K. A Conserved Rubredoxin Is Necessary for Photosystem II Accumulation in Diverse Oxygenic Photoautotrophs. *J. Biol. Chem.* **2013**, *288*, 26688–26696.

(9)   Liu, F.; Geng, J.; Gumpper, R. H.; Barman, A.; Davis, I.; Ozarowski, A.; Hamelberg, D.; Liu, A. An Iron Reservoir to the Catalytic Metal: The Rubredoxin Iron in an Extradiol Dioxygenase. *J. Biol. Chem.* **2015**, *290*, 15621–15634.

(10)   Luo, Y.; Niu, S.; Ichiye, T. Understanding Rubredoxin Redox Sites by Density Functional Theory Studies of Analogues. *J. Phys. Chem. A* **2012**, *116*, 8918–8924.

(11)   Tran, V. T.; Hendrickx, M. F. a. Molecular Structures for $FeS_4^{-/0}$ As Determined from an Ab Initio Study of the Anion Photoelectron Spectra.

J. Phys. Chem. **2013**, *117*, 3227-3234.

(12) Niu, S.; Wang, X.; Nichols, J. A.; Wang, L. S.; Ichiye, T. Combined Quantum Chemistry and Photoelectron Spectroscopy Study of the Electronic Structure and Reduction Potentials of Rubredoxin Redox Site Analogues. *J. Phys. Chem. A* **2003**, *107*, 2898–2907.

(13) Yang, X.; Wang, X. B.; Fu, Y. J.; Wang, L. S. On the Electronic Structure of [1Fe] Fe-S Complexes from Anionic Photoelectron Spectroscopy. *J. Phys. Chem. A* **2003**, *107*, 1703–1709.

(14) Swart, M.; Costas, M. *Spin States in Biochemistry and Inorganic Chemistry: General Introduction to Spin States*; Costas, M.; Swart, M., Eds.; 1 ed. JohnWiley & Sons, Ltd.: West Sussex, United Kingdom, 2015.

(15) Arantes, G. M.; Bhattacharjee, A.; Field, M. J. Homolytic Cleavage of Fe-S Bonds in Rubredoxin under Mechanical Stress. *Angew. Chem., Int. Ed.* **2013**, *52*, 8144–8146.

(16) Yson, R. L.; Gilgor, J. L.; Guberman, B. A.; Varganov, S. A. Protein Induced Singlet–triplet Quasidegeneracy in the Active Site of [NiFe]-Hydrogenase. *Chem. Phys. Lett.* **2013**, *577*, 138–141.

(17) Kaliakin, D. S.; Zaari, R. R.; Varganov, S. A. Effect of H_2 Binding on the Nonadiabatic Transition Probability between Singlet and Triplet States of the [NiFe]-Hydrogenase Active Site. *J. Phys. Chem. A* **2015**, *119*, 1066–1073.

(18) Lykhin, A. O.; Kaliakin, D. S.; dePolo, G. E.; Kuzubov, A. A.; Varganov, S. A. Nonadiabatic Transition State Theory: Application to Intersystem Crossings in the Active Sites of Metal-Sulfur Proteins. *Int. J. Quantum Chem.* **2016,** *116*, 750-761.

(19) Harvey, J. N. Spin-Forbidden Reactions: Computational Insight into Mechanisms and Kinetics. *WIREs Comput. Mol. Sci.* **2014**, *4*, 1–14.

(20) Cui, Q.; Morokuma, K.; Bowman, J. M. The Spin-Forbidden Reaction CH($^2\Pi$) + $N_2 \rightarrow$ HCN + N(^{4}S) Revisited. II. Ab Initio Study of the Potential Energy Surfaces. *Theor. Chem. Acc.* **1999**, *102*, 127-133.

(21) Perdew, J. P.; Burke, K.; Ernzerhof, M. Generalized Gradient Approximation Made Simple. *Phys. Rev. Lett.* **1996**, *77*, 3865–3868.

(22) Becke, A. D. Density-Functional Thermochemistry. III. The Role of Exact Exchange. *J. Chem. Phys.* **1993**, *98*, 5648-5652.

(23) Stephens, P. J.; Devlin, F. J.; Chabalowski, C. F.; Frisch, M. J. Ab Initio Calculations of Vibrational Absorption and Circular Dichroism Spectra Using Density Functional Force Field. *J. Phys. Chem.* **1994**, *98*, 11623–11627.

(24) Hertwig, R. H.; Koch, W. On the Parameterization of the Local Correlation Functional. What Is Becke-3-LYP? *Chem. Phys. Lett.* **1997**, *268*, 345–351.

(25) Iikura, H.; Tsuneda, T.; Yanai, T.; Hirao, K. A Long-Range Correction Scheme for Generalized-Gradient-Approximation Exchange Functionals. *J. Chem. Phys.* **2001**, *115*, 3540–3544.

(26) Tawada, Y.; Tsuneda, T.; Yanagisawa, S.; Yanai, T.; Hirao, K.; Tawada, Y.; Tsuneda, T.; Yanagisawa, S. A Long-Range-Corrected Time-Dependent Density Functional Theory. *J. Chem. Phys.* **2004**, *120*, 8425–8433.

(27) Hehre, W. J. Self-Consistent Molecular Orbital Methods. XII. Further Extensions of Gaussian-Type Basis Sets for Use in Molecular Orbital Studies of Organic Molecules. *J. Chem. Phys.* **1972**, *56*, 2257-2261.

(28) Francl, M. M. Self-Consistent Molecular Orbital Methods. XXIII. A Polarization-Type Basis Set for Second-Row Elements. *J. Chem. Phys.* **1982**, *77*, 3654-3665.

(29) Weigend, F.; Ahlrichs, R. Balanced Basis Sets of Split Valence, Triple Zeta Valence and Quadruple Zeta Valence Quality for H to Rn: Design and Assessment of Accuracy W. *Phys. Chem. Chem. Phys.* **2005**, *7*, 3297–3305.

(30) Lengsfield, B. H. On the Use of Corresponding Orbitals in the Calculation of Nonorthogonal Transition Moments. *J. Chem. Phys.* **1981**, *74*, 6849-6856.

(31) Schmidt, M. W.; Baldridge, K. K.; Boatz, J. A.; Elbert, S. T.; Gordon, M. S.; Jensen, J. H.; Koseki, S.; Matsunaga, N.; Nguyen, K. A.; Su, S. J. et al. General Atomic and Molecular Electronic Structure System.

J. Comput. Chem. **1993**, *14*, 1347–1363.

(32)   Gordon, M. S., Schmidt, M. W. Advances in Electronic Structure Theory: GAMESS a Decade Later. In *Theory and Applications of Computational Chemistry*; Dykstra C. E., Frenking, G., Kim, K. S., Scuseria, G. E., Eds.; Elsevier: Amsterdam, 2005; pp 1167–1189.

(33)   Werner, H.-J.; Knowles, P. J.; Knizia, G.; Manby, F. R.; Schütz, M. Molpro: A General-Purpose Quantum Chemistry Program Package. *Wiley Interdiscip. Rev. Comput. Mol. Sci.* **2012**, *2*, 242–253.

(34)   Werner, H.-J.; Knowles, P. J.; Knizia, G.; Manby, F. R.; Schütz, M.; Celani, P.; Korona, T.; Lindh, R.; Mitrushenkov, A.; Rauhut, G.; et al. MOLPRO, Version 2012.1, Package of Ab Initio Programs, 2012.

(35)   Lorquet, J. C.; Leyh-Nihant, B. Nonadiabatic Unimolecular Reactions. 1. A Statistical Formulation for the Rate Constants. *J. Phys. Chem.* **1988**, *92*, 4778–4783.

(36)   Harvey, J. N.; Aschi, M. Spin-Forbidden Dehydrogenation of Methoxy Cation: A Statistical View. *Phys. Chem. Chem. Phys.* **1999**, *1*, 5555–5563.

(37)   Heller, E. J.; Brown, R. C. Radiationless Transitions in a New Light. *J. Chem. Phys.* **1983**, *79*, 3336-3351.

(38)   Lorquet, J. C.; Leyh-Nihant, B. Nonadiabatic Unimolecular Reactions. 1. A Statistical Formulation for the Rate Constants. *J. Phys. Chem.* **1988**, *92*, 4778–4783.

(39)   Tully, J. C. Collision Complex Model for Spin Forbidden Reactions: Quenching of $O(^1D)$ by N_2. *J. Chem. Phys.* **1974**, *61*, 61-68.

(40)   Zahr, G. E.; Preston, R. K.; Miller W. H. Theoretical Treatment of Quenching in $O(^1D) + N_2$ Collisions. *J. Chem. Phys.* **1975**, *62*, 1127-1135.

(41)   Cui, Q.; Morokuma, K.; Bowman, J. M.; Klippenstein, S. J. The Spin-Forbidden Reaction $CH(^2\Pi)+N_2 \rightarrow HCN+N(^4S)$ Revisited. II. Nonadiabatic Transition State Theory and Application. *J. Chem. Phys.* **1999**, *110*, 9469-9482.

(42)   Miller, W. H.; Handy, N. C.; Adams, J. E. Reaction Path Hamiltonian for Polyatomic Molecules. *J. Chem. Phys.* **1980**, *72*, 99-112.

(43)   Baer, T.; Hase, W. L. *Unimolecular Reaction Dynamics: Theory and Experiments*; Oxford University Press: New York, 1995.

(44)   Green, N. J. B. Unimolecular Kinetics. Part 1: The Reaction Step; Elsevier Science: Amsterdam, The Netherlands, 2003.

(45)   Zaari, R. R.; Varganov, S. a. Nonadiabatic Transition State Theory and Trajectory Surface Hopping Dynamics: Intersystem Crossing Between States of SiH2. *J. Phys. Chem. A* **2015**, *119*, 1332-1338.

(46)   Landau, L. A Theory Of Energy Transfer. II. In *Collected Papers of L.D. Landau*; ter Haar, D., Ed.; Elsevier: Saint Louis, MO, 1965; pp. 63–66.

(47)   Zener, C. Non-Adiabatic Crossing of Energy Levels. Proc. R. Soc. London, Ser. A 1932, 137, 696−702

(48)   Wittig, C. The Landau−Zener Formula. *J. Phys. Chem. B* **2005**, *109*, 8428–8430.

(49)   Delos, J. B. On the Reactions of N_2 with O. *J. Chem. Phys.* **1973**, *59*, 2365-2369.

(50)   Fedorov, D. G.; Koseki, S.; Schmidt, M. W.; Gordon, M. S. Spin-Orbit Coupling in Molecules: Chemistry beyond the Adiabatic Approximation. *Int. Rev. Phys. Chem.* **2003**, *22*, 551–592.

(51)   Nikitin, E. E. Nonadiabatic Transition Near the Turning Point in Atomic Collisions. *Opt. Spectrosc.* **1961**, *11*, 246–248.

(52)   Fedorov, D. A.; Pruitt, S. R.; Keipert, K.; Gordon, M. S.; Varganov, S. A. Ab Initio Multiple Spawning Method for Intersystem Crossing Dynamics: Spin-Forbidden Transitions between $^3B_1$ and $^1A_1$ States of GeH_2. *J. Phys. Chem. A* **2016**, *120*, 2911–2919.

(53)   Curchod, B. F. E.; Rauer, C.; Marquetand, P.; González, L.; Martínez, T. J. Communication: GAIMS - Generalized Ab Initio Multiple Spawning for Both

Internal Conversion and Intersystem Crossing Processes. J. Chem. Phys. 2016, 144, 101102.

(54) Mai, S.; Marquetand, P.; González, L. A General Method to Describe Intersystem Crossing Dynamics in Trajectory Surface Hopping. *Int. J. Quantum Chem.* **2015**, *115*, 1215–1231.

(55) Granucci, G.; Persico, M.; Spighi, G. Surface Hopping Trajectory Simulations with Spin-Orbit and Dynamical Couplings. *J. Chem. Phys.* **2012**, *137*, 22A501.

(56) Jasper, A. W. Multidimensional Effects in Nonadiabatic Statistical Theories of Spin-Forbidden Kinetics: A Case Study of $^3O + CO \rightarrow CO_2$. *J. Phys. Chem. A* **2015**, *119*, 7339−7351.

(57) Goodrow, A.; Bell, A. T.; Head-Gordon, M. Are Spin-Forbidden Crossings a Bottleneck in Methanol Oxidation? *J. Phys. Chem. C* **2009**, *113*, 19361–19364.

(58) Kuki, A. Adiabaticity Factor for Electron Transfer in the Multimode Case: An Energy Velocity Perspective. *J. Phys. Chem.* **1993**, *97*, 13107–13116.

(59) Delcey, M. G.; Pierloot, K.; Phung, Q. M.; Vancoillie, S.; Lindh, R.; Ryde, U. Accurate Calculations of Geometries and Singlet-Triplet Energy Differences for Active-Site Models of [NiFe] Hydrogenase. *Phys. Chem. Chem. Phys.* **2014**, *16*, 7927–7938.

(60) Turro, N. J.; Ramamurthy, V.; Scaiano, J. C. *Modern Molecular Photochemistry of Organic Molecules*; University Science Books: Sausalito, CA, 2010.

Chapter V. Minimum Energy Crossing Point Search with the Fragment Molecular Orbital Method

Abstract

The nonadiabatic spin-forbidden electronic transitions are encountered in many important chemical processes, including catalytic reactions and electron transfer in the active sites of metal-sulfur proteins. The nonadiabatic transition state theory (NA-TST) offers a statistical approach to study the kinetics of nonadiabatic spin-forbidden transitions. The critical element of NA-TST is the finding of minimum energy crossing point (MECP), which plays the same role as transition state in the traditional transition state theory. In large complex systems, the MECP search is typically carried out on small models. For example, in our studies of spin-forbidden transitions in the metal-sulfur proteins we performed MECP search on the isolated active sites models without considering effects of the protein chains and the solvent molecules, which could be important. The size of the models used in the MECP search is limited by the size restrictions of the conventional electronic structure methods used to obtain the electronic energies and the energy gradients. In this work, we extend the applicability of the MECP search algorithm, and thus the applicability of NA-TST, to the large complex systems with thousands of atoms. To achieve this, we implement the MECP search algorithm for the fragment molecular orbital (FMO) method in the GAMESS suite of programs. We demonstrate the accuracy of the new FMO-MECP method on small models of the protein rubredoxin by comparing the FMO-MECP energy and geometry with the results obtained using the conventional MECP search method. We also demonstrate the scalability of the FMO gradient

calculations, a computational bottleneck of the MECP search method, on the 13,033 atom model of rubredoxin in water.

I. Introduction

Nonadiabatic processes involving the nonradiative transitions between different electronic states play important roles in different biologically and industrially important reactions. Examples include combustion,[1,2] reactions in the atmosphere and in interstellar space,[3,4] transition metal-based catalysis,[5] binding of small molecules to the active sites of metalloproteins,[6–9] visual perception[10,11] and the UV-light protective mechanisms in living organisms.[12–17]

If nonadiabatic processes involve the transitions between electronic states with different spin multiplicities, such transitions are called spin-forbidden transitions or intersystem crossings (ISC). The transitions between the electronic states with the same multiplicity are called internal conversions (IC).[12] Despite the fact that ICs were extensively studied over the last few decades, the ISCs received closer attention somewhat later.[18–20]

Description of ISC is possible with the statistical and molecular dynamical (MD) approaches. In the MD approach, one can account for multidimensional nature of the system, i.e. investigate the effects of multiple nuclear degrees of freedom on the transitions between the electronic states with different multiplicities. However, due to the computational demands, the applicability of MD is restricted to the description of ISC in relatively small systems, such as GeH_2[21], SiH_2[22] and CO_2[23] molecules. The alternative to computationally demanding MD simulations is the statistical nonadiabatic transition state

theory (NA-TST).[24–27] Unlike MD, which accounts for transitions between electronic states anywhere on potential energy surfaces (PES), NA-TST assumes that the transitions occur only at the minimum energy crossing point (MECP), which represents the minimum on the crossing seam between two PESs. This assumption significantly reduces the computational cost and makes NA-TST applicable to relatively large systems.[23,27]

The NA-TST was proved to be an efficient tool to describe the ISCs in systems such as acrylates[28], myoglobin,[29] and metal-sulfur proteins.[8,9,27,30] In our previous studies, we apply the NA-TST to the ISC kinetics in the active sites of ferredoxin,[27] [NiFe]-hydrogenase[8,9] and rubredoxin.[30] However, to achieve the more accurate description of the ISC kinetics in the active sites of metal-sulfur proteins it is important to account for the influence of the protein chains and the surrounding solvent molecules on the active site. Description of whole, or large part, of protein solvated by water molecules is impossible with conventional electronic structure methods and requires alternative methods. One such method is the hybrid quantum mechanical / molecular mechanical (QM/MM) approach in which the small part of the system, usually active site, is described with QM, while the surrounding protein chains and the solvent molecules are treated with MM.[31] One of the QM/MM challenges is the description of the interaction between the QM and MM regions.[31] Unlike the QM/MM approach, the fragment-based fully QM methods offer a uniform QM description of entire system, which is a more universal and potentially more accurate aproach.[32]

Among the fragment-based methods the fragment molecular orbital (FMO) method has been proven to be an especially useful tool for describing complex biological systems.[32] The FMO method, implemented in the quantum chemical package GAMESS,

has been successfully used to optimize molecular geometries corresponding to minima and transition states on PESs, and thus can be utilized for the conventional transition state theory (TST) rate calculations. The NA-TST rate calculations for nonadiabatic spin-forbidden transitions also require the ability to optimize the MECP geometry. Despite being available for conventional QM calculations, the MECP search algorithm has not been implemented for the FMO method. Here we report the implementation of new FMO-MECP search algorithm in GAMESS and demonstrate the application of this algorithm to study ISCs in the protein rubredoxin. The electronic structure methods and the MECP search algorithm for NA-TST are described in sections II and III, respectively. The implementation of the new FMO-MECP algorithm and its application to ISCs in rubredoxin are discussed in section IV. In subsection A of section IV, we demonstrate the FMO applicability to calculate the energy of the large rubredoxin model that includes the entire protein chain and surrounding water molecules. Subsection B describes the steps that were taken to combine the FMO method with the MECP search algorithm and discusses the scalability of the gradient calculations within FMO-MECP. Subsection C is focused on the validation of the new FMO-MECP algorithm by comparing the MECP energies and geometries for small rubredoxin models obtained with new and conventional algorithms. Concluding remarks and future outlook are presented in section V.

II. Computational Details

This study utilized multiple models of rubredoxin protein. Model 1, model 2 and model 3 contained 13033, 144 and 68 atoms, respectively (Figure 1a). The fragmentation

schemes of the FMO calculations for model 1, 2 and 3 were based on 844, 9 and 5 fragments, respectively (Figure 1b). The geometry of model 1 was based on the structure of rubredoxin that was obtained with macromolecular neutron crystallography (PDB 4K9F)[33] and solvated with the Chimera software[34] using the TIP4 solvation model.[35] Models 2 and 3 were made by reducing the size of model 1.
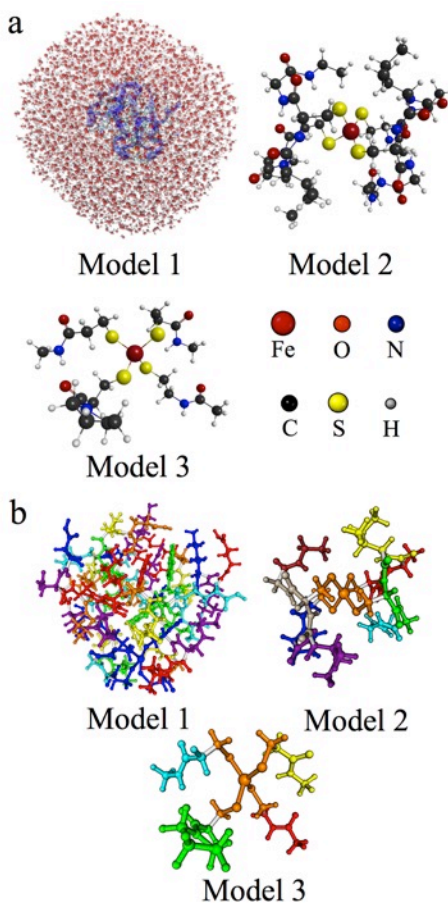
Figure 1. (a) Three models of rubredoxin protein used in the study. (b) FMO fragmentation schemes for the three models. Model 1 contains 815 fragments of solvent with five water molecules in each, and one water fragment with four water molecules. Water molecules are omitted from the picture for clarity.

The total charge of all models was set to -1 to keep the metal center in the formal oxidation state Fe(III). The focus of the study was on the lowest energy quartet and sextet

electronic states because our previous study on the isolated active site model indicated the presence of the intersection between these electronic states.[30] The single point energy calculations of quartet electronic spin state of rubredoxin were performed using model 1, FMO1 method, LC-BPBE functional,[36–38] and def2-SV(P) basis set.[39] The scalability of the FMO MECP code was tested with model 2, FMO2-UHF method and 3-21G basis set.[40–42] Finally, the FMO-MECP accuracy was tested by performing the MECP search on model 3 using the FMO2-LC-BPBE method with 6-31G basis set[43,44] and comparing the obtained MECP geometry to the one optimized with the conventional MECP algorithm using the same level of theory (LC-BPBE/6-31G). All calculations were performed in the GAMESS suite of programs.[45,46]

III. Theoretical Details

The detailed description of NA-TST is provided in our recent review.[27] Briefly, the microcanonical nonadiabatic transition rate constant, $k(E)$, for the transition between the electronic spin states with different multiplicity is,[18,47–52]

$$k(E) = \frac{N^*_{MECP}(E)}{h\rho_R(E)}$$

(1)

Here h is the Planck constant, $\rho_R(E)$ is the density of rovibrational states of the reactant, and $N^*_{MECP}(E)$ is the effective number of rovibrational states at the MECP that could be written as,

$$N^*_{MECP}(E) = \int_0^E \rho_{MECP}(E - \varepsilon_\perp)P_{trans}(\varepsilon_\perp)d\varepsilon_\perp$$

(2)

Here $\rho_{MECP}(E)$ is the density of rovibrational states at the MECP, E is the total internal energy of the system, $\varepsilon_\perp$ is the component of internal energy along the reaction coordinate that is orthogonal to the crossing seam, and $P_{trans}(\varepsilon_\perp)$ is the transition probability between two electronic states. As seen from eqs 1 and 2, the MECP properties plays a key role in NA-TST, thus the calculation of $k(E)$ requires the MECP geometry.

In the GAMESS package, the MECP search relies on the energies of two electronic spin states (E1, E2) and their energy gradient components (x, y and z) for each atom [GA(I), GB(I)] at a given geometry. These four scalar parameters are used to form a perpendicular *[PERPG(I)]*, a parallel *[PARG(I)]* and an effective [*G(I)*] gradients.

$$PERPG(I) = GA(I) - GB(I)$$

$$PARG(I) = GA(I) - \frac{PERPG(I)}{\sqrt{\sum_{i=1}^{N} PERPG(I)^2}} \times \frac{\sum_{i=1}^{N} GA(I) \times PERPG(I)}{\sqrt{\sum_{i=1}^{N} PERPG(I)^2}}$$

$$G(I) = (E1 - E2) \cdot PEPRG(I) + PARG(I) \tag{3}$$

The gradients *G(I)* and *PARG(I)* are used to satisfy the criteria of staying on the crossing seam, and finding the minimum on the crossing seam, respectively. Both gradients are used to determine the next molecular geometry during the MECP optimization procedure, and become zero at the MECP. The three- and two-dimensional representations of the crossing PESs with parallel and perpendicular gradients at MECP are shown on Figure 2.
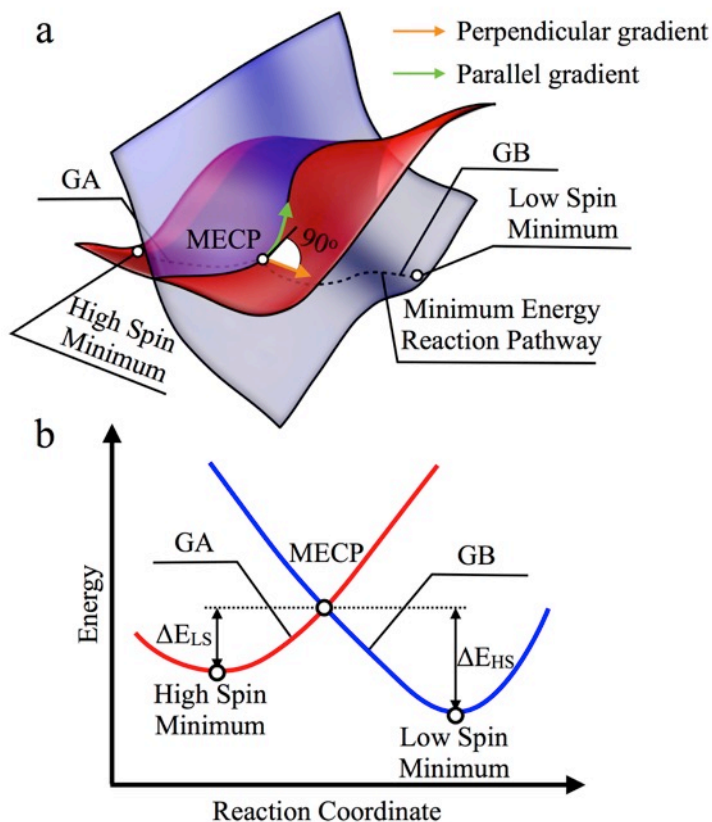
Figure 2. Two representations of the crossing PES of electronic states with different spin multiplicities. (a) The three-dimensional representation showing the perpendicular and parallel gradients, as defined in GAMESS. (b) The two-dimensional representation of along the minimum energy reaction pathway.

The gradients defined in GAMESS are connected to the gradients f and g commonly used in the literature through the following equations,[27,53–59]

$$f = (E1 - E2) \times PERPG(I)$$

$$g = PARG(I)$$

(4)

IV. Results and Discussion

A. Applicability of FMO to Large Rubredoxin Models

In order to test the applicability of FMO to nonadiabatic transitions in large models of rubredoxin we performed single point energy calculations with model 1, which includes the entire protein (796 atoms) and 4079 water molecules (Figure 3a). The model is partitioned into 844 fragments, including 28 fragments that represent the protein 815 fragments with five water molecules and one fragment with four water molecules describing the solvation shell. The active site fragment has the total charge of -1 and contains the Fe(III) metal center surrounded by four cysteine residues. The protein chain is fragmented in such a way that each fragment contains two amino acids. This model represents a good test case for applicability of the FMO method to ISC in the rubredoxin active site, because it includes both protein chain and solvent shell. Moreover, the fragment sizes in this model ensure approximately equal computational cost for each single fragment energy calculation. This is an important requirement for achieving a good load balance between computer cores in the massively parallel FMO calculations. The single point energy calculations on model 1 on 4096, 8192, 16384, 32768, 65536 and 131072 computer cores distributed between the 128 groups demonstrated a reasonable scalability with number of computer cores (Figure 3b).
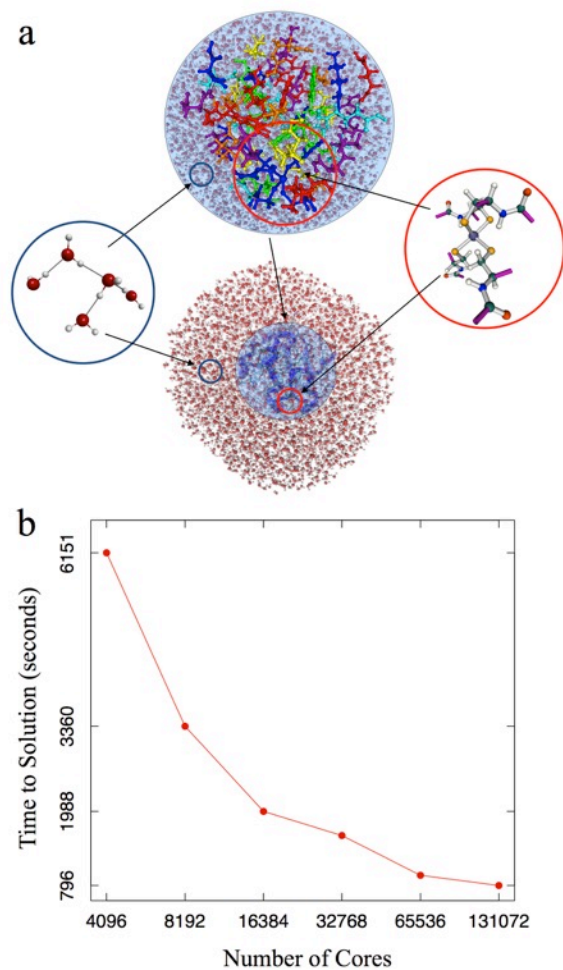
Figure 3. (a) Detailed representation of model 1 showing the structure of active site fragment, water fragments, and the solvation shell. (b) The scaling curve showing the time for one energy calculation as a function of the number of computer cores. Calculations are performed with the FMO1-LC-BPBE/def2-SV(P) level of theory.

As seen from Figure 3b, the energy calculations on model 1 efficiently scale to 16384 cores, but the efficiency is significantly reduced for the larger number of computer cores. However, these results could be improved by application of heuristic load balancing approach, as was previously demonstrated by Alexeev *et. al* in the FMO calculations on ubiquitin.[60]

B. FMO-MECP Algorithm

As could be seen from the eqs 3 and 4, the MECP search requires the energies of two electronic states [E1, E2], and the energy gradients for these states [GA(I), GB(I)]. The parallel, perpendicular and effective gradients used in the MECP search are formed from these state energies and gradients quantities, thus the FMO-MECP search algorithm requires the FMO energies and gradients to be passed to the MECP subroutine (Figure 4).
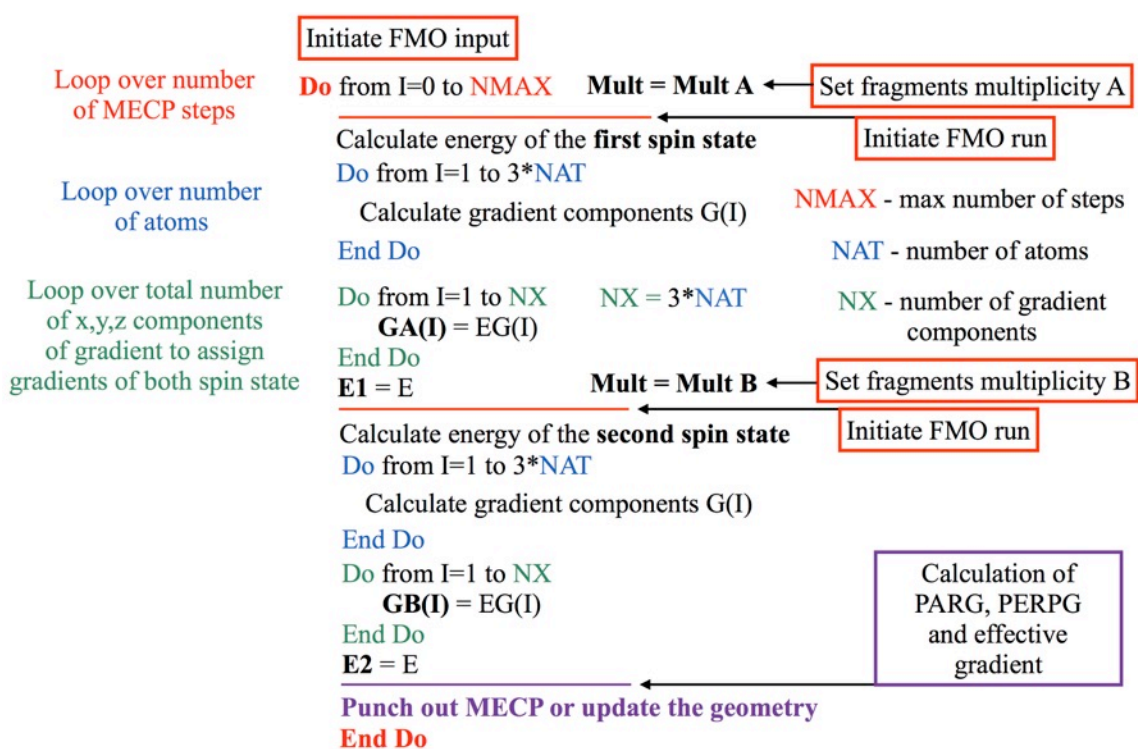
Figure 4. The scheme of the FMO-MECP search algorithm.

In order to make MECP search possible with the FMO method, we introduced the following modifications into the existing MECP and FMO subroutines in GAMESS. First, we enable communication between the FMO input subroutine and the MECP subroutine, so that the FMO-MECP search algorithm could utilize the standard GAMESS

FMO input format. Second, we enabled the assignment of multiplicities for the first and second electronic spin states as the arrays of multiplicities for each individual fragments. Finally, we enable the calculations of energies and gradients of first and second electronic spin states with FMO.

To test the scalability of the FMO-MECP calculations we performed gradient calculations for the quartet electronic state of rubredoxin with Fe(III) oxidation state in the active site (Figure 5). The calculations of gradient components are the most time-consuming step of the FMO-MECP algorithm and represent the computational bottleneck The gradient calculations were carried out on model 2 containing 144 atoms and nine FMO fragments. The active site fragment contained the Fe(III) center surrounded by four -SCH_2- groups. Other eight fragments contained the residues nearest to the metal center. Calculations utilized 128, 256, 512, 1024 and 2048 computer cores with dynamic load balancing between eight CPU groups.
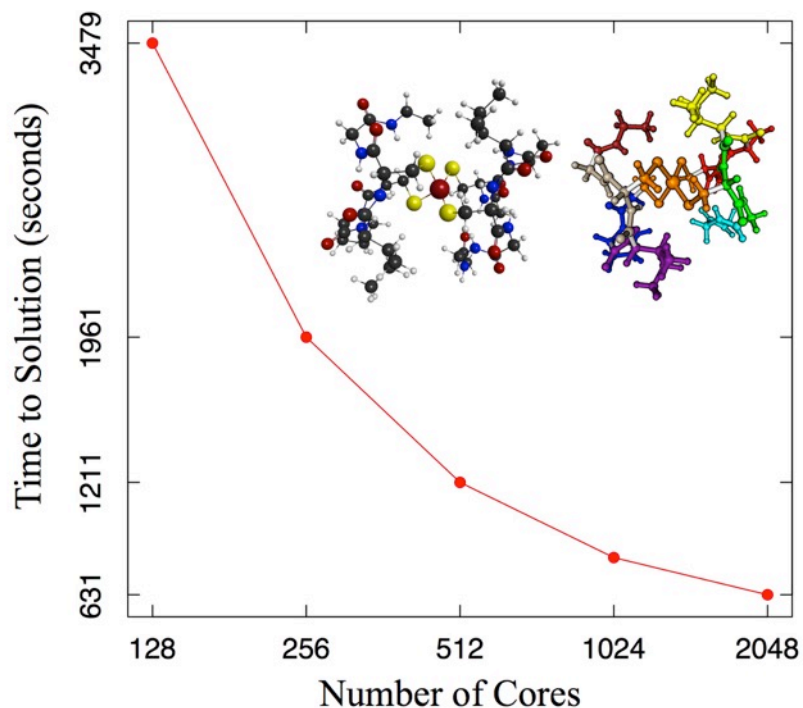
Figure 5. Time for gradient calculations as a function of number of computer cores. Calculations were performed with the FMO2-UHF/3-21G level of theory.

The gradient calculations on model 2 demonstrated that the FMO-MECP calculations scale well, and therefore can be performed on large protein models utilizing modern massively parallel computers.

C. Validation of New FMO-MECP Algorithm

To compare the accuracy of new FMO-MECP search algorithm with conventional MECP search we performed the MECP geometry optimization for quartet/sextet state intersection on model 3 with the FMO2-LC-BPBE/6-31G and LC-BPBE/6-31G levels of theory. The root mean square deviation (RMSD) between the obtained geometries is 0.0479 Å (Figure 6a), which indicates a close resemblance between the FMO-MECP and the conventional MECP structures. To compare the relative MECP energies obtained

with our FMO-MECP and the conventional MECP algorithms we also performed the FMO equilibrium geometry optimization for quartet and sextet states. The energies of the MECP structures with respect to quartet and sextet minima obtained with conventional DFT and FMO-DFT are shown in Figure 6b.
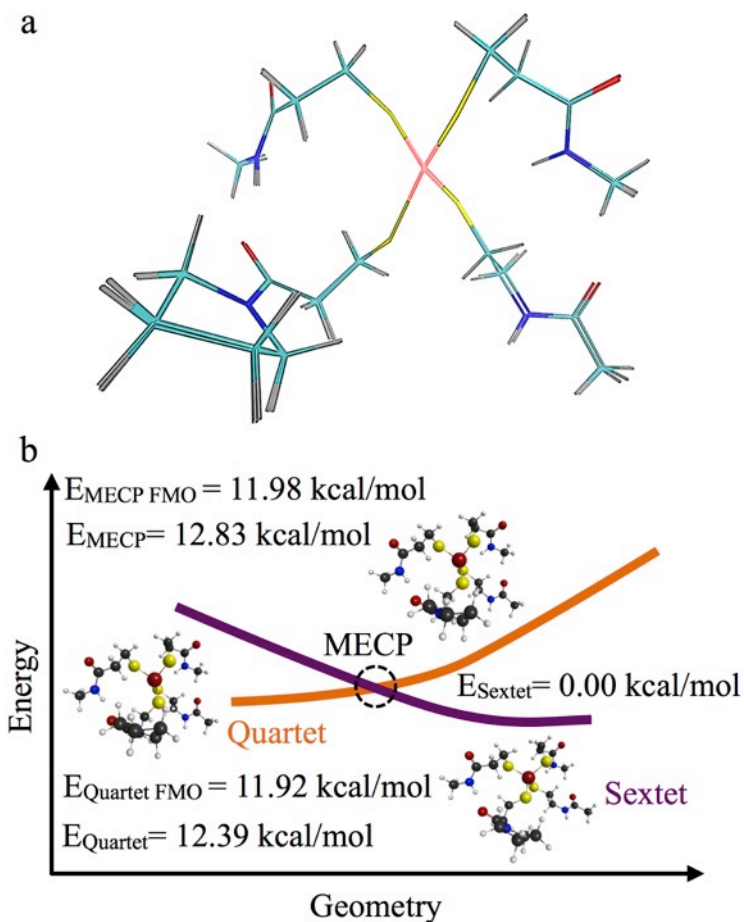
Figure 6. Comparison between the conventional MECP and FMO-MECP geometries. (a) An overlap between the MECP and FMO-MECP geometries. (b) The energies of quartet/sextet minima and MECP obtained with FMO-DFT and conventional DFT methods. The calculations were performed at the FMO2-LC-BPBE/6-31G and LC-BPBE/6-31G levels of theory.

As can be seen from Figure 6b, the relative energies obtained with DFT and FMO-DFT are in close agreement with each other. The differences between the DFT and

FMO-DFT energies do not exceed 0.85 kcal/mol. In our previous paper we demonstrated that the transitions between electronic spin states of rubredoxin are mediated by changes of torsion angles α, β and γ.[30] We compared the values for these angles obtained with the conventional MECP and FMO-MECP calculations to determine the effect of fragmentation on the torsion angles of active site (Figure 7).
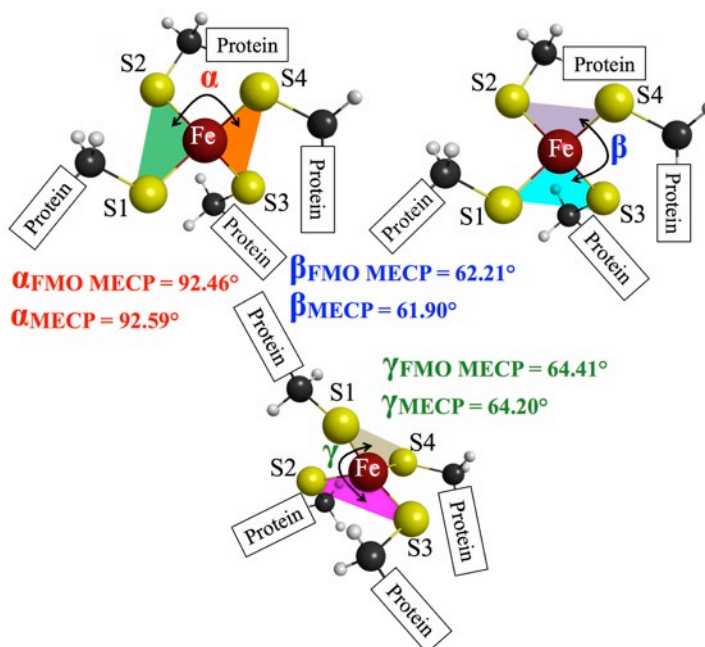
Figure 7. Torsion angles of Fe(III) rubredoxin active site at the MECP between the quartet and sextet electronic states. The values of torsion angles are obtained with the conventional MECP and FMO-MECP algorithms. The calculations were performed at the FMO2-LC-BPBE/6-31G and LC-BPBE/6-31G levels of theory.

The comparison of the MECP torsion angles obtained with the FMO-DFT and conventional DFT indicates the differences that do not exceed 0.31°, which means that FMO-MECP can accurately predict the geometrical parameters that play important role in the ISC kinetics.

V. Conclusions

In this work, we investigated the applicability of the FMO method to ISC in large complex systems, such as the protein rubredoxin. We implemented a new computational algorithm in the GAMESS suite of programs that enabled to optimize the MECP structure using the FMO method. We demonstrated that the FMO1-LC-BPBE/def2-SV(P) energy calculations on the full protein model of rubredoxin solvated by water (13033 atoms) could be successfully scaled up to 131,072 computer cores, which proves the usefulness of FMO as the tool to study ISC in large complex systems. We demonstrated that the gradient calculations, a computational bottleneck step the MECP search algorithm, can be scaled to 2048 computer cores by performing test calculations on the rubredoxin model with 144 atoms at the FMO2-UHF/3-21G level of theory.

The newly developed FMO-MECP search algorithm was compared to conventional MECP search with calculations carried out at the FMO2-LC-BPBE/6-31G and LC-BPBE/6-31G levels of theory on a small rubredoxin model. The FMO-MECP optimized geometry reproduces the conventional MECP geometry with small RMSD of 0.0479 Å. We also demonstrated that the relative energy of the quartet/sextet MECP obtained with FMO2-LC-BPBE/6-31G and LC-BPBE/6-31G levels of theory are within 0.85 kcal/mol of each other. Finally, we compared the values of torsion angles α, β and γ at MECP geometries obtained with the conventional and FMO calculations. As shown in our previous study these torsion angles play an important role in the ISC in the active site of rubredoxin.[30] The differences between the conventional and FMO values for α, β and γ are not exceeding 0.31°, which, in addition to relatively small RMSD, confirms the excellent agreement between the conventional and FMO-MECP geometries.

The newly developed FMO-MECP algorithm could be used to search for MECP geometries in the large complex systems that were previously out of reach for conventional electronic structure calculations. The use of large models to study the ISC kinetics in complex systems, such as rubredoxin and other metal-sulfur proteins, could provide a better understanding of the biological processes involving the nonadiabatic transitions between the electronic states with different spin multiplicities.

References

(1)   Jasper, A. W.; Dawes, R. Non-Born-Oppenheimer Molecular Dynamics of the Spin-Forbidden Reaction $O(^3P) + CO(X^1\sum{}^+) \rightarrow CO_2(X^1\sum{}_g^+)$. *J. Chem. Phys.* **2013**, *139*.

(2)   Balucani, N.; Leonori, F.; Casavecchia, P.; Fu, B.; Bowman, J. M. Crossed Molecular Beams and Quasiclassical Trajectory Surface Hopping Studies of the Multichannel Nonadiabatic O (^3P) + Ethylene Reaction at High Collision Energy. *J. Phys. Chem. A* **2015**, *119*, 12498−12511.

(3)   Maeda, S.; Taketsugu, T.; Ohno, K.; Morokuma, K. From Roaming Atoms to Hopping Surfaces: Mapping Out Global Reaction Routes in Photochemistry. *J. Am. Chem. Soc.* **2015**, *137*, 3433–3445.

(4)   Ahmadvand, S.; Zaari, R. R.; Varganov, S. A. Spin-Forbidden and Spin-Allowed Cyclopropenone (c-H_2C_3O) Formation in Interstellar Medium. *Astrophys. J.* **2014**, *795*, 1–5.

(5)   Goodrow, A.; Bell, A. T.; Head-Gordon, M. Are Spin-Forbidden Crossings a Bottleneck in Methanol Oxidation? *J. Phys. Chem. C* **2009**, *113*, 19361−19364.

(6)   Strickland, N.; Harvey, J. N. Spin-Forbidden Ligand Binding to the Ferrous-Heme Group: Ab Initio and DFT Studies. *J. Phys. Chem. B* **2007**, *111*, 841–852.

(7)   Alcantara, R. E.; Xu, C.; Spiro, T. G.; Guallar, V. A Quantum-Chemical Picture of Hemoglobin Affinity. *Proc. Natl. Acad. Sci.* **2007**, *104*, 18451–18455.

(8)   Yson, R. L.; Gilgor, J. L.; Guberman, B. A.; Varganov, S. A. Protein Induced Singlet–triplet Quasidegeneracy in the Active Site of [NiFe]-Hydrogenase. *Chem. Phys. Lett.* **2013**, *577*, 138–141.

(9)   Kaliakin, D. S.; Zaari, R. R.; Varganov, S. A. Effect of H_2 Binding on the Nonadiabatic Transition Probability between Singlet and Triplet States of the [NiFe]-Hydrogenase Active Site. *J. Phys. Chem. A* **2015**, *119*, 1066–1073.

(10)   Santoro, F.; Ferre, N.; Olivucci, M.; Frutos, L. M.; Andrunio, T. Tracking the Excited-State Time Evolution of the Visual Pigment with Multiconfigurational Quantum Chemistry. *Proc. Natl. Acad. Sci.* **2007**, *104*, 7764–7769.

(11)   Schoenlein, R. W.; Peteanu, L. A.; Mathies, R. .; Shank, C. V. The First Step in Vision : Femtosecond Isomerization of Rhodopsin. *Science.* **1991**, *254*, 5030.

(12)   Mai, S.; Marquetand, P.; González, L. A General Method to Describe Intersystem Crossing Dynamics in Trajectory Surface Hopping. *Int. J. Quantum Chem.* **2015**, *115*, 1215–1231.

(13)   Crespo-Hernandez, C. E.; Cohen, B.; Hare, P. M.; Kohler, B. Ultrafast Excited-State Dynamics in Nucleic Acids. *Chem. Rev.* **2004**, *104*, 1977–2019.

(14)   Weinkauf, R.; Schermann, J.; Vries, M. S. De; Kleinermanns, K. Molecular Physics of Building Blocks of Life under Isolated or Defined Conditions. *Eur. Phys. J. D* **2002**, *20*, 309–316.

(15)   Stephansen, A. B.; Brogaard, R. Y.; Kuhlman, T. S.; Klein, L. B.; Christensen, J. B.; Sølling, T. I. Surprising Intrinsic Photostability of the Disulfide Bridge Common in Proteins. *J. Am. Chem. Soc.* **2012**, *134*, 20279–20281.

(16)   Vries, M. S. De; Hobza, P. Gas-Phase Spectroscopy of Biomolecular Building Blocks. *Annu. Rev. Phys. Chem.* **2007**, *58*, 585–612.

(17)   Pe, M.; Lucas, B.; Barat, M.; Fayeton, J. A. Mechanisms of UV Photodissociation of Small Protonated Peptides. *J. Phys. Chem. A* **2010**, *114*, 3147–3156.

(18)   Harvey, J. N. Spin-Forbidden Reactions: Computational Insight into Mechanisms and Kinetics. *Wiley Interdiscip. Rev. Comput. Mol. Sci.* **2014**, *4*, 1–14.

(19)   Marian, C. M. Spin-Orbit Coupling and Intersystem Crossing in Molecules. *Wiley Interdiscip. Rev. Comput. Mol. Sci.* **2012**, *2*, 187–203.

(20)   Mai, S.; Marquetand, P.; González, L. A General Method to Describe Intersystem Crossing Dynamics in Trajectory Surface Hopping. *Int. J. Quantum Chem.* **2015**, *115*, 1215–1231.

(21)   Fedorov, D. A.; Pruitt, S. R.; Keipert, K.; Gordon, M. S.; Varganov, S. A. Ab Initio Multiple Spawning Method for Intersystem Crossing Dynamics: Spin-Forbidden Transitions between $^3B_1$ and $^1A_1$ States of GeH_2.

J. Phys. Chem. **2016**, *120*, 2911–2919.

(22) Zaari, R. R.; Varganov, S. a. Nonadiabatic Transition State Theory and Trajectory Surface Hopping Dynamics: Intersystem Crossing Between States of SiH_2. *J. Phys. Chem. A* **2015**, *119*, 1332–1338.

(23) Jasper, A. W. Multidimensional Effects in Nonadiabatic Statistical Theories of Spin-Forbidden Kinetics: A Case Study of $^3O + CO \rightarrow CO_2$. *J. Phys. Chem. A* **2015**, *119*, 7339−7351.

(24) Lorquet, J. C.; Leyh-Nihant, B. Nonadiabatic Unimolecular Reactions. 1. A Statistical Formulation for the Rate Constants. *J. Phys. Chem.* **1988**, *92*, 4778–4783.

(25) Harvey, J. N.; Aschi, M. Spin-Forbidden Dehydrogenation of Methoxy Cation: A Statistical View. *Phys. Chem. Chem. Phys.* **1999**, *1*, 5555–5563.

(26) Harvey, J. N. Spin-Forbidden Reactions: Computational Insight into Mechanisms and Kinetics. *WIREs Comput. Mol. Sci.* **2014**, *4*, 1–14.

(27) Lykhin, A. O.; Kaliakin, D. S.; DePolo, G. E.; Kuzubov, A. A.; Varganov, S. A. Nonadiabatic Transition State Theory: Application to Intersystem Crossings in the Active Sites of Metal-Sulfur Proteins. *Int. J. Quantum Chem.* **2016**, *116*, 750–761.

(28) Liu, S.; Srinivasan, S.; Tao, J.; Grady, M. C.; Soroush, M.; Rappe, A. M. Modeling Spin-Forbidden Monomer Self-Initiation Reactions in Spontaneous Free-Radical Polymerization of Acrylates and Methacrylates. *J. Phys. Chem. A* **2014**, *118*, 9310−9318.

(29) Harvey, J. N. Understanding the Kinetics of Spin-Forbidden Chemical Reactions. *Phys. Chem. Chem. Phys.* **2007**, *9*, 331–343.

(30) DePolo, G. E.; Kaliakin, D. S.; Varganov, S. A. Spin-Forbidden Transitions between Electronic States in the Active Site of Rubredoxin. *J. Phys. Chem. A* **2016**, *120*, 8691–8698.

(31) Duarte, F.; Amrein, B. A.; Blaha-Nelson, D.; Kamerlin, S. C. L. Recent Advances in QM / MM Free Energy Calculations Using Reference Potentials. *Biochim. Biophys. Acta* **2015**, *1850*, 954–965.

(32) Gordon, M. S.; Fedorov, D. G.; Pruitt, S. R.; Slipchenko, L. V. Fragmentation Methods: A Route to Accurate Calculations on Large Systems. *Chem. Rev.* **2012**, *112*, 632–672.

(33) Meilleur, F.; Munshi, P.; Robertson, L.; Stoica, A. D.; Crow, L.; Kovalevsky, A.;

Koritsanszky, T.; Chakoumakos, B. C.; Blessing, R.; Myles, D. A. A. The IMAGINE Instrument: First Neutron Protein Structure and New Capabilities for Neutron Macromolecular Crystallography. *Acta Crystallogr. Sect. D Biol. Crystallogr.* **2013**, *69*, 2157–2160.

(34)   Pettersen, E. F.; Goddard, T. D.; Huang, C. C.; Couch, G. S.; Al., E. UCSF Chimera - a Visualization System for Exploratory Research and Analysis. *J. Comput. Chem.* **2004**, *25*, 1605−1612.

(35)   Horn, H. W.; Swope, W. C.; Pitera, J. W.; Madura, J. D.; Dick, T. J.; Hura, G. L.; Head-gordon, T. Development of an Improved Four-Site Water Model for Biomolecular Simulations : TIP4P-Ew. *J. Chem. Phys.* **2004**, *120*, 9665–9678.

(36)   Iikura, H.; Tsuneda, T.; Yanai, T.; Hirao, K. A Long-Range Correction Scheme for Generalized-Gradient-Approximation Exchange Functionals. *J. Chem. Phys.* **2001**, *115*, 3540–3544.

(37)   Becke, A. D. Density-Functional Exchange-Energy Approximation with Correct Asymptotic Behavior. *Phys. Rev. A* **1988**, *38*, 3098–3100.

(38)   Perdew, J. P.; Burke, K.; Ernzerhof, M. Generalized Gradient Approximation Made Simple. *Phys. Rev. Lett.* **1996**, *77*, 3865–3868.

(39)   Weigend, F. Accurate Coulomb-Fitting Basis Sets for H to Rn. *Phys. Chem. Chem. Phys.* **2006**, *22*, 1057−1065.

(40)   Binkley, J. S.; Pople, J. A.; Hehre, W. J. Self-Consistent Molecular Orbital Methods. 21. Small Split-Valence Basis Sets for First-Row Elements. *J. Am. Chem. Soc.* **1979**, *102*, 939–947.

(41)   Gordon, M. S.; Binkley, J. S.; Pople, J. A.; Pietro, I. W. J.; Hehre, W. J. Self-Consistent Molecular-Orbital Methods. 22. Small Split-Valence Basis Sets for Second-Row Elements. *J. Am. Chem. Soc.* **1982**, *2657*, 2797–2803.

(42)   Dobbs, K. D.; Hehre, W. J. Molecular Orbital Theory of the Properties of Inorganic and Organometallic Compounds 4. Extended Basis Sets for Third-and Fourth-Row, Main-Group Elements. *J. Comput. Chem.* **1986**, *7*, 1986.

(43)   Ditchfield, R.; Hehre, W. J.; Pople, J. A. Self-Consistent Molecular-Orbital Methods . IX . An Extended Gaussian-Type Basis for Molecular-Orbital Studies of Organic Molecules. *J. Chem. Phys.* **1971**, *54*, 724–728.

(44)   Rassolov, V. A.; Pople, J. A.; Ratner, M. A.; Windus, T. L.; Rassolov, V. A.; Pople, J. A.; Ratner, M. A.; Windus, T. L. 6-31G* Basis Set for Atoms K through Zn. *J. Chem. Phys.* **2003**, *109*, 1223−1229.

(45) Schmidt, M. W.; Baldridge, K. K.; Boatz, J. A.; Elbert, S. T.; Gordon, M. S.; Jensen, J. H.; Koseki, S.; Matsunaga, N.; Nguyen, K. A.; Su, S. J. et al. General Atomic and Molecular Electronic Structure System. *J. Comput. Chem.* **1993**, *14*, 1347–1363.

(46) Gordon, M. S.; Schmidt, M. W. Advances in Electronic Structure Theory: GAMESS a Decade Later. In *Theory and Applications of Computational Chemistry*; Dykstra C.E.; Frenking G.; Kim K.S.; Scuseria G.E., Eds.; Elsevier: Amsterdam, 2005; pp. 1167–1189.

(47) Harvey, J. N.; Aschi, M. Spin-Forbidden Dehydrogenation of Methoxy Cation: A Statistical View. *Phys. Chem. Chem. Phys.* **1999**, *1*, 5555–5563.

(48) Heller, E. J.; Brown, R. C. Radiationless Transitions in a New Light. *J. Chem. Phys.* **1983**, *79*, 3336.

(49) Lorquet, J. C.; Leyh-Nihant, B. Nonadiabatic Unimolecular Reactions. 1. A Statistical Formulation for the Rate Constants. *J. Phys. Chem.* **1988**, *92*, 4778–4783.

(50) Tully, J. C. Collision Complex Model for Spin Forbidden Reactions: Quenching of $O(^1D)$ by N_2. *J. Chem. Phys.* **1974**, *61*, 61.

(51) Zahr, G. E.; Preston, R. K.; W.H., M. Theoretical Treatment of Quenching in $O(^1D) + N_2$ Collisions. *J. Chem. Phys.* **1975**, *62*, 1127–1135.

(52) Cui, Q.; Morokuma, K.; Bowman, J. M.; Klippenstein, S. J. The Spin-Forbidden Reaction $CH(^2\Pi)+N_2 \rightarrow HCN+N(^4S)$ Revisited. II. Nonadiabatic Transition State Theory and Application. *J. Chem. Phys.* **1999**, *110*, 9469.

(53) Yarkony, D. R. Systematic Determination of Intersections of Potential Energy Surfaces Using a Lagrange Multiplier Constrained Procedure. *J. Phys. Chem.* **1993**, *97*, 4407–4412.

(54) Harvey, J. N.; Aschi, M.; Schwarz, H.; Koch, W. The Singlet and Triplet States of Phenyl Cation. A Hybrid Approach for Locating Minimum Energy Crossing Points between Non-Interacting Potential Energy Surfaces. *Theor. Chem. Acc.* **1998**, *99*, 95–99.

(55) Bearpark, M. J.; Robb, M. A.; Bernhard Schlegel, H. A Direct Method for the Location of the Lowest Energy Point on a Potential Surface Crossing. *Chem. Phys. Lett.* **1994**, *223*, 269–274.

(56) Koga, N.; Morokuma, K. Determination of the Lowest Energy Point on the Crossing Seam between Two Potential Surfaces Using the Energy Gradient.

Chem. Phys. Lett. **1985**, *119*, 371–374.

(57)   Yarkony, D. R. Electronic Structure Aspects of Nonadiabatic Processes in Polyatomic Systems. In *Modern Electronic Structure Theory*; Yarkony, D. R., Ed.; World Scientific: Singapore, 1995; pp. 642–721.

(58)   Farazdel, A.; Dupuis, M. On the Determination of the Minimum on the Crossing Seam of Two Potential Energy Surfaces. *J. Comput. Chem.* **1991**, *12*, 276–282.

(59)   Chachiyo, T.; Rodriguez, J. H. A Direct Method for Locating Minimum-Energy Crossing Points (MECPs) in Spin-Forbidden Transitions and Nonadiabatic Reactions. *J. Chem. Phys.* **2005**, *123*, 94711.

(60)   Alexeev, Y.; Mahajan, A.; Leyffer, S.; Fletcher, G.; Fedorov, D. G. Heuristic Static Load-Balancing Algorithm Applied to the Fragment Molecular Orbital Method. In *International Conference for High Performance Computing, Networking, Storage and Analysis, SC*; Salt Lake City, Utah, USA, 2012.

Chapter VI. 3D Printed Potential and Free Energy Surfaces for Teaching Fundamental Concepts in Physical Chemistry

Danil S. Kaliakin, Ryan R. Zaari, Sergey A. Varganov

Abstract

Teaching fundamental physical chemistry concepts such as the potential energy surface, transition state, and reaction path is a challenging task. The traditionally used oversimplified 2D representation of potential and free energy surfaces makes this task even more difficult and often confuses students. We show how this 2D representation can be expanded to more realistic potential and free energy surfaces by creating surface models using 3D printing technology. The printed models include potential energy surfaces for the hydrogen exchange reaction and for rotations of methyl groups in 1-fluoro-2-methylpropene calculated using quantum chemical methods. We also present several model surfaces created from analytical functions of two variables. These models include a free energy surface for protein folding, and potential energy surfaces for a linear triatomic molecule and surface adsorption, as well as simple double minimum, quadruple minimum, and parabolic surfaces. We discuss how these 3D models can be used in teaching different chemical kinetics, dynamics, and vibrational spectroscopy concepts including the potential energy surface, transition state, minimum energy reaction path, reaction trajectory, harmonic frequency, and anharmonicity.

Keywords

Upper-Division Undergraduate, Physical Chemistry, Hands-On Learning / Manipulatives, Quantum Chemistry, Kinetics, Molecular Mechanics / Dynamics, Spectroscopy.

I. Introduction

Understanding how chemical reactions occur is the central goal of chemistry. Undergraduate students are exposed to the basic concepts of reaction kinetics and dynamics in general chemistry courses. The mastery of these topics is critical for academic success not only in freshman chemistry but also in advanced chemistry courses such as organic, inorganic, and physical chemistry. Many of the concepts related to chemical kinetics and dynamics are abstract and difficult for students to visualize.[1–3] Traditionally, the path of a chemical reaction is depicted by a 2D curve representing the potential energy as a function of a single reaction coordinate (Figure 1a).
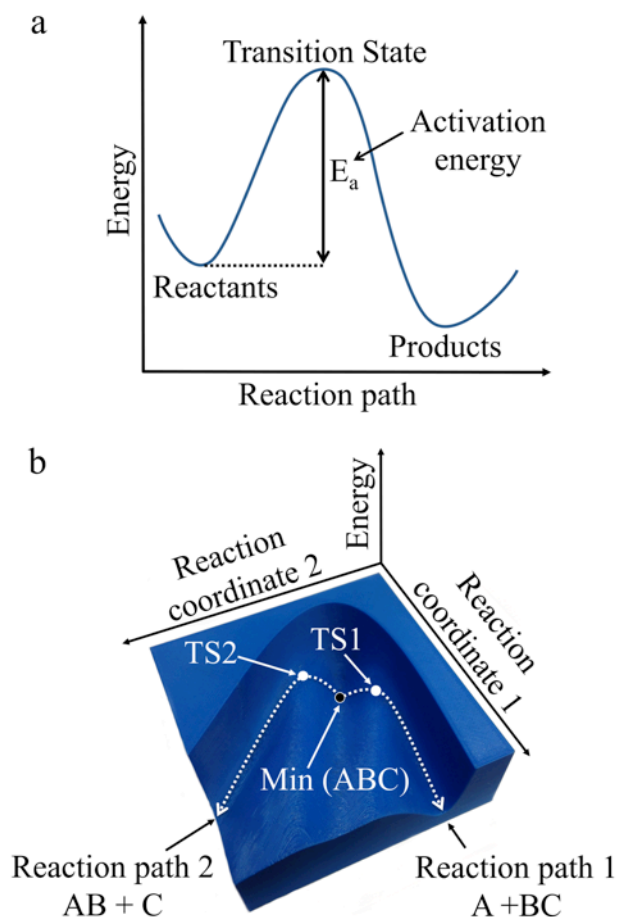
Figure 1. (a) Traditional 2D representation of a reaction path. (b) 3D printed potential energy surface for triatomic molecule ABC. The minimum corresponding to equilibrium geometry (Min ABC) and two possible reaction paths are shown. Path 1 corresponds to reaction ABC ⇄ A + BC. Path 2 corresponds to reaction ABC ⇄ AB + C. Transition states of these reaction paths are labeled as TS1 and TS2, respectively. The size of the 3D printed model is 12.5×12.5×4.5 cm.

When starting with the reactants a reaction proceeds through a transition state to yield the products, and this requires some activation energy. While simple, the 2D representation has serious limitations. Instead of conceptualizing the effects of varying bond lengths and angles on the potential or free energy, a very abstract notion of a single reaction coordinate is introduced, which can confuse students. In addition, the discussion of more realistic reactions, which often proceed along several different reaction paths,

becomes difficult. Students familiar with only 2D representations of a reaction path often have difficulties generalizing this overly simplified picture to higher dimensionalities, which is necessary for understanding chemical kinetics, dynamics, and quantum chemistry. These difficulties often contribute to students developing incorrect "alternative conceptions" of chemistry.[4,5] A 3D model of potential energy surface (PES), or free energy surfaces, can give a more realistic picture of chemical kinetics and dynamics, while using the familiar notion of bond lengths and angles as reaction coordinates (Figure 1b). Thus, the students' understanding of chemical kinetics and dynamics can be expanded beyond a 2D picture by using 3D printed models of the potential energy and free energy surfaces.

Several authors already demonstrated how 3D printed models can be used as effective tools for teaching different concepts in chemistry. Scalfani and Vaid showed the usefulness of printed molecular structure models for teaching symmetry and point groups,[6] while Casas and Estop demonstrated how interactive PDF files, a mobile app, and 3D printed crystal models could be used together to teach symmetry.[7] Lolur and Dawes manufactured 3D PES models of ozone and the spin-forbidden reaction $CO + O(^3P) \rightarrow CO_2$.[8] Teplukhin and Babikov used the isoenergy approach to visualize the PESs of triatomic molecules as a volume.[9] Blauch and Carroll designed 3D PESs associated with the change of dihedral angle in butane and for hypothetical S_N1 and S_N2 reactions.[10]

In this work we show how the quantum chemical package Molpro,[11,12] computational software Wolfram Mathematica,[13] and the 3D modeling software Blender[14] can be used to manufacture a variety of PESs and free energy surfaces for

teaching the basic concepts of reaction kinetics, dynamics and vibrational spectroscopy. We focus on (1) PES cross sections for the hydrogen exchange reaction $H + H_2 \leftrightarrows H_2 + H$ and for rotations of methyl groups in 1-fluoro-2-methylpropene both calculated using quantum chemical methods; (2) model surfaces for protein folding, the dissociation of triatomic molecule ABC and surface adsorption; (3) simple 3D models of double minimum, quadruple minimum, and parabolic surfaces.

II. Calculating and Printing 3D Surface Models

The 3D models of PESs were created using one of the two approaches. In the first approach, the potential energy was determined as a function of bond lengths and angles using quantum chemical package Molpro. The data was then imported into Mathematica to create the 3D object and to generate a stereolithography (STL) file. This approach was used to produce the PES models for the hydrogen exchange reaction and for rotation of methyl groups in 1-fluoro-2-methylpropene. It is important to note that any modern electronic structure package can be used to calculate PESs. Also, the STL files can be generated using a number of different software packages.[6-10] In the second approach, the 3D models were produced directly in Mathematica from analytical functions of two variables. This approach was used to generate the PES for hypothetical triatomic molecule ABC, PES for adsorption on a surface, free energy surface for protein folding, and also parabolic, double minimum, and quadruple minimum surfaces. The STL models produced using Mathematica were post processed using Blender to delete excess material or remove anomalous features in preparation for 3D printing. All 3D models were created using acrylonitrile butadiene styrene (ABS) plastic of varying colors on a uPrint SE Plus

printer. The specific steps for computing and printing the 3D surface models are shown in Figure 2.
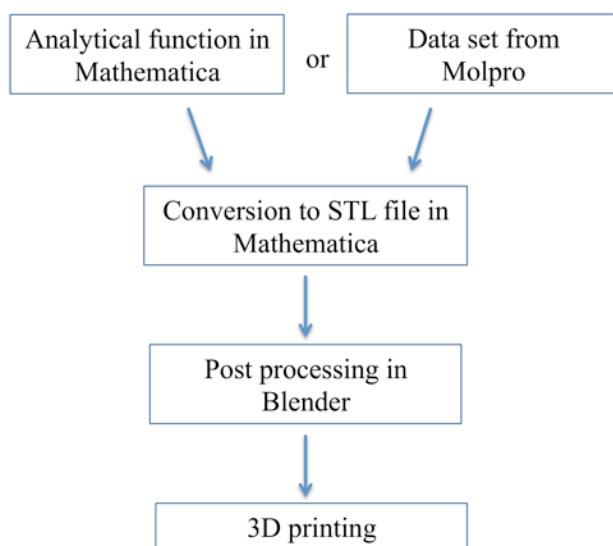
Figure 2. Steps for computing and printing the 3D surface models.

III. 3D Models of Potential Energy Surfaces

A. Calculated PESs for Hydrogen Exchange Reaction and Rotations of Methyl Groups in 1-Fluoro-2-Methylpropene

The collinear potential energy surface for the hydrogen exchange reaction $H + H_2$ $\leftrightarrows H_2 + H$ is a classical example discussed in undergraduate physical chemistry textbooks.[15] In the 3D representation, the potential energy (z-axis of PES) depends on the distances r_1 and r_2 between central (H2) and terminal (H1 and H3) hydrogen atoms that represent the x- and y-axes of the PES (Figure 3a). To obtain the hydrogen exchange reaction PES we calculated the potential energy of the system in Molpro for values of r_1 and r_2 varying from 0.4 to 2.1 Å with an increment of 0.1 Å. The calculations were done using multireference configuration interaction with singles and doubles (MRCISD) method and aug-cc-pVTZ basis set. The Molpro input file is included in the Supporting

Information. Figure 3b shows the generated STL model with minimum energy reaction path, H1-H2-H3 transition state (TS) and the full dissociation (H1 + H2 + H3 atomization) region of the PES. The actual 3D printed model with H1-H2 + H3 and H1 + H2-H3 dissociation channels are shown in Figure 3c.
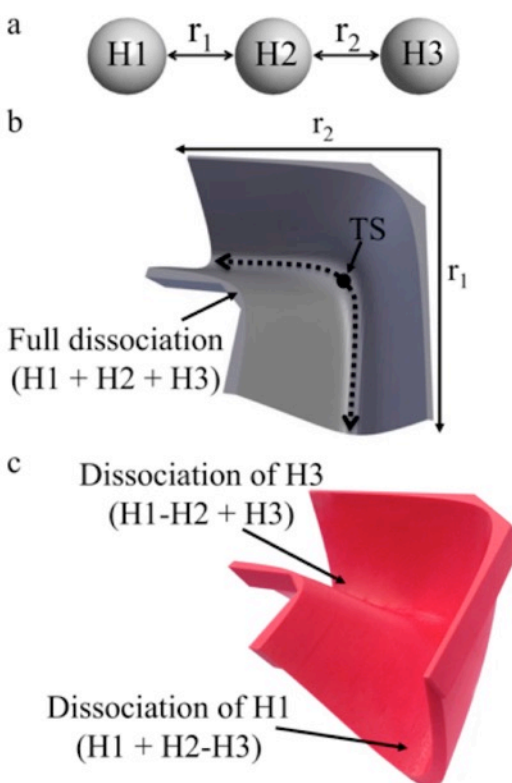
Figure 3. Collinear potential energy surface for H_2+H reaction. (a) Reaction coordinates defined as the interatomic distances r_1 and r_2. (b) STL model with the minimal energy reaction path (dashed curve) and transition state (TS). (c) 3D printed PES model with two dissociation channels (H1-H2 + H3 and H1 + H2-H3).

Collinear PES of the hydrogen exchange reaction has a single transition state and two symmetric reaction channels. Two valleys of the model represent two reaction channels in which one of the terminal hydrogen atoms dissociates from the transition state complex (H1-H2-H3). The dissociated of terminal hydrogen atoms are

indistinguishable from one another. This PES can be used to demonstrate such concepts as minimum energy, transition state, and different types of reaction paths. Also, the surface can be useful when discussing the kinetic isotope effect if one hydrogen atom is substituted with deuterium (H + HD $\leftrightarrows$ H$_2$ + D). Within the Born-Oppenheimer approximation the isotopic substitution does not affect the potential energy surface. However, the heavier mass of deuterium results in a smaller value for the zero point vibrational energy of HD compared with H$_2$, which reduces the forward reaction rate.[16]

The 3D model in Figure 4 represents the potential energy surface cross section associated with the rotation of two methyl groups in 1-fluoro-2-methylpropene. The x- and y- axes are defined by the dihedral angles ϕ_1=C1C2C3H2 and ϕ_2=C1C2C4H7 (Figure 4a), while the z-axis represents the potential energy of the molecule. Angle ϕ_1 defines rotation of the left methyl group interacting with hydrogen atom H1, while ϕ_2 governs rotation of the right methyl group interacting with F atom. Asymmetry in the 1-fluoro-2-methylpropene PES is a result of the methyl groups in close proximity either to H1 or to the F atom. Thus, rotations of the two methyl groups lead to different changes in the potential energy of the molecule, and to the presence of two unequal transition states on the PES. Figure 4b shows geometries of the molecule corresponding to the minima, two transition states and a second-order saddle point (stationary point with two negative eigenvalues of the Hessian matrix) on the PES. The potential energy of the molecule is a periodic function of ϕ_1 and ϕ_2, with periods of 120°. Therefore, to fully reproduce the PES model (Figure 4c) the energy was calculated for ϕ_1 and ϕ_2 values in the range from 0° to 120° only. The energy calculations were performed in Molpro using

unrestricted density functional theory with the B3LYP functional and 6-31G basis set. The Molpro input file is included in the Supporting Information.
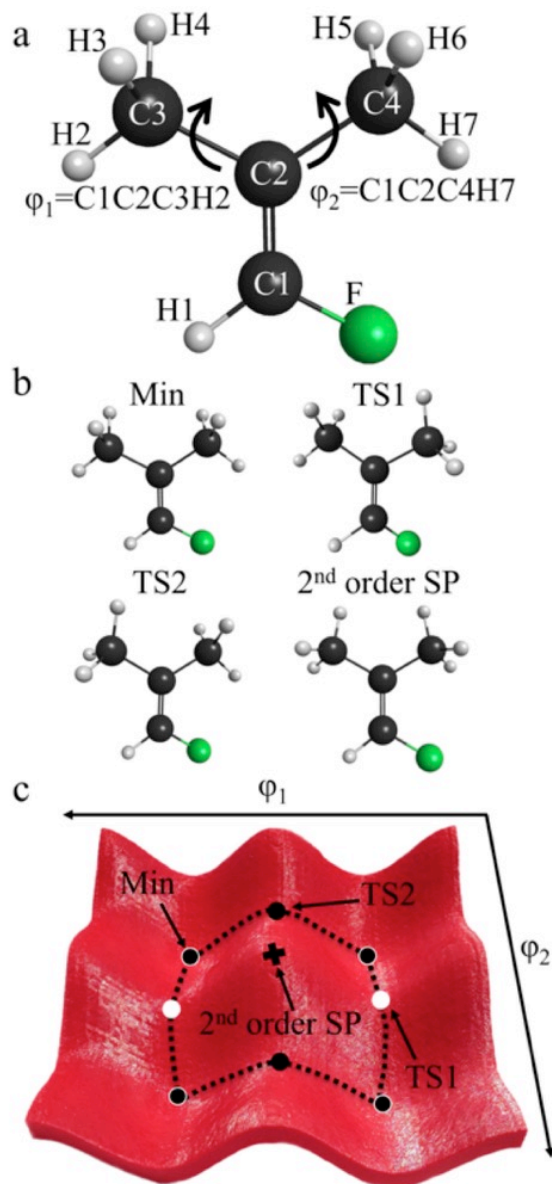
Figure 4. PES cross section associated with rotations of two methyl groups in 1-fluoro-2-methylpropene. (a) Rotations of methyl groups are defined by the dihedral angles ϕ_1 and ϕ_2. (b) Structures of the minimum (Min), two transition states (TS1 and TS2), and second-order saddle point (SP). (c) 3D printed model with minimum energy reaction paths shown by dashed curves.

Each minimum on the PES represents the energetically favorable conformation in which one of the hydrogen atoms of the left methyl group is in closest proximity to the hydrogen atom H1, and one of the hydrogen atoms of the right methyl group is in closest proximity to the F atom. When one of the methyl groups rotates, moving its hydrogen atom away from the H1 or F atom, the potential energy increases until the molecule reaches the transition states TS1 or TS2. The difference in steric interactions of two methyl groups with H1 and F atoms results in the different activation energies for TS1 and TS2. The structure with both methyl groups rotated into "high-energy" conformations corresponds to the second-order saddle point on the potential energy surface. This PES model can be used together with a molecular model of 1-fluoro-2-methylpropene assembled from a molecular kit to demonstrate the relationship between rotations of the methyl groups and corresponding thermodynamic stability of different conformers, highlighting the key geometries on the PES.

B. Model Surfaces for Protein Folding, Linear Triatomic Molecule, and Surface Adsorption

The 3D funnel surface demonstrates multiple conformations a protein can achieve as a result of folding.[17,18] It is believed that several diseases such as Alzheimer's and Parkinson's, as well as allergies, are associated with protein misfolding, thus the free energy surface of protein folding helps to demonstrate the importance of physical chemistry in biology and medicine. Our 3D model is based on the analytical function that represents the general form of a funnel surface.[18] We modified the Mathematica notebook obtained from Prof. T. G. Oas's group[19] to generate the STL model (Figure 5a) and print

the free energy surface (Figure 5b). Protein folding and unfolding can be represented by a small ball (classical trajectory) propagating on this free energy surface. Multiple minima correspond to the different folded states in which the protein can become trapped. One, or possibly several, of these states correspond to native functional protein conformations, while others correspond to misfolded structures. An ensemble of protein molecules can be simulated by multiple balls propagating on the free energy surface, with a different number of molecules trapped in global and local minima corresponding to different protein conformations.
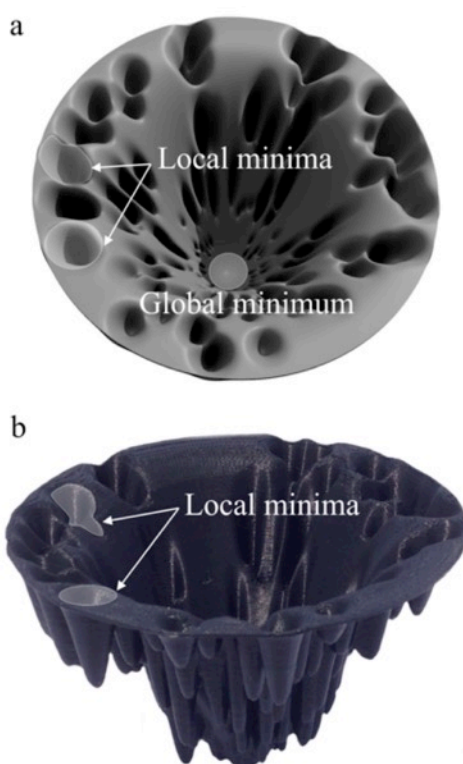
Figure 5. Funnel surface of protein folding. (a) STL model generated from analytical function using Mathematica and post processed in Blender. (b) 3D printed free energy surface. Global and two local minima corresponding to different protein conformations are shown.

The PES for hypothetical linear triatomic molecule ABC (Figure 6a) was obtained from the analytical potential energy function introduced by Wall and Porter,[20] in the form defined by Tannor, Kosloff and Rice.[21] The explicit form of the function, which is a generalization of the Morse potential, and the generated 3D model surface are provided in the Mathematica notebook within the Supporting Information. The post processed STL model and the 3D printed surface, which is a larger version of the surface shown in Figure 1b, are presented in Figure 6b and 6c. The z-axis designates the potential energy. The x- and y-axes are functions of the bond lengths r_1 and r_2 defined as $x = 2^{-1/2} r_1$ and $y = r_2 + r_1/2$. The PES has one minimum corresponding to the equilibrium structure of the linear molecule ABC, two reaction paths with transition states leading to dissociation products AB + C and A + BC, and a barrierless reaction path corresponding to A + B + C atomization. In contrast to the smaller model shown in Figure 1, the larger 20×20×8 cm surface can be used not only to demonstrate multiple reaction paths and transition states, but also for introducing students to molecular dynamics. Simple molecular dynamics simulations can be performed by rolling multiple bearing balls on the surface. An ensemble of trajectories with different initial conditions can be simulated by positioning balls in different parts of the PES. The relative reaction rates for AB + C and A + BC channels can be estimated by counting the number of balls exiting through each channel and comparing with number of balls still trapped in the equilibrium ABC well. However, we discovered that, to produce the quantitative results consistent with the relative reaction rates expected based upon the heights of the energy barriers, even larger model surfaces have to be fabricated.
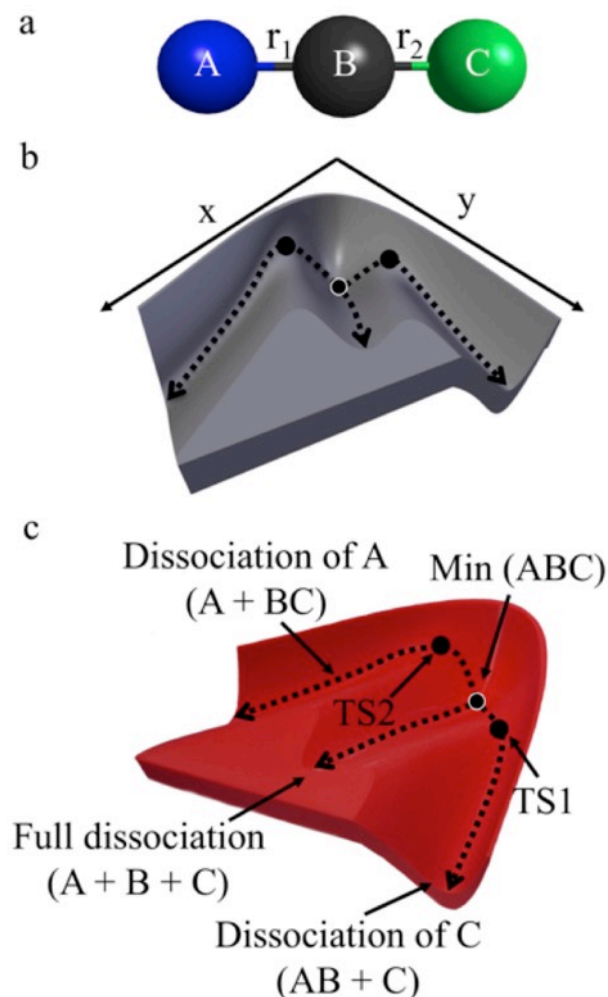
Figure 6. PES of hypothetical linear triatomic molecule ABC. (a) Geometry of ABC molecule with labeled atoms and bond lengths. (b) STL model generated from analytical function using Mathematica and post processed in Blender. (c) 3D printed model of PES. Minimum (Min) and two transition states (TS1, TS2) are labeled. Dashed curves show three minimum energy reaction paths.

The 3D model for surface adsorption was generated from the periodic function $z = sin(x)cos(y)$ (Figure 7a). The details are described in the Supporting Information. The x- and y-axes define positions on the hypothetical adsorbent surface, while the z-axis represents the binding energy of molecules or atoms to the surface (Figure 7b). Multiple minima correspond to energetically favorable adsorption sites, while maxima (also

second-order saddle points) correspond to energetically unfavorable sites. The minimum energy reaction paths connecting different minima and transition states are shown on the 3D model. The diffusion of adsorbed atom or molecules on the surface can be discussed in terms of activation energy required to proceed from one minimum to another through one of the transition states. Therefore, relation between the surface temperature and diffusion rate can be easily explained. This 3D model also makes it easy to point out the limitation of transition state theory by demonstrating nonminimal energy diffusion paths and can even be used to demonstrate diffusion dynamics by rolling bearing balls on the printed surface.
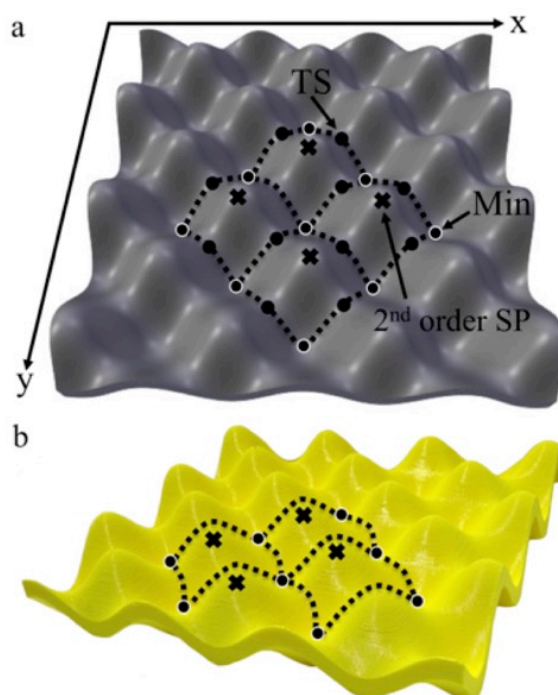
Figure 7. Model PES for adsorption on a surface. (a) STL model generated with Mathematica and post processed in Blender. (b) 3D printed model. Minima (Min), transition states (TS), and second-order saddle points (SP) are labeled. Dashed lines show the minimum energy reaction paths for surface diffusion of adsorbed molecules or atoms.

C. Double Minimum, Quadruple Minimum and Parabolic Surfaces

Simple double minimum, quadruple minimum and parabolic surfaces are useful for demonstrations of the effects of multiple minima, transition states, and surface curvature on kinetics and dynamics of chemical reactions, and also for introducing vibrational spectroscopy. For example, the dependence of vibrational frequency on the curvature of potential energy surface and reduced mass can be demonstrated by rolling small balls on these surfaces. Also, more advanced concepts from spectroscopy, such as fundamental vibrational frequencies, anharmonicity, vibrational mode coupling, overtones, and combination bands, can be illustrated.

The double minimum surface was generated in Mathematica from the analytical function $z = -3x^2 + 1.5x^4 - 0.9x + y^2 + y^4$ (Figure 8a). The x- and y-axes of the PES represent two general reaction coordinates, while the z-axis designates the potential energy of the system. The shallow well represents the local minimum (Min 2) of the system, while the deep well (Min 1) corresponds to the global minimum (Figure 8b). This model allows for simple demonstrations of a chemical reaction proceeding from reactants to products through a transition state. The height of the transition state represents the magnitude of the activation energy of reaction. More general nonminimal reaction parts, with kinetic energy larger than the activation energy, which do not proceed through transition state, also can be demonstrated. The anharmonic nature of the two potential wells introduced by the quartic terms $1.5x^4$ and y^4 can be used to discuss anharmonicity of vibrational modes. Coupling between different modes responsible for overtones in vibrational spectra can be demonstrated by using similar analytical surfaces with additional xy cross terms.
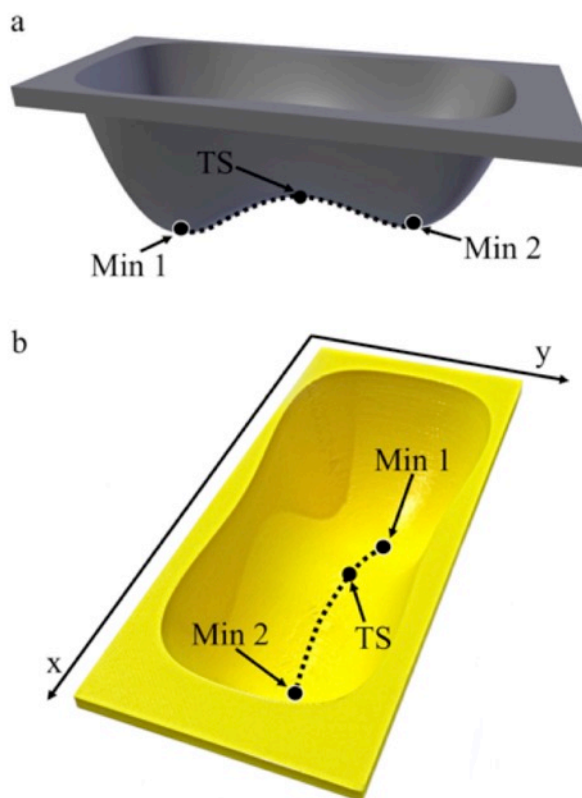
Figure 8. Double minimum surface. (a) STL model generated in Mathematica and post processed in Blender. (b) 3D printed model with labeled transition state (TS) and global (Min 1) and local (Min 2) minima. Dashed curve shows the minimum energy reaction path.

More complex STL model and corresponding 3D printed PESs with four minima are shown in Figures 9a and 9b, respectively. The PES was generated using the analytical function $z = -3x^2 + 1.5x^4 - 0.9x + y^2 + 3y^3 + y^4$. This function is an extension of the double minimum function through addition of the $3y^3$ term. All four minima on the PES have different depths, with the global minimum labeled as Min 1. The PES also has four nonequivalent transitional states (TS 1-4), and one second-order saddle point (SP).
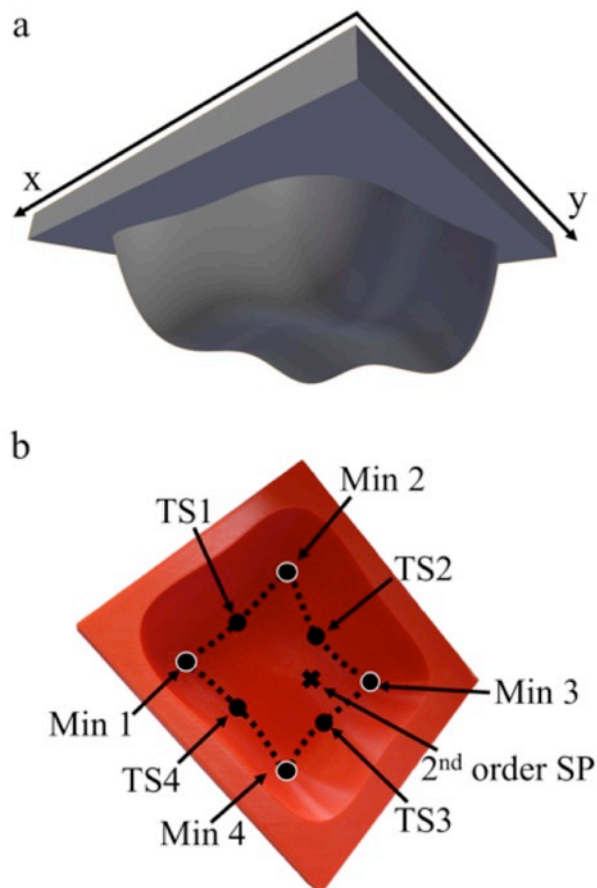
Figure 9. Quadruple minimum surface. (a) STL model generated in Mathematica and post processed in Blender. (b) 3D printed model of PES with four non-equivalent minima (Min 1-4), four different transition states (TS 1-4) and a second-order saddle point (SP).

We also printed a simple parabolic surface using the analytical function $z = x^2 + 2y^2$ (Figures 10a and 10b). This surface is useful for demonstrating solutions of the classical equation of motion for particle in a parabolic potential. Simple concepts such as conservation of the sum of potential and kinetic energies can be also discussed. In addition, the parabolic surface can be used for showcasing the dependence of harmonic vibrational frequency on the surface curvature and reduced mass of vibrational mode by rolling marbles or bearing balls of different masses. Because the ratio of the curvatures along the y- and x-axes is equal to the rational number 2, one can demonstrate that the

trajectories of small bearing balls rolling on the surface should follow the Lissajous curves (Figure 10a). In practice, due to the friction between the ball and the surface the total energy is not conserved exactly and the trajectories follow more general harmonograph curves.
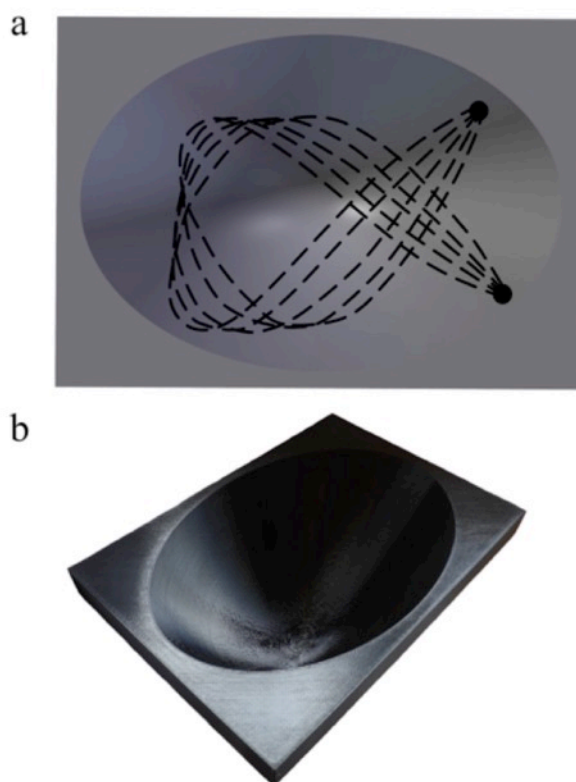
Figure 10. Parabolic surface. (a) STL model generated with Mathematica and post processed in Blender. The Lissajous curves produced by propagating a classical trajectory are shown with dashed lines. (b) 3D printed model.

IV. Conclusions

We created several ABS plastic models of potential and free energy surfaces using 3D printing technology. The models include potential energy cross sections for the hydrogen exchange reaction and for rotations of the methyl groups in

1-fluoro-2-methylpropene. We also printed model surfaces for protein folding, a linear triatomic molecule, and surface adsorption; as well as simple double minimum, quadruple minimum, and parabolic surfaces. The potential energy surfaces of real molecules were generated from quantum chemical calculations, while the surfaces of the model systems were obtained from analytical functions of two variables.

The created 3D models are helpful in explaining such concepts as potential energy surface, transition state, minimum energy reaction path, reaction trajectory, reaction rate, harmonic vibrational frequency, and anharmonicity. Moreover, these models can be combined with conventional educational materials such as molecular model kits to increase the effectiveness of teaching chemistry. We have already used the ABC and protein folding surface models for static demonstrations in upper undergraduate and graduate physical chemistry courses. Future plans include printing larger models of potential and free energy surfaces which are much better suited for classical molecular dynamics simulations performed by rolling small marbles or bearing balls on these surfaces. Another interesting direction is the 3D printing of molecular dynamics simulation kits with multiple potential energy surfaces to demonstrate photochemical reactions and nonadiabatic processes at conical intersections and intersystem crossings.

ASSOCIATED CONTENT

 Supporting Information

The Supporting Information is available on the ACS Publications website at DOI: 10.1021/acs.jchemed.5b00409. Molpro input files and Mathematica notebooks (STL files are not included but are available on request) (ZIP)

AUTHOR INFORMATION

Corresponding Author *E-mail: svarganov@unr.edu.

References

(1)   Swanson, M. S.; Sayers, D. K.; Kuntzleman, T. S. Visualizing the Transition State: A Hands-on Approach to the Arrhenius Equation. *J. Chem. Educ.* **2007**, *84*, 1776.

(2)   Fieberg, J. E. Visualizing Reaction Progress and the Geometry and Instability of the Transition State. J. Chem. Educ. 2012, 89, 1174− 1177.

(3)   Revell, L. E.; Williamson, B. E. Why Are Some Reactions Slower at Higher Temperatures? *J. Chem. Educ.* **2013**, *90*, 1024–1027.

(4)   Cakmakci, G. Identifying Alternative Conceptions of Chemical Kinetics among Secondary School and Undergraduate Students in Turkey. *J. Chem. Educ.* **2010**, *87*, 449–455.

(5)   Bauer, S. H.; Wilcox, C. F. What's in a Name-Transition State or Critical Transition Structure? *J. Chem. Educ.* **1995**, *72*, 13–16.

(6)   Scalfani, V. F.; Vaid, T. P. 3D Printed Molecules and Extended Solid Models for Teaching Symmetry and Point Groups. *J. Chem. Educ.* **2014**, *91*, 1174–1180.

(7)   Casas, L.; Estop, E. Virtual and Printed 3D Models for Teaching Crystal Symmetry and Point Groups. J. Chem. Educ. 2015, 92, 1338

(8)   Lolur, P.; Dawes, R. 3D Printing of Molecular Potential Energy Surface Models. *J. Chem. Educ.* **2014**, *91*, 1181–1184.

(9)   Teplukhin, A.; Babikov, D. Visualization of Potential Energy Function Using an Isoenergy Approach and 3D Prototyping. *J. Chem. Educ.* **2015**, *92*, 305–309.

(10)   Blauch, D. N.; Carroll, F. a. 3D Printers Can Provide an Added Dimension for Teaching Structure–Energy Relationships. *J. Chem. Educ.* **2014**, *91*, 1254–1256.

(11)   Werner, H.-J.; Knowles, P. J.; Knizia, G.; Manby, F. R.; Schütz, M. Molpro: A General-Purpose Quantum Chemistry Program Package. *Wiley Interdiscip. Rev. Comput. Mol. Sci.* **2012**, *2*, 242–253.

(12)   Werner, H.-J.; Knowles, P. J.; Knizia, G.; Manby, F. R.; Schütz, M.; Celani, P.; Korona, T.; Lindh, R.; Mitrushenkov, A.; Rauhut, G.; et al. *MOLPRO, Version 2012.1, Package of Ab Initio Programs*; 2012

(13)   *Mathematica, Version 8.0; Software for Technical Computation*; Wolfram Research: Champaign, IL, 2010.

(14)   *Blender, Version 2.72; 3D Modeling Software*; Stichting Blender Foundation: Amsterdam, The Netherlands, 2014.

(15)   Levine, I. N. *Physical Chemistry*, 5th ed.; McGraw-Hill: Boston, MA, 2002; pp 900-901.

(16)   Westheimer, F. H. The Magnitude of the Primary Kinetic Isotope Effect for Compounds of Hydrogen and Deuterium. *Chem. Rev.* **1961**, *61*, 265–273.

(17)   Dill, K. A.; Bromberg, S. *Molecular Driving Forces: Statistical Thermodynamics in Biology, Chemistry, Physics, and Nanoscience*, 2nd ed.; Garland Science: New York, NY, 2010; pp 379-380.

(18)   Dill, K. A.; Chan, H. S. From Levinthal to Pathways to Funnels. *Nat. Struct. Biol.* **1997**, *4*, 10–19.

(19)   Oas Lab. *Using Mathematica^{TM} to Draw Energy Landscape Funnels.* http://www.oaslab.com/Drawing_funnels.html (accessed Nov 4, 2013).

(20)   Wall, F. T.; Porter, R. N. General Potential-Energy Function for Exchange Reactions. *J. Chem. Phys.* **1962**, *36*, 3256–3260.

(21)   Tannor, D. J.; Kosloff, R.; Rice, S. A. Coherent Pulse Sequence Induced Control of Selectivity of Reactions. Exact Quantum-Mechanical Calculations. *J. Chem. Phys.* **1986**, *85*, 5805–5820.

Chapter VII. Conclusions

In this work we investigate the role of nonadiabatic spin-forbidden transitions in the catalytic and electron transfer processes taking place in the active sites of metal-sulfur proteins by means of nonadiabatic transition state theory (NA-TST). First, we focus on the nonadiabatic transitions between the lowest energy singlet and triplet states in the active sites of [NiFe]-hydrogenase with and without bound molecular hydrogen. The computational studies suggest that the binding of H_2 to the active site is likely to occur on Fe(II) center. The H_2 binding preserves the singlet-triplet state crossing, induced by the rotation of the terminal thiolate ligands on Ni(II) center. Within the biologically relevant temperature range, the Landau-Zener theory predicts the spin-forbidden transition probability from 42% to 38% for the bare active site model. While for the active site with bound H_2, the transition probability is reduced to 35% - 32% within the same temperature range. The high transition probabilities indicate that the nonadiabatic spin-forbidden transitions between the lowest energy singlet and triplet states could play an important role in the catalytic activity of [NiFe]-hydrogenase. We believe that it could be possible to increase the catalytic activity of the [NiFe]-hydrogenase mimics by facilitating spin-forbidden transitions through the ligand design.

Second, we studied the nonadiabatic transitions in the active site of rubredoxin for which we not only estimated the probabilities of transition between the electronic spin states, but also calculated the NA-TST transition rate constants. We focused on the lowest energy electronic states with different spin multiplicities in the rubredoxin active site models $[Fe(SCH3)4]^n$ (n=2-, 1-, 0). The lowest energy spin states in the

$[Fe(SCH3)4]^n$ complexes tend to cross as the geometries of the complexes change between tetrahedral and square planar. The obtained rate constants for transitions between different spin states can be smaller by up to four orders of magnitude than the rate constants obtained under the assumption of completely spin-allowed transitions. This indicates that even in qualitative discussions of reaction mechanisms associated with changes of the Fe coordination, the spin-forbidden nature of the transitions between different spin states must be taken into account. The knowledge about the role of spin-forbidden transitions could not only help with understanding of fundamental principles of electron transfer in biological systems, but also with designing novel bionano devices based on rubredoxin or its active site.

Third, we extended our NA-TST methodology to the large complex protein models by utilizing the fragment molecular orbital (FMO) method applicable to the systems with thousands of atoms. This was accomplished by implementing the fragment molecular orbital minimum energy crossing point (FMO-MECP) search algorithm in the GAMESS suite of programs. The newly implemented FMO-MECP algorithm demonstrates a good accuracy in predicting the MECP geometries and energies, which was shown by comparing the FMO-MECP and conventional density functional theory results. Therefore, the FMO-MECP search algorithm can be used to study spin-forbidden nonadiabatic processes in large complex systems that were previously out of reach for the fully quantum electronic structure methods.

Finally, we designed and created several ABS plastic models of potential and free energy surfaces using the 3D-printing technology for demonstrations in chemistry classes. The potential energy surfaces of real molecules were calculated with electronic

structure methods, while the surfaces of the model systems were obtained from analytical functions. The created 3D models are helpful in explaining such concepts as potential energy surface, transition state, minimum energy reaction path, reaction trajectory, reaction rate, harmonic vibrational frequency and anharmonicity. Moreover, these models can be combined with conventional educational materials such as molecular model kits to increase the effectiveness of teaching chemistry.

Appendix A - Supporting Information for Chapter III
Effect of H₂ Binding on the Nonadiabatic Transition Probability between Singlet
and Triplet States of the [NiFe]-Hydrogenase Active Site
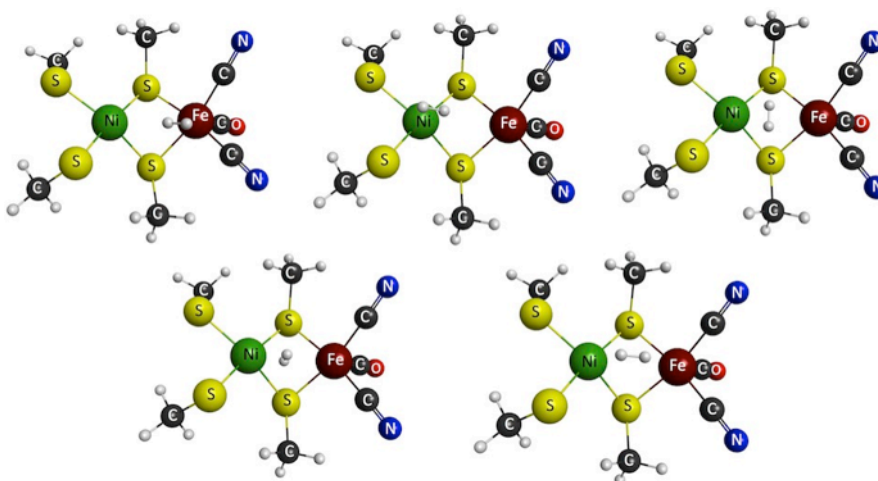
Figure S1. Sampled initial positions of H₂ on the active site of [NiFe]-hydrogenase.
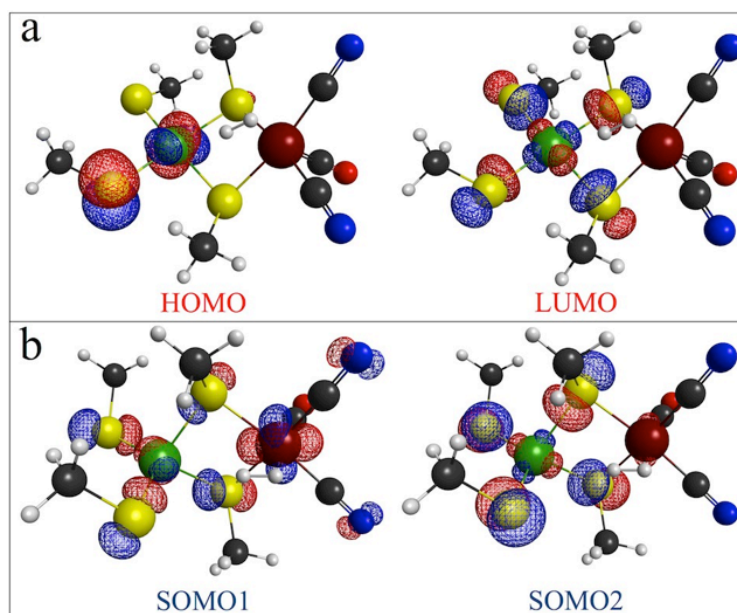
Figure S2. Active space molecular orbitals used in MCQDPT2 calculation of spin-orbit coupling. a) Singlet state orbitals. b) Triplet state orbitals.
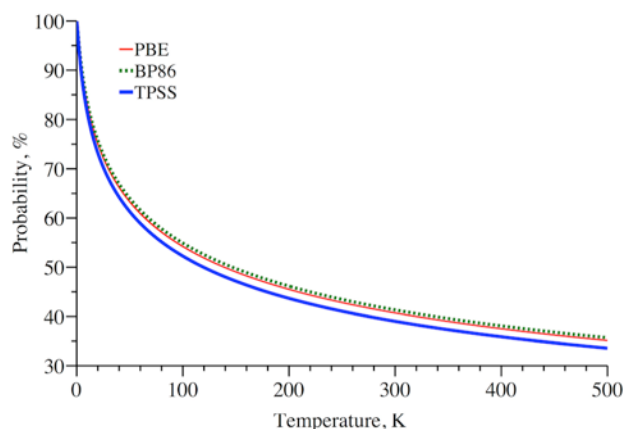
Figure S3. Landau-Zener transition probabilities between the singlet and triplet states of the bare active site and active site with bound H_2 as a function of temperature. Gradients obtained from PBE, BP86 and TPSS calculations with bs1 basis set and spin-orbit coupling calculated with MCQDPT2/6-31G**.
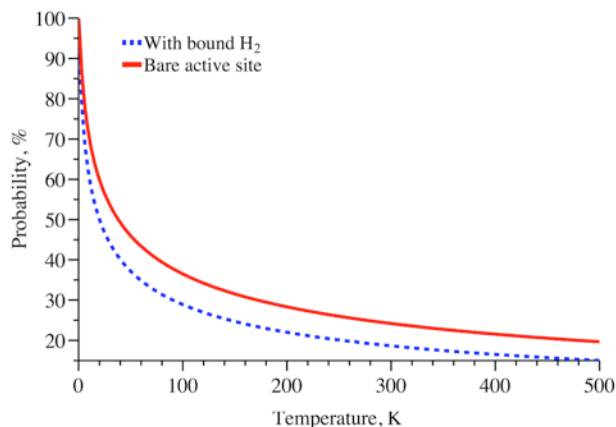
Figure S4. Landau-Zener transition probabilities between the singlet and triplet states of the bare active site and the active site with bound H_2 calculated with normalized probability distribution (Ref. 34) as functions of temperature. The mass-weighted gradients and spin-orbit coupling were calculated with PBE and MCQDPT2, respectively, using def2-TZVP basis set.

Table S1. Binding energies of H_2 (kcal/mol), with and without ZPE correction, to the active site calculated using bs1 basis set.

	PBE	BP86	TPSS	B3LYP
S2	-3.9	-2.4	-4.0	-2.8
S1	-2.6	-1.0	-2.5	-1.5
T2	-8.9	-7.0	-8.8	-6.7
T1	-6.5	-4.7	-6.3	-4.2
ZPE corrected calculations				
S2	0.7	1.9	0.6	2.1
S1	1.5	3.7	1.7	2.8
T2	-3.8	-2.3	-3.3	-2.6
T1	-2.2	0.5	-1.7	-0.5

Table S2. Binding energies of H_2 (kcal/mol), with the ZPE, Grimme's dispersion (D3) and entropy (S) corrections, to the active site calculated with def2-TZVP basis set and different functionals.

	PBE	BP86	TPSS	B3LYP
$E_{binding}$ *(no corrections)*				
S2	-3.9	-1.9	-3.9	-4.0
S1	-1.7	0.2	-1.6	-2.6
T2	-7.5	-5.9	-7.9	-6.3
T1	-4.6	-3.6	-5.4	-3.9
ΔZPE correction				
S2	4.7	4.3	4.6	4.9
S1	4.1	4.8	4.2	4.3
T2	5.1	4.7	5.5	3.8
T1	4.2	5.2	4.6	4.1
ΔD3 correction				
S2	-4.8	-6.3	-4.0	-5.7
S1	-4.6	-4.8	-3.6	-4.9
T2	-2.5	-4.8	-3.7	-6.7
T1	-4.1	-5.7	-4.7	-5.5
ΔS correction				
S2	8.9	7.9	8.5	9.7
S1	8.4	8.8	7.6	10.1
T2	9.6	9.4	9.8	11.1
T1	9.7	9.4	11.8	10.3
$E_{binding}$ + *ΔZPE* + *ΔD3* + *ΔS*				
S2	4.9	4.0	5.2	4.9
S1	6.2	9.0	6.6	7.0
T2	4.7	3.4	3.7	2.1
T1	5.2	5.3	6.2	4.7

Table S3. The difference between the singlet and triplet mass-weighted gradients (E_h $m_e^{-1/2}$ a_0^{-1}) for the bare active site and active site with bound H_2 obtained with different levels of theory.

	PBE/bs1	BP86/bs1	TPSS/bs1	PBE/def2-TZVP
Bare active site	1.04×10^{-4}	1.01×10^{-4}	1.12×10^{-4}	1.57×10^{-4}
Active site with H_2 bound	-	-	-	1.71×10^{-4}

Derivation of velocity averaged Landau-Zener transition probability formula

The Landau-Zener (LZ) probability of nonadiabatic transition for the specific mass-weighted velocity is

$$P_{LZ}(v) = 1 - \exp\left(\frac{-2\pi H_{SO}^2}{v|\Delta g|}\right).$$ (1)

Here we use mass-weighted coordinates and atomic units. The general equation for velocity averaged Landau-Zener (LZ) transition probability can be written as

$$\langle P_{LZ}\rangle = \int_0^\infty P_{LZ}(v)p(v)dv \bigg/ \int_0^\infty p(v)dv.$$ (2)

In the main text we use the Maxwell-Boltzmann velocity distribution,

$$p(v) = \exp\left(\frac{-v^2}{2k_BT}\right).$$ (3)

After substituting the equations (1) and (3) into (2), the averaged LZ probability reads

$$\langle P_{LZ}\rangle = \frac{\int_0^\infty \exp\left(\frac{-v^2}{2k_BT}\right)dv - \int_0^\infty \exp\left(\frac{-2\pi H_{SO}^2}{v|\Delta g|}\right)\exp\left(\frac{-v^2}{2k_BT}\right)dv}{\int_0^\infty \exp\left(\frac{-v^2}{2k_BT}\right)dv}.$$ (4)

Integration of the denominator gives

$$\int_0^\infty \exp\left(\frac{-v^2}{2k_BT}\right)dv = \left(\frac{\pi k_BT}{2}\right)^{1/2}.$$ (5)

The substitution of equation (5) into (4) simplifies the final expression to

$$\langle P_{LZ}\rangle = 1 - \left(\frac{2}{\pi k_BT}\right)^{1/2}\int_0^\infty \exp\left(\frac{-2\pi H_{SO}^2}{v|\Delta g|} - \frac{v^2}{2k_BT}\right)dv.$$ (6)

Equation (6) is equivalent to equation (1) in Ref. 36.

A slightly different form of the velocity averaged LZ formula can be derived with normalized velocity distribution proposed in Ref. 34,

$$p(v) = \frac{v}{k_BT}\exp\left(\frac{-v^2}{2k_BT}\right).$$ (7)

If this form of velocity distribution is used then equation (2) has the following form:

$$\langle P_{LZ}\rangle = \frac{\int_0^\infty \frac{v}{k_BT}\exp\left(\frac{-v^2}{2k_BT}\right)dv - \int_0^\infty \exp\left(\frac{-2\pi H_{SO}^2}{v|\Delta g|}\right)\frac{v}{k_BT}\exp\left(\frac{-v^2}{2k_BT}\right)dv}{\int_0^\infty \frac{v}{k_BT}\exp\left(\frac{-v^2}{2k_BT}\right)dv}.$$ (8)

The integral in the denominator is equal to 1, and the final expression reads

$$\langle P_{LZ}\rangle = 1 - \frac{1}{k_BT}\int_0^\infty v\exp\left(\frac{-2\pi H_{SO}^2}{v|\Delta g|} - \frac{v^2}{2k_BT}\right)dv.$$ (10)

This equation is identical to equation (A7) in Ref. 34.

The transition probabilities calculated using equation 10 (Figure S4) are somewhat lower than the probabilities obtained using equation 6 (Figure 5). However, in both cases the probabilities are large enough to make the nonadiabatic transitions between the lowest energy singlet and triplet states potentially important for the H_2 activation on [NiFe]-hydrogenase.

Calculation of difference between the singlet and triplet mass-weighted gradients, $|\Delta g|$

All equations are shown in atomic units. The Cartesian components of the singlet and triplet states gradients for each atom were obtained at the minimum energy crossing point geometry, as calculated using GAMESS. The vector gradient g_n, of each atom n, is defined as,

$$g_n = \left(\frac{\partial E}{\partial x_n}, \frac{\partial E}{\partial y_n}, \frac{\partial E}{\partial z_n} \right),$$ (1)

with energy derivatives with respect to atomic coordinates, $\frac{\partial E}{\partial x_n}, \frac{\partial E}{\partial y_n}$ and $\frac{\partial E}{\partial z_n}$.

The difference between the triplet and singlet state Cartesian gradients for each atom, Δg_n, can be written as,

$$\Delta g_n = g_n^{triplet} - g_n^{singlet},$$ (2)

and the subsequent squared norm,

$$|\Delta g_n|^2 = \Delta g_n(x)^2 + \Delta g_n(y)^2 + \Delta g_n(z)^2,$$ (3)

written in terms of each Cartesian component.

The difference between the singlet and triplet mass-weighted energy gradients, $|\Delta g|$, can be calculated as,

$$|\Delta g| = \left\{ \sum_{n=1}^{N} |\Delta g_n|^2 m_n^{-1} \right\}^{1/2},$$ (4)

with corresponding mass of each atom, m_n.

Atomic Cartesian coordinates of different conformers.
Atomic Cartesian coordinates (Å) of conformer S optimized with PBE/bs1 level of
theory, E= -2345.248343 Hartree

```
FE      26.0 -2.2294894074  1.0294984149  0.4466030348
NI      28.0  0.5484338995  0.1092731763  0.0430876407
S       16.0 -1.3619423002 -1.0794671960  0.0170153329
S       16.0 -0.7287443116  1.4866978240 -1.2109149330
C        6.0 -1.4393881674 -2.1422329764  1.5264322081
H        1.0 -0.4538612102 -2.1092985450  2.0157390706
C        6.0 -0.2207400192  3.2543208830 -1.2715427193
H        1.0 -0.1414662416  3.5536603675 -2.3293518754
H        1.0  0.7630831121  3.3173774355 -0.7723267492
H        1.0 -0.9644696447  3.8649048182 -0.7387693728
C        6.0 -3.6928587138  0.8990076624 -0.3738084742
O        8.0 -4.7115025293  0.7968711447 -0.9733324829
C        6.0 -2.9817993340  0.5281677962  2.1022833343
N        7.0 -3.4489990748  0.1819135540  3.1403424956
C        6.0 -2.5070384818  2.8453558627  0.8698453415
N        7.0 -2.6793468844  3.9999611153  1.0991533801
S       16.0  1.9724782193 -1.4845223891  0.6806242576
S       16.0  2.2755832669  1.5364920340  0.2934736149
C        6.0  1.3929510048 -3.0974482787 -0.0171848045
H        1.0  1.0744644549 -2.9816002456 -1.0652805020
H        1.0  0.5577799662 -3.5391790268  0.5502345458
H        1.0  2.2457271861 -3.7993216360  0.0178407857
C        6.0  3.2096928498  1.2209522096 -1.2539300367
H        1.0  4.1582389377  1.7886690854 -1.2291837346
H        1.0  2.6338743058  1.5321145468 -2.1441671505
H        1.0  3.4340345901  0.1427644708 -1.3293172546
H        1.0 -2.2094337750 -1.7400961187  2.2009962033
H        1.0 -1.6860116980 -3.1727859887  1.2221188439
```

Atomic Cartesian coordinates (Å) of conformer T optimized with PBE/bs1 level of
theory, E= -2345.236325 Hartree

```
Fe      26.0  1.5505926677 -0.4021128432  0.2219150535
Ni      28.0 -1.4606859837  0.4032446448  0.2783057347
S       16.0 -0.4033476154 -1.6573943129  0.0026753316
S       16.0  0.2578645312  0.6869097008  1.8238233369
C        6.0 -0.6810462303 -2.1555441542 -1.7514573074
H        1.0 -1.4193581598 -2.9735542200 -1.7655395740
H        1.0  0.2748113593 -2.4786928506 -2.1904639851
H        1.0 -1.0740253505 -1.2955879281 -2.3140156856
C        6.0  0.6562142289  2.4862832673  1.8932699263
```

H	1.0	0.3503754771	2.8772308729	2.8774715818
H	1.0	0.1006769641	3.0074185307	1.0992431291
H	1.0	1.7375310174	2.6200683341	1.7385676872
C	6.0	2.4066679903	-1.4372161980	1.2268354182
O	8.0	3.0033828683	-2.1693713842	1.9422179905
C	6.0	2.2924793456	-1.1348951596	-1.3491952549
N	7.0	2.7286278917	-1.6099286381	-2.3488167882
C	6.0	2.8847646184	0.9280412835	0.2718801847
N	7.0	3.7049832252	1.7883504886	0.3212027580
S	16.0	-3.4381454613	0.1555012304	1.3888966519
S	16.0	-2.0432305669	1.8223412252	-1.3767823904
C	6.0	-2.9714651860	-0.9871821280	2.7535104163
H	1.0	-2.2378245548	-0.5135767069	3.4262976617
H	1.0	-2.5220897364	-1.9093730479	2.3502867898
H	1.0	-3.8732263958	-1.2524924682	3.3359057321
C	6.0	-3.8205539999	2.2453223524	-1.1731461103
H	1.0	-4.1743074945	2.8018119466	-2.0595984561
H	1.0	-3.9758402041	2.8679628290	-0.2764195769
H	1.0	-4.4258312958	1.3313064335	-1.0573270556

Atomic Cartesian coordinates (Å) of conformer S1 optimized with PBE/bs1 level of theory, E= -2346.417078 Hartree

FE	26.0	1.7162035924	0.0439025238	0.1393124940
NI	28.0	-1.4839329349	-0.0717554374	-0.1460784674
S	16.0	0.0439163923	1.5270856526	-0.6556047383
S	16.0	0.1759854611	-1.3966122242	-0.9454732629
C	6.0	-0.1036811151	2.8483034843	0.6223518512
H	1.0	-0.6414431183	3.7066270561	0.1908321187
H	1.0	0.9123004870	3.1395690969	0.9277503816
H	1.0	-0.6689362163	2.4626893391	1.4834896962
C	6.0	0.2284609527	-3.0884606773	-0.2226458325
H	1.0	0.1743345137	-3.8156834329	-1.0495536387
H	1.0	-0.6520468415	-3.2011308285	0.4337475560
H	1.0	1.1727202279	-3.2136171874	0.3282631621
C	6.0	2.6935853214	0.1677660312	-1.2583846314
O	8.0	3.3868586385	0.2475808130	-2.2089339245
C	6.0	2.7263887383	1.4055388120	1.0014190233
N	7.0	3.3335458872	2.2838610956	1.5233265563
C	6.0	2.7998126409	-1.3624609746	0.8139216275
N	7.0	3.4407525056	-2.2748415815	1.2250165143
S	16.0	-3.2735605124	1.2114521181	0.1974407998
S	16.0	-2.7492896860	-1.7349915881	0.6911441416
C	6.0	-3.1362766080	2.7700892733	-0.7942299823

H	1.0	-2.4665934126	2.6298777258	-1.6582441746
H	1.0	-2.7595563732	3.6201439880	-0.1988071532
H	1.0	-4.1424052308	3.0337342591	-1.1674781041
C	6.0	-3.7116451362	-2.2254073202	-0.7940579357
H	1.0	-4.4729381271	-2.9730616422	-0.5044758992
H	1.0	-3.0663724773	-2.6636628882	-1.5765558595
H	1.0	-4.2188332107	-1.3346249922	-1.2021136385
H	1.0	1.1254661673	-0.0543519828	1.7858815381
H	1.0	0.4308352542	-0.1255749415	1.3796110819

Atomic Cartesian coordinates (Å) of conformer S2 optimized with PBE/bs1 level of theory, E= -2346.419250 Hartree

FE	26.0	1.8343149123	0.1117640749	0.1237071633
NI	28.0	-1.3954068356	-0.1641435549	-0.7076661814
S	16.0	0.0715340597	1.5418308173	-0.4763292234
S	16.0	0.5048585112	-1.2918046433	-1.2268374334
C	6.0	-0.4360351364	2.3705268114	1.0884057681
H	1.0	-1.3149352783	2.9998768281	0.8828101303
H	1.0	0.4189179530	2.9602364088	1.4533678678
H	1.0	-0.7139221179	1.6170590913	1.8414526121
C	6.0	0.5635458442	-2.9858548228	-0.5153508980
H	1.0	0.1240717235	-3.6891848488	-1.2389226294
H	1.0	-0.0265301278	-3.0217017020	0.4137746346
H	1.0	1.6169213194	-3.2272121590	-0.3087010192
C	6.0	2.8371171482	0.5924441008	-1.1765175975
O	8.0	3.5488789147	0.9207778340	-2.0570327393
C	6.0	2.6410065871	1.4122294229	1.2633670541
N	7.0	3.1080888156	2.2457560736	1.9693002483
C	6.0	3.0740605444	-1.2617675237	0.5865659851
N	7.0	3.8175456162	-2.1486676817	0.8554977114
S	16.0	-3.2063271955	1.1624299372	-0.6652367821
S	16.0	-2.5422038748	-2.0708225779	-0.5036470464
C	6.0	-2.8267379292	2.5934192427	-1.7629931787
H	1.0	-2.6738049347	2.2677288659	-2.8062258775
H	1.0	-1.9214241526	3.1326542864	-1.4403078136
H	1.0	-3.6860191125	3.2883943850	-1.7342401379
C	6.0	-4.3251039468	-1.7920103094	-0.1587853601
H	1.0	-4.5079121908	-1.5503842155	0.9032364119
H	1.0	-4.8792859697	-2.7140987409	-0.4100011862
H	1.0	-4.7030021777	-0.9549750824	-0.7704631577
H	1.0	1.2182343147	-0.2936038279	1.7033140562
H	1.0	0.5932104958	-0.4889129203	1.2353299187

Atomic Cartesian coordinates (Å) of conformer T1 optimized with PBE/bs1 level of theory, E= -2346.411294 Hartree

```
FE   26.0   1.6694905304   0.0074721981  -0.0464262911
NI   28.0  -1.4818770448   0.0299968338  -0.0441657324
S    16.0   0.0448035960  -1.3543491140   1.0371130470
S    16.0   0.0706323404   1.7214346193   0.3511176037
C     6.0  -0.0673034752  -2.9448168395   0.1126125799
H     1.0  -0.6619662665  -3.6520029688   0.7140834122
H     1.0   0.9495148082  -3.3356875858  -0.0475739851
H     1.0  -0.5713357047  -2.7782175846  -0.8522545110
C     6.0  -0.0223028133   2.7400553042  -1.1818951994
H     1.0  -0.6456973761   3.6256388127  -0.9756406879
H     1.0  -0.4873070495   2.1560437390  -1.9922251734
H     1.0   0.9966078163   3.0431414655  -1.4682562196
C     6.0   2.4639844740   0.3209565151   1.4404949231
O     8.0   3.0314662052   0.5364151208   2.4491304523
C     6.0   2.7938765366  -1.4986158690  -0.3596938176
N     7.0   3.4605885599  -2.4643761570  -0.5428894294
C     6.0   2.8295586969   1.2286415935  -0.9359926029
N     7.0   3.5217025128   2.0175757678  -1.4924056152
S    16.0  -3.3010118241   0.3700550532   1.3076688272
S    16.0  -2.3894924605  -0.5014674958  -2.0771067984
C     6.0  -2.5072979279   0.7893884578   2.9130567940
H     1.0  -1.8299926439   1.6509643217   2.7942943536
H     1.0  -1.9163955718  -0.0620247551   3.2895727560
H     1.0  -3.2817333068   1.0436530326   3.6602442406
C     6.0  -4.2081758134  -0.5442331099  -1.7972682132
H     1.0  -4.7189393903  -0.8779982256  -2.7185169992
H     1.0  -4.5877144858   0.4534260383  -1.5209608499
H     1.0  -4.4582407442  -1.2363239259  -0.9767449953
H     1.0   1.3445800506  -0.2033119191  -1.7325530064
H     1.0   0.6277135116  -0.3988774533  -1.4107279623
```

Atomic Cartesian coordinates (Å) of conformer T2 optimized with PBE/bs1 level of theory, E= -2346.415063 Hartree

```
FE   26.0   2.1213691947   0.3085937089   0.8107985704
NI   28.0  -0.9383254369  -0.1537113312  -0.5110866185
S    16.0   0.2627030448   1.6910331190   0.3542236205
S    16.0   1.2024506670  -1.0645687759  -0.8955391853
C     6.0  -0.5115728190   2.0383983214   1.9864918268
H     1.0  -1.3699972153   2.7145932353   1.8374615401
H     1.0   0.2420269153   2.5083199101   2.6376089560
```

H	1.0	-0.8631904662	1.1009247040	2.4466500972
C	6.0	1.2869901699	-2.7829365825	-0.2490788018
H	1.0	0.9090299374	-3.4699199905	-1.0237630853
H	1.0	0.6617427333	-2.8796020266	0.6529642571
H	1.0	2.3324431682	-3.0157626027	0.0043154547
C	6.0	3.1458326787	1.1590809229	-0.2696163408
O	8.0	3.8666961437	1.7418420234	-0.9970905993
C	6.0	2.6513455867	1.4304527162	2.2583474653
N	7.0	2.9350871723	2.1451484702	3.1639041893
C	6.0	3.5032528721	-0.9575242795	1.1584191256
N	7.0	4.3441538918	-1.7741160082	1.3512119994
S	16.0	-2.3338686965	0.7340202341	-2.0531553820
S	16.0	-1.7834938225	-1.5822612499	1.0398278528
C	6.0	-2.1552999875	2.5654628105	-2.1453757735
H	1.0	-1.8907063947	2.8734645442	-3.1719817786
H	1.0	-1.3588691738	2.9000956005	-1.4603235199
H	1.0	-3.1014757469	3.0644355809	-1.8690901945
C	6.0	-3.2899427421	-0.6614529399	1.5727452124
H	1.0	-4.0524142196	-1.3696582319	1.9442184420
H	1.0	-3.7053390571	-0.0948548455	0.7231728748
H	1.0	-3.0541453274	0.0484725292	2.3852024810
H	1.0	1.4357804605	-0.5368794881	2.1514718115
H	1.0	0.8088741714	-0.5441491824	1.6440138730

Atomic Cartesian coordinates (Å) of MECP(S2/T2) optimized with PBE/bs1 level of theory, E= -2346.410716 Hartree

FE	26.0	2.1440583127	0.3027918249	0.7884657137
NI	28.0	-0.9282634099	-0.0686856895	-0.4075922765
S	16.0	0.4500778895	1.7645162115	0.0558824481
S	16.0	1.1411550438	-1.0683212222	-0.8733958097
C	6.0	-0.3206913122	2.4852124560	1.5642373082
H	1.0	-1.0830698998	3.2203894711	1.2573682974
H	1.0	0.4678527225	2.9667506064	2.1625805899
H	1.0	-0.8024413008	1.6960135741	2.1627823281
C	6.0	1.2296931285	-2.7998654850	-0.2684187250
H	1.0	0.8470613691	-3.4680555543	-1.0570333045
H	1.0	0.6063141013	-2.9121369624	0.6334536218
H	1.0	2.2756302152	-3.0380628252	-0.0234071492
C	6.0	3.2966282155	0.9606837962	-0.2940600914
O	8.0	4.1058137209	1.4085659509	-1.0245212990
C	6.0	2.6863949519	1.5000556157	2.1673263402
N	7.0	2.9809695869	2.2715197258	3.0216668164
C	6.0	3.3939410402	-1.0451656200	1.2921178630
N	7.0	4.1614954834	-1.9084666850	1.5694398784

S	16.0	-2.6982389865	0.9266803240	-1.3834591291
S	16.0	-1.8750407757	-1.7902936469	0.6939996278
C	6.0	-2.5045291794	2.7569792396	-1.4327376199
H	1.0	-3.0446268778	3.1631002595	-2.3068977337
H	1.0	-1.4394403461	3.0310707118	-1.5122636484
H	1.0	-2.9189704473	3.2314296946	-0.5252614792
C	6.0	-3.3737036706	-1.0906376252	1.5074350539
H	1.0	-4.0695650911	-1.9072684465	1.7727033734
H	1.0	-3.8729373150	-0.3856997608	0.8229789522
H	1.0	-3.1052987654	-0.5510185901	2.4324269735
H	1.0	1.3273547112	-0.3503391199	2.1779211943
H	1.0	0.7556031874	-0.4280542919	1.6145162981

Atomic Cartesian coordinates (Å) of conformer S optimized with BP86/bs1 level of theory, E= -2346.854058 Hartree

FE	26.0	1.6595387528	0.0785956125	0.1978870809
NI	28.0	-1.2721472535	-0.0989197598	-0.6027268680
S	16.0	0.1861868979	1.6352951193	-0.6521962341
S	16.0	0.5736261912	-1.1541707268	-1.4083505802
C	6.0	-0.2605746758	2.8291657903	0.6828474251
H	1.0	-1.0276180380	3.5170550146	0.2936557306
H	1.0	0.6531182698	3.3671845749	0.9776608929
H	1.0	-0.6607397565	2.2891087294	1.5503531006
C	6.0	0.6736891418	-2.9677074965	-1.0830273068
H	1.0	0.7544147562	-3.4916476102	-2.0502821679
H	1.0	-0.2499405409	-3.2812166687	-0.5644672126
H	1.0	1.5492957080	-3.1647140083	-0.4458310237
C	6.0	3.0591686076	0.5322875438	-0.6219749494
O	8.0	4.0336407160	0.8504624950	-1.2203962226
C	6.0	2.0757774392	1.1200585085	1.7287174011
N	7.0	2.3351294399	1.7850391423	2.6804380233
C	6.0	2.4808571164	-1.4271258989	1.0016690521
N	7.0	2.9966399910	-2.3900243703	1.4743766281
S	16.0	-3.0766116401	1.2245200400	-0.3187201426
S	16.0	-2.4032257009	-2.0151745113	-0.4466903898
C	6.0	-2.9839599944	2.3706372082	-1.7640329138
H	1.0	-3.0772218201	1.8180222995	-2.7154635989
H	1.0	-2.0319457393	2.9281944566	-1.7842617199
H	1.0	-3.8214537332	3.0906331663	-1.6922139456
C	6.0	-4.0468276529	-1.8004537797	0.3537782204
H	1.0	-3.9515253728	-1.6645111807	1.4458842277
H	1.0	-4.6463317614	-2.7100862721	0.1629323765
H	1.0	-4.5607041278	-0.9181540679	-0.0651319631

Atomic Cartesian coordinates (Å) of conformer T optimized with BP86/bs1 level of theory, E= -2346.842553 Hartree

```
FE    26.0   1.4079987638  -0.5147738927   1.0245273019
NI    28.0  -1.4156440698   0.4913321121   0.1472584799
S     16.0   0.6397116597   0.4282315735  -0.9643984697
S     16.0  -0.6675281031  -1.5791201081   0.9197776263
C      6.0   1.2379533904   2.1690067420  -1.1590731679
H      1.0   1.1743466412   2.4415828144  -2.2261312869
H      1.0   2.2765321145   2.2328446213  -0.7985052448
H      1.0   0.5980178110   2.8417534236  -0.5676944048
C      6.0  -1.3729270311  -1.8476103818   2.6093696802
H      1.0  -2.1115288265  -2.6654108924   2.5530300482
H      1.0  -1.8699987097  -0.9242726845   2.9447457186
H      1.0  -0.5580039020  -2.1028508281   3.3044551501
C      6.0   2.3623500204  -1.7417629317   0.3814262738
O      8.0   3.0281469428  -2.6078320376  -0.0794142939
C      6.0   2.8528049393   0.7011714138   1.1520567625
N      7.0   3.7475326734   1.4840564080   1.2070691493
C      6.0   1.6878847841  -1.0669728975   2.8120369540
N      7.0   1.8301845076  -1.4217691424   3.9391535509
S     16.0  -3.1156521289   0.1803208381  -1.3518039698
S     16.0  -2.2142251508   2.2255372619   1.3586218073
C      6.0  -2.4793428813  -1.1897113567  -2.4122737318
H      1.0  -2.2721471407  -2.0871914336  -1.8054610513
H      1.0  -1.5433994741  -0.8885589835  -2.9117927368
H      1.0  -3.2333906229  -1.4416181988  -3.1823801847
C      6.0  -3.8801705489   2.6636354904   0.7010972915
H      1.0  -4.2711720910   3.5459372091   1.2413818452
H      1.0  -4.5845740650   1.8241377885   0.8287970996
H      1.0  -3.8257655024   2.8947790727  -0.3763321969
```

Atomic Cartesian coordinates (Å) of conformer S1 optimized with BP86/bs1 level of theory, E= -2348.032179 Hartree

```
FE    26.0   1.7587859889   0.0472382661   0.1459540691
NI    28.0  -1.4805574192  -0.1118941648  -0.1582010412
S     16.0   0.0470475882   1.5017824751  -0.6469191408
S     16.0   0.2152747556  -1.4195974930  -0.9162781111
C      6.0  -0.1105016471   2.8304393821   0.6300804612
H      1.0  -0.6563894173   3.6833456226   0.1955756092
H      1.0   0.9046247190   3.1299588594   0.9326653363
H      1.0  -0.6725554709   2.4432198374   1.4932544414
C      6.0   0.2869895888  -3.1093902824  -0.1740664330
H      1.0   0.2940557015  -3.8448327398  -0.9966830706
```

H	1.0	-0.6207021736	-3.2471326382	0.4395106419
H	1.0	1.2098763416	-3.2009621261	0.4187885927
C	6.0	2.7209009468	0.1810991073	-1.2679016261
O	8.0	3.4011030157	0.2691528874	-2.2280070683
C	6.0	2.7571593239	1.4331370420	0.9976066564
N	7.0	3.3544897542	2.3225324779	1.5133196975
C	6.0	2.8686854391	-1.3455800140	0.8225384837
N	7.0	3.5235424508	-2.2466160988	1.2382808825
S	16.0	-3.2668616005	1.1784869567	0.2049972864
S	16.0	-2.7650537115	-1.7964469308	0.6127504842
C	6.0	-3.1479649210	2.7350353463	-0.8025931440
H	1.0	-2.4846557990	2.5923630458	-1.6720185210
H	1.0	-2.7687291553	3.5916338017	-0.2158444884
H	1.0	-4.1596033936	2.9916516036	-1.1691338425
C	6.0	-3.8427445675	-2.1604888936	-0.8375556283
H	1.0	-4.5977913454	-2.9154169666	-0.5460492419
H	1.0	-3.2613730357	-2.5542990911	-1.6912454422
H	1.0	-4.3564089805	-1.2327706930	-1.1453853889
H	1.0	1.1779873149	-0.0549995585	1.7933756642
H	1.0	0.4850254891	-0.1286654509	1.3900551814

Atomic Cartesian coordinates (Å) of conformer S2 optimized with BP86/bs1 level of theory, E= -2348.034303 Hartree

FE	26.0	1.8451237080	0.1205768905	0.2253425121
NI	28.0	-1.3840478211	-0.1784134772	-0.6704595899
S	16.0	0.0692919353	1.5377882999	-0.4039804869
S	16.0	0.5278918466	-1.3137923585	-1.1178691667
C	6.0	-0.4856065383	2.3475469266	1.1610097585
H	1.0	-1.3625775147	2.9760850206	0.9406242269
H	1.0	0.3568025401	2.9397279785	1.5526342457
H	1.0	-0.7784936643	1.5846363571	1.8996024334
C	6.0	0.5771824090	-3.0006284541	-0.3729090443
H	1.0	0.1360206684	-3.7146802427	-1.0862639673
H	1.0	-0.0120607150	-3.0220701187	0.5583240939
H	1.0	1.6304861556	-3.2422755336	-0.1617783777
C	6.0	2.8487117525	0.5975591110	-1.0822351314
O	8.0	3.5588488801	0.9223710019	-1.9662642244
C	6.0	2.6333102368	1.4443790538	1.3613587558
N	7.0	3.0873235733	2.2881043149	2.0646288915
C	6.0	3.0960218111	-1.2446106190	0.7082543520
N	7.0	3.8438811202	-2.1250595111	0.9882478544
S	16.0	-3.2138720022	1.1256132955	-0.7176543928
S	16.0	-2.5350825600	-2.0802388214	-0.4222289908
C	6.0	-2.8011428318	2.5938894618	-1.7623388454

H	1.0	-2.6288418947	2.3025168125	-2.8138780769
H	1.0	-1.8985579047	3.1166797634	-1.4041587970
H	1.0	-3.6576994854	3.2937033309	-1.7286881650
C	6.0	-4.3358588759	-1.7764061022	-0.1702961172
H	1.0	-4.5318409115	-1.2111617918	0.7573451959
H	1.0	-4.8398594654	-2.7587609696	-0.1008134426
H	1.0	-4.7597340364	-1.2025455940	-1.0111149377
H	1.0	1.2235213751	-0.2783717692	1.8032827265
H	1.0	0.6045144292	-0.4801799059	1.3331476575

Atomic Cartesian coordinates (Å) of conformer T1 optimized with BP86/bs1 level of theory, E= -2348.026431 Hartree

FE	26.0	1.6934414285	0.0073576418	-0.0461025855
NI	28.0	-1.5057964044	0.0299696135	-0.0512028030
S	16.0	0.0434742030	-1.3557032558	1.0147993787
S	16.0	0.0691140366	1.7138739916	0.3327714398
C	6.0	-0.0582181226	-2.9540632245	0.0913989950
H	1.0	-0.6486908789	-3.6647183002	0.6947455165
H	1.0	0.9624136431	-3.3376499664	-0.0665450575
H	1.0	-0.5628305396	-2.7936328082	-0.8747859028
C	6.0	-0.0095766649	2.7456488116	-1.1994613013
H	1.0	-0.6288266873	3.6349941903	-0.9917466982
H	1.0	-0.4728470863	2.1695752659	-2.0170376768
H	1.0	1.0140614996	3.0436644246	-1.4768694854
C	6.0	2.4671127154	0.3252355977	1.4558309732
O	8.0	3.0194809353	0.5426790775	2.4733955021
C	6.0	2.8252097848	-1.5021838908	-0.3471853010
N	7.0	3.4941548647	-2.4683597226	-0.5243338963
C	6.0	2.8604489584	1.2353935413	-0.9286759948
N	7.0	3.5550645308	2.0256391908	-1.4814514464
S	16.0	-3.3124079963	0.3722556616	1.3209633832
S	16.0	-2.4339817503	-0.4964129853	-2.0780184015
C	6.0	-2.5179191702	0.7958869283	2.9313696888
H	1.0	-1.8376364745	1.6556807923	2.8104042309
H	1.0	-1.9310130952	-0.0564170919	3.3141901232
H	1.0	-3.2948763673	1.0561494200	3.6755487840
C	6.0	-4.2568681233	-0.5491033686	-1.7903568387
H	1.0	-4.7693088847	-0.8833973422	-2.7119297992
H	1.0	-4.6399663685	0.4468699936	-1.5100945408
H	1.0	-4.5000438308	-1.2456308543	-0.9706168039
H	1.0	1.3803427018	-0.2096405187	-1.7352346204
H	1.0	0.6642248832	-0.4014049427	-1.4176779622

Atomic Cartesian coordinates (Å) of conformer T2 optimized with BP86/bs1 level of theory, E= -2348.030236 Hartree

```
FE    26.0   1.6518706137   0.0973001777   0.2168929418
NI    28.0  -1.4503618962  -0.3667736497  -1.0498581272
S     16.0  -0.2357414358   1.4713763312  -0.1824689400
S     16.0   0.6859401404  -1.2881567706  -1.4627256921
C      6.0  -0.9761485780   1.8112369532   1.4734938811
H      1.0  -1.8312313592   2.4974147452   1.3470557963
H      1.0  -0.2041818062   2.2687293912   2.1130202692
H      1.0  -1.3280130874   0.8715260716   1.9304386040
C      6.0   0.7802951388  -3.0037414929  -0.7943465048
H      1.0   0.3854994257  -3.7010780681  -1.5525854412
H      1.0   0.1721505445  -3.0875799640   0.1214250707
H      1.0   1.8314066012  -3.2353524677  -0.5604297713
C      6.0   2.6270700023   0.9661584744  -0.9019760874
O      8.0   3.3140274845   1.5588089496  -1.6546590493
C      6.0   2.2158978801   1.2224504929   1.6583660856
N      7.0   2.5187541972   1.9333270053   2.5613719267
C      6.0   3.0679397285  -1.1557003986   0.5093241295
N      7.0   3.9275424160  -1.9599467784   0.6727111545
S     16.0  -2.8118044549   0.5212611558  -2.6265942967
S     16.0  -2.3035951974  -1.8054450051   0.4880628419
C      6.0  -2.5854238546   2.3504831490  -2.7634523085
H      1.0  -2.3055038856   2.6255537154  -3.7966242047
H      1.0  -1.7862373812   2.6821991725  -2.0791000780
H      1.0  -3.5217638776   2.8798043712  -2.5067840116
C      6.0  -3.8427651313  -0.9157393712   1.0011784986
H      1.0  -4.6098548759  -1.6464216918   1.3199269443
H      1.0  -4.2368200340  -0.3238838592   0.1579872450
H      1.0  -3.6447855966  -0.2334798245   1.8477920891
H      1.0   1.0611159450  -0.8301760676   1.5481917419
H      1.0   0.3839535342  -0.7212499569   1.1274501228
```

Atomic Cartesian coordinates (Å) of MECP(S/T) optimized with BP86/bs1 level of theory, E= -2346.838510 Hartree

```
FE    26.0   0.6329261231  -0.2626683674  -1.4377550258
NI    28.0  -0.9213259827   0.2087601876   1.1424123711
S     16.0  -1.6561851937  -0.2588483345  -1.0090681525
S     16.0   0.6340264087  -1.4090526799   0.5855400742
C      6.0  -2.4614594861   1.2872126382  -1.6315687523
H      1.0  -3.5299001343   1.0768387440  -1.8109331340
H      1.0  -1.9617734575   1.6021597104  -2.5611290317
H      1.0  -2.3701602170   2.0822080701  -0.8751359202
```

```
C      6.0   2.2042204778  -1.1810882073   1.5333712174
H      1.0   2.3517690235  -2.0623607386   2.1811263118
H      1.0   2.1026111112  -0.2692087608   2.1443060609
H      1.0   3.0379889874  -1.0677083063   0.8231691378
C      6.0   0.6863259381  -1.5644904889  -2.5067557919
O      8.0   0.7139971263  -2.4906776355  -3.2472446538
C      6.0   0.4692302237   1.0223349501  -2.8165653214
N      7.0   0.3250237541   1.8358606292  -3.6734816876
C      6.0   2.5124930426  -0.0449754952  -1.4172249209
N      7.0   3.6969949763   0.0660206740  -1.3817505544
S     16.0  -2.7972599369   0.0124737269   2.4113992845
S     16.0   0.1447962690   1.7849871660   2.3736271161
C      6.0  -3.9517189114  -1.1117804132   1.5105639366
H      1.0  -3.4422446316  -2.0432860329   1.2132378987
H      1.0  -4.3515910539  -0.6376870087   0.5985886652
H      1.0  -4.7970916898  -1.3649316905   2.1783035906
C      6.0  -0.4876032493   1.7298589265   4.1042548135
H      1.0  -0.0952649981   2.5983723122   4.6659633785
H      1.0  -0.1692765563   0.8053815646   4.6181690671
H      1.0  -1.5903739632   1.7638248599   4.1150630225
```

Atomic Cartesian coordinates (Å) of MECP(S2/T2) optimized with BP86/bs1 level of theory, E= -2348.025924 Hartree

```
FE    26.0   1.6998281511   0.1096053196   0.2270108213
NI    28.0  -1.4156095789  -0.2450388050  -0.9412906316
S     16.0  -0.0138508165   1.5801205929  -0.4699762396
S     16.0   0.6510442912  -1.2630388831  -1.4168231572
C      6.0  -0.7447145228   2.3173143298   1.0570075038
H      1.0  -1.5063425290   3.0599820403   0.7630539481
H      1.0   0.0631028516   2.7940990187   1.6344662526
H      1.0  -1.2200632802   1.5359430187   1.6717021140
C      6.0   0.7327603901  -2.9992693345  -0.8060933056
H      1.0   0.3416758535  -3.6673868771  -1.5919714090
H      1.0   0.1116120968  -3.1058027702   0.0988533248
H      1.0   1.7797035917  -3.2429045614  -0.5667673745
C      6.0   2.8331320968   0.7587724039  -0.8882957338
O      8.0   3.6276325897   1.1967617439  -1.6416230763
C      6.0   2.2812551591   1.3086297405   1.5961743408
N      7.0   2.6047164086   2.0786862042   2.4420484583
C      6.0   2.9539730123  -1.2486192151   0.7142159509
N      7.0   3.7204482225  -2.1157902611   0.9847718579
S     16.0  -3.1697047377   0.7665249358  -1.9363646197
S     16.0  -2.3745044013  -1.9809099021   0.1292596744
C      6.0  -2.9987618478   2.6053812313  -1.9278888988
```

```
H       1.0  -3.4665952219  3.0271789358  -2.8369512605
H       1.0  -1.9335919663  2.8949164324  -1.9080067169
H       1.0  -3.4992097329  3.0507855568  -1.0481214427
C       6.0  -3.9301603787  -1.3318253808  0.8885058564
H       1.0  -3.7218339610  -0.8206636036  1.8458523814
H       1.0  -4.6221907532  -2.1715303726  1.0880347277
H       1.0  -4.4077366974  -0.6127961126  0.2019233311
H       1.0   0.9004179468  -0.5404027381  1.6279208048
H       1.0   0.3227029589  -0.6174003519  1.0742440046
```

Atomic Cartesian coordinates (Å) of conformer S optimized with TPSS/bs1 level of theory, E= -2346.562297 Hartree

```
Fe     26.0   1.6046569949  -0.2176741208  0.2133384134
Ni     28.0  -1.2888952035   0.4672057212  0.2314162680
S      16.0  -0.2660037286  -1.4499412978  0.8515481938
S      16.0   0.4195898875   1.3216088098  1.4288340626
C       6.0  -0.6205384380  -2.7872648210  -0.3791309990
H       1.0  -0.8906538579  -3.6974318002  0.1723142644
H       1.0   0.2776508683  -2.9555486532  -0.9803843270
H       1.0  -1.4551538905  -2.4610379737  -1.0116812867
C       6.0   0.9019025517   3.0662915649  1.0696529691
H       1.0   0.9388858511   3.6079297336  2.0235549893
H       1.0   0.1238893429   3.4862957643  0.4189874262
H       1.0   1.8774897113   3.0746167219  0.5740579027
C       6.0   2.7113323907  -0.7986736516  1.3565188973
O       8.0   3.4655956779  -1.2006911873  2.1741557834
C       6.0   2.1487635892  -1.4625794306  -1.1196801913
N       7.0   2.4704810981  -2.2585485687  -1.9392673176
C       6.0   2.8192085365   1.0690287752  -0.4813959017
N       7.0   3.5760796341   1.8891975223  -0.8851785074
S      16.0  -3.2267426390  -0.4492013434  -0.4266881394
S      16.0  -1.9940398061   2.4152409402  -0.6568344003
C       6.0  -3.6437786982  -1.7590542356  0.8156128836
H       1.0  -3.4757985021  -1.3960205251  1.8363482786
H       1.0  -3.0629511816  -2.6798078357  0.6749057484
H       1.0  -4.7111217646  -2.0002733476  0.6975172348
C       6.0  -3.4557775136   2.8881126310  0.3586163782
H       1.0  -3.9487426899   3.7524713765  -0.1121753133
H       1.0  -3.1602977509   3.1662781596  1.3804980828
H       1.0  -4.1536229296   2.0418136419  0.3981282370
```

Atomic Cartesian coordinates (Å) of conformer T optimized with TPSS/bs1 level of theory, E=-2346.555124 Hartree

```
FE      26.0   1.4071434967  -0.5120637872   1.0308143537
NI      28.0  -1.4283778301   0.5111798159   0.1539891736
S       16.0   0.6366620463   0.4399332489  -0.9601235353
S       16.0  -0.6747026231  -1.5720799262   0.9279040074
C        6.0   1.2357562773   2.1810478871  -1.1396278391
H        1.0   1.1393703954   2.4684404544  -2.1941490350
H        1.0   2.2801199823   2.2303778342  -0.8154054506
H        1.0   0.6212198882   2.8422038352  -0.5205214984
C        6.0  -1.3744583848  -1.8287665395   2.6211379363
H        1.0  -2.1279889743  -2.6243033992   2.5631216359
H        1.0  -1.8454305816  -0.9007802684   2.9613296780
H        1.0  -0.5654270143  -2.1078522135   3.3035592551
C        6.0   2.3404144156  -1.7475574799   0.3533381354
O        8.0   2.9877063593  -2.6111186794  -0.1259729371
C        6.0   2.8757476224   0.6921802956   1.1434014788
N        7.0   3.7775821111   1.4619020743   1.1902792611
C        6.0   1.7083714178  -1.0984302405   2.8147799975
N        7.0   1.8634655331  -1.4725441101   3.9300969817
S       16.0  -3.1208459997   0.1725612526  -1.3633972942
S       16.0  -2.2406254347   2.2553633854   1.3629389262
C        6.0  -2.4577401073  -1.2009362341  -2.4010919732
H        1.0  -2.2526081636  -2.0841011700  -1.7841024050
H        1.0  -1.5247501694  -0.8937820867  -2.8885079627
H        1.0  -3.1974954363  -1.4637170652  -3.1728900881
C        6.0  -3.9029820581   2.6634225162   0.6785152779
H        1.0  -4.3105842036   3.5354964846   1.2109895586
H        1.0  -4.5884877776   1.8159030704   0.8007515961
H        1.0  -3.8330607870   2.8928920453  -0.3916132346
```

Atomic Cartesian coordinates (Å) of conformer S1 optimized with TPSS/bs1 level of theory, E= -2347.744463 Hartree

```
FE      26.0   1.7384193049   0.0385431626   0.0547380431
NI      28.0  -1.4622892473  -0.1001356717  -0.2105552410
S       16.0   0.0514851898   1.5240791029  -0.7091155143
S       16.0   0.2045570342  -1.3998613476  -1.0452221155
C        6.0  -0.0980995361   2.8313660268   0.5905659269
H        1.0  -0.6352695873   3.6881158744   0.1678845710
H        1.0   0.9130166324   3.1193075982   0.8949040946
H        1.0  -0.6606045962   2.4335688595   1.4407525787
C        6.0   0.2842270098  -3.1093918532  -0.3530294156
H        1.0   0.2306071060  -3.8154292650  -1.1917521687
H        1.0  -0.5826507402  -3.2471706224   0.3048451021
H        1.0   1.2318500633  -3.2293201340   0.1813656386
```

```
C       6.0   2.7093613976   0.2018301315  -1.3573265653
O       8.0   3.3901328191   0.3093975226  -2.3103117361
C       6.0   2.7460836979   1.3992750094   0.9556842515
N       7.0   3.3480905284   2.2657107281   1.4966577980
C       6.0   2.8472216541  -1.3776776927   0.7124661970
N       7.0   3.5013844372  -2.2839705515   1.1079705413
S      16.0  -3.2399431525   1.1912922790   0.1938317419
S      16.0  -2.7239330494  -1.7924396097   0.5859274221
C       6.0  -3.1404345829   2.7420686916  -0.8227226985
H       1.0  -2.4835027462   2.6021173777  -1.6897098027
H       1.0  -2.7714519183   3.5980062592  -0.2403194320
H       1.0  -4.1523652454   2.9826420762  -1.1815666056
C       6.0  -3.8289485545  -2.1352981731  -0.8475975105
H       1.0  -4.5774142896  -2.8860927391  -0.5514509388
H       1.0  -3.2621676815  -2.5204396857  -1.7069780424
H       1.0  -4.3372922043  -1.2054271540  -1.1336595261
H       1.0   1.1259845363  -0.1154588051   1.7134109469
H       1.0   0.4476015007  -0.1472238247   1.3111837597
```

Atomic Cartesian coordinates (Å) of conformer S2 optimized with TPSS/bs1 level of theory, E= -2347.746837 Hartree

```
FE     26.0   1.8338564052   0.1095074565   0.1188329040
NI     28.0  -1.3936261301  -0.1540322272  -0.6903828051
S      16.0   0.0811888423   1.5556846682  -0.4859356184
S      16.0   0.5014423620  -1.2905623101  -1.2353661034
C       6.0  -0.4095170488   2.4054204038   1.0784084724
H       1.0  -1.2850185190   3.0298598104   0.8721694936
H       1.0   0.4459502076   2.9965989385   1.4219485089
H       1.0  -0.6772575732   1.6635224177   1.8384759738
C       6.0   0.5567974822  -2.9905759111  -0.5234991516
H       1.0   0.1094864603  -3.6849687038  -1.2429674386
H       1.0  -0.0223580471  -3.0201170202   0.4057490746
H       1.0   1.6060335891  -3.2349746978  -0.3292791019
C       6.0   2.8427883537   0.5911655103  -1.1904971587
O       8.0   3.5493597647   0.9173333158  -2.0718773993
C       6.0   2.6513783676   1.4043493768   1.2822512278
N       7.0   3.1250381191   2.2237309677   1.9957340114
C       6.0   3.0729633662  -1.2805057273   0.5959780039
N       7.0   3.8126368713  -2.1648706759   0.8714341428
S      16.0  -3.1992547886   1.1836764461  -0.6014899821
S      16.0  -2.5436384876  -2.0649125402  -0.5095030405
C       6.0  -2.8369008030   2.5781218224  -1.7584451935
H       1.0  -2.6796099673   2.2083314748  -2.7799908277
H       1.0  -1.9447387645   3.1400085209  -1.4560389599
```

H	1.0	-3.7045168369	3.2554000143	-1.7582038640
C	6.0	-4.3313756528	-1.7907850905	-0.1594885296
H	1.0	-4.5081441144	-1.5621956291	0.9009023968
H	1.0	-4.8767018778	-2.7111457538	-0.4165546892
H	1.0	-4.7086573824	-0.9547797239	-0.7614966741
H	1.0	1.1736451833	-0.3023420777	1.7086986876
H	1.0	0.5724063990	-0.4939594858	1.2413049399

Atomic Cartesian coordinates (Å) of conformer T1 optimized with TPSS/bs1 level of theory, E= -2347.743459 Hartree

FE	26.0	1.6691920975	0.0074258155	-0.0416852871
NI	28.0	-1.4878562316	0.0364801107	-0.0394641534
S	16.0	0.0462790450	-1.3581370413	1.0454767280
S	16.0	0.0786570185	1.7324237833	0.3583648036
C	6.0	-0.0669960391	-2.9496217006	0.1127708866
H	1.0	-0.6677775386	-3.6497161433	0.7073451691
H	1.0	0.9446909196	-3.3415893244	-0.0366999775
H	1.0	-0.5591501148	-2.7777471637	-0.8508641242
C	6.0	-0.0156158992	2.7472420306	-1.1835487145
H	1.0	-0.6371159565	3.6281003791	-0.9782394202
H	1.0	-0.4770244498	2.1612945845	-1.9868864158
H	1.0	0.9986788212	3.0483660129	-1.4661757186
C	6.0	2.4705853114	0.3210119464	1.4551293816
O	8.0	3.0355823129	0.5340184816	2.4620063035
C	6.0	2.8010291340	-1.5097038974	-0.3676650429
N	7.0	3.4697927954	-2.4698708306	-0.5552272409
C	6.0	2.8398086463	1.2276156462	-0.9529720264
N	7.0	3.5342393467	2.0053696654	-1.5164074224
S	16.0	-3.3132952304	0.3756498746	1.3232685220
S	16.0	-2.3864176160	-0.4983851577	-2.0880231161
C	6.0	-2.5126918042	0.7944652568	2.9311009748
H	1.0	-1.8426146310	1.6543902852	2.8107069455
H	1.0	-1.9251613118	-0.0549550879	3.3009427506
H	1.0	-3.2861371427	1.0440101307	3.6738389900
C	6.0	-4.2101566662	-0.5454779570	-1.8054891196
H	1.0	-4.7119269796	-0.8756678154	-2.7271246987
H	1.0	-4.5863518856	0.4471661083	-1.5295273036
H	1.0	-4.4545375262	-1.2405177688	-0.9935317542
H	1.0	1.3060334309	-0.2080118561	-1.7453671293
H	1.0	0.6139938838	-0.4030724976	-1.4199618899

Atomic Cartesian coordinates (Å) of conformer T2 optimized with TPSS/bs1 level of theory, E= -2347.747387 Hartree

```
FE      26.0   1.6446654557   0.0888555212   0.1280635596
NI      28.0  -1.4533798536  -0.3389807962  -1.1306598167
S       16.0  -0.2217755791   1.4945994932  -0.2638668993
S       16.0   0.6839189463  -1.2636064522  -1.5770284552
C        6.0  -0.9506696104   1.7997301226   1.4030980113
H        1.0  -1.8167779992   2.4647610119   1.2915426536
H        1.0  -0.1855425326   2.2627376979   2.0353873862
H        1.0  -1.2748798697   0.8506484789   1.8458422352
C        6.0   0.7643086801  -2.9880142104  -0.9312842824
H        1.0   0.3496528874  -3.6637378428  -1.6899077937
H        1.0   0.1739926718  -3.0729723384  -0.0116782582
H        1.0   1.8101318588  -3.2338629385  -0.7203940642
C        6.0   2.6522738174   0.9547939855  -0.9738950519
O        8.0   3.3527788362   1.5431321545  -1.7117234328
C        6.0   2.2159621830   1.1919996064   1.5942289936
N        7.0   2.5269465044   1.8870819124   2.5025223097
C        6.0   3.0352220905  -1.1983664963   0.4457262106
N        7.0   3.8761779875  -2.0145424334   0.6227385321
S       16.0  -2.8953505825   0.5666917365  -2.6431416935
S       16.0  -2.2567135242  -1.7860016862   0.4426365380
C        6.0  -2.6863471681   2.3996013027  -2.7302686275
H        1.0  -2.4186816289   2.6992321201  -3.7530949782
H        1.0  -1.8901697667   2.7176579149  -2.0467768705
H        1.0  -3.6238234862   2.9047035905  -2.4554288932
C        6.0  -3.7835561551  -0.8922592394   0.9820420845
H        1.0  -4.5276584094  -1.6178623012   1.3423842004
H        1.0  -4.2041063262  -0.3297080646   0.1398624132
H        1.0  -3.5582069359  -0.1925562170   1.7987219518
H        1.0   0.9516693123  -0.7793267974   1.4754531316
H        1.0   0.3312908743  -0.7752556906   0.9898664664
```

Atomic Cartesian coordinates (Å) of MECP(S2/T2) optimized with TPSS/bs1 level of theory, E= -2347.740315 Hartree

```
FE      26.0   1.6772121833   0.1000000211   0.1112644656
NI      28.0  -1.4261629791  -0.1908459189  -0.9758378281
S       16.0   0.0018178969   1.6132648450  -0.5719569361
S       16.0   0.6018315313  -1.2328580643  -1.5333580726
C        6.0  -0.6925318600   2.3628015478   0.9650952854
H        1.0  -1.4327808548   3.1216645608   0.6827965416
H        1.0   0.1319112922   2.8142270817   1.5270460804
H        1.0  -1.1769196387   1.5938588080   1.5769404919
C        6.0   0.6784511465  -2.9733596566  -0.9366109593
H        1.0   0.2306386966  -3.6230125931  -1.6988297063
H        1.0   0.1089157839  -3.0660207343  -0.0045851448
```

```
H        1.0   1.7259481636  -3.2371676965  -0.7604335846
C        6.0   2.8228382087   0.7407959274  -1.0051012723
O        8.0   3.6181265738   1.1714813935  -1.7560182479
C        6.0   2.2886490983   1.2706640784   1.5055129565
N        7.0   2.6301416166   2.0175166176   2.3604295413
C        6.0   2.9142655700  -1.2887801943   0.5934846579
N        7.0   3.6709227667  -2.1615598889   0.8588969657
S       16.0  -3.2710009827   0.8626892040  -1.7373415802
S       16.0  -2.3717869856  -2.0015461267   0.0045451155
C        6.0  -3.0034706588   2.6845570587  -1.8638870071
H        1.0  -3.5909525775   3.0769714050  -2.7070279119
H        1.0  -1.9427058185   2.9050718981  -2.0331835067
H        1.0  -3.3292563254   3.2010578433  -0.9496409903
C        6.0  -3.8561941559  -1.3976014103   0.9275049926
H        1.0  -3.6030919858  -1.2014810619   1.9793146275
H        1.0  -4.6526712239  -2.1555654020   0.8955354660
H        1.0  -4.2094668802  -0.4715150337   0.4612132077
H        1.0   0.8448841773  -0.5554981490   1.5222945045
H        1.0   0.2752073833  -0.6194492571   0.9833352295
```

Atomic Cartesian coordinates (Å) of conformer S optimized with B3LYP/bs1 level of theory, E= -2345.860730 Hartree

```
FE     26.0   1.7416477969  -0.2750844310   0.1939416590
NI     28.0  -1.4470981304   0.5231267203   0.7459645010
S      16.0  -0.2403166348  -1.4801622375   0.6323614273
S      16.0   0.6126068859   1.1966676112   1.6226631638
C       6.0  -0.7753623025  -2.3189813325  -0.9153010714
H       1.0  -1.6436807061  -2.9451078222  -0.6949074028
H       1.0   0.0542239989  -2.9202520762  -1.2906882780
H       1.0  -1.0605149479  -1.5808506085  -1.6660910638
C       6.0   1.0768136140   2.9477411507   1.3164935041
H       1.0   0.8150637955   3.5389601525   2.1984915980
H       1.0   0.5231296816   3.3301150934   0.4562317318
H       1.0   2.1488089641   2.9964631806   1.1195406292
C       6.0   2.7425287275  -1.0651923736   1.3493909925
O       8.0   3.4132402246  -1.5943523586   2.1370429734
C       6.0   2.2811230335  -1.4482515245  -1.2518774549
N       7.0   2.5821821988  -2.1699661610  -2.1274428027
C       6.0   3.1029161946   1.0164134341  -0.2795153685
N       7.0   3.9172069736   1.8199331578  -0.5432302358
S      16.0  -3.5137688719  -0.4237919057   0.4635605264
S      16.0  -2.1367991379   2.6676098789   0.4348642375
C       6.0  -3.5399313225  -1.9141318096   1.5449410645
H       1.0  -3.4451787382  -1.6413261690   2.6023278786
```

```
H    1.0 -2.7350186097  -2.6144483114  1.3055407258
H    1.0 -4.5019975390  -2.4249484278  1.4087468822
C    6.0 -3.8230235598   2.7238371419 -0.2933506204
H    1.0 -3.8350362594   2.3375426307 -1.3184664337
H    1.0 -4.1538397298   3.7701726607 -0.3137957160
H    1.0 -4.5255265493   2.1341912358  0.3015595829
```

Atomic Cartesian coordinates (Å) of conformer T optimized with B3LYP/bs1 level of theory, E= -2345.869613 Hartree

```
FE    26.0   1.4771794788 -0.5498449713  1.0265001745
NI    28.0  -1.5579603458  0.5327384040  0.1173565317
S     16.0   0.6235155195  0.5828825233 -0.8807346054
S     16.0  -0.6839043577 -1.5459484920  0.9820579949
C      6.0   1.2030154754  2.3310953393 -0.9285351994
H      1.0   1.0774780321  2.7098669724 -1.9476522874
H      1.0   2.2541923203  2.3684155459 -0.6367698814
H      1.0   0.6055728991  2.9396547612 -0.2461994038
C      6.0  -1.3322750018 -1.7488190563  2.6952769040
H      1.0  -2.1964305730 -2.4194770922  2.6616623106
H      1.0  -1.6468157849 -0.7839535648  3.1001475563
H      1.0  -0.5482619967 -2.1688133830  3.3279893318
C      6.0   2.3035368013 -1.8057653977  0.1821614261
O      8.0   2.8580515897 -2.6518604182 -0.3875131935
C      6.0   3.0345784546  0.5949400881  1.1176788979
N      7.0   3.9609266284  1.3150441702  1.1566201015
C      6.0   1.8637773491 -1.2907892717  2.7724006149
N      7.0   2.0601925012 -1.7425275469  3.8380424370
S     16.0  -3.1830237190  0.0672814945 -1.4817389287
S     16.0  -2.3454064715  2.4043163655  1.2529744118
C      6.0  -2.4487198699 -1.3596714847 -2.3844065488
H      1.0  -2.2683406047 -2.2011123616 -1.7088167765
H      1.0  -1.4961235136 -1.0772807350 -2.8434494186
H      1.0  -3.1360234486 -1.6837445963 -3.1766234929
C      6.0  -4.0048118619  2.7501543015  0.5309681557
H      1.0  -4.4116935298  3.6646903679  0.9798017179
H      1.0  -4.6985927903  1.9261399288  0.7221739022
H      1.0  -3.9356391803  2.8872591090 -0.5518287325
```

Atomic Cartesian coordinates (Å) of conformer S1 optimized with B3LYP/bs1 level of theory, E= -2347.034899 Hartree

```
FE    26.0   1.7118937536  0.0539937123 -0.0126446290
NI    28.0  -1.7262255248  0.0762765993 -0.2580762147
```

```
S      16.0 -0.0160118968   1.6377486366  -0.5193704038
S      16.0  0.0062794774  -1.3876918195  -0.8866098834
C       6.0 -0.1420903038   2.6993216580   0.9781834192
H       1.0 -0.8420782236   3.5162217070   0.7853014280
H       1.0  0.8515046803   3.0947695912   1.1992556483
H       1.0 -0.5069200384   2.1249391104   1.8339993422
C       6.0  0.0122830457  -2.9953024308   0.0075989191
H       1.0 -0.2402584050  -3.7951435880  -0.6964440014
H       1.0 -0.7424501916  -2.9643365817   0.7982701491
H       1.0  1.0115009687  -3.1709563021   0.4106766946
C       6.0  2.4643588930   0.2302243853  -1.5886747246
O       8.0  2.9758228240   0.3449593448  -2.6208246772
C       6.0  2.8792767955   1.4181109253   0.7522942130
N       7.0  3.5475219103   2.2635396698   1.2163734500
C       6.0  2.9208785293  -1.4048237218   0.4564378677
N       7.0  3.6118649947  -2.3087280028   0.7432648667
S      16.0 -3.5050309104   1.4709910492  -0.3477728591
S      16.0 -3.1333596486  -1.5232868308   0.6065097579
C       6.0 -3.0377769535   3.0559938942  -1.1758231302
H       1.0 -2.3477830980   2.8941288268  -2.0086575068
H       1.0 -2.5755766817   3.7723114189  -0.4870152033
H       1.0 -3.9548202478   3.5152952675  -1.5672067455
C       6.0 -3.5360098980  -2.5390193446  -0.8729189024
H       1.0 -4.2123666946  -3.3530369123  -0.5834664927
H       1.0 -2.6364291168  -2.9741254542  -1.3222473226
H       1.0 -4.0368022668  -1.9228051234  -1.6277655918
H       1.0  0.7182399960  -0.3480948371   1.4268708923
H       1.0  1.2942200117   0.0805087225   1.7213529403
```

Atomic Cartesian coordinates (Å) of conformer S2 optimized with B3LYP/bs1 level of theory, E= -2347.037013 Hartree

```
FE     26.0  1.8722004239   0.1144765110   0.2439300321
NI     28.0 -1.4122877129  -0.1742103418  -0.6851515702
S      16.0  0.0824317979   1.5573141466  -0.3955989773
S      16.0  0.5404550586  -1.3424835706  -1.0999500506
C       6.0 -0.4704653959   2.3831361112   1.1501612191
H       1.0 -1.3383595728   3.0085059669   0.9292215449
H       1.0  0.3600523734   2.9797783545   1.5345024150
H       1.0 -0.7621557495   1.6421537461   1.8990015193
C       6.0  0.5766593478  -3.0226470162  -0.3595706836
H       1.0  0.1166736978  -3.7276400035  -1.0564040533
H       1.0  0.0132339760  -3.0432976766   0.5765238567
H       1.0  1.6198932448  -3.2852165470  -0.1729409631
C       6.0  2.8658346260   0.6023724890  -1.1170847772
```

```
O        8.0   3.5355537818   0.9212433666  -2.0061353533
C        6.0   2.6999680342   1.4603656423   1.3931634078
N        7.0   3.1645518744   2.2900268705   2.0804313234
C        6.0   3.1607338317  -1.2708665055   0.7334904220
N        7.0   3.9111906085  -2.1298421698   1.0087118782
S       16.0  -3.2557030751   1.1467857809  -0.7211607507
S       16.0  -2.5782863899  -2.1004596588  -0.4986995306
C        6.0  -2.8425226296   2.6165248755  -1.7520845051
H        1.0  -2.6530706265   2.3319209964  -2.7934328702
H        1.0  -1.9607625211   3.1472543452  -1.3831921018
H        1.0  -3.7003936333   3.3012649486  -1.7340436656
C        6.0  -4.3688212161  -1.8018674974  -0.2103863866
H        1.0  -4.5425817558  -1.2311900918   0.7076843324
H        1.0  -4.8628455080  -2.7772890503  -0.1143028701
H        1.0  -4.8172550064  -1.2481655348  -1.0392494762
H        1.0   1.2213669395  -0.2918740914   1.8534514609
H        1.0   0.6316527444  -0.4957947177   1.3926542584
```

Atomic Cartesian coordinates (Å) of conformer T1 optimized with B3LYP/bs1 level of theory, E= -2347.048110 Hartree

```
FE      26.0   1.7522091662  -0.0029055587   0.0057680667
NI      28.0  -1.5881264217   0.0284953428   0.0613317281
S       16.0   0.0639547677  -1.3823881266   1.0618086792
S       16.0   0.0940665685   1.7224902871   0.3950060566
C        6.0  -0.0304391150  -2.9857581537   0.1629249170
H        1.0  -0.6314653868  -3.6841416826   0.7542913987
H        1.0   0.9800438032  -3.3798751638   0.0332548294
H        1.0  -0.5099518147  -2.8468284566  -0.8094061747
C        6.0  -0.0003595718   2.7781866129  -1.1116005619
H        1.0  -0.6176584758   3.6550153888  -0.8914381707
H        1.0  -0.4561549731   2.2273102265  -1.9396797777
H        1.0   1.0092978064   3.0901743160  -1.3878330689
C        6.0   2.5116699852   0.3303045010   1.5567576295
O        8.0   3.0290970109   0.5484414891   2.5680990120
C        6.0   2.9284155015  -1.5281096639  -0.2860327755
N        7.0   3.6061684212  -2.4719255913  -0.4481085223
C        6.0   2.9477687628   1.2429236596  -0.9020555679
N        7.0   3.6310511464   2.0211384445  -1.4533803604
S       16.0  -3.4119899432   0.3723875309   1.4614026072
S       16.0  -2.4761598480  -0.6601035473  -1.9937323694
C        6.0  -2.6012203678   0.8428070744   3.0463294580
H        1.0  -1.9347659159   1.6986146699   2.9028537461
H        1.0  -2.0109518822   0.0109746910   3.4435924832
H        1.0  -3.3663954630   1.1128021869   3.7855087568
```

C	6.0	-4.3046000395	-0.5606043149	-1.7848110580
H	1.0	-4.7952363188	-1.0055073149	-2.6594258836
H	1.0	-4.6379812924	0.4772991273	-1.6879656008
H	1.0	-4.6217099217	-1.1013159437	-0.8887055656
H	1.0	1.1485119035	-0.7080941498	-1.5104985795
H	1.0	0.9606476480	0.0407479892	-1.5881644315

Atomic Cartesian coordinates (Å) of conformer T2 optimized with B3LYP/bs1 level of theory, E= -2347.052076 Hartree

FE	26.0	1.7014789000	0.0915910001	0.2503913828
NI	28.0	-1.4465131152	-0.3483671191	-1.0874248442
S	16.0	-0.2109815627	1.4960602720	-0.1550293055
S	16.0	0.7322104322	-1.3078661164	-1.4649323056
C	6.0	-0.9647798188	1.8304098786	1.4883868162
H	1.0	-1.8116207641	2.5129559448	1.3616541126
H	1.0	-0.2090567810	2.2863829302	2.1322502572
H	1.0	-1.3198828746	0.8999054971	1.9399142401
C	6.0	0.7831294094	-3.0233319882	-0.8088204706
H	1.0	0.3890398524	-3.7068994030	-1.5674515368
H	1.0	0.1726091417	-3.1089766788	0.0937370000
H	1.0	1.8185764659	-3.2786115437	-0.5728006000
C	6.0	2.6783340729	0.9769623166	-0.9142424550
O	8.0	3.3364264442	1.5573419808	-1.6688521952
C	6.0	2.2940507472	1.2499707099	1.7073367156
N	7.0	2.6076362719	1.9607623345	2.5865427849
C	6.0	3.1505057613	-1.1842710667	0.5462306254
N	7.0	4.0023194087	-1.9749681473	0.7064849475
S	16.0	-2.9234517110	0.5413071433	-2.6549513178
S	16.0	-2.3438340555	-1.7620575735	0.5171135058
C	6.0	-2.6975441922	2.3695637768	-2.7340073154
H	1.0	-2.4193527035	2.6736701736	-3.7498543321
H	1.0	-1.9085488783	2.6857956198	-2.0465692644
H	1.0	-3.6288108217	2.8839463534	-2.4665885908
C	6.0	-3.9145979657	-0.8969072011	0.9508691271
H	1.0	-4.6719363948	-1.6334422339	1.2465200999
H	1.0	-4.2871224320	-0.3309565633	0.0923448311
H	1.0	-3.7664788301	-0.2058441784	1.7892812970
H	1.0	1.0966788071	-0.8508985137	1.6121697076
H	1.0	0.4380286901	-0.7412556778	1.2146872136

Atomic Cartesian coordinates (Å) of MECP(S2/T2) optimized with B3LYP/bs1 level of

theory, E= -2347.034467 Hartree

```
FE   26.0   1.8586605107   0.1336177384   0.2500580222
NI   28.0  -1.4404534351  -0.1667396353  -0.6878914339
S    16.0   0.0835953593   1.5993576882  -0.4015605266
S    16.0   0.5722498975  -1.3116098074  -1.1630344183
C     6.0  -0.4933310612   2.4485858284   1.1233572266
H     1.0  -1.2484495959   3.1919049801   0.8537587892
H     1.0   0.3657405483   2.9303063262   1.5958662385
H     1.0  -0.9381659717   1.7324152157   1.8189278118
C     6.0   0.6307936155  -3.0196803508  -0.4929262778
H     1.0   0.2162893011  -3.7057879296  -1.2364624474
H     1.0   0.0317285036  -3.0926717197   0.4182085015
H     1.0   1.6718939722  -3.2670746305  -0.2763517954
C     6.0   2.8761561436   0.6565884049  -1.0819327130
O     8.0   3.5608092005   0.9980574328  -1.9506640097
C     6.0   2.6538811281   1.4583689735   1.4435298731
N     7.0   3.0934528375   2.2778648304   2.1589589731
C     6.0   3.1468646486  -1.2525132938   0.7342423337
N     7.0   3.8998872402  -2.1104799259   1.0055718585
S    16.0  -3.3267041985   1.0671504424  -1.0447296896
S    16.0  -2.5599014238  -2.1065157195  -0.2151598619
C     6.0  -2.9001718264   2.7830282533  -1.5629554138
H     1.0  -3.5551681720   3.0811326718  -2.3915653200
H     1.0  -1.8613382943   2.8468960936  -1.8957347533
H     1.0  -3.0450113749   3.5017223062  -0.7461386774
C     6.0  -4.3261432436  -1.7674381380   0.1687379585
H     1.0  -4.4387654144  -1.1456079379   1.0627367722
H     1.0  -4.8308446956  -2.7265077556   0.3423352171
H     1.0  -4.8214330503  -1.2567269038  -0.6621451184
H     1.0   1.1718585714  -0.2750378450   1.8415145881
H     1.0   0.6205302635  -0.5415283939   1.3650733463
```

Atomic Cartesian coordinates (Å) of conformer S2 optimized with PBE/def2-TZVP level of theory, E= -4823.509835 Hartree

```
FE   26.0  -1.8718029213   0.0024662296  -0.2020112786
NI   28.0   1.4596306157  -0.0991881343   0.1571877549
S    16.0  -0.1133924783   1.4948501951   0.2137533004
S    16.0  -0.2597894773  -1.3517734362   0.8245754227
C     6.0   0.1362403315   2.4170445907  -1.3470278000
H     1.0   1.0005179774   3.0828311761  -1.2213383892
H     1.0  -0.7843855061   2.9786498698  -1.5565752942
H     1.0   0.3450933923   1.7269024396  -2.1746781440
C     6.0  -0.3113992031  -3.0233465671   0.0865447012
```

H	1.0	0.3075563113	-3.6914633646	0.7011025716
H	1.0	0.0975233403	-3.0103488356	-0.9334455472
H	1.0	-1.3591014576	-3.3519948346	0.0751679494
C	6.0	-2.6803645735	0.3429874071	1.2733048334
O	8.0	-3.2556743783	0.5694090350	2.2652702713
C	6.0	-2.9281055151	1.3155726775	-1.1000640807
N	7.0	-3.5478077447	2.1494700048	-1.6554566341
C	6.0	-3.0933682668	-1.4281013687	-0.5289624843
N	7.0	-3.8144954149	-2.3403668959	-0.7174967212
S	16.0	3.1804471477	1.3045601606	0.0127622358
S	16.0	2.6422891049	-1.8830346654	-0.4165264576
C	6.0	2.8426869143	2.7165731372	1.1293151295
H	1.0	2.7636446872	2.3912187788	2.1780736529
H	1.0	1.9124392304	3.2444019868	0.8717391042
H	1.0	3.6854993575	3.4233249397	1.0442164207
C	6.0	4.3361049741	-1.4568398566	-0.9490824215
H	1.0	4.3509447195	-0.9553632728	-1.9303604464
H	1.0	4.9165920364	-2.3914188031	-1.0206706117
H	1.0	4.8121196825	-0.7813617563	-0.2214267185
H	1.0	-1.4944325907	-0.2133572328	-1.8768147668
H	1.0	-0.8302755153	-0.5056984144	-1.5120876217

Atomic Cartesian coordinates (Å) of conformer T2 optimized with PBE/def2-TZVP level of theory, E= -4823.495878 Hartree

FE	26.0	-1.7848917133	0.0621662673	-0.1117858918
NI	28.0	1.5556146608	-0.2434677214	0.3026055288
S	16.0	0.0913121045	1.4320261307	-0.4263619422
S	16.0	-0.3482633422	-1.0775964438	1.3713048551
C	6.0	0.3561255662	1.5484842940	-2.2310160526
H	1.0	1.2466017403	2.1692837351	-2.4112837438
H	1.0	-0.5312313435	2.0062867829	-2.6901123747
H	1.0	0.5202202243	0.5497837581	-2.6600313832
C	6.0	-0.5700940708	-2.8613891581	1.0478929098
H	1.0	0.0248366620	-3.4222620566	1.7839412084
H	1.0	-0.2139568191	-3.1108549795	0.0382876504
H	1.0	-1.6354714342	-3.1124733037	1.1396956240
C	6.0	-2.4308782321	1.0656199280	1.1265741460
O	8.0	-2.8960049031	1.7429926887	1.9566472654
C	6.0	-2.7665765692	1.0267644109	-1.4369722228
N	7.0	-3.3331626136	1.6329785791	-2.2728684026
C	6.0	-3.1959479971	-1.1901620852	0.1784744303
N	7.0	-4.0457896059	-1.9821105205	0.3731670917
S	16.0	3.2737431791	0.8780719269	1.1832629116
S	16.0	2.0063274526	-1.9339430288	-1.0953337837

C	6.0	3.1438410911	2.6809204881	0.8921447889
H	1.0	3.2537692456	3.2309817769	1.8411051804
H	1.0	2.1629008397	2.9250765528	0.4565626408
H	1.0	3.9350329361	3.0227164069	0.2042629430
C	6.0	3.3210391908	-1.2486973813	-2.1731388684
H	1.0	3.8742353854	-2.0739478134	-2.6527750445
H	1.0	4.0195286409	-0.6364986499	-1.5839152219
H	1.0	2.8931924431	-0.6161702594	-2.9679001020
H	1.0	-1.5876863615	-0.9995144461	-1.4491932817
H	1.0	-0.8162510074	-0.8708967386	-1.2273014589

Atomic Cartesian coordinates (Å) of MECP(S/T) optimized with PBE/def2-TZVP level of theory, E= -4822.315699 Hartree

FE	26.0	1.5514086659	-0.2673098677	0.1952080360
NI	28.0	-1.3794190365	0.3725631366	0.3227045693
S	16.0	-0.2708482383	-1.6256809708	0.4386516379
S	16.0	0.3471610570	0.9701639472	1.7064468146
C	6.0	-0.6276965666	-2.6112585288	-1.0658901993
H	1.0	-1.2931933496	-3.4402046261	-0.7835171592
H	1.0	0.3152086598	-2.9878123343	-1.4829478926
H	1.0	-1.1252415683	-1.9833085541	-1.8153214567
C	6.0	0.6808781611	2.7662842968	1.5820728663
H	1.0	0.3344199346	3.2450970481	2.5104053333
H	1.0	0.1303059833	3.1680693920	0.7207871235
H	1.0	1.7584034850	2.9221437652	1.4398218246
C	6.0	2.6489087511	-1.0363140151	1.2172982952
O	8.0	3.4047095961	-1.5762861653	1.9391711147
C	6.0	2.1662723386	-1.2209611415	-1.3185999123
N	7.0	2.5266339010	-1.8502451176	-2.2488272684
C	6.0	2.7617317058	1.1457623995	-0.1641254031
N	7.0	3.5163900818	2.0322877170	-0.3522298462
S	16.0	-3.4869349933	-0.0771536446	0.9835616166
S	16.0	-1.8585872205	2.0398665407	-1.0936983456
C	6.0	-3.4234524531	-1.6186025283	1.9649499852
H	1.0	-2.7543942592	-1.5096810804	2.8314695629
H	1.0	-3.0595787219	-2.4658532436	1.3657129249
H	1.0	-4.4389165839	-1.8510862298	2.3281535945
C	6.0	-3.4462123861	2.7929827057	-0.5966332867
H	1.0	-3.7255034573	3.5718624053	-1.3251544737
H	1.0	-3.3772860273	3.2495224902	0.4027399754
H	1.0	-4.2407684091	2.0310787036	-0.5632134014

Atomic Cartesian coordinates (Å) of MECP(S2/T2) optimized with PBE/def2-TZVP level of theory, E= -4823.493347 Hartree

```
FE      26.0   2.1287143205   0.2918637448   0.8009308459
NI      28.0  -0.9439234360  -0.0725290373  -0.4172830783
S       16.0   0.4360796317   1.7369937955   0.0907460605
S       16.0   1.1206974958  -1.0601303313  -0.8484086325
C        6.0  -0.3191812818   2.4883516548   1.5781249166
H        1.0  -1.0838597584   3.2112924183   1.2552377518
H        1.0   0.4652658345   2.9924711756   2.1592034075
H        1.0  -0.7924701269   1.7167718363   2.2003310022
C        6.0   1.2200850426  -2.7922570755  -0.2785119946
H        1.0   0.8235240432  -3.4412131294  -1.0735061860
H        1.0   0.6147354188  -2.9268562130   0.6292039206
H        1.0   2.2682536690  -3.0374218233  -0.0609969820
C        6.0   3.2774923294   0.9577729813  -0.2881926662
O        8.0   4.0767707929   1.4060839623  -1.0133327109
C        6.0   2.6925217374   1.4966272759   2.1676514928
N        7.0   3.0066225017   2.2644690487   3.0041441547
C        6.0   3.3990393101  -1.0469133571   1.2862759721
N        7.0   4.1758694775  -1.8905925077   1.5550094023
S       16.0  -2.6323390393   0.9176983397  -1.4834436297
S       16.0  -1.8481687896  -1.7489052406   0.7476013799
C        6.0  -2.4960598892   2.7422803251  -1.4496831183
H        1.0  -3.0339643992   3.1671773048  -2.3134468180
H        1.0  -1.4414267168   3.0550768456  -1.4947331094
H        1.0  -2.9391803417   3.1596009169  -0.5305056925
C        6.0  -3.3700176100  -1.0787030063   1.5153176605
H        1.0  -4.0498944986  -1.9091653897   1.7707508937
H        1.0  -3.8716263197  -0.3919075508   0.8174877332
H        1.0  -3.1361770134  -0.5278112283   2.4406824240
H        1.0   1.3328493261  -0.3635197159   2.1920466672
H        1.0   0.7529945917  -0.4429180827   1.6295533456
```

Appendix B - Supporting Information for Chapter IV
Spin-Forbidden Transitions between Electronic States in the Active Site of
Rubredoxin
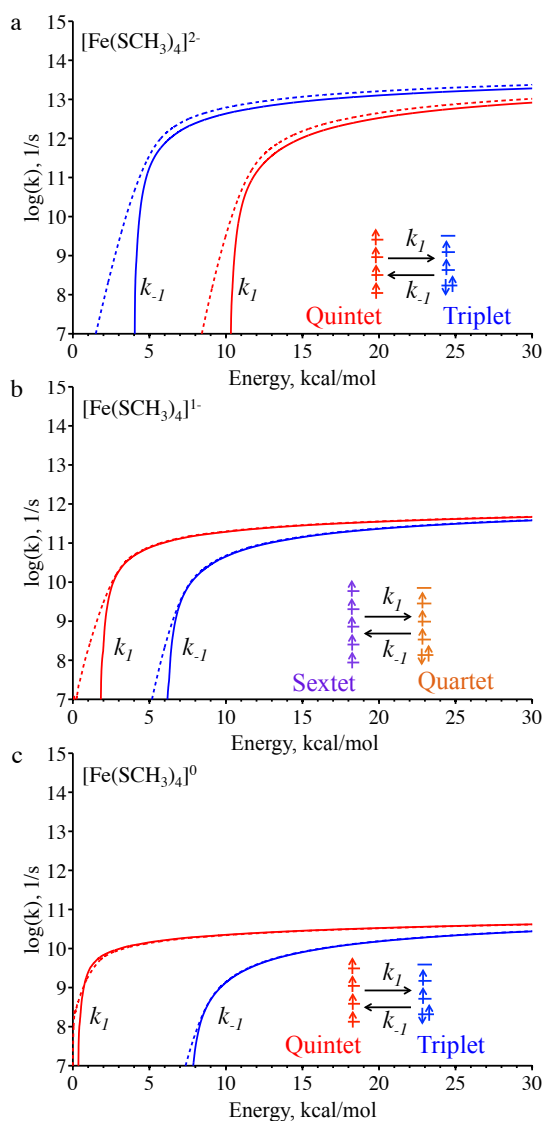
Figure S1. Rate constants for transitions between electronic spin states of rubredoxin active site models calculated with the LZ (solid lines) and WC (dashed lines) probabilities as functions of internal energy. Rate constant k_1 (red lines) represents the transition from high-spin state to low-spin states, while k_{-1} (blues lines) is the rate constant for opposite process. a) Quintet-triplet transitions in $Fe(SCH_3)_4^{2-}$ cluster b) Sextet-quartet transitions in $Fe(SCH_3)_4^{1-}$ cluster. c) Quintet-triplet transitions in $Fe(SCH_3)_4^0$ cluster. The geometries, energies, energy gradients and Hessians were obtained at the PBE/def2-TZVP level of theory. SOC was calculated at CASCI/def2-TZVP level of theory using the high-spin ROHF molecular orbitals.

Weak coupling formula

The weak coupling (WC) formula accounts for quantum tunneling through the MECP barrier:[1–4]

$$P^{WC}\left(\varepsilon_\perp\right) = 4\pi^2 H_{SO}^2 \left(\frac{2\mu_\perp}{\hbar^2 \bar{G} |\Delta G|}\right)^{2/3} \text{Ai}^2\left(-\left(\varepsilon_\perp - E_{MECP}\right)\left(\frac{2\mu_\perp |\Delta G|^2}{\hbar^2 \bar{G}^4}\right)^{1/3}\right).$$

Here Ai is the Airy function and $\bar{G} = \left(G_1 G_2\right)^{1/2}$ is the geometric mean of the gradients G_1 and G_2 of two spin-diabatic states at MECP.

Table S1. Geometries of the rubredoxin active site models obtained with different levels of theory. rFe-S is the bond length between iron and sulfur. θ S-Fe-S is the average of the bond angles between S1-Fe-S4 and S2-Fe-S3. θ S-Fe-S' is the average of the bond angles between S1-Fe-S2, S1-Fe-S3, S2-Fe-S4, and S3-Fe-S4. φ C-S-Fe-S is the average of the dihedral angles C3-S3-Fe-S4 and C2-S2-Fe-S1. φ C'-S'-Fe-S is the average of the dihedral angles C1-S1-Fe-S2 and C4-S4-Fe-S3.

	r Fe-S (Å)	θ S-Fe-S (deg)	θ S-Fe-S' (deg)	φ C-S-Fe-S (deg)	φ C'-S'-Fe-S (deg)
B3LYP/def2-TZVP					
$[Fe(SCH_3)_4]^0$ triplet	2.156	120.8	104.2	178.6	20.7
$[Fe(SCH_3)_4]^0$ quintet	2.230	133.2	99.1	177.3	25.1
$[Fe(SCH_3)_4]^{1-}$ quartet	2.316	163.6	91.2	179.2	17.0
$[Fe(SCH_3)_4]^{1-}$ sextet	2.320	111.7	108.4	178.5	42.4
$[Fe(SCH_3)_4]^{2-}$ triplet	2.339	164.3	91.1	178.8	14.3
$[Fe(SCH_3)_4]^{2-}$ quintet	2.430	111.0	108.7	170.6	49.6
B3LYP/6-31G**					
$[Fe(SCH_3)_4]^0$ triplet	2.160	120.3	104.4	177.9	18.4
$[Fe(SCH_3)_4]^0$ quintet	2.231	132.0	99.5	166.9	31.1
$[Fe(SCH_3)_4]^{1-}$ quartet	2.260	138.2	97.3	167.3	26.5
$[Fe(SCH_3)_4]^{1-}$ sextet	2.318	111.1	108.6	177.2	56.2
$[Fe(SCH_3)_4]^{2-}$ triplet	2.341	169.4	90.5	179.3	11.3
$[Fe(SCH_3)_4]^{2-}$ quintet	2.431	112.8	107.9	170.5	48.3
$[Fe(SCH_3)_4]^0$ quintet[a]	2.228	133.0	99.0	167.4	30.9
$[Fe(SCH_3)_4]^{1-}$ sextet[a]	2.315	110.5	108.9	179.4	58.7
$[Fe(SCH_3)_4]^{2-}$ quintet[a]	2.428	113.7	107.4	170.5	47.8
PBE/6-31G**					
$[Fe(SCH_3)_4]^0$ triplet	2.128	121.9	103.7	178.1	20.8
$[Fe(SCH_3)_4]^0$ quintet	2.209	134.3	98.7	170.7	33.2
$[Fe(SCH_3)_4]^{1-}$ quartet	2.215	139.4	96.9	167.2	25.4
$[Fe(SCH_3)_4]^{1-}$ sextet	2.303	110.3	109.0	177.5	57.0
$[Fe(SCH_3)_4]^{2-}$ triplet	2.282	173.1	90.2	178.3	8.5
$[Fe(SCH_3)_4]^{2-}$ quintet	2.358	114.2	107.2	170.8	48.3
PBE/def2-TZVP					
$[Fe(SCH_3)_4]^0$ triplet	2.124	122.4	103.5	178.8	22.6
$[Fe(SCH_3)_4]^0$ quintet	2.198	131.9	99.3	154.7	31.4
$[Fe(SCH_3)_4]^{1-}$ quartet	2.204	139.5	96.1	168.7	26.8
$[Fe(SCH_3)_4]^{1-}$ sextet	2.296	110.9	108.8	179.8	59.2

[Fe(SCH$_3$)$_4$]$^{2-}$ triplet	2.268	170.2	90.4	179.3	10.4
[Fe(SCH$_3$)$_4$]$^{2-}$ quintet	2.350	111.7	108.4	170.7	49.3
Experimental					
[Fe(SCH$_3$)$_4$]$^{1-}$ [b]	2.263	114.2	107.0	173.0	63.9

[a]B3LYP/6-31G** (Ref. 5); [b] Experiment (Ref. 6)

Table S2. Adiabatic detachment energies (eV).

	B3LYP		PBE		MP2	CCSD	CCSD(T)
	6-31G**	def2-TZVP	6-31G**	def2-TZVP		def2-TZVP	
Triplet/Quartet					1.80	3.84	3.29
$[Fe(SCH_3)_4]^{1-/0}$	3.03	2.61	2.27	2.31			
$[Fe(SCH_3)_4]^{2-/1-}$	-2.73	-2.01	-2.91	-2.78	-2.46	-2.49	-2.67
Quintet/Sextet							
$[Fe(SCH_3)_4]^{1-/0}$	3.15	3.12	2.47	2.44	3.41	4.03	3.55
$[Fe(SCH_3)_4]^{2-/1-}$	-2.15	-1.76	-2.65	-2.19	-1.45	-1.76	-1.95
$[Fe(SCH_3)_4]^{1-/0}$ [a]	3.24						
$[Fe(SCH_3)_4]^{2-/1-}$ [a]	-2.08						
$[Fe(SCH_3)_4]^{1-/0}$ [b]	3.38						
$[Fe(SCH_3)_4]^{2-/1-}$ [c]	-1.74						

[a] B3LYP/6-31G** (Ref. 5); [b] Experiment (Ref. 7); [c] Experiment (Ref. 8)

Table S3. MECP geometries of the rubredoxin active site obtained with different levels of theory. All geometries obtained with def2-TZVP basis set. The MECP intersections for active site complexes with charge 0 and -2 are for triplet (S=1)/quintet (S=3) states. The MECP intersections for the active site with charge -1 are for quartet (S=3/2)/sextet (S=5/2) states. r Fe-S is the bond length between iron and sulfur. θ S-Fe-S is the average of the bond angles between S1-Fe-S4 and S2-Fe-S3. θ S-Fe-S' is the average of the bond angles between S1-Fe-S2, S1-Fe-S3, S2-Fe-S4, and S3-Fe-S4. φ C-S-Fe-S is the average of the dihedral angles C3-S3-Fe-S4 and C2-S2-Fe-S1. φ C'-S'-Fe-S is the average of the dihedral angles C1-S1-Fe-S2 and C4-S4-Fe-S3.

MECP Geometries	r Fe-S (Å)	θ S-Fe-S (deg)	θ S-Fe-S' (deg)	φ C-S-Fe-S (deg)	φ C'-S'-Fe-S (deg)
$[Fe(SCH_3)_4]^0$					
PBE MECP S=1,2	2.189	132.6	100.0	165.6	29.1
LC-BLYP MECP S=1,2	2.137	133.7	98.9	177	24.9
$[Fe(SCH_3)_4]^{1-}$					
PBE MECP S=3/2,5/2	2.266	119.1	104.9	174.7	48.7
LC-BLYP MECP S=3/2,5/2	2.227	123.2	103.1	172.1	43.0
$[Fe(SCH_3)_4]^{2-}$					
PBE MECP S=1,2	2.299	143.9	95.5	166.4	33.4
LC-BLYP MECP S=1,2	2.302	146.8	94.7	172.5	24.1

Table S4. Twist angles (degrees), $<S^2>$ values, and H_{SO} (cm^{-1}) for MECP geometries with different levels of theory. All geometries obtained with def2-TZVP basis set. The MECP intersections for active site complexes with charge 0 and -2 are for triplet (S=1)/quintet(S=3) states. The MECP intersections for the active site with charge -1 are for quartet (S=3/2)/sextet (S=5/2) states.

MECP Geometries	Twist Angles			$<S^2>$ value		H_{SO}
	α	β	γ			
[Fe(SCH$_3$)$_4$]^0						
PBE MECP S=1,2	63.4	63.4	89.8	6.056	2.077	8
LC-BLYP MECP S=1,2	62.9	61.8	91.2	6.064	2.091	6
[Fe(SCH$_3$)$_4$]$^{1-}$						
PBE MECP S=3/2,5/2	79.4	79.5	90.0	8.764	3.849	23
LC-BLYP MECP S=3/2,5/2	74.8	74.8	90.0	8.770	3.830	56
[Fe(SCH$_3$)$_4$]$^{2-}$						
PBE MECP S=1,2	49.6	49.5	90.0	6.030	2.049	157
LC-BLYP MECP S=1,2	45.7	45.8	89.9	6.016	2.031	15
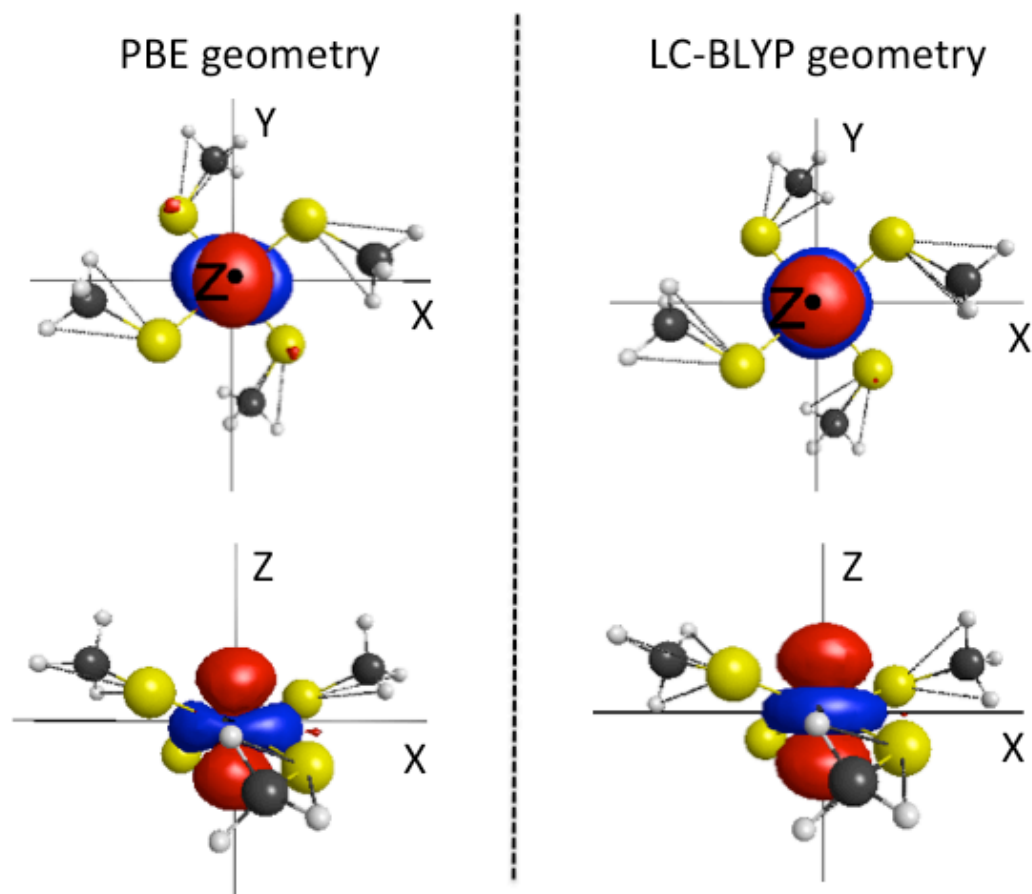
Figure S2. ROHF molecular orbital 2 of the $Fe(SCH_3)_4^{2-}$ complex (see Figure 5 in the paper). Geometry of the complex was optimized using the PBE (left panel) and LC-BLYP (right panel) density functionals. Two different orientations (upper and lower panels) are shown. At the PBE optimized geometry, mixing of the d_{z2} orbital with other orbitals (mostly d_{xz}) of Fe is significant. At the LC-BLYP geometry, the molecular orbital is almost identical to the d_{z2} orbital of Fe.

Geometries of the minima and MECPs for each oxidation state obtained at the PBE/def2-TZVP level of theory

[Fe(SCH$_3$)$_4$]$^{2-}$ Singlet Minima:
E = -3015.189621 hartrees

FE	26.0	-0.0002174477	0.0049445462	-0.0048234719
S	16.0	-1.7877567970	-1.3507052467	0.2478311284
S	16.0	-1.3568956055	1.7937109233	-0.2419443943
S	16.0	1.3541832482	-1.7839148040	-0.2542810154
S	16.0	1.7899132200	1.3604923686	0.2296959004
C	6.0	-3.3907198144	-0.4922674313	0.5161144968
C	6.0	-0.4997711268	3.3978494232	-0.5077554370
C	6.0	0.4948716692	-3.3887635170	-0.5085554464
C	6.0	3.3957358893	0.5022045949	0.4812788589
H	1.0	-4.2099372701	-1.2240725200	0.3932161703
H	1.0	-1.2308776517	4.2164650918	-0.3782659652
H	1.0	1.2273913274	-4.2069959869	-0.3844798605
H	1.0	4.2136112409	1.2337872640	0.3491342405
H	1.0	-3.5285461281	0.3313695722	-0.2030988420
H	1.0	0.3272079352	3.5333357615	0.2078567473
H	1.0	-0.3249782334	-3.5227634633	0.2155302289
H	1.0	3.5257748655	-0.3217332388	-0.2389598839
H	1.0	-3.4564194737	-0.0554095455	1.5274775347
H	1.0	-0.0673262054	3.4667810902	-1.5207654647
H	1.0	0.0525316150	-3.4600126850	-1.5171666411
H	1.0	3.4722247426	0.0656978029	1.4919611162

[Fe(SCH$_3$)$_4$]$^{2-}$ Triplet Minima:
E = -3015.207002 hartrees

FE	26.0	-0.0003664361	0.0047582229	-0.0046437537
S	16.0	-1.8037721141	-1.3564331931	0.1959553496
S	16.0	-1.3624085378	1.8089514109	-0.1926479253
S	16.0	1.3601807633	-1.7993836847	-0.2040566002
S	16.0	1.8044074428	1.3660011480	0.1823363415
C	6.0	-3.4106368408	-0.4957489871	0.4339077908
C	6.0	-0.5026579052	3.4170272097	-0.4255551793
C	6.0	0.4988183584	-3.4081692045	-0.4260160255
C	6.0	3.4147641784	0.5058557190	0.3984420842
H	1.0	-4.2277005765	-1.2205400904	0.2655525569
H	1.0	-1.2269166761	4.2332359619	-0.2505398597
H	1.0	1.2241919036	-4.2239574964	-0.2539675594
H	1.0	4.2291160003	1.2315676785	0.2211673130
H	1.0	-3.5215154094	0.3459105312	-0.2687987665
H	1.0	0.3414985282	3.5243408115	0.2747843949
H	1.0	-0.3399920089	-3.5130862898	0.2809788707

H   1.0 3.5174925206 -0.3344777928 -0.3070327494
H   1.0 -3.5077665003 -0.0838790486 1.4529023204
H   1.0 -0.0946136518 3.5193111598 -1.4455974359
H   1.0 0.0831072109 -3.5135295541 -1.4426023358
H   1.0 3.5247697498 0.0922454894 1.4154311687

[Fe(SCH₃)₄]²⁻ Quintet Minima:
E = -3015.217104 hartrees
FE   26.0 -0.0009723651 0.0007994889 -0.0049086561
S   16.0 -1.2788893365 -1.4724411873 1.3064407063
S   16.0 -1.4679583071 1.2718055029 -1.3306109851
S   16.0 1.4805973725 -1.2643094964 -1.3192026660
S   16.0 1.2568585307 1.4760949267 1.3241097032
C   6.0 -2.5522501242 -0.3691557592 2.0396516566
C   6.0 -0.3640420860 2.5468431659 -2.0597329930
C   6.0 0.3855739255 -2.5372765877 -2.0651863885
C   6.0 2.5313195655 0.3803660088 2.0662625167
H   1.0 -3.2426364955 -0.9403859280 2.6887808594
H   1.0 -0.9328407483 3.2332942157 -2.7151540546
H   1.0 0.9619294028 -3.2188205893 -2.7191717793
H   1.0 3.2077039865 0.9539471041 2.7280218952
H   1.0 -3.1371059620 0.1299281880 1.2511294889
H   1.0 0.1274383434 3.1358024821 -1.2694904751
H   1.0 -0.1111402625 -3.1320377803 -1.2825968876
H   1.0 3.1314638926 -0.1074319805 1.2821674940
H   1.0 -2.0702220790 0.4165908405 2.6429410707
H   1.0 0.4276686964 2.0655029150 -2.6556679681
H   1.0 -0.4020175829 -2.0549188819 -2.6658115105
H   1.0 2.0495216333 -0.4141966487 2.6580289720

[Fe(SCH₃)₄]²⁻ MECP Singlet/Quintet:
E = -3015.186307 hartrees
FE   26.0 0.0081023974 0.0024289706 -0.0209517162
S   16.0 -1.7367226315 -1.3695183996 0.4790338809
S   16.0 -1.3692122516 1.7453549989 -0.5144306448
S   16.0 1.3859822424 -1.7471603566 -0.4816021996
S   16.0 1.7569955931 1.3835759674 0.4365920913
C   6.0 -3.2921003748 -0.4702384664 0.8680351651
C   6.0 -0.4783397189 3.3018941727 -0.9197326902
C   6.0 0.4937864756 -3.3112452419 -0.8536516791
C   6.0 3.3172128013 0.4939079355 0.8292871534
H   1.0 -4.1168267452 -1.1969722645 0.9883265651
H   1.0 -1.2085164476 4.1272650627 -1.0127326201
H   1.0 1.2232025634 -4.1386867852 -0.9299363981
H   1.0 4.1389516616 1.2263692684 0.9332027930

```
H        1.0  -3.5503632145   0.2378332232   0.0647733320
H        1.0   0.2533570944   3.5553694437  -0.1361215364
H        1.0  -0.2373458476  -3.5468003390  -0.0642414058
H        1.0   3.5738266995  -0.2254068378   0.0353528669
H        1.0  -3.1959772173   0.1148416478   1.7978584135
H        1.0   0.0779186185   3.2124688017  -1.8678764704
H        1.0  -0.0631389126  -3.2407033468  -1.8027022961
H        1.0   3.2291572145  -0.0775474549   1.7683773958
```

[Fe(SCH₃)₄]²⁻ MECP Triplet/Quintet:
E = -3015.200554 hartrees

```
FE       26.0  -0.0062007469   0.0111809947  -0.1568411365
S        16.0  -1.6815172789  -1.3935641887   0.5580674479
S        16.0  -1.4132545472   1.6911392430  -0.8454603952
S        16.0   1.3986442615  -1.6555412975  -0.8833942036
S        16.0   1.6750231112   1.4063863516   0.5646575302
C         6.0  -3.1117215838  -0.4502655402   1.2292681687
C         6.0  -0.4976184768   3.2392579195  -1.2197203606
C         6.0   0.5123819329  -3.2418164879  -1.1504408718
C         6.0   3.1072249439   0.4597419761   1.2260462399
H         1.0  -4.0326898696  -1.0605597823   1.1734065199
H         1.0  -1.2125059235   4.0683280064  -1.3777949507
H         1.0   1.2405362896  -4.0341521082  -1.4069516054
H         1.0   4.0308832543   1.0644010604   1.1559082191
H         1.0  -3.2554041801   0.4778440258   0.6556861512
H         1.0   0.1787693630   3.5042143845  -0.3915264410
H         1.0  -0.0377447785  -3.5422080078  -0.2447724034
H         1.0   3.2368626708  -0.4727241498   0.6561984639
H         1.0  -2.9481395294  -0.1723616504   2.2861322569
H         1.0   0.1205368856   3.1327020302  -2.1274083667
H         1.0  -0.2232495562  -3.1620774449  -1.9679975890
H         1.0   2.9535737583   0.1911046654   2.2867573264
```

[Fe(SCH₃)₄]¹⁻ Doublet Minima:
E = -3015.289093 hartrees

```
FE       26.0  -0.0165959237   0.0144853943   0.0455891087
S        16.0  -1.5334576033  -1.3251550594   0.8417638809
S        16.0  -1.3886445292   1.5786924880  -0.6491014938
S        16.0   1.3700315121  -1.5522604804  -0.6275159771
S        16.0   1.4971639974   1.3199683946   0.9163094733
C         6.0  -3.0848058082  -0.4399515825   1.2415105189
C         6.0  -0.4203534915   2.9969785568  -1.2847632961
C         6.0   0.4355197958  -2.9938050150  -1.2593044227
C         6.0   3.0775625774   0.4554664966   1.2284447081
H         1.0  -3.7676643529  -1.1472733298   1.7367359009
```

H	1.0	-1.1168172720	3.7425577440	-1.6983760546
H	1.0	1.1469136676	-3.6965866460	-1.7204177382
H	1.0	3.7667763296	1.1590149821	1.7199600670
H	1.0	-3.5606184846	-0.0498344313	0.3307765497
H	1.0	0.1679425050	3.4542839463	-0.4759907186
H	1.0	-0.0982552358	-3.4999693110	-0.4421752503
H	1.0	3.5230832993	0.1005834276	0.2884161426
H	1.0	-2.8828954513	0.4053595184	1.9125790919
H	1.0	0.2730633494	2.6734923391	-2.0726048016
H	1.0	-0.3031774161	-2.6801115691	-2.0092336921
H	1.0	2.9152285350	-0.4159358632	1.8773980029

$[Fe(SCH_3)_4]^{1-}$ Quartet Minima:

E = -3015.306652 hartrees

FE	26.0	-0.0002217962	0.0039930964	-0.0052214374
S	16.0	-1.5615835351	-1.3498246504	0.7623584908
S	16.0	-1.3566863114	1.5651231595	-0.7685926662
S	16.0	1.3544872825	-1.5597874883	-0.7660773973
S	16.0	1.5628266091	1.3609658748	0.7530961756
C	6.0	-3.0860874504	-0.4419856729	1.2146044380
C	6.0	-0.4513846232	3.0908842809	-1.2215844373
C	6.0	0.4473474771	-3.0859481928	-1.2141232947
C	6.0	3.0901921857	0.4564361090	1.2022253164
H	1.0	-3.8417897524	-1.1766453671	1.5334002458
H	1.0	-1.1875311273	3.8459075483	-1.5385488937
H	1.0	1.1825152434	-3.8424023758	-1.5299563194
H	1.0	3.8458935850	1.1930976256	1.5163972695
H	1.0	-3.4709813871	0.1264364914	0.3563456795
H	1.0	0.1182686928	3.4758369274	-0.3641938500
H	1.0	-0.1217302546	-3.4683118218	-0.3551861213
H	1.0	3.4729345410	-0.1136166359	0.3440959887
H	1.0	-2.8952315766	0.2610295722	2.0364948475
H	1.0	0.2503039018	2.9014789596	-2.0449442568
H	1.0	-0.2549774075	-2.8980088652	-2.0372778249
H	1.0	2.9034357031	-0.2446585750	2.0266880470

$[Fe(SCH_3)_4]^{1-}$ Sextet Minima:

E = -3015.299791 hartrees

FE	26.0	0.0026359368	0.0079699333	-0.0047044882
S	16.0	-1.1592657952	-1.4799323942	1.3023118550
S	16.0	-1.4894286658	1.1735827544	-1.3031178144
S	16.0	1.4857708531	-1.1620354969	-1.3102357550
S	16.0	1.1765188656	1.4950899506	1.2922755803
C	6.0	-2.2520736752	-0.3319242374	2.2209431981
C	6.0	-0.3446162805	2.2589910216	-2.2343978990

C	6.0	0.3331352194	-2.2548135772	-2.2230338720
C	6.0	2.2619845968	0.3454025505	2.2174044046
H	1.0	-2.7349432872	-0.8745931701	3.0471260368
H	1.0	-0.8916681001	2.7398536467	-3.0588585680
H	1.0	0.8732580536	-2.7430611863	-3.0477451603
H	1.0	2.7478854325	0.8895974838	3.0408263791
H	1.0	-3.0268320360	0.0794387959	1.5591382804
H	1.0	0.0737502182	3.0353826524	-1.5789270532
H	1.0	-0.0804722574	-3.0250885378	-1.5574635295
H	1.0	3.0341802742	-0.0746662583	1.5581202567
H	1.0	-1.6604027485	0.5013605330	2.6233652935
H	1.0	0.4840626119	1.6631100974	-2.6402064813
H	1.0	-0.4983753504	-1.6618008262	-2.6271500869
H	1.0	1.6648961354	-0.4818637355	2.6243294227

[Fe(SCH$_3$)$_4$]$^{1-}$ MECP Doublet/Sextet:

E = -3015.286867 hartrees

FE	26.0	0.0257433081	0.0077935249	0.0279539893
S	16.0	-1.3572435664	-1.3598710693	1.0772805825
S	16.0	-1.3972830701	1.4676318677	-0.8565439681
S	16.0	1.4470820402	-1.4311107250	-0.8910108224
S	16.0	1.4187847236	1.3859073886	1.0408780131
C	6.0	-2.7978018347	-0.4112716604	1.6828153795
C	6.0	-0.4052527288	2.7400312511	-1.7209380153
C	6.0	0.4428672177	-2.7202713371	-1.7162411689
C	6.0	2.8465865163	0.4279067902	1.6645102213
H	1.0	-3.5124520981	-1.1110198301	2.1433359142
H	1.0	-1.0857350956	3.5040400662	-2.1275326007
H	1.0	1.1166649110	-3.4887907802	-2.1256990896
H	1.0	3.5810872522	1.1280225156	2.0918489171
H	1.0	-3.2891280434	0.1208773096	0.8568015833
H	1.0	0.3023193144	3.2146852792	-1.0268694693
H	1.0	-0.2500733300	-3.1850288510	-1.0008897314
H	1.0	3.3170418836	-0.1410619584	0.8509465089
H	1.0	-2.4857635082	0.3267669203	2.4354836099
H	1.0	0.1661477745	2.2951671964	-2.5480182657
H	1.0	-0.1464028660	-2.2892907403	-2.5382218889
H	1.0	2.5285111999	-0.2775631582	2.4452503013

[Fe(SCH$_3$)$_4$]$^{1-}$ MECP Quartet/Sextet:

E = -3015.29688 hartrees

FE	26.0	0.0065381031	0.0186872825	-0.0201325658
S	16.0	-1.2933950359	-1.4310864765	1.1390406642
S	16.0	-1.4472761713	1.3265455572	-1.1650981768
S	16.0	1.4545002930	-1.2931505765	-1.1683150761

```
S       16.0   1.3223557481   1.4696815088   1.1190437806
C        6.0  -2.5559952612  -0.3712162727   1.9347229915
C        6.0  -0.3885304761   2.5883027266  -1.9633271174
C        6.0   0.3937329989  -2.5594995534  -1.9566160040
C        6.0   2.5751432464   0.4060207236   1.9245669988
H        1.0  -3.2028264283  -0.9997917590   2.5659026300
H        1.0  -1.0214049257   3.2433464458  -2.5813626731
H        1.0   1.0244537080  -3.2183107084  -2.5729454602
H        1.0   3.2361088491   1.0373424721   2.5380180828
H        1.0  -3.1721564259   0.1336579221   1.1779448873
H        1.0   0.1301029483   3.1960709477  -1.2090792041
H        1.0  -0.1232523495  -3.1627389402  -1.1976050441
H        1.0   3.1773951380  -0.1243680348   1.1739783089
H        1.0  -2.0773405437   0.3942400068   2.5609526625
H        1.0   0.3658249590   2.1094635823  -2.6026930730
H        1.0  -0.3615468919  -2.0833721271  -2.5969177599
H        1.0   2.0888185176  -0.3386647269   2.5697111482
```

$[Fe(SCH_3)_4]^0$ Singlet Minima:
E = -3015.217909 hartrees

```
FE      26.0   0.0011290567   0.0058735389   0.5641415124
S       16.0  -1.5082944912  -1.0352434562   1.6179790415
S       16.0  -1.3277000663   1.2199885860  -0.5273498669
S       16.0   1.3258651353  -1.2125582306  -0.5274080008
S       16.0   1.5140183776   1.0499543507   1.6100461225
C        6.0  -3.2294360057  -0.4799490606   1.3902318908
C        6.0  -0.2605434122   2.2808223665  -1.5597311496
C        6.0   0.2549274345  -2.2765965434  -1.5524570993
C        6.0   3.2343982892   0.4942501119   1.3773724854
H        1.0  -3.8701581787  -1.1647268127   1.9616365343
H        1.0  -0.9128087961   2.9124122313  -2.1789032717
H        1.0   0.9050246589  -2.9110572465  -2.1709868083
H        1.0   3.8771764681   1.1803074656   1.9448959720
H        1.0  -3.5141515190  -0.5088442446   0.3304344136
H        1.0   0.3717490607   2.9093771081  -0.9193225654
H        1.0  -0.3760682522  -2.9022370188  -0.9079370530
H        1.0   3.5155096824   0.5210687659   0.3165540976
H        1.0  -3.3534569669   0.5414151135   1.7720514334
H        1.0   0.3760885926   1.6620192738  -2.2043298982
H        1.0  -0.3831250145  -1.6599136819  -2.1976891474
H        1.0   3.3598559467  -0.5263626171   1.7607713570
```

$[Fe(SCH_3)_4]^0$ Triplet Minima:
E = -3015.224207 hartrees

```
FE      26.0   0.0004286963   0.0045421647   0.3593028225
```

```
S      16.0  -1.4436059644  -1.1949325024   1.3657079968
S      16.0  -1.3666401426   1.2408495239  -0.6855757034
S      16.0   1.3645040766  -1.2345786996  -0.6861132743
S      16.0   1.4474109794   1.2086643964   1.3558981505
C       6.0  -3.0729171468  -0.3987894144   1.5294857407
C       6.0  -0.3658989429   2.4338242574  -1.6365516559
C       6.0   0.3608430572  -2.4302233733  -1.6306277301
C       6.0   3.0777328598   0.4140976667   1.5169383749
H       1.0  -3.7093609203  -1.0732782831   2.1180004879
H       1.0  -1.0532867771   3.0359890261  -2.2469902709
H       1.0   1.0463326101  -3.0343539323  -2.2412392974
H       1.0   3.7164013452   1.0921935920   2.0988762189
H       1.0  -3.5225236677  -0.2370450248   0.5408473667
H       1.0   0.1977613660   3.0833104662  -0.9545693065
H       1.0  -0.2010726042  -3.0774664672  -0.9450774020
H       1.0   3.5231953432   0.2472538138   0.5272597041
H       1.0  -2.9755065283   0.5625791813   2.0481295625
H       1.0   0.3350746922   1.9015633140  -2.2907472573
H       1.0  -0.3419944254  -1.8997958905  -2.2843086908
H       1.0   2.9831220935  -0.5444038147   2.0413541628
```

[Fe(SCH$_3$)$_4$]^0 Quintet Minima:
E = -3015.212662 hartrees

```
FE     26.0   0.0488955340  -0.1622705851   0.2528846446
S      16.0  -1.5760042321  -1.3732813775   1.1101736875
S      16.0  -1.2731851296   1.0269420795  -1.0372707144
S      16.0   1.3014826421  -1.8907120694  -0.2917660368
S      16.0   1.4347272405   1.3517135410   1.0169013912
C       6.0  -2.9556472586  -0.2789248055   1.5716785171
C       6.0  -0.4502324432   2.5889822346  -1.4933135972
C       6.0   0.4038559303  -2.7016758958  -1.6556891989
C       6.0   3.0102076076   0.5256576533   1.4287372304
H       1.0  -3.7363679150  -0.9169093825   2.0090207425
H       1.0  -1.1123470305   3.0959309756  -2.2092574705
H       1.0   1.0859584495  -3.4289530271  -2.1157500673
H       1.0   3.6575479695   1.2744506937   1.9038624193
H       1.0  -3.3518717303   0.2343385614   0.6854614606
H       1.0  -0.3180780278   3.2274824667  -0.6108203006
H       1.0  -0.4745565962  -3.2226399891  -1.2534439239
H       1.0   3.4889716634   0.1544779050   0.5141596918
H       1.0  -2.6388633283   0.4669619625   2.3111660571
H       1.0   0.5247366106   2.4022811070  -1.9566929510
H       1.0   0.0841301060  -1.9670305562  -2.4036918279
H       1.0   2.8466399378  -0.3068214923   2.1236502461
```

[Fe(SCH$_3$)$_4$]^0 MECP Singlet/Quintet:
E = -3015.2109 hartrees

FE	26.0	0.0236575755	-0.0479824519	0.2187754161
S	16.0	-1.4740511979	-1.3719874902	1.0735642122
S	16.0	-1.3394661270	1.3585948654	-0.7353486312
S	16.0	1.3893219367	-1.5410112319	-0.5929875708
S	16.0	1.4429650738	1.3503550618	1.0840715835
C	6.0	-2.9524958293	-0.4226946354	1.5532688330
C	6.0	-0.3352245123	2.6417894320	-1.5519119148
C	6.0	0.3817523634	-2.6775494425	-1.6024649703
C	6.0	2.9991059425	0.4892152855	1.4835511333
H	1.0	-3.6499796750	-1.1273424102	2.0260444462
H	1.0	-1.0299864025	3.3059757396	-2.0846036892
H	1.0	1.0625147011	-3.4232000266	-2.0348795488
H	1.0	3.6463396446	1.2092907159	2.0017020374
H	1.0	-3.4255502569	0.0216524255	0.6672078957
H	1.0	0.2304644882	3.2127692813	-0.8046047440
H	1.0	-0.3669627604	-3.1731982542	-0.9716279361
H	1.0	3.4930443726	0.1493224051	0.5635175351
H	1.0	-2.6908744843	0.3684584464	2.2657872552
H	1.0	0.3620143592	2.1925219066	-2.2690043049
H	1.0	-0.1239883480	-2.1335411619	-2.4092319493
H	1.0	2.8065991360	-0.3702184603	2.1363249117

[Fe(SCH$_3$)$_4$]^0 MECP Triplet/Quintet:
E = -3015.212100 hartrees

FE	26.0	0.0168202827	-0.1233892777	0.2481223792
S	16.0	-1.5570436471	-1.3859276217	1.0987308088
S	16.0	-1.3345655807	1.1944041829	-0.8600514887
S	16.0	1.3517896882	-1.7329611877	-0.4155265617
S	16.0	1.3947959064	1.3409611406	1.0973360731
C	6.0	-2.9761624020	-0.3599583543	1.5965713440
C	6.0	-0.3591783374	2.5836898080	-1.5244564589
C	6.0	0.3973806319	-2.6801811526	-1.6470944171
C	6.0	2.9904249821	0.5300095758	1.4504220219
H	1.0	-3.7104363319	-1.0348620582	2.0580250184
H	1.0	-1.0214864615	3.1405739807	-2.2019877839
H	1.0	1.0803406685	-3.4123786611	-2.0981888579
H	1.0	3.6403097510	1.2792857858	1.9211998070
H	1.0	-3.4272845039	0.1259815607	0.7211130304
H	1.0	-0.0283769519	3.2399997042	-0.7096201276
H	1.0	-0.4322207892	-3.2031854496	-1.1537538443
H	1.0	3.4513076309	0.1778634717	0.5187732103
H	1.0	-2.6759492705	0.4036851446	2.3245191773
H	1.0	0.5145978790	2.2252068168	-2.0806027788

H	1.0	0.0019914457	-2.0194039132	-2.4275576347
H	1.0	2.8519254097	-0.3155134957	2.1347070832

Geometries of the MECPs for each oxidation state obtained at the LC-BLYP/def2-TZVP level of theory

$[Fe(SCH_3)_4]^{-2}$ MECP Singlet/Quintet:
E = -3014.658249 hartrees

FE	26.0	0.0045711172	0.0033809085	-0.0253802181
S	16.0	-1.3381390678	-1.2130886171	1.0888750565
S	16.0	-1.4331281620	1.6604636459	-0.4578261304
S	16.0	1.4352632403	-1.6590066513	-0.4334939491
S	16.0	1.3687853114	1.2403460483	1.0408289276
C	6.0	-2.9071591338	-0.3697700968	1.4255457478
C	6.0	-0.4558531834	2.7575679815	-1.5263796605
C	6.0	0.4610365880	-2.7825883404	-1.4775606099
C	6.0	2.9420090161	0.4084069097	1.3931602991
H	1.0	-3.5837854735	-1.0619491097	1.9482513581
H	1.0	-1.0773744404	3.5837779687	-1.9038845028
H	1.0	1.0883138535	-3.6160241676	-1.8279929348
H	1.0	3.6173412059	1.1181902296	1.8939867950
H	1.0	-3.3850658656	-0.0287268598	0.4993356820
H	1.0	0.3891890013	3.1699392379	-0.9628716500
H	1.0	-0.3867293745	-3.1849729740	-0.9102985935
H	1.0	3.4199993888	0.0433956651	0.4759634911
H	1.0	-2.7499467327	0.5158003467	2.0534453336
H	1.0	-0.0396800495	2.2180122803	-2.3876040339
H	1.0	0.0501555109	-2.2664361447	-2.3558470428
H	1.0	2.7901472500	-0.4596882611	2.0466066352

$[Fe(SCH_3)_4]^{-2}$ MECP Triplet/Quintet:
E = -3014.702942 hartrees

FE	26.0	0.0066084694	0.0026645118	0.0090923653
S	16.0	-1.6695629291	-1.4164299769	0.6965430078
S	16.0	-1.4239341979	1.6826246475	-0.6511806588
S	16.0	1.4197444345	-1.6883672179	-0.6550903013
S	16.0	1.7012976379	1.4339771525	0.6285843549
C	6.0	-3.1694846132	-0.4683026341	1.0645049873
C	6.0	-0.4699448339	3.1647533583	-1.0744447681
C	6.0	0.4598845863	-3.1716024892	-1.0582400473
C	6.0	3.1824287082	0.4860215653	1.0688273114
H	1.0	-3.9406365191	-1.1381624852	1.4718079070
H	1.0	-1.1454756516	3.9443424178	-1.4558092031
H	1.0	1.1341859074	-3.9607065164	-1.4214837338
H	1.0	4.0162214754	1.1745898964	1.2699041990

H	1.0	-3.5632917348	0.0164747576	0.1644257601
H	1.0	0.0642013048	3.5563622572	-0.2016769257
H	1.0	-0.0825092033	-3.5448605518	-0.1829372318
H	1.0	3.4725388199	-0.1945933667	0.2614202998
H	1.0	-2.9712733040	0.3271521068	1.7910590013
H	1.0	0.2862541656	2.9482577288	-1.8370995322
H	1.0	-0.2894720848	-2.9642557360	-1.8302060801
H	1.0	3.0166095626	-0.1289094257	1.9618192886
H	1.0	-2.6759492705	0.4036851446	2.3245191773
H	1.0	0.5145978790	2.2252068168	-2.0806027788
H	1.0	0.0019914457	-2.0194039132	-2.4275576347
H	1.0	2.8519254097	-0.3155134957	2.1347070832

[Fe(SCH$_3$)$_4$]$^{-1}$ MECP Doublet/Sextet:
E = -3014.765757 hartrees

FE	26.0	0.0200982310	0.0081241625	0.0315956542
S	16.0	-1.4066617827	-1.3357174770	0.9762581161
S	16.0	-1.4007537736	1.5049387402	-0.7226610891
S	16.0	1.4325383572	-1.4702039435	-0.7623639495
S	16.0	1.4426947709	1.3518941847	0.9749959860
C	6.0	-2.8789765501	-0.3924244734	1.4264815959
C	6.0	-0.4196004284	2.8295439612	-1.4633113163
C	6.0	0.4578445349	-2.8214090257	-1.4652397993
C	6.0	2.9301705424	0.4223506379	1.4045044319
H	1.0	-3.5524609050	-1.0437647965	1.9933859309
H	1.0	-1.0967648655	3.5672705291	-1.9070320484
H	1.0	1.1407982571	-3.5684565047	-1.8836354451
H	1.0	3.5982566490	1.0767529260	1.9745529672
H	1.0	-3.3975962967	-0.0239828370	0.5368800716
H	1.0	0.2005333346	3.3179403228	-0.7068414320
H	1.0	-0.1622757077	-3.2916446570	-0.6969890895
H	1.0	3.4488545644	0.0747434366	0.5068437666
H	1.0	-2.6108524813	0.4704063738	2.0410912062
H	1.0	0.2395526958	2.4407633372	-2.2440775700
H	1.0	-0.2007264547	-2.4624149337	-2.2607829282
H	1.0	2.6810273084	-0.4511599637	2.0114849408

[Fe(SCH$_3$)$_4$]$^{-1}$ MECP Quartet/Sextet:
E = -3014.780039 hartrees

FE	26.0	0.0057445606	0.0139655809	-0.0165483824
S	16.0	-1.3279104284	-1.4175163638	1.0480398583
S	16.0	-1.4289614197	1.3508295037	-1.0734358162
S	16.0	1.4377280475	-1.3229473403	-1.0758279636
S	16.0	1.3420407671	1.4494305339	1.0388480810
C	6.0	-2.6424057220	-0.3766183535	1.7267468594

```
C        6.0  -0.3954047950   2.6687585883  -1.7565468909
C        6.0   0.4007044086  -2.6426261973  -1.7500101904
C        6.0   2.6623490371   0.4160976844   1.7172522640
H        1.0  -3.3146483562  -0.9976796921   2.3284802702
H        1.0  -1.0225331058   3.3386117444  -2.3545924375
H        1.0   1.0244559154  -3.3148173587  -2.3488905111
H        1.0   3.3323940748   1.0425262464   2.3157473625
H        1.0  -3.2153332931   0.0985946655   0.9256836794
H        1.0   0.0820295446   3.2437819446  -0.9582812630
H        1.0  -0.0731715104  -3.2145937525  -0.9475206561
H        1.0   3.2365981298  -0.0585043212   0.9167992158
H        1.0  -2.2255321943   0.4101784782   2.3616333075
H        1.0   0.3893472744   2.2553950184  -2.3961947493
H        1.0  -0.3870443172  -2.2309093232  -2.3869943423
H        1.0   2.2508033820  -0.3707972863   2.3554023050
```

[Fe(SCH$_3$)$_4$]^0 MECP Singlet/Quintet:

E = -3014.661139 hartrees

```
FE      26.0   0.0161139306   0.0017736549   0.0025299615
S       16.0  -1.2456015180  -1.3595233000   0.9838946101
S       16.0  -1.3328104442   1.2588855343  -1.0013154559
S       16.0   1.3767727929  -1.2584065694  -0.9841582166
S       16.0   1.2625141162   1.3605850339   1.0079480259
C        6.0  -2.4668585648  -0.3618002416   1.8565194633
C        6.0  -0.3269815902   2.4811244107  -1.8640357666
C        6.0   0.3778894266  -2.4859412917  -1.8480992974
C        6.0   2.5043448508   0.3688758872   1.8583306985
H        1.0  -3.0580796644  -1.0348105336   2.4836538212
H        1.0  -0.9853502328   3.0393146788  -2.5355951126
H        1.0   1.0493028015  -3.0775087270  -2.4765519039
H        1.0   3.0662339832   1.0355026834   2.5185522155
H        1.0  -3.1251096927   0.1458138911   1.1474698498
H        1.0   0.1345987009   3.1693166299  -1.1518918982
H        1.0  -0.1245696104  -3.1431810793  -1.1345045586
H        1.0   3.1871282468  -0.0889446935   1.1387418321
H        1.0  -1.9765077070   0.3804682373   2.4897043363
H        1.0   0.4534720897   1.9928731735  -2.4512380466
H        1.0  -0.3691488536  -2.0003835864  -2.4792097699
H        1.0   2.0318469388  -0.4128137925   2.4564052119
```

[Fe(SCH$_3$)$_4$]^0 MECP Triplet/Quintet:

E = -3014.66066 hartrees

```
FE      26.0   0.0070809615   0.0005323062   0.2291277329
S       16.0  -1.4271189970  -1.3314274248   1.0817415588
S       16.0  -1.3653011151   1.4175562479  -0.5982711713
```

```
S       16.0   1.3766972967  -1.4139576357  -0.6065164630
S       16.0   1.4465482465   1.3326034462   1.0739091973
C        6.0  -2.9613371973  -0.4544466217   1.4188230507
C        6.0  -0.3530694600   2.6215331693  -1.4778448394
C        6.0   0.3635775621  -2.6301096865  -1.4683711593
C        6.0   2.9826780691   0.4572716359   1.4061924210
H        1.0  -3.6270517779  -1.1489365629   1.9378774084
H        1.0  -1.0284862517   3.2946107686  -2.0129389325
H        1.0   1.0373157184  -3.2864332836  -2.0260295272
H        1.0   3.6534078574   1.1552824733   1.9140127554
H        1.0  -3.4349290263  -0.1304101109   0.4883619500
H        1.0   0.2551545323   3.1929402233  -0.7722041401
H        1.0  -0.2143392119  -3.2183176683  -0.7510890778
H        1.0   3.4494365384   0.1244731666   0.4754183917
H        1.0  -2.7796522314   0.4155813918   2.0525889753
H        1.0   0.3049664037   2.1293727426  -2.1965274151
H        1.0  -0.3227056966  -2.1461400125  -2.1658283274
H        1.0   2.8061077790  -0.4076785647   2.0482476117
```

References

(1)   Nikitin, E. E. Nonadiabatic Transition Near the Turning Point in Atomic Collisions. *Opt. Spectrosc.* **1961**, *11*, 246–248.

(2)   Nikitin, E. E.; Umanskii, S. Y. *Theory of Slow Atomic Collisions*; Springer-Verlag Berlin Heidelberg: New York, 1984.

(3)   Delos, J. B. On the Reactions of N_2 with O. *J. Chem. Phys.* **1973**, *59*, 2365.

(4)   Coveney, P. V; Child, M. S.; Barany, A. The Two-State S Matrix for the Landau-Zener Potential Curve Crossing Model: Predissociation and Resonant Scattering. *J. Phys. B At. Mol. Phys.* **1985**, *18*, 4557–4580.

(5)   Luo, Y.; Niu, S.; Ichiye, T. Understanding Rubredoxin Redox Sites by Density Functional Theory Studies of Analogues. *J. Phys. Chem. A* **2012**, *116*, 8918–8924.

(6)   Maelia, L. E.; Millar, M.; Koch, S. A. General Synthesis of Iron (III) Tetrathiolate Complexes. Structural and Spectroscopic Models for the [Fe(Cys-S)$_4$] Center in Oxidized Rubredoxin. *Inorg. Chem.* **1992**, *31,* 4594-4600.

(7)   Yang, X.; Wang, X. Bin; Fu, Y. J.; Wang, L. S. On the Electronic Structure of [1Fe] Fe-S Complexes from Anionic Photoelectron Spectroscopy. *J. Phys. Chem. A* **2003**, *107*, 1703–1709.

(8)   Niu, S.; Wang, X. Bin; Nichols, J. a.; Wang, L. S.; Ichiye, T. Combined Quantum Chemistry and Photoelectron Spectroscopy Study of the Electronic Structure and Reduction Potentials of Rubredoxin Redox Site Analogues. *J. Phys. Chem. A* **2003**, *107*, 2898–2907.

Appendix C - Supporting Information for Chapter VI
3D Printed Potential and Free Energy Surfaces for Teaching Fundamental Concepts in Physical Chemistry

MOLPRO input file for hydrogen exchange reaction

```
memory, 100,m

symmetry,x,y

geometry={
H;
h1,H,r1;
h2,H,r2,h1,theta;}

basis=aug-cc-pVTZ

theta=180 DEG

mind2=0.4
maxd2=2.1

mind1=0.4
maxd1=1.5
dr=0.025

r1=0.74
r2=0.74

{HF
}
{casscf
occ,2,0,0,0
closed,0,0,0,0
wf,3,1,1
ORBITALS,2140.3}

i=0
do r1=mind1,maxd1,dr,ANG
do r2=mind2,maxd2,dr,ANG

i=i+1

vr2(i)=r2
vr1(i)=r1
```

```
HF
{casscf
occ,2,0,0,0
closed,0,0,0,0
wf,3,1,1}

{mrci
maxiter, 100, 100
wf,3,1,1
save,4010.1}

e1(i)=energy(1)

end do

{table, vr1, vr2, e1
head, r1,r2, e1
digits,4,4,8
save, H3.tab}
i=0
end do
```

MOLPRO input file for rotations of methyl groups in 1-fluoro-2-methylpropene
memory,500,m
angstrom
geometry={
C
C 1   r1
C 2   r2 1 r3
C 2   r4 1 r5 3 r6
H 1   r7 2 r8 3   r9
F 1   r10 5 r11 2 r12
H 3   r13 2 r14 5 rd1
H 4   r15 2 r16 6 rd2
H 4   r17 8 r18 2 r19
H 4   r20 9 r21 8 r22
H 3   r23 7 r24 2 r25
H 3   r26 11 r27 7 r28}

basis=6-31G

r1=1.34131
r2=1.45831
r3=120.8794
r4=1.48502
r5=121.5034
r6=180.0000
r7=1.097285
r8=122.46
r9=0.00
r10=1.097185
r11=115.29
r12=180.00
r13=1.10537
r14=114.8552
r15=1.11732
r16=111.3582
r17=1.11855
r18=108.3850
r19=-121.3595
r20=1.11855
r21=108.2571
r22=117.3631
r23=0.90361
r24=107.1705
r25=120.6992
r26=0.92954

```
r27=109.4941
r28=-114.5766

mind2=0.0
maxd2=120.0
dr2=2

mind1=0.0
maxd1=120.0
dr1=2

i=0
do rd1=mind1,maxd1,dr1
do rd2=mind2,maxd2,dr2

i=i+1

vrd2(i)=rd2
vrd1(i)=rd1

{HF
wf,40,1,0}

{uks,b3lyp
wf,40,1,0}

{optg
inactive,rd1,rd2}

e1(i)=energy(1)

end do

{table,vrd1,vrd2,e1
head, r1,r2,e1
digits,4,4,8
save, C4H7F_DFT.tab}

i=0
end do
```